October 2019

The Impact of Protostellar Feedback on Astrochemistry

Brandt Gaches

THE IMPACT OF PROTOSTELLAR FEEDBACK ON ASTROCHEMISTRY

A Dissertation Presented

by

BRANDT A. L. GACHES

Submitted to the Graduate School of the
University of Massachusetts Amherst in partial fulfillment
of the requirements for the degree of

DOCTOR OF PHILOSOPHY

September 2019

Astronomy

THE IMPACT OF PROTOSTELLAR FEEDBACK ON ASTROCHEMISTRY

A Dissertation Presented

by

BRANDT A. L. GACHES

Approved as to style and content by:

Ron Snell, Chair

Stella Offner, Member

Mark Heyer, Member

Bret Jackson, Member

Karin Öberg, Member

D. Calzetti, Department Chair
Astronomy

DEDICATION

To my amazing family who have provided endless support over the years, and to my faithful companion of 9 years, through thick and thin, a true best friend, Mojo the beagle.

EPIGRAPH

"The value of ζ for any species is a function of depth into an interstellar cloud, although this dependence is most frequently ignored because it is difficult to calculate." - V. Wakelam 2013, *Astrochemistry: Synthesis and Modelling*

ACKNOWLEDGMENTS

This thesis would not have been possible without the incredible support of my dissertation adviser, Prof. Stella Offner. My most sincere gratitude goes to her for her patience, guidance, and advice throughout my time as her graduate student. She has provided a huge amount of time during my tenure as her student to support my research, both as a collaborator and a mentor, and in the preparation of papers which have been accepted for publication. Her mentoring has led to great improvement in every aspect of academic life. She has continuously encouraged attending international conferences and applying for external funding sources, which through her mentoring, have funded the majority of my conference trips. I am eternally grateful to have such a fantastic adviser, and I am anticipating a long-lasting collaboration.

I am extremely grateful to the many collaborators and colleagues who have assisted me throughout my graduate career. I acknowledge the support of my fellow graduate students, Dr. Kathryn Grasha, Dr. Andrew Battisti, Riwaj Pokhrel, Duo Xu, and Dr. Yao-Lun Yang, and collaborators Dr. Anna Rosen and Dr. Aaron Lee for assisting with everything from brainstorming to coding advice to career advice and personal support. I wish to thank my long time collaborator, Dr. Thomas Bisbas, for his continued support and help through many early-morning/late-night telecons. I am incredibly grateful to my undergraduate mentors Prof. Romeel Davé, Prof. Phil Pinto and Prof. Daniel Eisenstein for providing the opportunity to develop coding skills that were necessary for dissertation work. I wish to thank Prof. Neal Evans for his continued advice and help, particularly in guiding new observational proposals.

The work presented in this dissertation was supported by the National Science Foundation (NSF) grant AST-1510021 and the Massachusetts Space Grant Consor-

tium (MSGC). I acknowledge support from the American Astronomical Society and the University of Massachusetts Department of Astronomy Mary Dailey Irvine travel grant for support allowing me to attend numerous international and domestic conferences. The work presented in this thesis utilized the Massachusetts Green High Performance Computing Center (MGHPCC) in Holyoke, Massachusetts supported by the University of Massachusetts, Boston University, Harvard University, MIT, Northeastern University and the Commonwealth of Massachusetts. I also wish to acknowledge important software packages which were essential to this dissertation: Matplotlib, NumPy, SciPy, JupyterLab, Plotly, 3d-pdr, Radmc-3d and Orion2.

ABSTRACT

THE IMPACT OF PROTOSTELLAR FEEDBACK ON ASTROCHEMISTRY

SEPTEMBER 2019

BRANDT A. L. GACHES

B.S., UNIVERSITY OF ARIZONA

Ph.D., UNIVERSITY OF MASSACHUSETTS AMHERST

Directed by: Professor Ron Snell

Star formation is the process by which gas within a galaxy is converted into stars. In the Milky Way, star formation occurs in molecular clouds, regions of the interstellar medium in which hydrogen exists in its molecular form, H_2. However, molecular hydrogen is a perfectly symmetric molecule, rendering it largely invisible at the temperatures of molecular clouds. Therefore, studies of star formation rely on tracers of the gas mass. Molecular line emission at sub-millimeter and millimeter wavelengths from rotational transitions provides crucial information into the dynamical state of the gas through Doppler shifts in the line. There are currently over 200 molecules which have been detected in the interstellar medium, ranging from simple diatomic molecules, such as cyanide (CN) and carbon monoxide (CO), to complex organic molecules, such as methyl acetate (CH_3COOCH_3). Carbon monoxide is among the most important molecules for astronomers: it is the most abundant molecule after H_2 making it ubiquitous in molecular clouds. Emission from CO is used to study

the dynamics of molecular clouds, and thus star formation, from locally star forming regions in the Milky Way to galaxies in the early universe. As such, understanding the chemistry of the molecular phase of the interstellar medium is vital to interpreting physics form molecular line emission.

In the first part of the dissertation, we present a statistical study quantifying how emission from different molecules changes the inferred properties of turbulence. We post-process a simulation of a molecular cloud with an astrochemical code providing the spatial distribution of over 200 molecules. We perform synthetic observations for a subset of these molecules, those of particular importance, to generate predictions for the molecular line emission. Having synthetic observations of many different molecules for the same simulated molecular cloud allows us to directly quantify how the appearance of turbulence changes with the tracer used. We find three different groupings of molecules which trace similar density regimes: diffuse, intermediate and dense densities. We show that the turbulence traced by neutral carbon emission is statistically consistent with that traced by carbon monoxide. We conclude that turbulence appears quite different when traced by a variety of molecules. The physics derived through molecular emission is thus observed through a chemical lens. Understanding this lens allows a proper inference of physics through the chemistry.

In the second part, we present our methodology for generating synthetic protoclusters using semi-analytic accretion models. We calculate the bolometric, far ultraviolet and ionizing luminosities of protoclusters using different accretion models. We find that the Tapered Turbulent Core model best explains the observed bolometric luminosities of clusters in Milky Way star forming regions. We generate synthetic protoclusters using the Tapered Turbulent Core model for clusters with a wide range of constituent numbers, from 10^2 to 10^6 protostars and a range of star formation efficiencies. We use the average far ultraviolet luminosities of these clusters as input into astrochemical models of molecular clouds. We conclude that far ultraviolet radi-

ation has a small effect on the total emission from carbon monoxide, but significantly changes thermo-chemistry of dense gas and the emission from optically thin species.

The third part of the thesis focuses on the possibility of cosmic ray acceleration in protostellar accretion shocks. We use semi-analytic accretion models to calculate the acceleration of cosmic rays in accretion shocks on the surface of protostars. We find that protostars can accelerate cosmic ray protons to energies of 10 - 20 GeV in their accretion shocks. Our protostellar cosmic ray models explain the increased ionization found in the protocluster OMC-2 FIR 4. We calculate the attenuation of protostellar cosmic rays through their natal cores and the resulting ionization rate gradient. We generate synthetic protoclusters and conclude that the cosmic rays accelerated by embedded protostars can exceed that of external sources for clusters hosting more than a few hundred protostars.

We extend a photo-dissociation region astrochemistry code to include cosmic ray attenuation in-situ. We use the modified code to quantify the impact of cosmic ray attenuation, different external spectra, and the inclusion of embedded sources on molecular cloud chemistry. We find that embedded sources significantly alter the chemistry of molecular clouds, although the H_2 is left unaltered. Molecular ions, such as HCO^+ are enhanced while neutral species, such as carbon monoxide and ammonia, are reduced by orders of magnitude. Furthermore, the abundance of atomic carbon within dense gas is increased by several orders of magnitude, providing a reservoir of atomic carbon in dense well-shielded gas. The astrochemical-cosmic ray models are consistent with the inferred cosmic ray ionization rates observed in diffuse and intermediate column density sight-lines.

We finish the dissertation by presenting simulations of a giant molecular cloud with far ultraviolet radiation transfer. We implement a novel adaptive six-ray algorithm to calculate the background radiation field yielding a better numerical scaling than the typical method. The simulations include the far ultraviolet radiation from protostars.

We examine the distribution of far ultraviolet radiation within the molecular cloud and the impact of internal sources. We show that there is only a weak correlation between the integrated line-of-sight column density and the background far ultraviolet radiation.

TABLE OF CONTENTS

LIST OF TABLES

LIST OF FIGURES

Figure **Page**

CHAPTER 1

OVERVIEW OF STAR FORMATION, PROTOSTELLAR FEEDBACK AND ASTROCHEMISTRY

1.1 The Molecular Phase of the Interstellar Medium

Ever since the first detection of diatomic molecules in the 1930's and 1940's through ultraviolet absorption [2, 3, 4], it has become increasingly clear that we live in a universe with a significant molecular reservoir. The first molecules were detected via their electronic transitions, when the electrons are excited to higher energies, in absorption at optical and ultraviolet wavelengths. Optical and ultraviolet molecular spectroscopy primarily detects diatomic molecules and probes diffuse gas with UV/optical bright background sources, the most popular of which is the high-mass star ζ Oph [5]. Molecules can also be detected via their vibrational excitations in the infrared [6, 7, 8] although this is quite difficult to do from the ground since the atmosphere blocks the infrared light. Predominately, molecules are found using their rotational excitations at radio wavelengths. In fact, roughly 80% of new molecule detections are found using radio techniques from submillimeter to centimeter wavelengths [9]. Since the first detection of diatomic molecules, astronomers have discovered over 200 unique molecule, plus isomers (where the constituents are the same but the structure different, e.g. HCN and HNC) and isotopes (where one or more element in the molecule has an extra neutron) [9]. There are two public databases of molecules detected in the interstellar medium: the Astrochymst's *Hyper-bibliography*

of Known Astromolecules[1] and the Cologne Database for Molecular Spectroscopy's *List of Molecules in Space*[2].

Molecular clouds are regions where hydrogen exists almost entirely in molecular form, H_2. However, H_2 is very difficult to observe: it is a perfectly symmetric molecule with no permanent dipole moment, thus at the cold temperatures of the molecular gas (around 10 - 30 Kelvin), it does not emit radiation. In regions where there are sources of radiation nearby, the gas can get warm enough for H_2 to emit radiation from vibrational and rotational excitations in the infrared [i.e. 10]. H_2 can also be observed via absorption in ultraviolet wavelengths [e.g. 11], although this necessitates an ultraviolet-bright background source. Due to the lack of a dipole moment and sparsity of regions where H_2 can be observed in the infrared or ultraviolet, studies of molecular gas largely rely on tracer molecules. The most important of these is the molecular carbon monoxide (CO). CO has a low excitation temperature and has relatively high abundance, typically the second most abundance molecule with $[CO]/[H_2] \approx 10^{-4}$, where [X] denotes the amount of molecule X with respect to hydrogen. Since CO was first detected in 1970 in the Orion Nebula [12], it has been the workhorse in the study of the molecular universe.

Figure 1.1 shows a map of the Milky Way in CO emission from the J=1-0 transition at 115 GHz. The disk of the Milky Way is quite evident in the CO emission. The molecular gas in the Milky Way accounts for 22% of the gas mass, making it a significant phase of the interstellar medium [13]. The molecular phase condenses when gas becomes dense enough for H_2 to form on dust grains. The gas cools through H_2 and C^+ line emission until it is cold enough to form further molecules. CO radiation constitutes a major coolant allowing the inner regions of molecular clouds to reach temperatures as low as 10 Kelvin.

---

[1] `http://astrochymist.org/astrochymist_mole.html`

[2] `https://www.astro.uni-koeln.de/cdms/molecules`

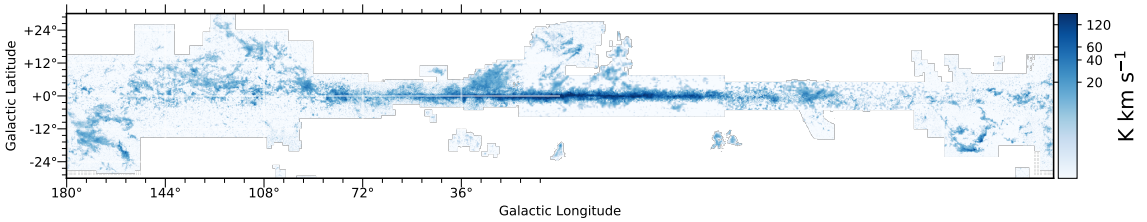

Figure 1.1. Integrated ^{12}CO (J = 1-0) 115 GHz emission from the Milky Way survey of Dame et al. [1]. The white areas indicate regions not sampled in the survey. Data from the Harvard Dataverse Repository[4]

Most importantly, astronomers now understand that effectively all star formation in the Milky Way and Local Galaxies occurs in complexes known as Giant Molecular Clouds (GMCs). Giant Molecular Clouds are complexes (not necessarily bound) of gas composed predominately of, and in order of the mass fraction, H_2, Helium, cold dust, and molecules. GMCs have structures dominated by the interplay between gravity, turbulence and magnetic fields. Since the physics of star formation is directly tied to the dynamics of molecular clouds, understanding their chemical is crucial to interpreting physics from molecular line observations.

1.2 Astrochemistry of Photo-dissociation Regions

Astrochemistry, also known as Molecular Astrophysics, is the study of molecular chemistry in astrophysical environments, the influence of chemistry on the dynamics of gas in these environments, and the emission from molecules across all wavelength regimes. An astronomical environment of particular interest is so called "photo-dissociation regions," or photon-dominated regions (PDRs). These are regions of mainly neutral gas, in that the hydrogen is neutral, where the chemistry is primarily influenced by ultraviolet light with energies between 6 eV and 13.6 eV, labeled the Far Ultraviolet (FUV). In terms of mass budget, the majority of the gas in a galaxy

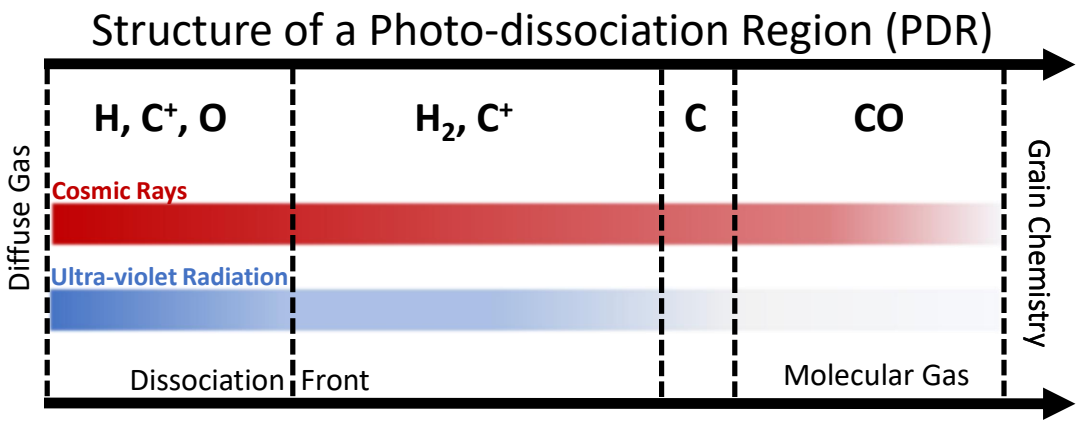

Figure 1.2. Structure of a Photo-dissociation Region indicating important chemical transitions and the driving energy sources, ultra-violet radiation and cosmic rays.

exists in a PDR, underscoring how important it is to understand the chemistry of PDRs. An important example of a PDR is the boundary of a GMC: here, the gas has too low of a column density to remove all the FUV radiation. FUV radiation that is impinging on the surface of molecular clouds comes from high-mass stars nearby in the galaxy. PDRs can also exist inside molecular clouds where star formation has occurred. Some of these internal PDRs are the most well studied, such as the Horsehead Nebula and the Orion Bar. Radiation with higher energies than FUV is called "ionizing" radiation, since it provides enough energy to ionize atomic hydrogen. The canonical PDR model comes from Hollenbach and Tielens [14], in which the gas is treated as a one-dimensional slab of gas which is irradiated on one side. Figure 1.2 shows a schematic of this canonical model. The diffuse gas is the regime where the hydrogen is mostly ionized (carbon and oxygen will be further ionized also). The transition between the diffuse gas and PDR is the ionization front. Further into the cloud, the UV field and temperature have decreased enough to enable molecular hydrogen, H_2, to form on the surface of grains. Where hydrogen suddenly becomes molecular is the dissociation front and in most PDR models is a sharp transition.

The lack of a permanent dipole greatly inhibits the formation of H_2. However, the symmetry of the molecule also means that it cannot dissociate immediately from the ground level. Instead, the molecule must be put into an increased ionization state, and during recombination there is a chance it recombines into an unbound ground level state. This quirk is called "self-shielding": only specific wavelengths of light are able to ionize H_2, photons with energies between 11.2 and 13.6 eV, called the Lyman-Werner bands. As H_2 begins to build up, gas on the surface layers of the PDR begin to shield the gas deeper in from the UV radiation. This model also produces a "layered-cake" interpretation of carbon chemistry. Towards the surface, the radiation field is sufficient to singly ionize carbon. Carbon becomes neutral as the radiation field decreases. However, quickly after that, the majority of the carbon gets processed into carbon monoxide (CO) resulting in a thin layer of neutral carbon. It is now widely thought that this model is incomplete: neutral carbon is found to be much more prevalent than if it were confined to just a thin layer. Real molecular clouds have complex porous structures brought on by turbulence allowing radiation to penetrate much further into the cloud. PDRs are also permeated by high-energy relativistic ions, called cosmic rays. The canonical model assumes that the flux of cosmic rays through the cloud is constant, meaning the ionization rate is also constant. However, it is known that this is not the case [15], but only until recently has it been numerically feasible to include any physics of cosmic ray propagation in astrochemical codes [16]. These cosmic rays drive the chemistry beyond the C-CO transition region.

The chemistry of a PDR is dominated by ion-neutral reactions. Many neutral-neutral reactions have a barrier: they require a small amount of input energy to occur. Ion-neutral reactions, however, occur freely. The most important reaction in starting the complex chemistry in PDRs, after the formation of H_2, is the formation of the ion H_3^+ through

$$\mathrm{CR} + \mathrm{H_2} \rightarrow \mathrm{H_2^+} + \mathrm{e^-} + \mathrm{CR'}$$

$$H_2^+ + H_2 \rightarrow H_3^+ + H,$$

where e^- is an electron, CR represents a cosmic ray particle, almost always assumed to be a proton, and CR' is the same cosmic ray as CR with less energy. The electron in the production of H_2^+ can lead to secondary ionizations depending on its energy. Once H_3^+ forms, a much more complex chemistry can rapidly follow through pathways such as

$$X + H_3^+ \rightarrow [XH]^+ + H_2.$$

This reaction leads to the formation of molecules such as N_2H^+ and HCO^+ through reactions with N_2 and CO, respectively. Since CO is a molecule of particular importance, it is worthwhile to review the chemistry of CO formation. CO has several ion-neutral reaction channels through C^+ via

$$OH + C^+ \rightarrow CO + H^+$$

$$OH + C^+ \rightarrow CO^+ + H$$

followed by the ion-neutral reaction

$$CO^+ + H \rightarrow CO + H^+$$

and through dissociations of the molecular ion HCO^+

$$HCO^+ + e^- \rightarrow CO + H$$

$$HCO^+ + \gamma \rightarrow CO^+ + H$$

where γ represents a photon. In more dense regimes, CO can also be efficiently formed through neutral-neutral reactions with simple carbon or oxygen molecules,

$$C[X] + O \rightarrow CO + X$$

where X can be H, H_2 or N.

$$C + OH \rightarrow CO + H$$

$$C + O_2 \rightarrow CO + O$$

On the surface of molecular clouds, CO can be efficiently destroyed through photo-dissociation,

$$CO + \gamma \rightarrow C + O$$

however, CO photo-dissociation is also affected by self-shielding and H_2. The primary destruction mechanism for CO follows after the ionization of Helium by a cosmic ray

$$He^+ + CO \rightarrow He + O + C^+.$$

These reactions are encoded for through reaction networks. Figure 1.3 shows the carbon subset of a reduced network to model CO. These networks are compiled from hundreds to thousands of reactions. Two examples of such networks which are publicly available are the UMIST network [18] and the Kinetic Database for Astrochemistry (KIDA) gas-phase network [19]. These networks have been expanded to include grain chemistry, deuterium and isotope chemistry, and spin chemistry, as well as many other more specialized uses [i.e. 20, 21, 22, 23, 24]. There are two different sizes of networks typically discussed. *Reduced* networks have on order tens of species and a hundred reactions typically selected to model CO, such as the Nelson-Langer network [25] or the updated Glover2010 network [26]. These networks are used mainly in hydro-dynamic codes or in three-dimensional astrochemical models due to numerical constrains. *Full* networks contain hundreds of species and thousands of reactions and result in higher accuracy models and knowledge of formation pathways. Due to

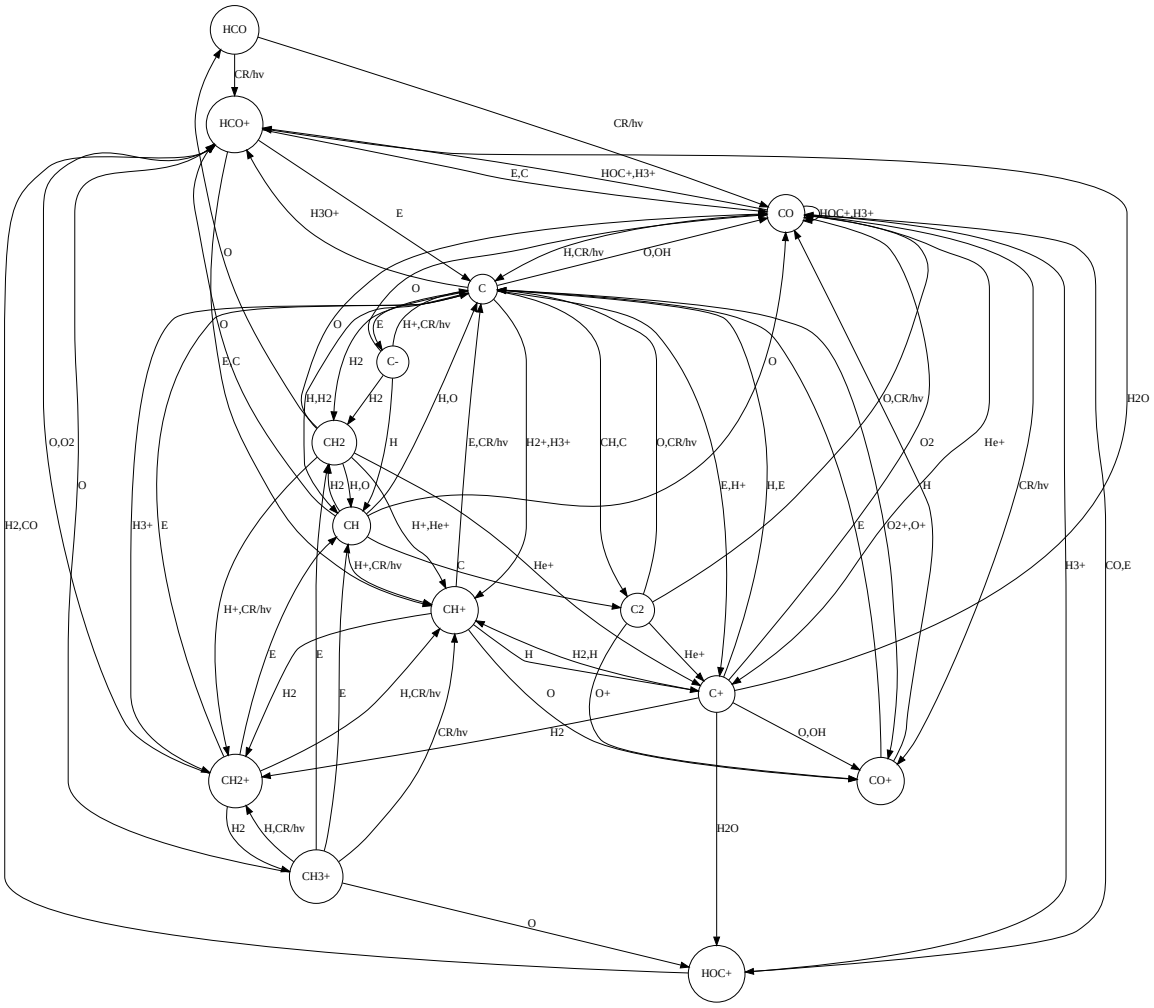

Figure 1.3. Carbon chemistry network generated using the KROME microphysics package [17] for a reduced CO network. The nodes indicate the species and the connecting lines show different reactions with the reaction partners annotated along the line.

the high numerical cost, use of these networks is constrained to 0D or 1D models. Astrochemical codes solve the following network of equations to evolve the chemistry:

$$\frac{dn_i}{dt} = \left(\sum_j \sum_k n_j n_k R_{jki} + \sum_l n_l \zeta_{li} \right) - n_i \left(\sum_l \zeta_{il} + \sum_l \sum_j n_j R_{ijl} \right) \tag{1.1}$$

where n_i is the number density of molecule, i, R_{ijk} is the reaction rate of equation $\mathrm{X_i + X_j \rightarrow X_k + ...}$, and ζ_{ij} is the reaction rate for interactions involving radiation or cosmic rays (e.g. $\mathrm{CO} + \gamma \rightarrow \mathrm{C} + \mathrm{O}$). Numerical codes to model PDRs sometimes make one of two different approximations to solve the network of equations: steady-state ($\frac{dn_i}{dt} = 0$) (e.g. MEUDON PDR code) or equilibrium ($t \rightarrow \infty$) (e.g. 3D-PDR). Within a network, there is a large range of timescales resulting in a stiff system of differential equations. Furthermore, there is a super-linear relation between the number of species and the number of reactions. This numerical constraint greatly limits the number of spatial dimensions or complexity of the physics included in astrochemistry codes.

There are two main types of astrochemical codes. PDR codes[5], such as UCLPDR [27, 28, 29], 3D-PDR [30], MEUDON PDR [31], KOSMA-τ [32] and CLOUDY [33, 34], include mainly gas-phase only chemistry along with detailed calculations for the thermal balance and radiation transfer of FUV radiation. Astrochemistry (or gas-grain) codes[5], such as UCLCHEM [24] and NAUTILUS[22], contain large networks with gas-phase and gas-grain chemistry, with NAUTILUS extending this further to reactions in ice mantles. While these codes solve very large networks of equations, they typically make assumptions on the physical nature of the gas, with the temperature and FUV radiation as inputs. Of these astrochemical codes, only 3D-PDR is extendable to 3D.

The chemistry of a region is a sensitive probe of the density, temperature, FUV radiation and cosmic rays of the constituent gas. Therefore, surveys of different

[5]Codes referenced here are public or easily accessible online

molecules, or their line transitions, provide useful diagnostics for physics. Optically thin molecular emission, such as from hydrogen cyanide (HCN), ammonia (NH_3) or methanol (CH_3OH) provide the total column density of that molecule. The temperature can be modeled if numerous lines are detected of the same molecule, however this requires significant observational time. With this information, non-local thermodynamic equilibrium models using codes such as RADEX[35] can be used to constrain the density and temperature. Furthermore, astrochemical modeling can be done to constrain the density and temperature structure if multiple molecules are observed for the same region. Emission from optically thick CO is observed and converted into the total gas mass or molecular hydrogen column density using conversion factors, α_{CO} and X_{CO}, respectively [36].

Nearly all the dynamical information we have about GMCs comes through line emission. The shape of the emission line, through the Doppler effect, provides the line-of-sight velocity profile. This information can be used to constrain bulk velocities, turbulence, and regions of quiescence. Surveys of molecular line emission, such as the "Milky Way CO Survey" [1], the "COordinated Molecular Probe Line Extinction Thermal Emission Survey of Star Forming Regions" (COMPLETE) [37] or the more recent "Green Bank Ammonia Survey" (GAS) [38], provide line-of-sight velocity information across a multitude of scales. The physics being interpreted from the line emission is observed through a chemical lens. Understanding this lens requires constraining the chemistry as best as possible, especially quantifying the impact of different physics on the chemistry.

1.3 Star Formation and Protostellar Evolution

Stars are the building blocks of galaxies, intrinsically tying the evolution of galaxies to that of stars. The star formation process is the cycling of gas into stars then back into gas [39]. The formation and deaths of stars leads to metal enrichment of the gas

with important atomic species, such as carbon and oxygen, in the universe. High-mass stars, in particular, are incredibly important for the evolution of galaxies since their high temperatures ionize large regions of the galaxy and their deaths lead to spectacular energetic events, such as supernova and the creation of black holes and neutron stars [40].

The process of star formation acts as initial conditions for planet formation. Planets form in the disks which rotate around the central forming star. The chemical composition of the gas in the disk is tied to the chemistry of star forming regions leading to an enrichment of organic molecules throughout the disk.

Stars are nearly perfectly spheres of gas in which the main form of energy generation is provided by the fusion of atoms. The energy generated through nuclear fusion balances the compressive force of gravity. The stage of a stars lifetime in which hydrogen fusion is the dominant source of energy is called the Main Sequence. One of the great triumphs of theoretical astrophysics was the description of the lifetime of a star on the main sequence. In fact, there are now incredibly powerful predictive theories of main sequence star evolution, in which the radius, luminosity (brightness), temperature and even lifespan can be predicted quite accurately solely by the mass. Theoretical and observational studies have greatly constrained the life-time and the deaths of stars. However, there is still much which is uncertain in the formation of stars and the earliest stages of their evolution.

The qualitative story of the formation of low mass stars is fairly well understood [41, 42]. Molecular cloud complexes are highly turbulent, with supersonic shocks traveling through the gas [43]. Regions which are more dense, particularly where shocks collide, begin to gravitationally contract [41]. The contraction leads the filamentary structures and hierarchical structure [44]. These regions can form dense cores, starting the earliest phase of the star formation process [45]. These dense cores are tenths of a parsec across and have densities over a hundred thousand particles

per cubic centimeter. The core continues to collapse slowly heating up the gas in the central regions until it becomes opaque to radiation leading to the formation of the first hydrostatic core. As gas continues to accrete onto the central object, the gas temperature rises until it is sufficient to dissociate molecules. The dissociation of molecules leads to a second collapse, ending in a hot confined object, a *protostar*. Any rotation from the natal cloud (and thus the core) leads to the formation of a disk. Disk rotation and the gas collapse pull magnetic fields, observed to be threaded through the molecular gas [i.e. 46], and creates jets and winds (discussed below). The protostar continues to accrete mass, from the envelope, at early times, and through the disk, at later times, although the exact mechanisms are not known. During this process, the disk undergoes evolution starting the formation of planets.

The formation of high mass stars is significantly more complicated [40], particularly since high-mass star formation is almost ubiquitously tied to the formation of groups of protostars, called a cluster (or protocluster). The closest region with ongoing high-mass star formation is the Orion Molecular Cloud, at a distance of 414 parsecs [47], and hosts the Orion Nebula Cluster and over a thousand protostellar objects[48]. High mass stars form from significantly denser regions and in regions with stronger turbulence. Their formation is much more violent and energetic than low-mass star formation, as will be shown below. High mass stars are also formed primarily in multiples [49], leading the collapse of their companion cores to become co-eval.

Protostars are categorized into four categories based on their spectrum [42]. Class 0 sources are protostellar objects which have tightly collimated jets with a surrounding envelope that is more massive than the protostar. Class 1 sources have a reduced envelope exposing the central embedded protostar and disk. Class II sources are totally exposed leaving the protostar and protostellar disk exposed. Finally Class III sources have little to no disk left and signal the end of the star formation process. The

majority of the work presented in this dissertation is confined to Class 0/I sources when the protostar is actively accreting from the surrounding envelope.

There are several important problems of interest to solve in star formation. The first of which is the *luminosity problem*: protostars are observed to be fainter than theoretical predictions [42, 50]. One way to solve this problem is to invoke episodic or tapered accretion [i.e. 50], which will be showed with respect to protoclusters in Chapter 4. Second, main-sequence stars are found to have nearly the same distribution in mass, called the Initial Mass Function [51, 52]. It is not clear exactly why this should be the case, or how it occurs that the star formation should lead to an identical mass distribution. Finally, many stars are found to exist in multiples [49, 53, 54]. The formation mechanisms which lead to different separations between stars is still debated [55], although there are two leading theories: turbulent fragmentation [56, 57] and disk instabilities [58].

Solving the problem of star formation is intrinsically difficult in both observations and theory due to the wide range of scales involved. The density range is between 10^3 cm^{-3}, the average molecular cloud density, and 10^{23} cm^{-3}, the bulk density of a Sun-like star. The length scale range is also significant, from the GMC scales of tens of parsecs to the radius of a protostar, 10^{-8} parsecs. The dynamic ranges mean that the puzzle of star formation has to be looked at in pieces through the physics and chemistry at each step and stitched together to form a cohesive picture.

1.4 Protostellar Feedback

Star formation is hardly a quiescent process: gas falls onto the surface of the protostar, and in the process gets heated from tens of degrees Kelvin in the envelope to millions of degrees near the surface of the protostar. Star formation is also quite inefficient[39, 41]: observations show that typically only a few percent of the gas mass in a GMC is turned into protostars [59]. Theoretically explaining this is quite difficult

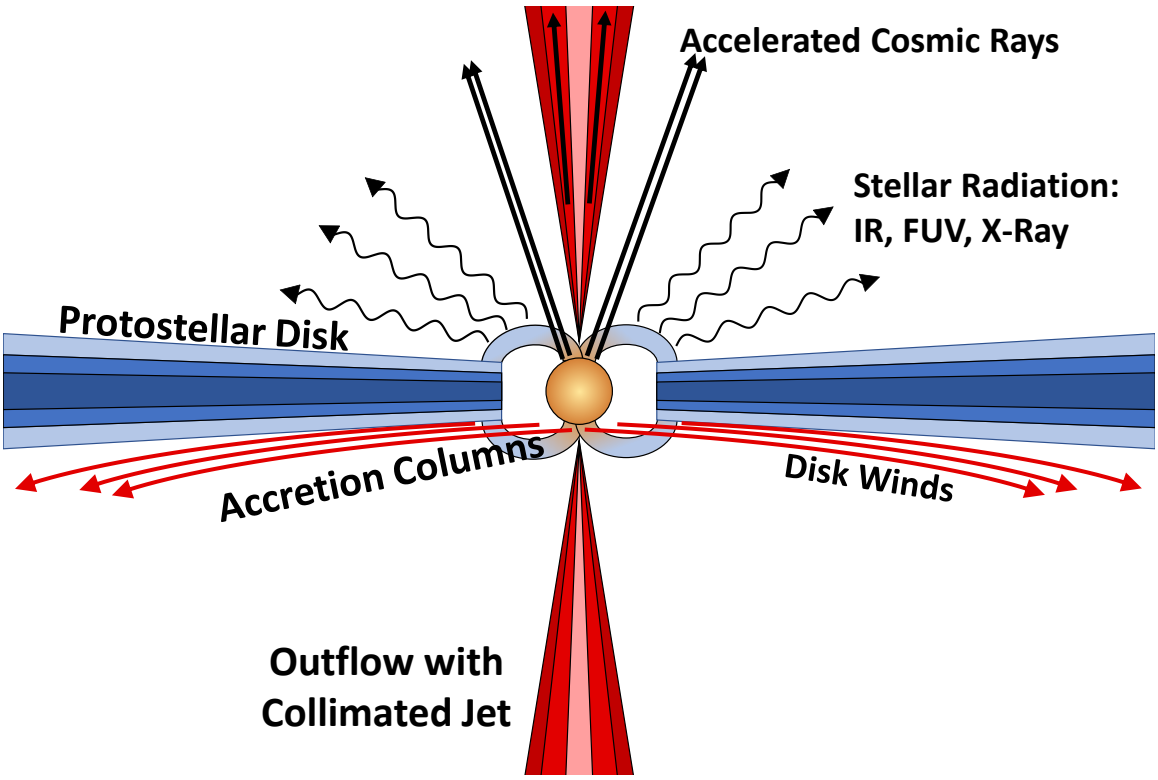

Figure 1.4. Schematic of protostellar feedback processes.

without envoking feedback from the protostars onto the natal gas. However, if protostars couple to the gas through feedback mechanisms, the star formation efficiency can be substantially decreased. Feedback can be separated into three different categories, following Krumholz et al. [60]: momentum, explosive and thermal. Cosmic ray feedback is introduced at the end as a separate subsection, although it can lead to feedback in each of the previously mentioned categories. Momentum feedback alters the the dynamical state of the gas by imparting momentum rather than energy. These mechanisms act either over long enough periods or with low enough energy such that the gas can radiate away the energy on timescales similar to that of the injection. Explosive feedback, conversely, imparts enough energy rapidly enough that the gas cannot radiate it away. Thus, the gas heats to high temperatures resulting in a pressure gradient. Finally, thermal feedback will increase the temperature but not directly affect the dynamical state of the gas. This is particularly important for

theories of fragmentation and the thermo-chemical evolution of the gas. Figure 1.4 shows a general schematic of protostellar feedback processes and different components of the system. The following sections will give a cursory introduction to feedback, a topic which could fill many theses.

Momentum Feedback

Momentum feedback consists of mechanisms in which the protostar can directly inject momentum into the surrounding natal gas even on parsec scales.

Protostars radiate at wavelengths across the electromagnetic spectrum. Photons with energies under 13.6 eV, the ionization potential of hydrogen, heat the dust within molecular clouds. The dust couple to the gas through the photoelectric effect or, at high enough densities, collisionally. The impact of radiation pressure is particularly enhanced for protostars with masses above Solar. The light-to-mass ratio increases rapidly as a function of mass, $L/M \propto M^{2.5}$, where L is the luminosity and M is the mass. For the highest mass stars, L/M approaches 1000. However, for such stars, much of the radiation is at ionizing wavelengths. Even for low mass stars, the gas can become dense enough to be optically thick, changing the gas into an adiabatic state. Optically thick gas traps the radiation and impacts more momentum from the radiation due to increased scatterings [61]. In intermediate and high mass protostars, the radiation pressure can drive Rayleigh-Taylor instabilities in the boundary between the outflow cavity and the surrounding dense gas leading to enhanced accretion [62].

Protostars are observed to drive large scale outflows, coupling the physics of accretion to the dynamical evolution of molecular clouds [63, 64]. While the exact physical mechanism that drives outflows is not known, the general properties of such a mechanism are known. The gas in the accretion disk is funneled onto the protostar through columns along magnetic field lines. The protostellar, and thus accretion, disk is rotating, such that as the gas is funneled onto the protostar, it must remove

angular momentum. This naturally leads to a collimated outflow ejecting a fraction of the mass being accreted onto the protostar [64]. There are numerous different theoretical models for outflows which have different launching radii and velocities. Outflows, including jets and winds, stir up the gas on large scales helping to drive turbulence [65, 66, 67, 68]. The outflows from clustered star formation can dominate the dynamics of entire GMCs molecular clouds hosting low-mass star formation [69]. Magnetic fields enhance this impact since the outflows drag magnetic field lines and drive Alfvén waves faster than the sound speed [70].

Explosive Feedback

High mass protostars, those which will form O and B stars, are bright in ionizing radiation. The ionizing radiation dissociates any molecular gas and ionizes the hydrogen leaving a bubble of hot gas, an HII region [71]. Classically, ionizing radiation results in a Strömgren sphere [72], a bubble of ionized gas with a radius, $R_{\rm str} = \left(\frac{3}{4\pi}\frac{Q}{n_e^2\alpha_2}\right)^{1/3}$ where Q is the emission rate of ionizing radiation, n_e is the electron density and α_1 is the recombination rate to the $n = 2$ excitation level. The hot gas leads to the pressurized expansion of the bubble. The shock propagates through the ambient medium piling up gas [13, 73], potentially enough to trigger star formation in the surrounding gas [see 60, and citations within]. However, the classical picture makes a crucial assumption: that the surrounding medium is uniform in density and infinite in size. These assumptions lead to perfectly spherically symmetric expansion of the shell. However, the gas in molecular clouds is highly turbulent resulting in a non-uniform density distribution. These deviations will lead significant deviations from spherical collapse, although this can expose larger regions of the cloud to ionizing radiation [74, 75]

High mass protostars, with surface temperatures above $\approx 2 \times 10^4$ Kelvin, produce incredibly strong winds. When these winds collide with the surrounding dense

ISM, the temperature can exceed 10^5 - 10^7 Kelvin, depending on the shock physics considered. Radiative cooling is no longer efficient at these temperatures. The hot gas acts as a strong pressure against the cooler surrounding gas resulting in rapidly moving shock waves. The heated gas also becomes X-ray bright, providing a useful diagnostic to measure the temperature and density of the gas. The X-ray bright gas provides substantial pressure, especially since it is almost always coupled to photoionizing pressure [76, 77, 78]. For lower mass protostars, or for clusters which will not form such high mass protostars, this form of feedback will only ever act to enhance radiation pressure.

Lastly, the highest mass stars may form and die while embedded in, or near, their natal molecular cloud complex. When these stars die, the result is a spectacular Type II supernova, injecting approximately 10^{51} erg of energy (equivalent to the entirety of the Sun's total energy output through its lifespan). On galactic scales, supernova feedback from star cluster formation helps drive turbulence throughout the galaxy, enrich the gas, and expel gas from the galaxy [79].

Thermal Feedback

Thermal feedback enhances the temperature, but does not directly impart momentum. There are different sources of thermal feedback throughout the star formation process. During the initial collapse, gravitational energy is converted into thermal energy [41]. Eventually, the gas heats to temperatures where radiative cooling is no longer efficient. The collapse of the core is then adiabatic until the temperature is high enough to dissociate the molecular hydrogen. As described above, after this phase, the core collapses into a protostellar object. Once a protostar forms, there are two main luminosity sources. The accretion luminosity of protostars, $L_{\rm acc} = \frac{GM\dot{m}}{R}$, dominates for low mass protostars; for intermediate mass protostars the accretion luminosity competes with the protostellar luminosity; for high mass protostars the radiation is

dominated by the protostellar component. When the gas is optically thin, it will raise the temperature but impart little momentum. These feedback mechanisms can heat the gas in the core to 100 Kelvin, inhibiting fragmentation, evaporating ice on dust grains and driving a complex organic chemistry.

Cosmic Rays

Cosmic rays are relativistic charged particles with energies from keV to TeV in molecular clouds. The exact sources of cosmic rays are still debated, although supernova appears to be the best candidate to accelerate cosmic rays to TeV energies [15]. The sources for accelerating the lowest energy cosmic rays is still currently unknown, although one candidate are protostars [80, 81], which will be discussed in detail in Chapter 5. Cosmic rays with energies from keV to MeV directly heat the gas through ionizations [13]. Cosmic rays, particularly lower energy cosmic rays, easily couple to magnetic field. The coupling leads to Alfvén waves, potentially driving turbulence in the surface layers of GMCs [82]. The cosmic rays which penetrate into molecular clouds are the primary drivers of chemistry, as discussed above [83]. In galactic regions of enhanced star formation, accelerated cosmic rays heat the gas to tens to hundreds degrees Kelvin.

There is growing evidence that protostars can accelerate cosmic rays, producing relativistic protons and electrons into deeply embedded dense gas. Radio spectrum of protostellar jets shows synchrotron emission [84, 85], a signature of accelerated electrons. Furthermore, several astrochemical studies have shown ionization rates that can only be explained by an embedded source of ionzation [86, 87, 88, 89]. Protostellar cosmic rays will heat the gas in the core substantially and increase the impact of outflows by coupling to the magnetic field.

CHAPTER 2

ASTROCHEMICAL CORRELATIONS IN MOLECULAR CLOUDS

This chapter[1] focuses on investigating how turbulence appears when observed with different molecular line tracers.

2.1 Abstract

We investigate the spectral correlations between different species used to observe molecular clouds. We use hydrodynamic simulations and a full chemical network to study the abundances of over 150 species in typical Milky Way molecular clouds. We perform synthetic observations in order to produce emission maps of a subset of these tracers. We study the effects of different lines of sight and spatial resolution on the emission distribution and perform a robust quantitative comparison of the species to each other. We use the Spectral Correlation Function (SCF), which quantifies the root mean squared difference between spectra separated by some length scale, to characterize the structure of the simulated cloud in position-position-velocity (PPV) space. We predict the observed SCF for a broad range of observational tracers, and thus, identify homologous species. In particular, we show that the pairs C and CO, C^+ and CN, NH_3 and H_2CS have very similar SCFs. We measure the SCF slope variation as a function of beam size for all species and demonstrate that the beam size has a distinct effect on different species emission. However, for beams of up to

[1]These results are based on research published by Gaches et al. [90] and is reproduced with permission from the AAS.

10", placing the cloud at 1 kpc, the change is not large enough to move the SCF slopes into different regions of parameter space. The results from this study provide observational guidance for choosing the best tracer to probe various cloud length scales.

2.2 Introduction

In molecular clouds, the largest component of the mass is in the form of molecular hydrogen. However, the lowest transition of H_2 is excited at temperatures greater than 500 K, an order of magnitude hotter than typical molecular clouds (10-100 K). Therefore, observational studies of molecular cloud properties and dynamics must use low-abundance tracer species, the most important being CO [see 28, 91, 92]. Despite its utility, CO is an imperfect gas tracer in a variety of regimes. It is photo-dissociated at cloud boundaries and near stellar sources. It also becomes optically thick quickly in high density regions. Furthermore, CO suffers greatly from depletion onto dust grains at gas densities greater than $\sim 10^4$ cm^{-3}, further reducing its ability to probe high density environments [93, 94, 95]. In contrast, high-density tracers such as N_2H^+ provide a better means to study the dense gas where CO depletion becomes severe.

Consequently, in order to construct a complete picture of molecular clouds, it is necessary to piece together information from a variety of different tracers and line transitions, each of which is sensitive to different densities, temperatures, and size scales [e.g. 96]. For diffuse gas, species such as OH^+ [97] and C^+ are used. Shock dominated regions are traced by molecules such as SiO [98]. Observers also use a wide array of species, including HCN, NH_3, H_2CO, H_2CS, CS, HCO^+ and N_2H^+ to study dense environments [99, 100, 101, 102, 103]. However, astrochemistry is highly nonlinear and is sensitive to the gas density, temperature and radiation field. Detailed modeling is necessary to understand the distribution of species and how they are correlated with each other.

Observationally, new instruments make studying many different chemical species much more feasible. In particular, the wide spectral bandwidth of Atacama Large Millimeter Array (ALMA) allows many different molecular species to be be mapped simultaneously. For example, the ALMA Band 3 contains CN (N=1=0, J=$\frac{1}{2}$-$\frac{1}{2}$), ^{12}CO (J=1-0), ^{13}CO (J=1-0), HCN (J=1-0), HCO^+ (J=1-0), HNC (J=1-0), and N_2H^+ (J=1-0). These species alone span environments ranging from diffuse, large scale structure (^{12}CO) to dense cores (N_2H^+). Altogether, these lines provide a rich and detailed view of star forming gas.

However, interpreting this data is not always straight forward. Astrochemistry is a highly nonlinear function of the underlying gas density and temperature. Numerical modeling of the underlying structure and astrochemistry is essential to provide an interpretive framework. There have been numerous recent advancements in astrochemistry codes [see 104]. Reducing the dimensionality can be helpful for modeling disk or outflow cavities [e.g. 105, 106], where the underlying density structure is symmetric is some manner. However, observations show that molecular clouds contain complex density and velocity structure. To account for this, some studies have adopted analytic prescriptions for clumpiness [107, 108]. Such approaches have been able to model the correlation between ^{13}CO and C, CO emission (the "X-factor") and reproduce observed line profiles [e.g. 36, 109], however, they underestimate the influence of cloud morphology in the abundances of species such as C [110, 111, 112]. A fully three dimensional method for modeling photo-dissociation regions (PDRs) is necessary to represent the complex geometries of molecular clouds. However, a three dimensional time dependent astrochemistry simulation coupled to the hydrodynamics with an extended network is still computationally infeasible.

Many astrochemical studies have focused only on the formation of H_2 and CO. These species represent most of the molecular cloud gas and can be modeled with a simple chemical network [see 113]. This can reduce the problem of solving thousands

of coupled equations to merely dozens. However, as more elements are added to the network, the number of species increases drastically, sometimes with significant effects [14]. For instance, the inclusion of Sulfur chemistry leads to the addition of CS, which in turn impacts the abundance of CO. Since CO and CS have similar formation rates in diffuse environments from their atomic constituents, CS will reduce some of the atomic carbon available for the formation of CO. Likewise, CH_3 is a reactant with both H_2CS and H_2CO. Without the inclusion of Sulfur chemistry, the abundance of H_2CO cannot be properly modeled. When studying many species simultaneously, reducing the number of reactions while maintaining accuracy is nearly *impossible*, requiring a very large network to properly account for the gas phase chemistry alone [104]. Including grain surface chemistry, which requires also modeling the dust distribution and gas-dust surface reactions, further complicates astrochemical studies.

The goal of this paper is to study the distribution of a large variety of species and understand the correlations between them. We model a Milky Way-like molecular cloud using the magnetohydrodynamic code, ORION. We then post processes these results with the 3D astrochemistry code, 3D-PDR [30], using an extended chemical network to obtain the abundances of over 200 different species. For a subset of this network, we calculate synthetic emission maps of their lowest transition with the radiative transfer code RADMC-3D. We compare the spectral structure of all the species to determine the similarity of different species. This is the first study to quantitatively compare the underlying structure of many species. In §2.3 , we discuss the models and the methodology we use to generate the emission maps, as well as the way we quantify their spectral structure. In §2.4 we investigate how the following factors affect the spectral structure: viewing angle, species and spatial resolution. Finally, in §2.5 we discuss how the results are relevant to observational studies and general implications.

2.3 Methods

2.3.1 Hydrodynamic Simulation

We use a turbulent hydrodynamic simulation to model a typical Milky Way cloud. The simulation was performed using the Adaptive Mesh Refinement (AMR) code ORION [114, 115]. It was previously discussed in Offner et al. [116] and Offner et al. [112] as simulation *Rm6*, so we only briefly summarize its properties here.

The simulation represents a piece of a typical local molecular cloud. The domain is 2 pc on a side and contains 600 $M_\odot$. The gas temperature is 10 K and the 1D gas velocity dispersion is 0.72 km s^{-1} such that the cloud satisfies the linewidth-size relation (e.g., McKee and Ostriker 41). The gas turbulence is initialized by adding random velocity perturbations with wave numbers $k = 1..2$ for two box crossing times without self-gravity.

Once self-gravity is turned on collapse proceeds. The base grid is 256^3 but four additional AMR levels are inserted to ensure that the gas obeys the Jeans criterion with a Jeans number of 0.125 [117]. On the highest level ($\Delta x_{\rm min}$=0.001 pc), sink particles ("stars") are added when the gas exceeds the maximum density [118]. The output we analyze in this study is at 1 global free fall time at which point $\sim 18\%$ of the gas resides in stars.

2.3.2 Astrochemistry

The chemical abundances were computed using 3D-PDR[2], a three-dimensional photodissociation code coupled with a full chemical network [30]. Offner et al. [112] presented an analysis of the line emission based upon the abundances of molecular hydrogen, atomic carbon, and carbon monoxide (run Rm6_1.0_12_1f_a). In this study, we perform an additional analysis of the most common astrochemical species in the

[2] `https://uclchem.github.io/3dpdr.html`

chemical network. Here, we describe the astrochemistry calculation procedure and refer the reader to Bisbas et al. [30] and Offner et al. [112] for additional details.

We irradiated the simulated cloud by an isotropic 1 Draine FUV field, where "1 Draine" is the standard interstellar radiation field [119]. 3D-PDR uses the hydrodynamic densities and assumed external field to compute the temperature and abundance distribution for points in the cloud with densities $200 \leq n \leq 10^5$ cm^{-3}. Below $n = 200$ cm^{-3} we consider the gas as ionized, using limiting conditions on abundances and gas temperature, whereas above $n = 10^5$ cm^{-3} we assume it is fully molecular. We do not calculate the chemistry in those two regimes. 3D-PDR computes the radiation field using a resolution of 12 HEALPIX rays [120], emanating from each grid point. The input grid is the density field of the hydrodynamic calculation resampled to a resolution of $256^3/12$, i.e. a new grid comprised of every 12th data point. (See Offner et al. [116] for a discussion of spatial resolution convergence.)

3D-PDR employs the UMIST2012 chemical database [18], which includes 215 species and approximately 3000 reactions. The calculation includes the formation of H_2 on dust grains following Cazaux and Tielens [121, 122], photodissociation of H_2 and CO and self-shielding. The initial elemental abundances are [He] $= 1.0 \times 10^{-1}$, [C] $= 1.41 \times 10^{-4}$, [O] $= 3.16 \times 10^{-4}$, [Mg] $= 5.1 \times 10^{-6}$, [S] $= 1.4 \times 10^{-6}$, and [Fe] $= 3.6 \times 10^{-7}$ [123], which are similar to values estimated for local molecular clouds. We adopt a cosmic ionization rate of 5×10^{-17} s^{-1}, which is the average value found in the Milky Way. 3D-PDR solves the chemical network in equilibrium, with the final time parameter representing the time allowed for the chemistry to come to equilibrium.We analyze the calculation after advancing the chemistry to equilibrium at 10 Myr.

The 3D-PDR calculation does not consider shock chemistry or dust-grain chemistry, which includes the freeze-out of species such as CO onto dust grains, surface reactions (with the exception of H_2 formation), or release of grain mantle species

into the gas phase by means of evaporation, photodesorption or desorption [e.g. 124]. While these processes may impact abundances under certain conditions, we expect them to have a minimal impact on our results. For example, turbulent intermittency in the form of strong, thin shocks within the diffuse gas may enhance the emission and abundance of tracers such as CH^+, H_2 and CO [125, 126]. However, excitation by FUV photons likely dominates the populations of the lowest energy states, which are what we study here. Dust grain freeze-out primarily affects gas with densities $\geq 10^4$ cm^{-3}; here, only 1% of the volume of our model cloud has $n_{H_2} \geq 10^4$ cm^{-3} (see further discussion of the impact of molecular freeze-out in the Appendix). Other grain processes, such as photodesorption, may impact the species abundances over a larger range of densities. Namely, [127] find that photodesorption is needed to reproduce the measured enhanced abundance of H_2CO in the Horsehead PDR region. In contrast, they find that grain-chemistry is not required to model the H_2CO abundance within a UV-shielded dense core, which is instead well-fit by a pure gas-phase model. This suggests that the higher UV radiated outer regions of our cloud may require consideration of additional processes, at least with respect to H_2CO. However, we note that grain chemistry involves a high-degree of uncertainty and is sensitive to the local UV field, grain properties, and cosmic-ray flux, which make it difficult to apply conclusions from case-studies in the literature to our particular conditions. We quantitatively examine the impact of potential effects of dust-grain chemistry and shock chemistry in the Appendix.

In this study, we essentially assume a "one-way" coupling between the hydrodynamics and chemistry. Performing the chemistry by post-processing the simulations allows us to consider much larger chemical networks that would otherwise be computationally impossible when evolving the chemistry in parallel. However, the chemistry is not coupled to the hydrodynamics, so, although 3D-PDR calculates the gas temperature due to UV heating and cooling, it does not influence the gas evolution, and

consequently the hydrodynamics and chemistry are not fully consistent. However, even for the warmer ($\approx$ 100 K) gas, motions are dominated by turbulence rather than thermal broadening, so we do not expect large differences. For further discussion of the chemistry modeling, see Offner et al. [116]. Even though the chemistry considered here is not time-dependent, the approach exhibits good agreement with Glover and Clark [128]. While their chemistry network is considerably simpler than ours, the equilibrium time scales they find are the same order of magnitude of the times at which we evolve the chemistry to in this study, and are the same order of magnitude of the free fall timescale of the modeled cloud.

2.3.3 Synthetic Emission Maps

We carry out synthetic observations for the 16 difference species in Table 2.1 and compare our theoretical results to observations. We study these species because they are commonly used tracers. We use the Leiden Atomic and Molecular Database (LAMBDA) [3] for the reaction rates and cross sections for the different molecules. When performing these calculations, we use the collisional partners defined in the LAMBDA database files, mainly H_2, H and He, assuming most of the H_2 is para-H_2.

To compute the emission, we use the radiative transfer code RADMC-3D [4] with the Large Velocity Gradient (LVG) approach [92], a radiative transfer method that does not assume local thermodynamic equilibrium (LTE). This method computes the molecular level populations given the density, velocity and temperature fields. We use the velocity information from the ORION calculation, while 3D-PDR calculates the temperature and abundance information. Before performing the radiative transfer, we interpolate all data to a 256^3 resolution. We calculate the synthetic spectra for velocities within $\pm$ 3 km s^{-1} of the line center. While 3D-PDR computes the level

[3] http://home.strw.leidenuniv.nl/ moldata/

[4] http://www.ita.uni-heidelberg.de/dullemond/software/radmc-3d/

populations for all levels in the LAMBDA data, we only analyze the emission from ground level transitions.

We use a constant microturbulence value of 0.1 km s^{-1} to account for unresolved turbulence. We adopt a "Doppler catching" parameter $d_c = 0.025$, which forces an interpolation of the velocity field between cells if there is a jump greater than 0.025 times the local linewidth. We use collisional excitation and line data from the Leiden atomic database for all 16 species [129].

Since the main goal is to study the structure of the tracer species, we do not include the dust continuum in the emission calculation. We neglect heating and UV feedback due to embedded protostellar sources. However, since the cloud is forming low-mass stars, radiative feedback likely has a small impact on the emission. We convert the line emission into a brightness temperature T_b using the Rayleigh-Jeans approximation:

$$T_b = \frac{c^2 I_\nu}{2\nu_i^2 k_b} \tag{2.1}$$

where I_ν is the specific intensity and ν_i is the frequency of the line transition.

2.3.4 Statistical Analysis: Spectral Correlation Function

In this study, we use the Spectral Correlation Function (hereafter denoted as SCF), first introduced by Rosolowsky et al. [130] to study the spectral structure of the emission cubes. We define a position-position-velocity (PPV) cube as spectral line data consisting of two spatial dimensions and one velocity dimension. Likewise, a position-position-position (PPP) cube is data consisting of the density information in all 3 spatial dimensions. The SCF is sensitive to the temperature and sonic Mach numbers and weakly sensitive to the the magnetic field strength [131, 132]. Previous studies have only focused on the SCF of ^{13}CO emission, in both simulated and observed molecular clouds. We calculate the SCF for all 16 species emission and density

cubes to study how the SCF changes for the same cloud but different observational tracers.

There are several different functional forms for the SCF. We use the form given in Padoan et al. [131], where the SCF is a function of length scale, l and denoted by $S(l)$:

$$S(l) = \left\langle 1 - \left\langle \sqrt{\frac{\sum_v |O(\mathbf{r},v) - O(\mathbf{r}+\mathbf{l},v)|^2}{\sum_v |O(\mathbf{r},v)|^2 + \sum_v |O(\mathbf{r}+\mathbf{l},v)|^2}} \right\rangle_{\mathbf{r}} \right\rangle_{|\mathbf{l}|=l} \tag{2.2}$$

Here $\mathbf{r}$ is a two dimensional position on the image plane, $\mathbf{l}$ is the offset vector with length l, and $O(\mathbf{r}, v)$ is any PPV spectral data set. By definition $S(0) \equiv 1$. The SCF is defined to be bounded between 0 and 1, with 0 indicating no correlation. Padoan et al. [131] found that in driven turbulence simulations, the SCF can be analytically fit by a power law on small scales. They fit the SCF for ^{13}CO (1-0) maps of several observed and simulated molecular clouds and demonstrated that the parameter correlations can be used as theoretical model tests. Likewise, we fit the SCF on small length scales using a power law:

$$S(l) = S_0 l^{\alpha} \tag{2.3}$$

where S_0 is the value of the SCF at $l = 1$ pc. We fit the power laws in log space for length scales between $3\times$ $l_{\rm min}$, where $l_{\rm min}$ corresponds to either the simulation resolution, or the beam size, and l =1 pc corresponding to half the maximum length scale. This was to remove beam size effects from the SCF power law fit. Figure 2.1 shows the SCF for four different tracers. The tracers follow a tight power law behavior for small values of l, as illustrated by the black lines fits. However, Figure 2.1 also shows that at some length scale, the SCF function appears to flatten and become noisy.

When comparing SCFs for different spectral maps, it is useful to define a quantitative scalar value that describes how similar two SCFs are to one another. We use

the distance metric between two SCFs as defined by Yeremi et al. [132]:

$$d_{SCF} = \sqrt{\sum_{l} [S_1(l) - S_2(l)]^2} \tag{2.4}$$

Using this distance metric provides a quantitative measure of how similar the spectral structures are between different species, resolutions, and sight lines. Yeremi et al. [132] showed that this metric is sensitive to global hydrodynamic parameters, although not to the magnetic field strength. Since the distance metric is a 1D statistic we can't compute a chi-squared value, i.e. a probability measure of uncertainty. In §2.4.2 we will describe an example of using the distance metric to quantitatively comparing SCFs.

2.4 Results

2.4.1 Power Law Range

Figure 2.1 shows that the SCFs of species which trace dense gas transition away from power law behavior at larger scales and shows that the power law description holds only up to some scale $l \ll L$ where L is the cloud size. At larger length scales, the SCFs start to flatten for all species. For example, the CO SCF is a continuous power-law up to nearly 2 pc, while the SCF for NH_3 starts to flatten around 0.4 pc. This flattening indicates where the gas is not dense enough to thermally emit. CO remains correlated at large scales throughout the cloud, with a high surface filling fraction of $f_s = 0.82$, and samples both diffuse and dense structures. CO has an low volume filling fraction, $f_v = 0.07$ since it is still contained mostly in dense environments with emission coming from diffuse regions because of its substantially smaller critical density. The emission from high density regions is constrained by its high optical depth. In our study, the surface filling fraction, f_s, is the fraction of the area containing the brightest 95% of the emission. The volume filling fraction, f_v,

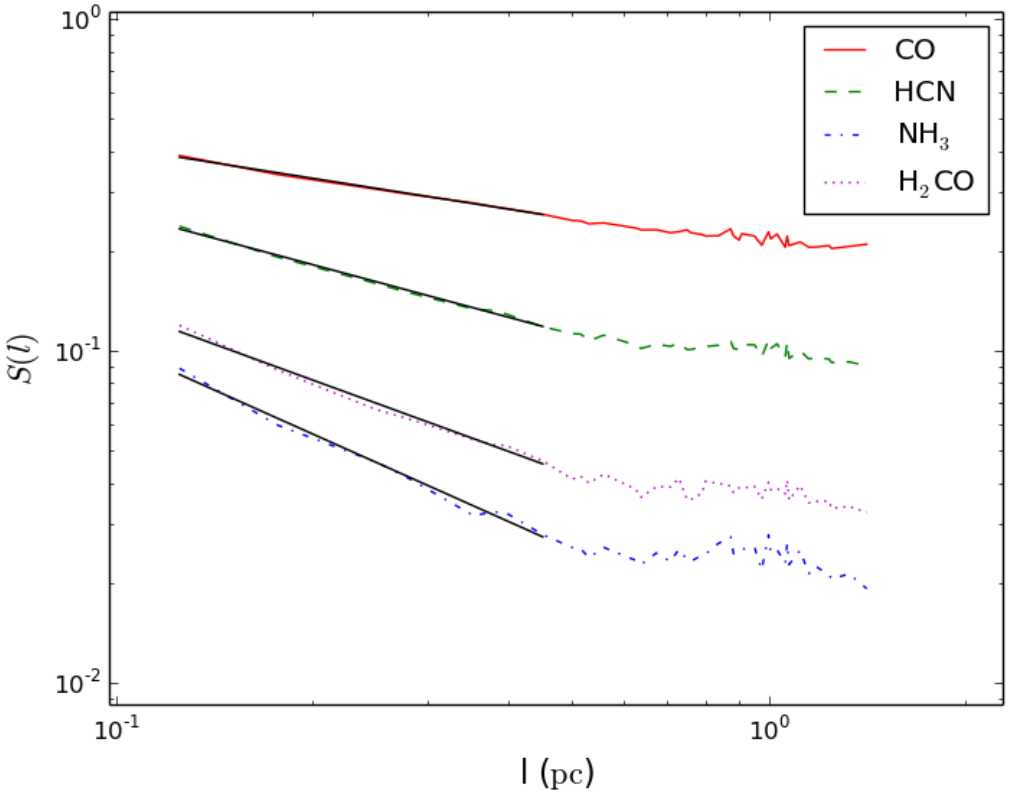

Figure 2.1. Spectral correlation functions for four different species. The black lines indicate a power-law fit.

is defined from the 3D abundances, being the fraction of the volume containing the top 95% of the mass. However, NH_3 becomes quickly uncorrelated, because it traces only compact emission, i.e. dense cores, illustrated its much smaller volume filling fraction, $f_v \sim 0.005$ and small surface filling fraction $f_s \sim 0.25$.

Figure 2.2 displays the SCF slope as a function of offset, S_0 for 16 synthetic emission cubes, where S_0 is the value of the SCF at 1 pc. While we define the SCF in terms of a slope and an offset, we show in Figure 2.2 that these two parameters are tightly correlated. Therefore, henceforth, we only discuss the slope of the SCF. Padoan et al. [131] also found a strong correlation between the slope and the offset for simulated clouds.

2.4.2 Viewing Angle

A statistic describing cloud structure is only meaningful if it does not vary strongly as a function of cloud viewing angle. Here we verify that this is the case.

We calculate the emission for 9 different lines of sights through the cloud in 45 degree increments about the x-axis for all 16 tracers. We find that the SCF slopes change by only $\approx 10\%$ over all viewing angles. This variation, though small, is useful as a benchmark to define when two tracers are truly similar. To define an effective uncertainty, we calculate the maximum distance between any two SCFs for all lines of sight. Figure 2.3 shows this maximum distance for 6 different species. We find that there is a power law relation between the average slope, $< |\alpha| >$, and the maximum distance, d_{max}. This relation now provides a quantitative way of identifying homologous tracers. We define two tracers as "complementary" if their SCF distance for a given line of sight is less than the maximum $d_{\rm max}$ of either tracer. Therefore, species A and B are complementary if

$$d_{\rm SCF}(B \Leftrightarrow A) \leq \max(d_{\rm max}(A), d_{\rm max}(B)) \tag{2.5}$$

Figure 2.3 also suggests that diffuse species are more likely to have complements because they have shallower slopes. We can see this by comparing the SCFs of CO and NH_3. If we fix the CO offset and alter the slope by the maximum $\pm$ 10% error, the total rms difference is geometrically d_{max}. Since the SCF slope is shallower for CO, the magnitude of the SCF remains higher. In contrast, if the NH_3 SCF is altered in a similar manner, the magnitude of the SCF becomes smaller much faster as a result of the steeper power law. Therefore, the rms difference between the SCFs is much smaller than what it would be for CO. As such, there is an expectation that d_{max} should decrease with increasing slope.

Figure 2.4 shows the SCF slopes for all the species in this study with their line of sight scatter. The species are seemingly separated into three distinct groups, though

only two of the groups show a large jump in slope. Based on these groupings, we will refer to *diffuse* tracers as those with $\alpha \sim -0.3$, *intermediate* tracers as those with $\alpha \sim -0.5$, and *dense* tracers as those with $\alpha \sim -0.75$. CO and C both have the same SCF slope within 1 σ of each other and within 2 σ of all the other diffuse tracers except C^+, where σ is the line of sight slope error. The larger errors for C^+ seem to correspond to different diffuse structures being superimposed at different sight lines giving somewhat different structures. Note that while the species whose SCFs are within the line of sight error limits are homologous (meaning they trace similar density regimes), they are only complementary if they also satisfy the distance metric criteria (Equation 5).

The simulated molecular cloud that we study has no magnetic fields. While Yeremi et al. [132] find that the SCF only weakly depends on the magnetic field, the presence of a strong magnetic field could create asymmetries in the gas distribution. Large asymmetries could in turn increase the SCF dependence on the viewing angle.

2.4.3 Chemical Species

We use 16 common astrophysical tracers to investigate how the SCF depends on species. We generate synthetic emission maps for the lowest energy state transitions shown in Table 2.1. Figures 2.5 and 2.6 show integrated emission maps in position-position (PP) and position-velocity (PV) space, respectively. The various tracers span different ranges of position and velocity space depending on their abundance and excitation. For example, astronomers commonly use N_2H^+ to trace dense gas, so it is unsurprising that N^2H^+ exhibits very compact emission in both figures. The velocity plots indicate structure that may be hidden by projection. Dense cores stand out in both maps.

We find that the filling fractions in PP and PV are similar: tracers with compact spatial emission are also compact in velocity space. This is essentially Larson's

Table 2.1. Chemical Species and Properties

Name	Transition	Frequency (GHz)	n_c (cm^{-3})	f_s	f_v	Notes
C	J=1-0	492.160651	820	0.87	0.45	
C^+	J=$\frac{3}{2}-\frac{1}{2}$	1900.5369	7700	0.87	0.48	
CN	N=1-0, J=$\frac{1}{2}-\frac{1}{2}$	113.1686723	1.3×10^6	0.87	0.14	
CO	J=1-0	115.2712018	2180	0.82	0.07	
CS	J=1-0	48.9909549	5×10^4	0.73	0.05	
HCN	J=1-0	88.6316023	1×10^6	0.65	0.40	No hfs
HCO^+	J=1-0	89.188523	1.6×10^5	0.62	0.14	
HNC	J=1-0	90.663568	2.7×10^5	0.21	0.01	
OH	J=$\frac{3}{2}$,F = 1,P = +/-	1.66	2.60	0.22	0.15	No hfs
OH^+	N=1-0	909.15880	4270	0.63	0.36	
H_2CO	J=1-0	72.837948	1.5×10^5	0.41	0.03	p-H_2CO, hfs
H_2CS	J=1-0	34.3543	8400	0.24	0.006	p-H_2CS
NH_3	(J,K)=(1,1)	23.6944955	1990	0.25	0.005	p-NH_3, hfs
N_2H^+	J=1-0	93.17370	1.4×10^5	0.21	0.005	No hfs
SiO	J=1-0	43.42376	3.8×10^4	0.51	0.005	
SO	J=1-0,N=0-1	30.00158	7.7×10^4	0.28	0.005	

Notes. Species name, transition, critical density, surface filling fraction and volume filling fraction for all the species in which we do radiative transfer post processing. We define the surface filling fraction as the fraction of the area that constitutes 95% of the total intensity. The volume filling fraction is the fraction of the volume that constitutes 95% of the total mass. Hyperfine splitting is denoted by hfs. Species that have hfs defined in the LAMBDA database files but are not included in the radiative transfer modeling are denoted by "No hfs", while those that have hfs that is included in the radiative transfer modeling are indicated by "hfs". Critical densities were calculated for gas at T = 10 K.

relation [133], which states that small structures should have small velocity extents. CO has a high surface filling factor ($f_s \sim 0.82$) and traces both high and low density regions, with a relatively high abundance across the entire spatial region, exhibited by its spatial emission distribution. CO is chemically connected to the high density tracer H_2CO through a number of reactions. H_2CO is photodissociated to form CO when the density becomes low enough that it is no longer shielded from the external UV field. CO can get turned into H_2CO through intermediaries, such as HCO^+ in both gas phase reactions and dust grain chemistry. As expected then, the H_2CO emission has a much smaller surface filling fraction of $f_s \sim 0.41$ and is resides mostly in dense environments, requiring a relatively high density to be excited ($n_c \sim 10^5$ cm^{-3}).

Optical depth indicates the degree of transparency. Tracers that are optically thin, such as NH_3, have emission that reflects the underlying density structure more accurately. Figure 2.7 shows the optical depth of each line transition at the line center calculated by RADMC-3D. The figure shows that C, CO, CN and C+ all have high optical depths. This is a result of having a lower critical density with a relatively high abundance. The intermediate density tracers, CS, SiO, HCN, HNC and HCO+ are similar, with the gas only being optically thick towards the highest density regions. High density tracers, NH_3, H_2CO, H_2CS and N_2H^+ remain optically thin throughout almost all of the entire volume. NH_3 is an exception because of its fairly low critical density, allowing it to be excited down to lower densities, though still relatively optically thin except in the densest regions of the filaments. OH^+ suffers from a very low abundance, and it is not easy to excite, so its emission appears very diffuse.

Figure 2.8 displays two different integrated maps with spectra at two different points. It shows that the CO emission is mostly dominated by gas motions. The red star spectrum shows a single feature with a width of ~ 0.7 km s^{-1}, which is consistent

with the characteristic turbulence velocity. The CO white star spectrum is broad in part because it is a superposition of multiple density features along that particular line of sight. Similarly, the NH_3 white star spectrum shows a superposition of several density features at different velocities along the line of sight. However, the NH_3 red star spectrum, which is along a rather diffuse line of sight, shows a much narrower feature with a width of 0.3 km s^{-1}. The average sound speed of a cold molecular cloud is approximately 0.2 km s^{-1}, indicating that the NH_3 in the red star region is undergoing purely thermal motion rather than dominated by turbulence.

2.4.4 Resolution

Beam resolution is one of the most important factors in observations and it impacts the apparent gas structure and mean optical depth. A larger beam averages out the emission within the beam size, lowering the overall optical depth. We convolve the emission maps with a Gaussian beam to simulate a realistic resolution observation. We place the simulated cloud at a distance of 1 kpc to establish the angular size. Larger beams significantly blend the dense cores and diffuse gas structure. Interestingly, we find that some species' spectral structures are artificially similar at one resolution and then deviate significantly at some lower resolution. To quantify this, at each resolution we calculate the SCF for each species and then compare their distance metrics. Figure 2.9 shows the evolution of the SCF slopes for all 16 species as a function of spatial resolution. The overlapping regions indicate where tracers at a particular spatial resolution have similar emission distributions. Note that this only impacts the emission. Therefore, overlapping regions do not indicate similar density distributions, unless the SCF slopes are similar at good (near simulation) resolutions. Thus, Figure 2.9 quantifies which tracers are statistically similar and useful for studying particular densities and size scales.

At the highest resolution (i.e. no smoothing), C, CO, CN and C^+ are all very similar tracers since they all trace diffuse gas. The positive correlation between C and ^{12}CO has been observationally studied for years [e.g. 134, 135, 136, 137, 138], although historically C was theoretically predicted to only exist in a PDR surface layer [14]. Papadopoulos et al. [110] predicted that C should be more prevalent in clouds than previously predicted by 1D models due to a combination of non-equilibrium processes and clumpy cloud morphology. Glover et al. [111] and Offner et al. [112] both qualitatively demonstrated the similarity between the C and CO distributions in 3D PDR calculations. Our SCF comparison demonstrates that CO and C spectral cubes are *quantitatively* similar.

At higher densities, species such as SO and NH_3 also appear very similar. As expected, HCN and HNC structures appear nearly identical in spectral space. At lower spatial resolution, several species intersect: NH_3, N_2H^+, SO and H_2CO. This occurs as larger beams increasingly blend dense, compact emission.

We note that some species have a non-monotonic dependence on resolution where the SCF slope decreases until $\sim$ 15-20" and then increases again. The decrease in the slope is due to overlapping Gaussian structures creating artificial cores. Figure 2.10 shows the emission spectral structure evolution with beam size visually for NH_3 emission in both PP and PV space. Figures 2.11 and 2.12 illustrate these trends as a function of beam size using the distance metric. The change in the slope occurs because species with significant compact emission (those which are generally optically thin) have their emission smoothed on larger scales, making their emission more extended and thus appear similar to other more optically thick species. Smoothing also somewhat affects the more diffuse tracers C, CO, CN and C+, which experience blending on larger scales. This can give the appearance of a more core-like structure where these smoothed regions overlap. At lower density, the emission smooths into am even more diffuse looking component.

2.4.5 Comparison of Density and Emission

In §3.3 we demonstrate that many tracers produce similar SCFs. However, similarity between the SCFs of two emission maps does not guarantee that the underlying densities are also similar. In this section, we compare the SCFs of the emission and density data directly. We obtain a PPV cube based on the gas density (hereafter denoted by PPV_ρ) by taking the simulated density and velocity cubes and constructing a PPV cube where each spectral bin contains the number density (calculated as $N_i = N_{\mathrm{H}} \cdot n_i$) within a given velocity bin. Here, "V" is the velocity vector projected along a given line of sight. For the PPV_ρ cube, the $(\mathrm{i,j,k})^{\mathrm{th}}$ voxel contains the total mass along some line of sight through the point $(\mathrm{x}_i, \mathrm{y}_i)$ within a particular line of sight velocity range $\Delta \mathrm{v}_k$. We compare the emission and density SCFs in Figure 2.12. This figure shows the distance between the emission SCFs and PPV_ρ SCFs for each species. For C, CO, CN and C+, PPV_ρ does not match the emission structure well. In fact, as the spatial resolution of the PPV cube becomes coarser, agreement between density and emission worsens. High opacity tracers exhibit poor correspondence between emission and density.

In contrast, species with optically thin emission have very similar density and emission SCFs, as indicated by the darker cells in Figure 2.12. For example, CO has a low critical density, $n_c \sim 2000$ cm^{-3}, and a relatively high abundance. It becomes optically thick as the gas density approaches 10^4 cm^{-3}. Figure 2.7 demonstrates that CO is very optically thick throughout most of the simulation box. High optical depth effectively flattens the perceived distribution, i.e. as the gas becomes optically thick the emission no longer traces higher density regions. On the other hand, $\mathrm{N_2H^+}$ is optically thin throughout the domain and has a small distance ($\mathrm{d} < 0.1$) between its emission and density SCF. $\mathrm{N_2H^+}$ has a high critical density of 10^5 cm^{-3} and has a much lower abundance than CO.

Differences between the true density and the emission arises from a combination of chemistry, which changes the abundance, and excitation, which impacts the line shape. For example, OH^+ has a low critical density of ~ 4000 cm^{-3} but its emission remains optically thin due to its very low abundance. However, HCN is optically thin because it is only excited at gas densities above 10^6 cm^{-3} despite its modest abundance: $[HCN]/[H_2] \sim 10^{-7}$.

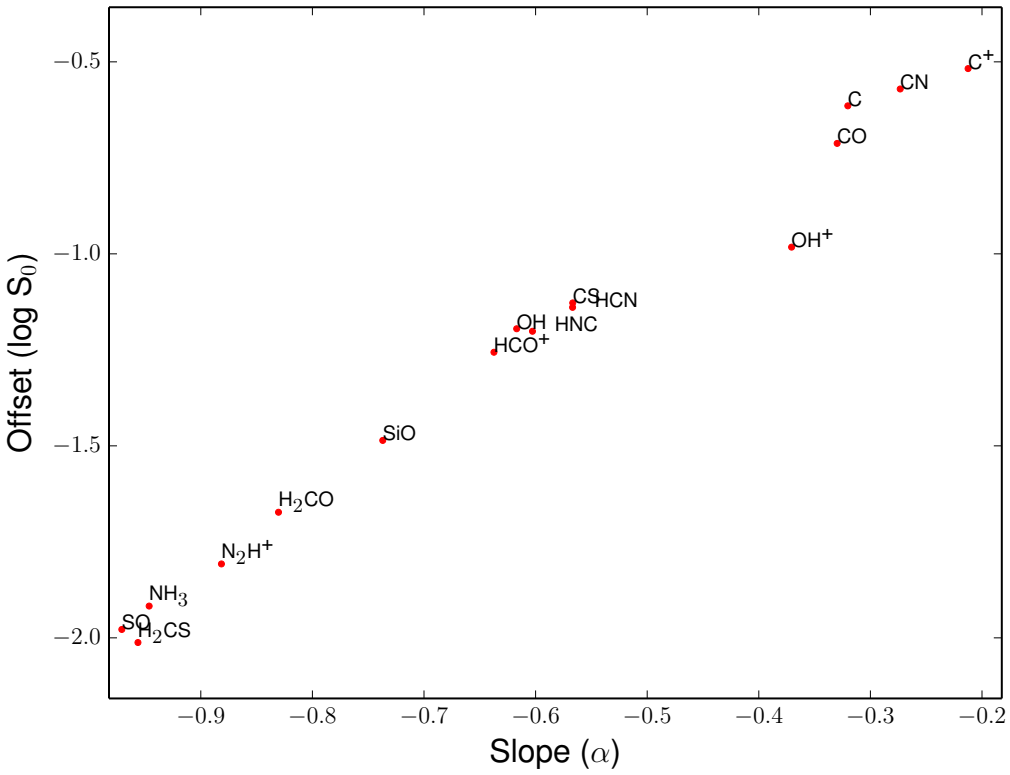

Figure 2.2. Slope, α, versus offset, S_0, for the SCFs calculated for 16 PPV emission maps. The same trend holds for the density data, so we only show the emission parameters.

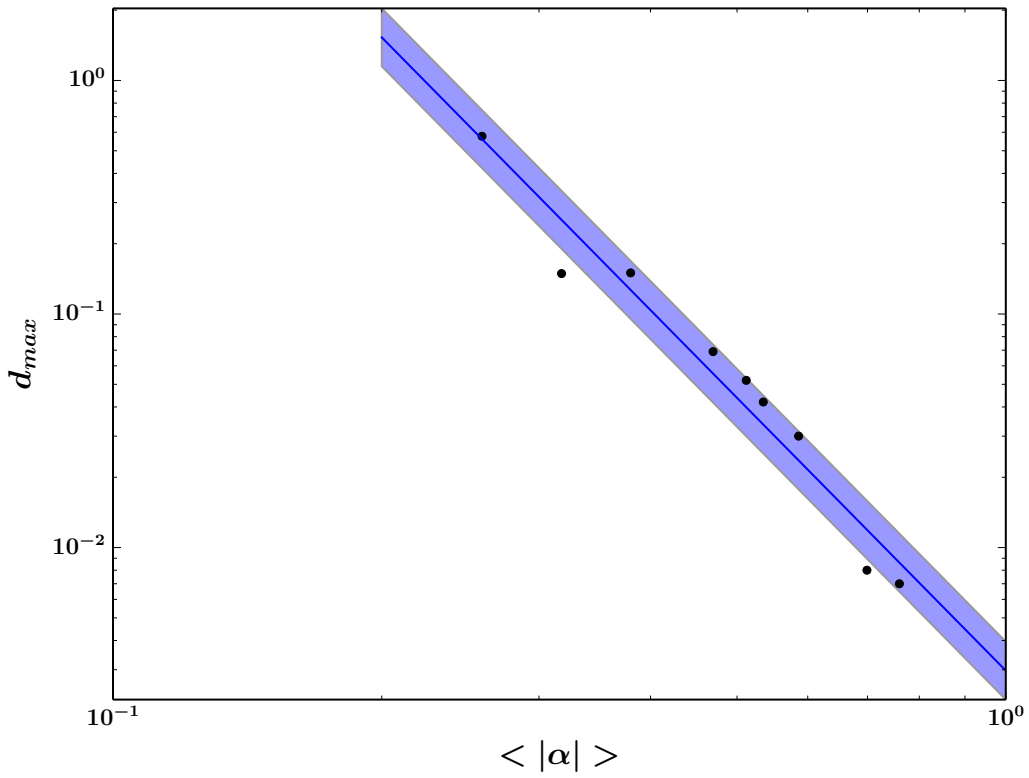

Figure 2.3. Maximum SCF distance, d_{max}, as a function of the average of the SCF slope magnitude, $< |\alpha| >$, for different tracers. The blue line indicates a power law fit to the points with a slope of -3.2. The shaded region shows $\pm$ 1 σ from the fit.

2.5 Discussion

2.5.1 Comparisons with Observations

We now compare our results to observations of two local molecular clouds (MCs), Perseus and Ophiuchus. We use the ^{12}CO data from the COMPLETE survey [37], which were taken using the Five College Radio Astronomy Observatory (FCRAO). The ^{12}CO observations have an angular resolution of 46″. Since the Perseus and Ophiuchus clouds are approximately 250 pc and 150 pc away [37] corresponding to physical scales of 0.06 pc and 0.03 pc, respectively, we can compare at the to length scales represented in our simulation. We calculate the ^{12}CO SCF for the full extent of both clouds. We also divide Perseus into two parts and compute the SCF of each

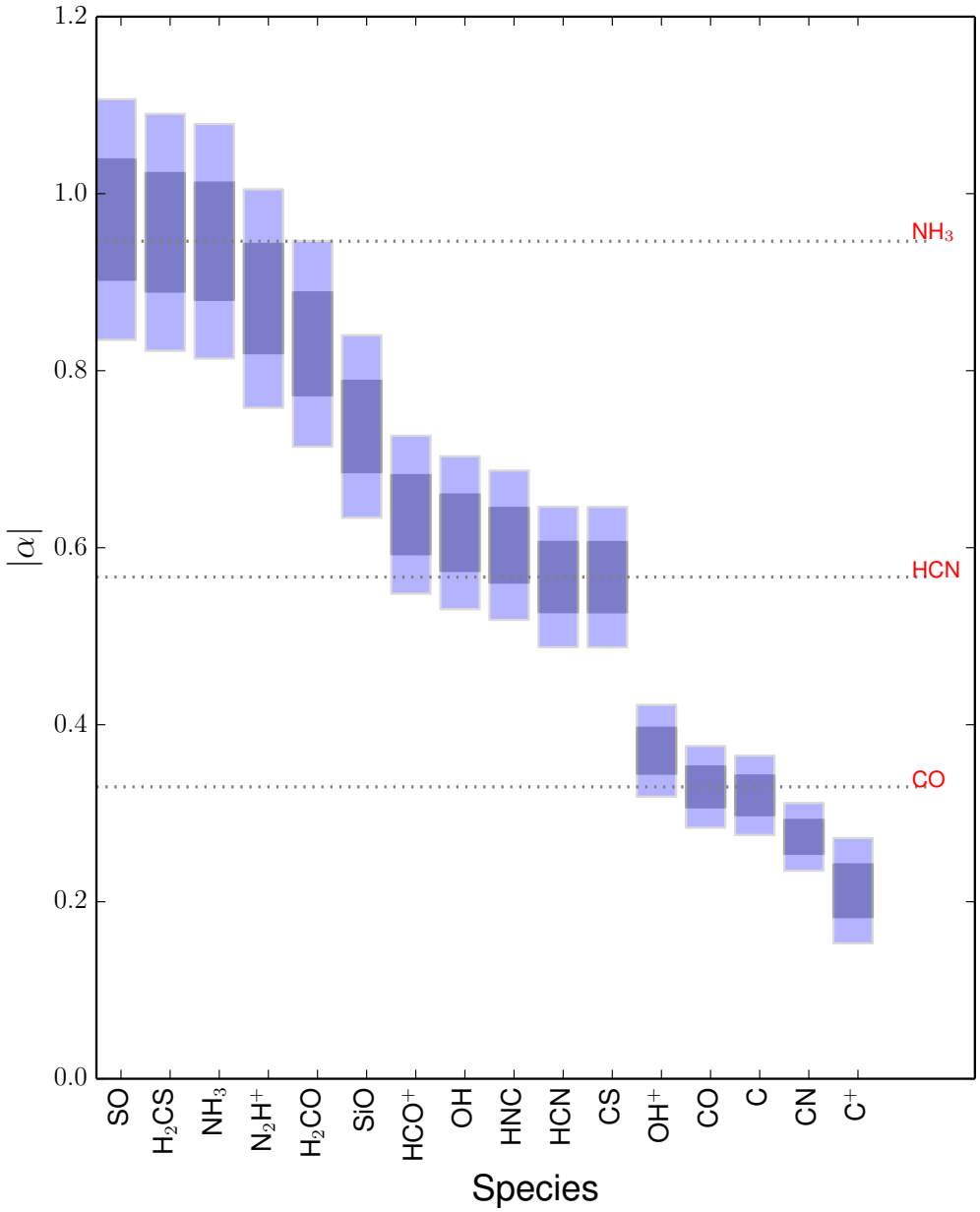

Figure 2.4. Plot of the SCF slopes for all the species used in the study. The blue and gray boxes are the 1 and 2 σ errors on the slope, respectively, from line of sight variations. The horizontal grey lines indicate the measured slopes for three common tracers.

half. Table 2.2 displays the resulting SCF slopes and power law fit errors. We plot the full SCFs in Figure 2.13.

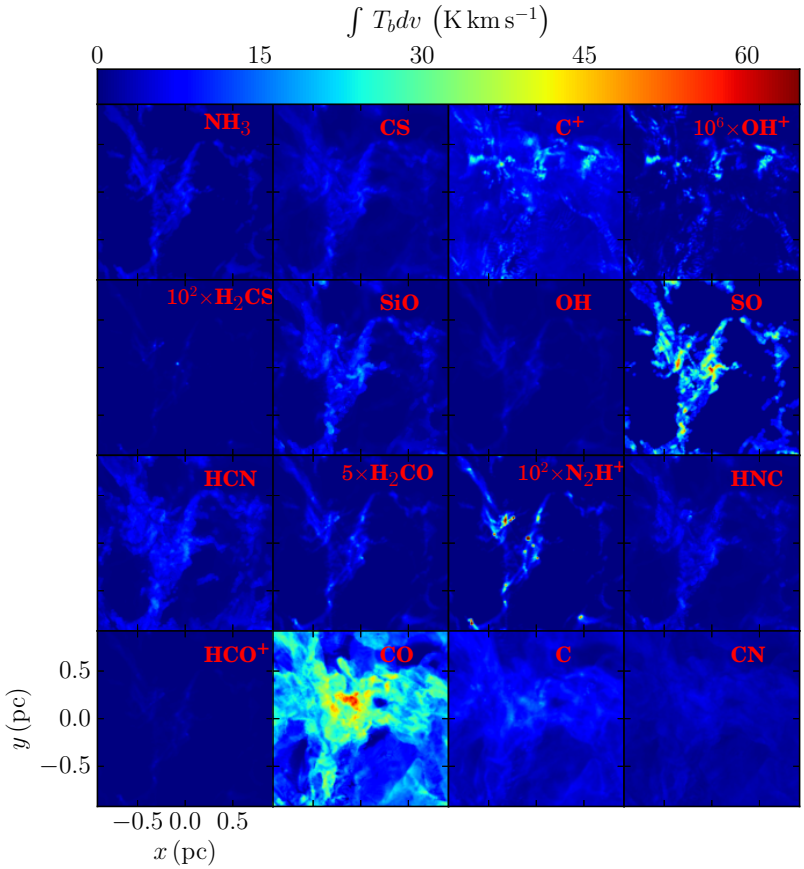

Figure 2.5. Integrated intensity maps for 16 different species, in units of K km s^{-1}. The species OH^+, H_2CS, N_2H^+ and H_2CO have their emissions multiplied by the value shown shown to see their structures.

In order to properly compare the model to the observations, we perform several procedures on the observational data. First, we smooth the data with a Gaussian beam corresponding to the FCRAO 46″ beam resolution. Then, we regrid the data so that each pixel has the same spatial pixel scale of the two different clouds. Third, we apply a detection limit where we remove pixels with emission less than $0.01\times <T_b>$. Finally, we add noise corresponding to Gaussian thermal noise with a standard deviation of $\sigma_T \sim 0.3$ K to model the noise in the Perseus COMPLETE data. We did not perform biased sampling, which may affect the longest length scales of the SCF due to the irregular observational stencil.

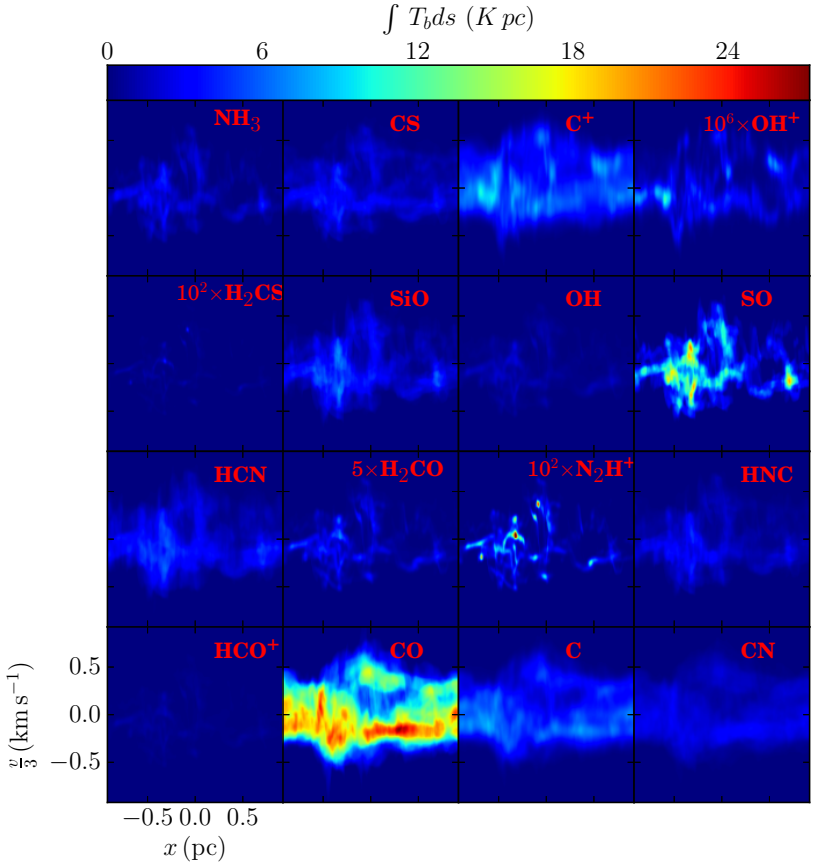

Figure 2.6. Integrated emission maps of velocity versus position, in units of K pc. The velocity on the vertical axis is scaled by 3 kms^{-1}. We multiply the emission of OH^+, H_2CS, N_2H^+ and H_2CO emission by the value shown to increase contrast.

Table 2.2 gives the values of the slopes and the associated error of the power law fit. The model cloud SCF initially has a slope of -0.29. However, after matching to the observational resolution the SCF slope changes by quite a bit to -0.13 and -0.19 for the Ophiuchus and Perseus resolutions, respectively. Furthermore, the fit error indicated in the table shows that the power law fits are all well constrained. Figure 2.13 shows that the model cloud and the Perseus cloud have similar SCFs when taking into account observational biases, such as beam size and pixel resolution. This is indicated by the similar power law fits shown in the bottom of the figure. The Ophiuchus SCF is steeper than the mode SCF at the Ophiuchus pixel and beam

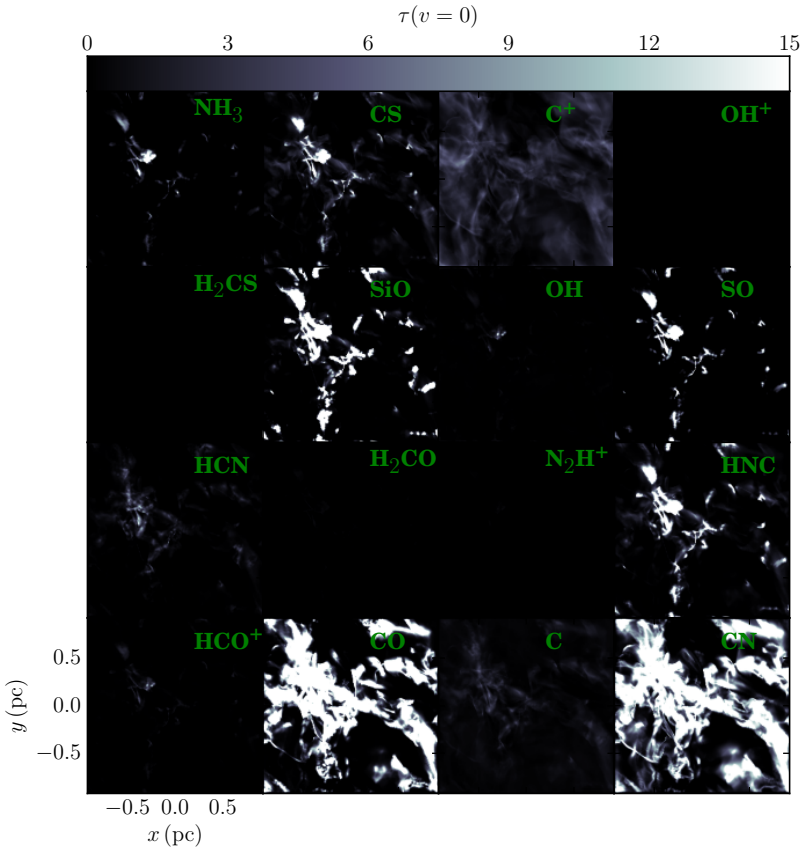

Figure 2.7. Line center optical depths calculated by RADMC-3D. The HCN and CO density profiles in this plot are treated with a crude dust treatment described in the Appendix. The HCN optical depth is divided by a factor of three to approximate the addition of the fine structure component to the transition.

resolution, though it is similar to both the Perseus SCF and the model SCF at Perseus resolution. The flattening of the SCF at small scales is due to the beam resolution. While the emission is still correlated, the turbulence has been resolved out within the beam area. There is still some difference between the simulation and observations which may be due to other biases. However the model and observations match within the 10% error mentioned in §2.4.2.

In Figure 2.1, the SCFs for all of the tracers appear to flatten out at some large scale, with the exact scale seemingly changing depending on the tracer. Padoan et al.

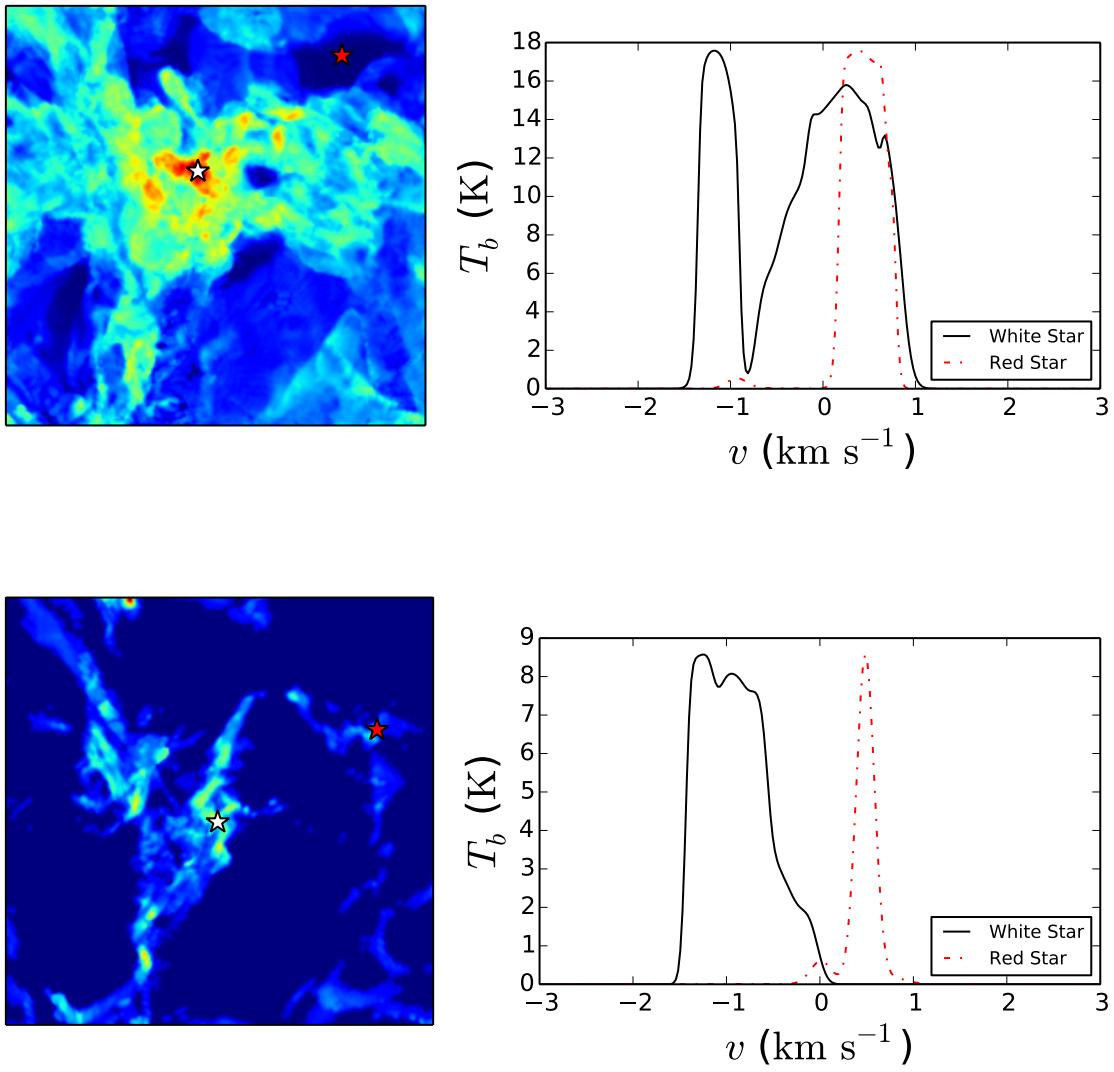

Figure 2.8. Integrated emission maps (left) and line-of-sight velocity spectra (right) for CO (top) and NH_3 (bottom). The white and red star locations represent emission from compact regions and diffuse regions, respectively.

[131] also found that their SCFs from simulated clouds traced by ^{13}CO flatten, but the SCFs for local clouds, also traced by ^{13}CO, steepen. We were not able to replicate this discrepancy with our simulations, though we conclude that the steepening effect is most likely due to some observational bias at large length scales.

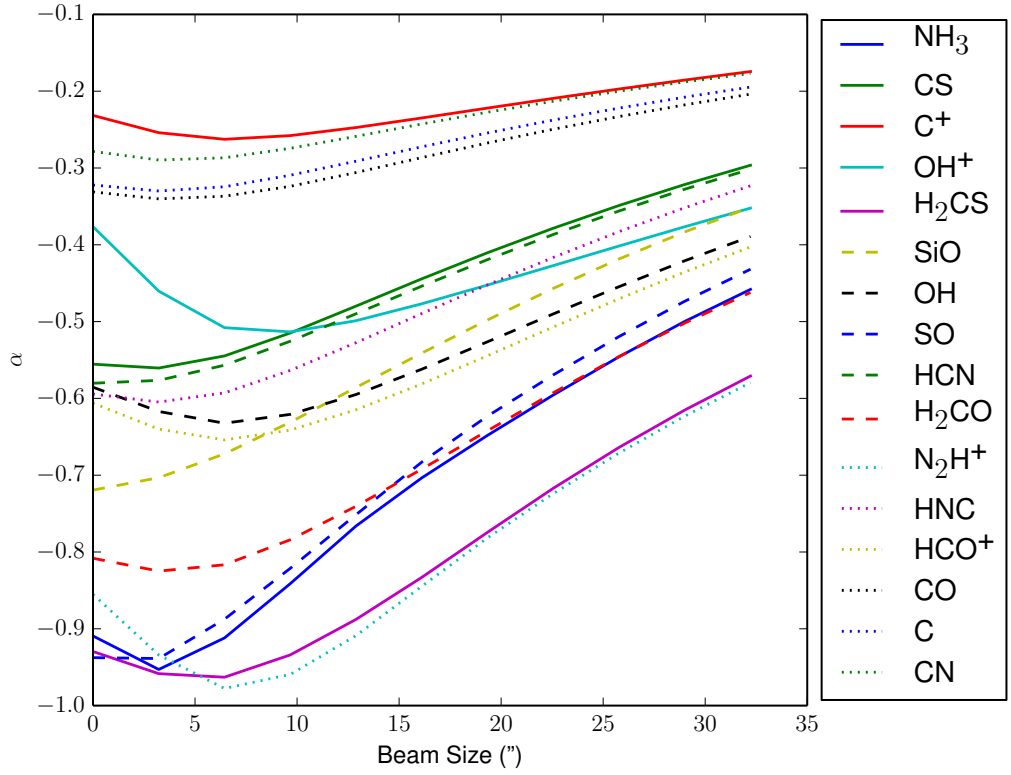

Figure 2.9. SCF slope, α, versus beam resolution. We calculate the angular beam size by placing the model cloud at a distance of 1 kpc. The clouds are then convolved with a Gaussian of the given beam size.

2.5.2 Understanding Chemistry from the SCF

A fundamental question of this work is: what does the SCF reveal about the chemistry of various tracers? Using Figures 2.9 and 2.4 we group the SCF slopes into three emission categories: diffuse, intermediate, and compact. C is an example diffuse tracer which is excited down to lower densities of ~ 800 cm^{-3} and is abundant throughout the entire volume. HCN is excited at fairly high densities and it becomes quite abundant once it is shielded from the UV field, so it traces up to intermediate scales. A common dense core tracer is N_2H^+ which also gets excited at higher densities, where it is also shielded from photodissociation. Commonly studied tracers such as CO, C^+, HCN, NH_3 and N_2H^+ confirm that the SCF slope reflects the

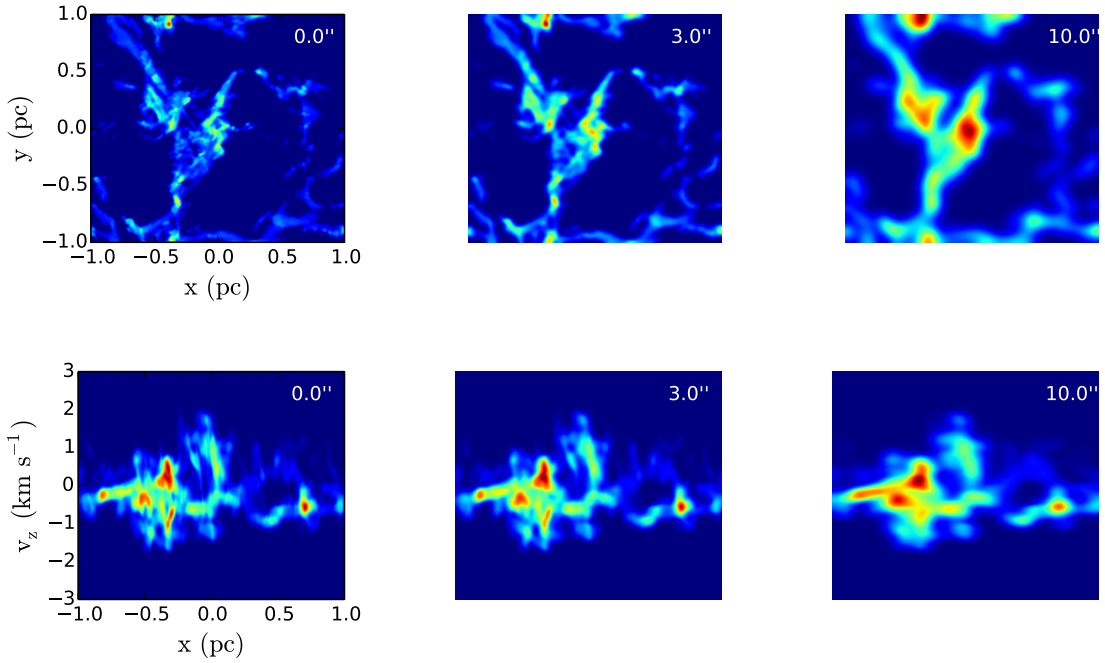

Figure 2.10. NH_3 integrated emission maps for PP (top) and PV (bottom) at different spatial resolutions for a distance of 1 kpc. The beam size appears in the top right.

expected optical depth, filling fraction, and critical density of the emission. While it is impossible to compute the true density distribution from the SCF alone, the slope does indicate the scale the species traces. For instance, shallower slopes, such as that of CO, show that the gas remains correlated on larger scales.

CO is a species of particular astrophysical importance. Over the past several decades, CO has become the most prominently utilized cloud mass tracer and has received significant theoretical attention. Our results show that the SCF of CO traces diffuse regions, as indicated by its shallow slope. Our results also show that CO traces the gas up to high densities, although proper treatment of dust grain depletion could change this. Since CO has a low critical density (see Table 2.1), the lowest level transition is easily excited throughout most of the cloud. This allows the cloud to produce emission in both the lower density environments and the dense cores (where

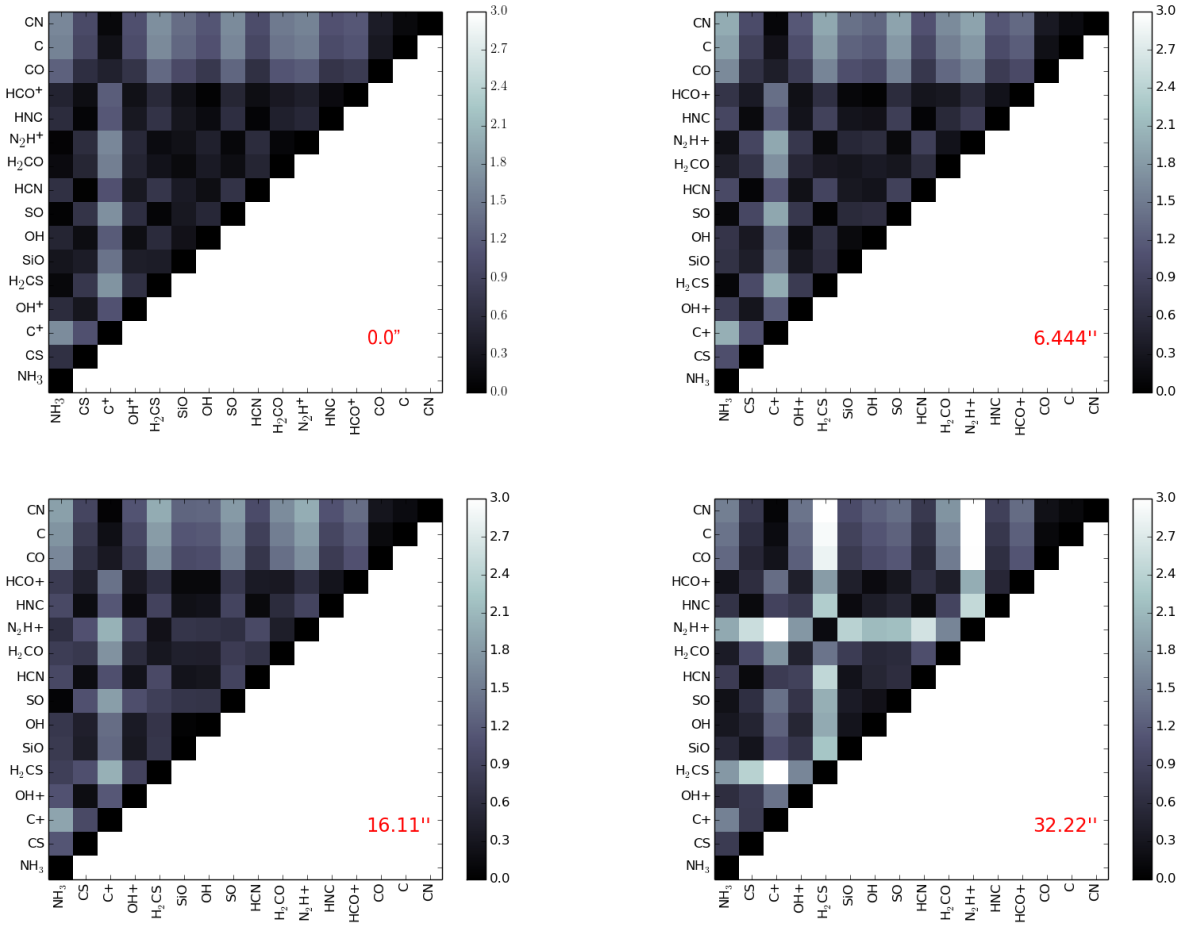

Figure 2.11. Distant metrics for all 16 species, where darker colors indicate more similar SCFs. We calculate the resolution by setting the cloud at a distance of 1 kpc for the beam size shown in the bottom right.

the emission saturates due to optical depth). For this reason, CO also has a high volume and surface filling fraction. Figure 2.7 confirms that CO has the highest average optical depth, which is due to its low critical density and higher abundance.

However, the SCF analysis identifies several tracers that exhibit similar emission. We find that C and CN are homologous to CO. The correlations between these species makes chemical sense since all three depend upon the abundance of neutral carbon. The UMIST chemical network shows that both CO and CN form rapidly in the original diffuse environment. Their behavior at higher densities though is quite different.

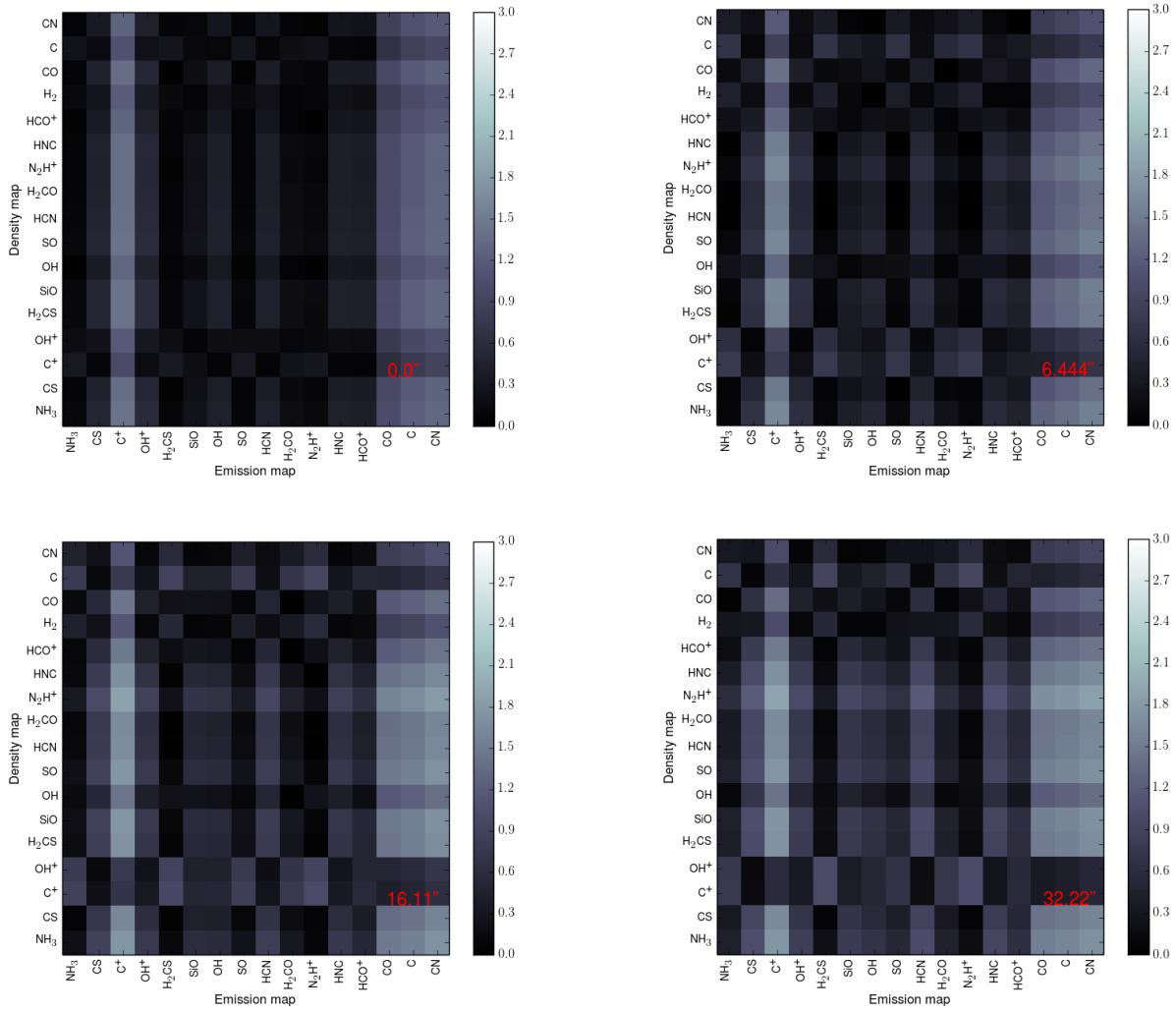

Figure 2.12. Distance between the density PPV cube SCF (vertical) and the intensity PPV cube SCF (horizontal) for each species pair. The beam resolution for the intensity PPV cube as placed at a distance of 1 kpc, appears at the bottom right. The PPV_ρ cube is not blurred with the beam.

CN is photodissociated much more rapidly towards lower densities than CO because it cannot self shield. CN is depleted through reactions forming more complex molecules faster than CO. This results in a factor of several orders of magnitude difference between the abundances of the two molecules. Therefore, it is reasonable to expect CO and CN to be very similar in low density environments. In regions of high mass star

Table 2.2. Comparison between Model and Observed Clouds

Cloud	α	$\sigma_{\rm fit}$
Model	-0.29	0.01
Model (Oph Res)	-0.13	0.01
Model (Per Res)	-0.19	0.006
Ophiuchus	-0.22	0.01
Perseus	-0.21	0.007

Notes. Comparison of ^{12}CO SCF power law fit values, α. Per Res indicates the model cloud at the spatial resolution of the Perseus cloud, and likewise for Oph Res. $\sigma_{\rm fit}$ is the error of the power law fit in log space.

formation, CN could be used as a proxy for CO, which is optically thick, or of the surrounding diffuse gas.

Another common molecular gas tracer is HCN, which is frequently used to trace gas with densities above 10^6 cm^{-3}. The SCF slope implies it also traces intermediate density regions in filaments, i.e. $n \sim 10^3$ to 10^4 cm^{-3}, although, the emission level may be too low to detect. Recent work by Forbrich et al. [139] confirms that HCN and HNC are good tracers of dense environments over a wide range of extinctions. The optical depths we calculate for HCN are off by a factor of three since we do not model the HCN fine structure for the ground state transition.

Finally, there are a variety of species that trace dense cores, including NH_3 and N_2H^+. Figure 2.6 confirms the trend that species tracing more diffuse regions have shallower slopes than species that typically trace high density regions. Here, the regions the species trace are clear in the velocity information. Diffuse gas tracers have significant emission in a broad range of velocities, as illustrated by the horizontal bands in species CO, C and CN in Figure 2.6. Species which trace higher densities show no diffuse component. Instead, the emission is located in clumps or filaments, which exhibit a smaller range of velocities.

While the density is important, the gas must also have a high enough temperature to excite the transition. We define a characteristic line temperature T, where $h\nu_i =$

kT_i, where ν_i is the line frequency. All the species have line temperatures below 10 K except C, C^+ and OH^+, which have line temperatures of 23 K, 91 K and 44 K, respectively. The average gas temperature in diffuse regions is around 100 K, so even these species are easily excited from their ground states. However, OH^+ is mostly observed in absorption. This is due to its low abundance and higher excitation making measurements from absorption in the dust continuum easier than trying to detect the very small emission signal (as noted by the multiplicative factor of $\sim 10^6$ in Figures 2.5 and 2.6).

Complex molecules, such as NH_3 require higher densities to form, and photodissociate rapidly at lower densities where the UV field is higher. Simple light diatomic molecules such as CN form in diffuse regions. An exception is CS, which appears only in intermediate density regions. It photodissociates faster than CO but slower then CN. However, due to the much lower initial abundance of sulfur, it forms only where the sulfur is concentrated. Most of the tracers in this study that have a shallow slope also tend to have a very high optical depth. The only exception is OH^+ which has a very low abundance.

2.5.3 Discussion of Observational Implications

The results from Figures 2.9 and 2.11, as well as our definition of complementary species, suggest sets of homologous species. These are groups of species whose spectral structure is very similar in PPV space, indicating that, especially for the optically thin tracers, they should trace similar density regimes.

Recent theoretical studies, such as Glover et al. [111] and Offner et al. [112], found that C is a good alternative tracer to CO. C has several advantages, including a ground state transition at 609 μm and a lower optical depth than CO. These recent studies challenge the idea that C traces only the surface of the PDR. Our study confirms this picture by showing that C and CO have very similar SCFs, with CO

being complementary to C. Our study *also* predicts that CN is an alternative tracer to CO and C. CN (1-0) has a similar transition frequency with an optical depth around an order of magnitude less than CO, although its slope is slightly flatter indicating that it traces even lower density regions, and it has a similarly high filling fraction. The slightly flatter slope is expected; CN is destroyed faster than CO in higher density environments due to its role as a reactant in reactions forming more complex molecules. Since CN and CO form very quickly and depend on the relatively high-abundance of C, they both have very high filling fractions. Their surface filling fractions are both over 90%, and their volume filling fractions are greater than 0.3. In fact, Table 2.1 shows that CN is both more surface filling and volume filling than CO. The cosmic-ray induced photodissociation rates (i.e. CX + CRPHOT $\rightarrow$ C + X) given by the UMIST2012 network are $R_{CN} = 1.4 \times 10^{-13}$ s^{-1} and $R_{CO} = 7.5 \times 10^{-16}$ s^{-1}. Cosmic rays penetrate further into the cloud than the external UV radiation, indicating the CN will be destroyed by cosmic rays inside the cloud faster than CO. Indeed, CO has an abundance several orders of magnitude greater. Singly ionized carbon traces more diffuse regions but is not as abundant in higher density regions where it combines with O to form CO. The C^+ (1-0) transition is in the infrared, which can be observed using space-based instruments, such as the Herschel Space Observatory [e.g. 140] and the GREAT Spectrometer on Stratospheric Observatory for Infrared Astronomy (SOFIA).

A commonly used high density tracer is N_2H^+, which has a ground state transition at 93 GHz. Our study predicts several homologous tracers to N_2H^+ including: H_2CO, H_2CS, NH_3, and SO. All of these species exist in similar environments and have surface filling fractions between 0.01 and 0.25. However, some of these tracers only form the high density cores which such as N_2H^+, with a volume filling fraction of 0.21. H_2CO has a higher volume filling fraction than N_2H^+ ($f_v = 0.37$) which indicates that it traces a larger fraction of the core gas. We find that H_2CO and SO have higher

brightness temperatures indicating that they should be easier to detect than species with fainter emission such as H_2CS and N_2H^+. NH_3 and SO show significant emission in filaments, but N_2H^+ is brightest in dense "cores". NH_3 has a relatively low critical density ($n_c = 1991$ cm^{-3}), so it is excited at lower densities than high densities tracers like N_2H^+. However, it is not as bright as other low critical density tracers like CO ($n_c \sim 2000$ cm^{-3}) because of its low abundance outside of dense regions. Some of these correlations could change with the inclusion of dust grain chemistry. This would lower the abundances of the higher density tracers, such as NH_3, H_2CO, H_2CS and SO, and reduce their emission. However, these molecules only begin to deplete for H_2 number densities $\geq 10^7$, greater than the maximum density in this simulation. Detailed treatment of gas-grain chemistry is beyond the scope of this work.

2.6 Conclusions

We use numerical simulations of a Milky Way-like molecular cloud to study how the SCF varies between different species. We post process the hydrodynamical simulation with the astrochemistry code 3D-PDR, which uses a full chemical network to obtain abundances of over 200 different species. We produce synthetic line observations for a subset of these. We calculate the SCF for each of the species for both the density and emission distributions and define a "distance" metric to compare them. On the basis of this, we draw the following conclusions:

1. The SCF is sensitive to the chemistry of the tracer. Species tracing diffuse gas tend to have shallower SCF slopes, whereas species that trace dense regions ("cores") have steeper slopes.

2. We confirm that the emission structure, as characterized by the SCF, poorly traces the density structure for species with optically thick emission. The decoupling is due to line saturation in the highest density regions.

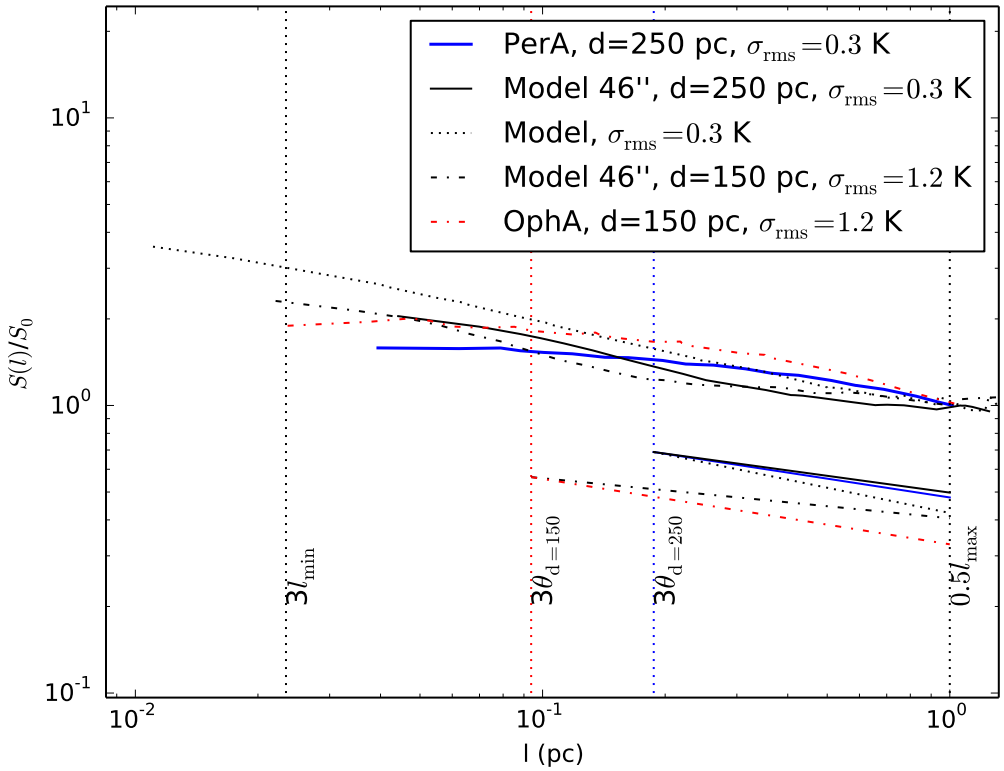

Figure 2.13. SCF as a function of size for two clouds in the COMPLETE survey and the model cloud at different resolutions. The dashed-dot red line is the SCF for the Ophiuchus cloud, while the solid blue line is the Perseus cloud. We divide the Perseus cloud into two components at the cloud center (dashed blue lines). The different black line styles indicate different spatial resolutions, where the dotted line represents the simulation resolution, the solid line represents a 46" beam at 250 pc, and the dot-dashed line represents 46" at 125 pc to match with the line styles of the observed clouds. The vertical lines represent the minimum length scales used for the power law fitting, with θ representing the beam size. The power law fits are shown below, with the line styles matching their corresponding SCF.

3. Spatial resolution has a distinct effect on the SCF slope, but even with relatively low beam resolution the slopes remain in a similar region of parameter space. However, for poor resolution, some species have artificially similar SCFs.

4. Velocity resolution has no effect on the SCF slope, since the SCF only measures the rms velocity between spatial regions. This will only hold while the spectral

features are resolved, namely that the velocity channels are smaller than the linewidth. Noise variation also has little effect on the slope, since variations cancel as long as the noise is Gaussian.

5. We find that C, C^+, CN, CO, and OH^+ are homologous diffuse gas tracers. OH, CS, HCN, HNC and SiO are homologous intermediate gas tracers. Finally, H_2CO, H_2CS, N_2H^+ and NH_3 are homologous dense core tracers when gas phase chemistry is dominant. The statistical similarity of the SCFs suggest that they trace similar cloud structure and likely provide complementary information.

This study takes the first steps in exploring the 3D astrochemical correlations in molecular clouds. In this study, we show that the SCF slope can be used as an indicator of the density of environments where specific species form. This provides insight into the gas chemistry of particular species. Future work can still expand on this in several ways. We do not investigate the SCF evolution as a function of time. Also, we do not include either dust grain chemistry or shock chemistry. Future studies can investigate higher level transitions, such as CS (2-1) and CO (3-2), and isotopologues such as ^{13}CO.

2.7 Appendix

In this appendix, we discuss briefly how effects such as dust-grain chemistry and shock chemistry could affect our results.

2.7.1 Dust-Grain Chemistry

2.7.1.1 CO and HCN

Both CO and HCN, as well as other high-density tracers, may be affected by depletion at high-densities. CO depletion is extreme at high-densities with the mean abundances declining by several orders of magnitude [see 93, 94, 95]. HCN also freezes out, but at higher densities. In order to assess the impact of depletion on our CO

and HCN results, we adopt crude treatments for dust freeze-out and recalculate the optical depth and SCF. We set the abundance of CO to 0 where the H_2 number density exceeds 10^4 cm^{-3}. For HCN we set a limit of [HCN]/[H_2] = 10^{-8} in cells where $n_{H_2} \geq 10^4$ cm^{-3}. We compare the SCF slopes of the tracers with and without depletion and find that the change in slope is less than 10%. Setting a maximum HCN abundance of 10^{-8} relative to H_2 reduced the HCN optical depths to $\tau < 10$ across the entire cube, with the typical optical depth being $\sim$ 1-4. Furthermore, since in these high densities the HCN gas will remain optically thick, it should not drastically impact the SCF correlations. Overall, we conclude that the exclusion of dust depletion does not significantly affect our results due to the small percentage of the simulation volume at high-densities (1%).

2.7.1.2 N_2H^+

When CO starts to freeze-out onto dust grains, several molecules, such as N_2H^+ will see an increase in their abundances. This occurs because H_3^+ reacts with CO to form HCO^+ which is the main destruction mechanism for H_3^+. As the amount of CO decreases there is a surplus of H_3^+. In high density environments, H_3^+ can be destroyed to form N_2H^+ [141, 142, 143, see] by the following mechanism:

$$H_3^+ + N_2 \rightarrow N_2H^+ + H_2 \tag{2.6}$$

In order to test whether this effect has an impact, we adopt a simple approximation in which the amount of N_2H^+ increases at high densities. Since CO starts to deplete at H_2 densities above n(H_2) $\geq 10^4$ cm^{-3}, we multiply the N_2H^+ abundance by a factor of 4 where the gas fits this criteria. Since the emission is mostly optically thin, this merely scales the emission by a constant factor. Similar to the case for CO and HCN depletion, we find that this mechanism has no statistical impact on our results. It

is noteworthy that the enhancement of N_2H^+ is not universal, with studies such as Tafalla et al. [144, 145] showing either no N_2H^+ increase or showing N_2H^+ depletion.

2.7.2 Shock Chemistry: SiO

Since our hydrodynamic simulation doesn't resolve shock fronts to the necessary resolution to calculate post-shock densities and temperatures, well known shock tracers such as SiO will not be properly modeled. In shocks, changes in the density and temperature can lead to a large enhancement of the abundance of SiO. Furthermore, at higher temperatures, the abundance of SiO can be increased by sputtering from dust grains. This mechanism is the ejection of Si and SiO from a grain surface following a high enough energy impact of gaseous species. At lower temperatures, the sputtering rate is expected to be small [146]. Even though sputtering from shock chemistry, and other shock effects, will affect the abundance, the inclusion of shock chemistry is beyond the scope of this work. Finally, the increased brightness of the SiO emission is an artifact of using a non-depleted Si abundance, which is over an order of magnitude larger that observed depleted abundances [147].

CHAPTER 3

A MODEL FOR PROTOSTELLAR CLUSTER LUMINOSITIES AND THE IMPACT ON THE CO-TO-H_2 CONVERSION FACTOR

This chapter[1] focuses on developing the formalism to generate synthetic protoclusters and calculating their luminosities. These methods are used to couple the radiation from protostars to astrochemical models of molecular clouds.

3.1 Abstract

We construct a semi-analytic model to study the effect of far-ultraviolet (FUV) radiation on gas chemistry from embedded protostars. We use the Protostellar Luminosity Function (PLF) formalism to calculate the total, FUV, and ionizing cluster luminosity for various protostellar accretion histories and cluster sizes. We compare the model predictions with surveys of Gould Belt star-forming regions and find the Tapered Turbulent Core model matches best the mean luminosities and the spread in the data. We combine the cluster model with the photo-dissociation region astrochemistry code, 3D-PDR, to compute the impact of the FUV luminosity from embedded protostars on the CO to H_2 conversion factor, $X_{\rm CO}$, as a function of cluster size, gas mass and star formation efficiency. We find that $X_{\rm CO}$ has a weak dependence on the FUV radiation from embedded sources for large clusters due to high cloud optical depths. In smaller and more efficient clusters the embedded FUV increases $\rm X_{CO}$ to

[1]These results are based on research published by Gaches and Offner [148] and is reproduced with permission from the AAS.

levels consistent with the average Milky Way values. The internal physical and chemical structure of the cloud are significantly altered, and $X_{\rm CO}$ depends strongly on the protostellar cluster mass for small efficient clouds.

3.2 Introduction

In the local universe, star formation occurs exclusively within molecular clouds [41]. These clouds exhibit complex structure regulated by a combination of turbulence, gravity and magnetic fields [149]. The relative balance between these forces determines the amount of dense gas where the star formation occurs. Studying the dynamics and structure of molecular gas is paramount to understanding the star formation process. Star formation acts as a clock within molecular clouds, when internal feedback mechanisms turn on and start to impact the evolution of their natal host cloud. During star formation, knowing the dynamics is necessitated by understanding the feedback mechanisms.

Molecular clouds are composed primarily of molecular hydrogen, H_2. However, H_2 has no permanent dipole, and thus is not visible at the cold temperatures of molecular clouds. Instead, most studies rely on the emission from carbon monoxide (CO) as a proxy for total molecular gas mass. CO has the second highest molecular abundance after H_2, a permanent dipole and is readily excited at the temperatures and densities of molecular clouds. In addition to CO, astronomers also use a wide array of other molecules that span a range of physical and chemical conditions, including tracers of denser gas like HCN and N_2H^+ [96, 99, 100, 103].

Because H_2 is not directly observable, molecular gas mass must be determined indirectly by assuming a fixed dust-to-gas ratio or some simple relationship between H_2 and another molecular species. The most common conversion is $X_{\rm CO}$, which is defined as

$$X_{\rm CO} = \frac{N_{\rm H_2}}{W_{\rm CO}}, \tag{3.1}$$

where N_{H_2} is the column density of molecular hydrogen in units of cm^{-2} and W_{CO} is the integrated intensity in K km s^{-1}. The typical Milky Way value is $X_{CO} = 2 \times 10^{20}$ K km s^{-1} cm^{-2} [36]. This value implicitly assumes CO is optically thick and that molecular clouds are in rough virial equilibrium [36]. The related conversion factor denoted α_{CO} relates the total CO luminosity to the molecular gas mass M_{gas}.

However, X_{CO} is subject to a variety of uncertainties. It varies significantly within clouds [e.g., 150]. Distance reduces the accuracy of measured CO luminosities. Outside the MW, the measured X_{CO} between clouds has a large dispersion, and multiple clouds may occupy an observational beam [151]. It also varies with metallicity, C/O ratio, cosmic ray ionization rate and the local Far-Ultraviolet (FUV) radiation field [28, 92, 113, 152, 153, 154, 155]. Consequently, understanding the gas chemistry and related thermal processes is crucial to interpret observations and derive accurate conversion factors.

Numerical models provide an important means to predict how abundances and gas properties vary as a function of local environment. These models range from simple one-zone models to full chemo-hydrodynamics simulations. Simple gas models [i.e., 107, 108] allow for the use of large chemical networks (hundreds of species) and parameter studies spanning diverse physical environments. Often, in these models the gas is treated as a one-dimensional, semi-infinite slab of uniform density [104]. This assumption necessarily ignores the complex 3D physical structure of molecular clouds. In contrast, chemo-hydrodynamic simulations are time-intensive and, thus, restricted to smaller networks (dozens of species), but they allow for a much more accurate treatment of cloud physical conditions [25, 79, 91, 92, 156, 157]. Both approaches treat the gas as a photodissociation region (PDR) and solve chemical networks coupled to the physical environment.

By convention, the FUV radiation field is assumed to be a one-dimensional, monochromatic flux incident on the cloud boundary, which represents the interstellar

radiation field (ISRF). This treatment implicitly assumes that only external stellar sources influence the cloud chemistry. However, forming stars radiate their environment, producing chemical changes deep within the cloud. Protostellar radiation is produced by both accretion and stellar processes, such that embedded sources often have luminosities much higher than that of main sequence stars of the same mass [60, 61, 158, 159]. The protostellar spectrum includes radiation at FUV wavelengths and, for high-mass stars, ionizing radiation. Therefore, once molecular clouds begin forming stars the local radiation field is set by both the ISRF and radiation from embedded star formation.

To date, no PDR studies have directly included embedded sources. Instead, some recent theoretical work indirectly modeled how the star formation rate (SFR) affects X_{CO}. Papadopoulos [160] studied the physio-chemical nature of high-density star formation systems, such as ULIRGS. They derived a correlation between the supernova rate (and hence star formation rate) and the galactic average FUV background and cosmic ray ionization rate. They found that while the FUV radiation is quickly attenuated, cosmic rays are able to penetrate and heat the entire cloud. Bisbas et al. [154, 161] used one-zone models to study the destruction of CO by cosmic rays across a parameter space spanning many different types of galaxies. Clark and Glover [152] combined the Papadopoulos [160] model with hydrodynamic simulations and post-processing to study the impact of the star formation rate on X_{CO}. They found that X_{CO} increased with the star formation rate. However, none of these studies included embedded radiation or cosmic rays from protostars.

In this paper, we formulate a simple cloud model that includes internal sources of FUV radiation in order to study variations in CO chemistry as a function of star formation activity. §3.3 describes the semi-analytic model we use to calculate the cluster luminosities and our astrochemistry method. §3.4 shows the results of the calculations for two different physical models: one where the cloud gas mass is fixed

and a second where the cloud gas mass is varied as a function of star formation efficiency. §3.5 discusses the implications of our study for observations and compares the results to prior work.

3.3 Modeling the CO Emission of Star-Forming Clouds

3.3.1 Star Cluster Model

We summarize the Protostellar Luminosity Function (PLF) formalism from Offner and McKee [50] here for completeness and discuss our extensions to the work.

The PLF is derived by adopting an accretion model, which in turn prescribes the underlying distribution of protostellar masses assuming that the final masses of the protostars obey a specified stellar initial mass function (IMF). In this framework, the accretion rate of a particular protostar, $\dot{m}$, is solely a function of its current mass, m, and its final mass, m_f. The Protostellar Mass Function (PMF) describes the distribution of current protostellar masses, i.e., the present-day protostellar mass function. McKee and Offner [162] define the PMF as:

$$\psi_p(m) = \int_{m_{f,\ell}}^{m_u} \psi_{p2}(m, m_f) d\ln m_f, \tag{3.2}$$

where $\psi_{p2}(m, m_f)$ is the bi-variate PMF which defines the fraction of protostars in a star-forming region with current masses in the range dm and final masses in the range dm_f. The bi-variate PMF is related to the bi-variate number density, dN_p^2, within a cluster by:

$$dN_p^2 = N_p \psi_{p2}(m, m_f) d\ln m d\ln m_f, \tag{3.3}$$

where N_p is the number of protostars in the cluster. We denote the stellar IMF as $\Psi(m_f)$. For a steady star formation rate,

$$\psi_{p2}(m, m_f) = \frac{m\Psi(m_f)}{\dot{m}\langle t_f \rangle}, \tag{3.4}$$

where $\Psi(m_f)$ is the stellar IMF, t_f is the time it takes to form a star with mass m_f and $\langle t_f \rangle$ is the average time to form a star:

$$\langle t_f \rangle = \int_{m_l}^{m_u} d \ln m_f \Psi(m_f) t_f(m_f). \tag{3.5}$$

Following McKee and Offner [162], we assume $\Psi(m_f)$ is a Chabrier IMF [51] truncated at some maximum mass, m_u.

Offner and McKee [50] parameterize the accretion model as:

$$\dot{m} = \dot{m}_1 \left(\frac{m}{m_f} \right)^j {m_f}^{j_f} \left[1 - \delta_{n1} \left(\frac{m}{m_f} \right)^{1-j} \right]^{1/2}, \tag{3.6}$$

where $\dot{m}_1$ is a constant, j and j_f are model parameters, and δ_{n1} is a parameter determining whether the accretion rate limits to zero at t_f ("tapered"). In this study, we consider three different accretion histories:

1. Inside out collapse of an Isothermal Sphere (IS) [163], which gives

$$\dot{m} = \dot{m}_{\rm IS} = 1.54 \times 10^{-6} (T/10\,K)^{3/2} \quad M_\odot \text{ yr}^{-1}, \tag{3.7}$$

   where T is the gas temperature. In this model, the accretion rate is constant for a given temperature and is independent of stellar mass.

2. Turbulent Core (TC) model [164] in which the turbulent pressure exceeds thermal pressure. The accretion rate is

$$\dot{m}_{\rm TC} = 3.6 \times 10^{-5} \Sigma_{\rm cl}^{3/4} \left(\frac{m}{m_f} \right)^j {m_f}^{3/4} \quad M_\odot \text{ yr}^{-1}, \tag{3.8}$$

   where $\Sigma_{\rm cl}$ is the surface mass density, given in units of g cm^{-2}, and m and m_f defined above. $\dot{m}_1 = \dot{m}_{\rm TC} = 3.6 \times 10^{-5} \Sigma_{\rm cl}^{3/4}$. Following McKee and Tan [164], we use $j = \frac{1}{2}$. In this model, higher mass stars accrete at higher rates.

3. Tapered Turbulent Core (TTC) model [50]

$$\dot{m}_{\rm TTC} = \dot{m}_{\rm TC}\left[1-\left(\frac{m}{m_f}\right)^{1-j}\right]^{1/2} \quad M_\odot \text{ yr}^{-1} \tag{3.9}$$

where the parameters are taken to be the same as the turbulent core model but $\delta_{n1} = 1$. The tapered accretion rate produces smaller luminosities in later stages of protostellar evolution.

For accretion histories formulated in this way, the formation time of an individual star is:

$$t_f = t_{f1} m_f^{1-j_f}(1+\delta_{n1}), \tag{3.10}$$

where

$$t_{f1} = \frac{1}{(1-j)\dot{m}_1} \tag{3.11}$$

and t_{f1} is the time to form a star of 1 $M_\odot$. We discuss the impact of adopting a different tapering model in Appendix 3.7.2.

The PLF, $\psi_p(L)$, is defined such that $\psi_p(L) d\ln L$ is the fraction of protostars within the luminosity range dL. Offner and McKee [50] showed that the bi-variate PLF is related to the bi-variate PMF by

$$\psi_{p2}(L, m_f) d\ln L \, d\ln m_f = \psi_{p2}(m, m_f) d\ln m \, d\ln m_f, \tag{3.12}$$

such that the PLF is defined

$$\psi_p(L) = \int d\ln m \cdot \psi_{p2}(L, m). \tag{3.13}$$

Offner and McKee [50] calculate the PLF by transforming Equation 3.13 to:

$$\psi_p(L) = \int_{m_{f,l}(L)}^{m_u} d\ln m_f \frac{\psi_{p2}(m(L), m_f)}{\left|\frac{\partial L}{\partial m}\right|}, \tag{3.14}$$

where $m_{(f,l)}(L) = \max(m_l, m(L))$.

To calculate the luminosities, we adopt the model in Offner et al. [61], which is based on McKee and Tan [164]. This model represents the protostellar luminosity as the sum of two parts, $L = L_{\rm acc} + L_{\rm int}$, where $L_{\rm acc}$ is the accretion luminosity and $L_{\rm int}$ is the internal protostellar luminosity, including Kelvin-Helmholz contraction and nuclear burning. The total accretion luminosity is defined by:

$$L_{\rm acc} = f_{\rm acc}\frac{Gm\dot{m}}{r}, \tag{3.15}$$

where $f_{\rm acc}$ is the efficiency at which mechanical energy is converted to radiation, G is the gravitational constant, m is the protostar mass, $\dot{m}$ is the accretion rate (given by Equation 3.6) and r is the protostar radius calculated following Offner et al. [61]. Following Offner and McKee [50], we use $f_{\rm acc} = 0.75$. The total internal luminosity is approximated by the main sequence mass - luminosity relationship given in Tout et al. [165]:

$$L_{\rm int} = \frac{\alpha M^{5.5} + \beta M^{11}}{\gamma + M^3 + \delta M^5 + \epsilon M^7 + \zeta M^8 + \eta M^{9.5}}. \tag{3.16}$$

Coupling this model to our PDR calculation requires some assumption about the shape of the protostellar spectrum. We assume that each luminosity component is a blackbody as described by the Planck function, such that the luminosity in a given energy range is

$$L_{\Delta \rm E} = f_{\Delta \rm E}(L_{\rm acc}) \times L_{\rm acc} + f_{\Delta \rm E}(L_{\rm int}) \times L_{\rm int}, \tag{3.17}$$

where $f_i(L)$ is the fraction of the Planck function within the given energy range of interest. The blackbody temperature is derived using the Stefan-Boltzmann law with the protostar radius and luminosity from the Offner et al. [61] model. In the limiting case where $\Delta E \to \infty$, $L_{\Delta \rm E} \to L$.

This model is intended to represent relatively young clusters, whose membership is dominated by protostars. Appendix 3.7.3 discusses the results for clusters which include a secondary population of main sequence stars.

3.3.2 Statistical Sampling

The PMF describes the likelihood that a cluster contains a protostar with a specific instantaneous mass and final mass. Because lower mass stars are much more numerous than higher mass stars, small clusters are statistically unlikely to include any high-mass stars. Under the assumption of a perfectly sampled PMF, the number of stars in a cluster, N_p, can be related to final mass of the highest mass star within the cluster, m_u. McKee and Offner [162] show that the cluster size, highest mass star in the cluster and the maximum possible stellar mass, $m_{\rm max}$ are related by:

$$\frac{1}{N_p(m_u)} = \int_{m_u}^{m_{\rm max}} \psi_p(m) d\ln m. \tag{3.18}$$

From an observational stand-point, the maximum mass, $m_{\rm max}$, is highly uncertain due to a variety of factors. Crowding in clusters and unresolved binarity make measurements of individual high-mass stars challenging [40]. Furthermore, constraining $m_{\rm max}$ requires measuring the populations of very young massive clusters, which are rare and distant. This work focuses mainly on small to intermediate clusters ($N_p \sim 10 - 10^5$), so we adopt $m_{\rm max} = 100 M_\odot$. The total cluster mass is then $\mathrm{M_{cl}} = \mathrm{N}_p \times \langle m \rangle$, where $\langle m \rangle = \int_{m_l}^{m_{\rm max}} d\ln m m \Psi(m)$. Figure 3.1 shows $N_p(m_u)$ as a function of the highest mass star in the cluster. We adopt a minimum mass, $m_{\rm min} = 0.033$ $\mathrm{M}_\odot$. For the TTC model, the average mass $\langle m \rangle \approx 0.2$ $\mathrm{M}_\odot$.

Equation 3.14 can be numerically integrated given a protostellar model for $L(m)$ and $r(m, m_f)$. This approach allows the distribution to be calculated exactly, i.e., direct integration produces perfect sampling of the underlying function. However, the stellar radius undergoes several discontinuous jumps due to changes in the nuclear

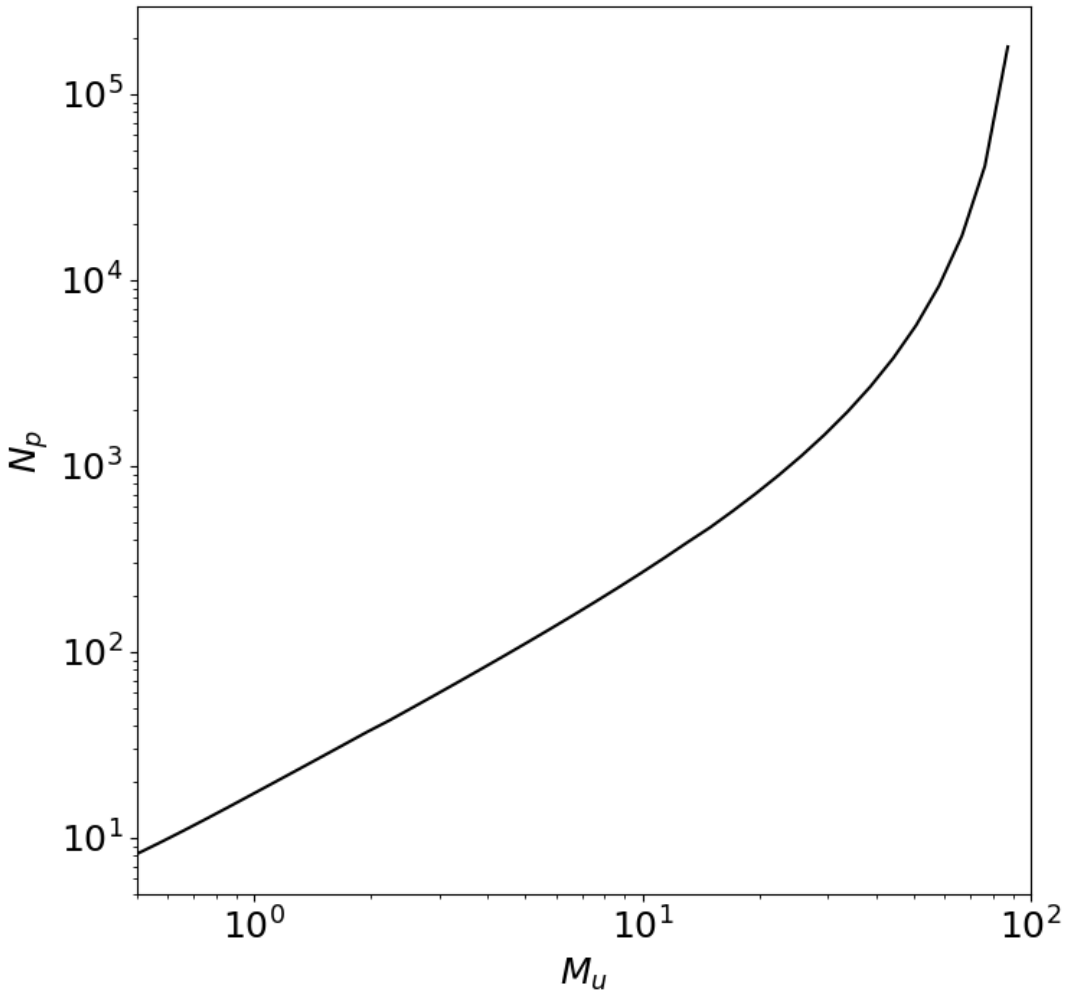

Figure 3.1. Number of stars as a function of the highest mass star in the cluster.

state [e.g., Fig. 5 in 166] and is consequently difficult to invert. Moreover, the mass functions of small clusters are subject to Poisson statistics and, thus, not perfectly sampled. We therefore adopt a statistical approach to compute the PLF and cluster properties.

We calculate the PLF and PMF of a cluster using the conditional probability method. The first step of the method is to marginalize the bivariate PMF (3.4) over the protostar final mass, m_f. This one-dimensional distribution function is then sampled for a protostar mass, m using the inversion method numerically. We then calculate the conditional probability distribution for the final mass given the current mass, $\psi(m_f|m) = \frac{\psi_{\rm p2}(m=m,m_f)}{\psi_p(m=m)}$. The conditional probability is then sampled using the inversion method again to obtain the final mass, m_f. This procedure is done for as many protostars as in each cluster. The protostellar masses drawn this way converge to the analytic PMF with a sample of 10^5 protostars. Figure 3.2 shows the convergence of the PMF distribution to the analytic result for the isothermal sphere accretion model as a function of the number of stars included in the distribution. We find that the distribution converges well to the analytic distribution by $N_* \approx 10^5$.

To calculate cluster statistics, we draw N_* protostars for a number of mock clusters, $N_{\rm cl}$, using the procedure described above. For each mock cluster, we calculate the bolometric, FUV and ionizing luminosities for each protostar using Equation 3.17. The total luminosities and masses are calculated for the mock cluster. After drawing $\rm N_{cl}$ mock clusters, we calculate the average and spread of the different total luminosities and the mass. When we compare to observations in S3.4 to achieve statistical robustness for the mean and the spread. For the chemistry, we use the average of the total cluster luminosities and masses. As such, we optimize the procedure by calculating the running mean of the total bolometric luminosity and drawing clusters until the running mean converges to 0.1% relative error. We find that the running mean converges in $N_{cl} \approx 15 - 20$ across 4 dex of $\rm N_*$.

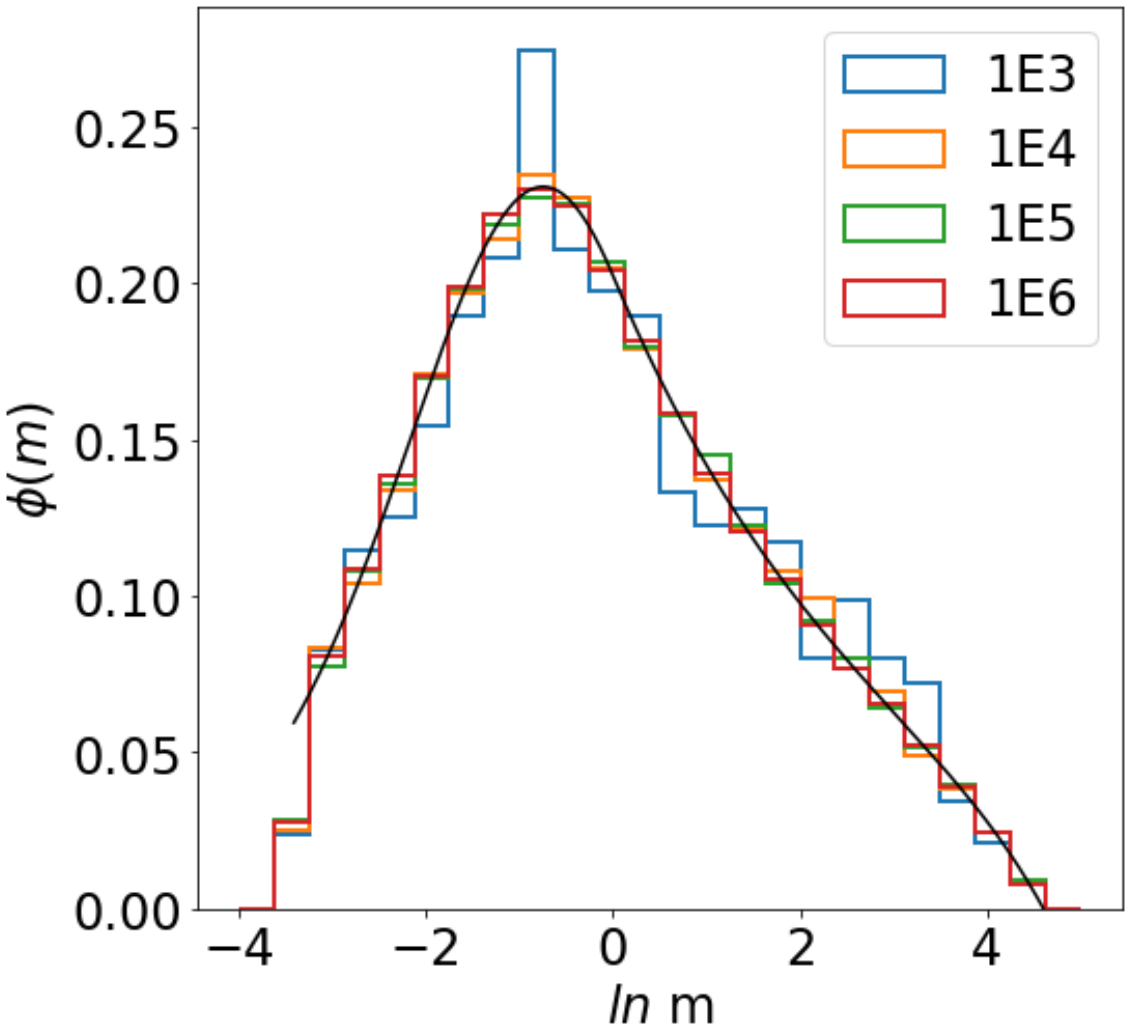

Figure 3.2. Protostellar Mass Function as a function of the logarithm of the protostellar mass for the isothermal sphere accretion model. The different colored histograms represent different distributions from the indicated number of protostars in the legend. The black line indicates the analytic PMF calculated integrating Equation 3.2 directly.

3.3.3 PDR Chemistry

We use the photo-dissociation region code 3D-PDR[2] [30] to model the chemistry of the molecular gas in our models. 3D-PDR obtains the gas temperature and abundance distributions for a given input density distribution by balancing the heating and cooling. Cooling mainly occurs due to [CI], [OI] and [CII] forbidden line emission. 3D-PDR includes four heating mechanisms: i) photoelectric heating of dust grains due to FUV radiation, ii) de-excitation of vibrationally excited H_2, iii) cosmic-ray heating of the gas and iv) heating due to turbulent dissipation. 3D-PDR also requires the strength of the incident radiation field, information about any embedded sources, the cosmic ionization rate and the gas velocity dispersion. See Bisbas et al. [30] for further technical details. We adopt the UMIST12 chemical reaction network [18], which uses 215 species and follows approximately 3,000 reactions. We use the initial atomic abundances in Table 3.1 from Sembach et al. [167]. By construction, the gas is initially entirely atomic and neutral.

3.3.4 Cloud Model

Each molecular cloud is represented by a one-dimensional slab of constant density. The depth of the cloud is determined by the total molecular gas mass,

$$R_c = \left(\frac{3M_{\rm gas}}{4\pi n \mu m_p} \right)^{1/3}, \tag{3.19}$$

where m_p is the mass of a proton, n is the gas number density and μ is the mean molecular weight, taken to be $\mu = 1.4$ since the cloud is assumed to be initially atomic and neutral (see below). The total gas mass is set according to two different gas models as described below.

[2]https://uclchem.github.io/

In these models, there are two FUV components: an external field, $F_{\rm ext} = 1$ Draine [119], and an internal field $F_{\rm src}$, from embedded sources as given by the average cluster FUV luminosity from the mock clusters. We scale the latter to the Draine field by renormalizing the units by $\chi_0 = 1.7G_0$ where $G_0 = 1.6 \times 10^{-3}$ erg s^{-1} cm^{-2} is the Habing field [168]. We adopt the fiducial cosmic ray ionization rate from Bell et al. [28] of $\xi_0 = 1.3 \times 10^{-17}$ s^{-1} per H_2 molecule. Previous studies of H_3^+ chemistry [169] and H_nO^+ chemistry [170] towards diffuse clouds find larger cosmic ray ionization rates on the order of 10^{-16}. However, there is a large spread in observed values, and the cosmic ray ionization rate appears to decrease towards clouds with higher column density [171]. We study the implications of cosmic ray ionization rates higher than the fiducial value in §3.4.

Figure 3.3 displays a schematic of our cloud model. The field from embedded sources is indicated by blue arrows and the external field is represented by green arrows. We define A_V, the dust extinction through the cloud, such that the surface has $A_V = 0$ and the stars are located at high A_V in the cloud center. We place the cluster within an evacuated bubble to approximate the effects of feedback mechanisms. The bubble has a size $R_{\rm bubble}$ given by

$$R_{\rm bubble} = \max(1\,{\rm pc}, R_s) \tag{3.20}$$

where R_s is the Strömgren sphere radius for the given density and ionizing luminosity from the cluster model

$$R_s = \left(\frac{3Q_0}{4\pi\alpha_B n_e^2} \right)^{\frac{1}{3}} \tag{3.21}$$

where we approximate $Q_0 = \frac{L_{\rm Ionizing}}{18\,{\rm eV}}$ following Draine [13] for first-order computation, α_B is the recombination case B coefficient, and we assume $n_e \approx n_H$.

In addition to the abundances, 3D-PDR computes the line-integrated emissivities for C, C^+ and CO assuming non-local thermodynamic equilibrium (NLTE) and

Table 3.1. Initial abundances used in model.

Species	Abundance Relative to H
H	1.0
He	0.1
C	1.41×10^{-4}
N	7.59×10^{-5}
O	3.16×10^{-4}
S	1.17×10^{-5}
Si	1.51×10^{-5}
Mg	1.45×10^{-5}
Fe	1.62×10^{-5}

Notes. Atomic abundances adopted from Sembach et al. [167]

accounting for optical depth via the escape probability method. We use the line-integrated emissivities, ϵ, to calculate the CO (1-0) integrated line intensity following Röllig et al. [104]:

$$I = \frac{1}{2\pi} \int_0^R \epsilon \, dz \quad (\text{erg s}^{-1} \text{ cm}^{-2} \text{ sr}^{-1}), \tag{3.22}$$

where

$$W = \frac{1}{10^5} \frac{c^3}{2k_b\nu^3} I \quad (\text{K km s}^{-1}) \tag{3.23}$$

and c is the speed of light, k_b is the Boltzmann constant and $\nu = 115.3$ GHz is the frequency of the CO (1-0) line. We calculate the H_2 column density directly from the 3D-PDR abundances

$$N(H_2) = \int_0^R n(H_2) \, dz \quad (\text{cm}^{-2}), \tag{3.24}$$

where $n(H_2) = n_{\text{gas}} X(H_2)$ and $X(H_2)$ is the H_2 abundance.

3.3.5 A Coupled Cluster and PDR Model

We use two different models for the total gas mass and cloud velocity dispersion. The first, denoted by CM, is a constant-mass model where the total gas mass is $M_{\text{gas}} = 10^4 \, M_\odot$. This model also assumes a constant velocity dispersion of 1 km s^{-1}, making it slightly sub-virial. The second model, denoted by CE, is a constant

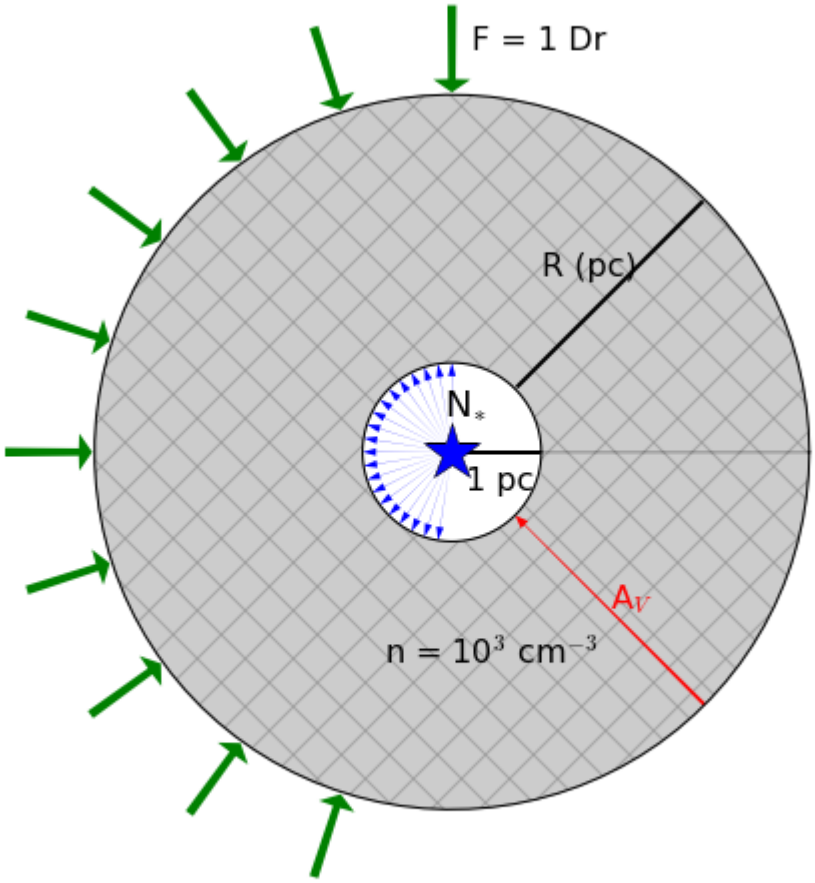

Figure 3.3. Schematic of the geometry assumed in our cloud models. The number of stars in the cluster is N_* and the radius of the cloud is calculated assuming the gas has a constant density. The external and internal fluxes are isotropic, with only half the arrows being shown for clarity.

Table 3.2. Chemistry Models

Model Name	Constant Mass	Constant Efficiency	Velocity Dispersion	Density (cm^{-3})	ξ	Internal Sources
CM_1000D_1kms_1ξ	✓		1 km/s	1000	ξ_0	✓
CE_1000D_V_1ξ		✓	Virial	1000	ξ_0	✓
CE_500D_V_1ξ		✓	Virial	500	ξ_0	✓
CE_1000D_1kms_1ξ		✓	1 km/s	1000	ξ_0	✓
CE_1000D_V_100ξ		✓	Virial	1000	$100\xi_0$	✓
CE_1000D_V_1ξ_NS		✓	Virial	1000	ξ_0	

Notes. Names and parameters for the different chemical models used. Virial denotes the velocity is calculated using Eq. 3.26.

efficiency model where the total gas mass depends on the stellar mass: $M_{\rm gas} = \frac{M_*}{\varepsilon_g}$, where ε_g is related to the star formation efficiency:

$$\varepsilon_{\rm tot} = \frac{M_*}{M_{\rm gas} + M_*} = \frac{\varepsilon_g}{\varepsilon_g + 1}. \tag{3.25}$$

We vary ε_g between 0.01 and 0.2, or $\varepsilon_{\rm tot}$ between 0.01 and 0.166. This produces total gas masses from 10^3 $M_\odot$ to 10^8 $M_\odot$. We calculate the velocity dispersion for the constant efficiency models assuming the clouds are in virial equilibrium, such that

$$\sigma_v = \left(\frac{4\pi G}{15}\right)^{1/2} R\rho^{1/2}, \tag{3.26}$$

where G is the Gravitational constant.

Table 3.2 summarizes the six models we consider. The fiducial CM model is denoted CM_1000D_1kms_1ξ and the fiducial CE model is denoted CE_1000D_V_1ξ. We include a model with a lower number density of 500 cm^{-3} (500D), models that vary and fix the velocity dispersion (V and 1 kms, respectively), one model with enhanced cosmic ray ionization rates, and a model without internal sources. This last model allows us to compare the influence of stellar sources relative to the external field.

3.4 Results

3.4.1 Cluster Luminosities and Comparison with Local Milky Way Regions

We compare our PLF cluster model to data from three recent surveys of molecular clouds. Dunham et al. [59] and Kryukova et al. [48] each survey a number of well-studied clouds located in the Gould Belt. Kryukova et al. [172] present a survey of the Cygnus X region, which is 1.4 kpc away and is one of the most massive star-forming complexes within 2 kpc of the Sun. Cygnus X contains multiple evolved OB associations with dozens of O stars and hundreds of B stars. It is also the largest cluster in our comparison with nearly 2,000 identified protostars.

The surveys adopt slightly different conventions for identifying protostars. Dunham et al. [59] define protostars as point sources with at least one detection at $\lambda \geq 350\mu$m. They argue this constraint removes older, non-protostellar sources, while including only sources that are still deeply embedded in dusty envelopes. Kryukova et al. [48] use color magnitude diagnostics to identify protostellar sources and do not require a sub-millimeter detection. Both surveys thus have their own biases: Dunham et al. [59] likely underestimate the number of dim sources, since protostars embedded in very low-mass cores, which fall below the sub-millimeter detection limit, are excluded. Kryukova et al. [48] possibly over-estimates the number of low-luminosity sources, by including older, less embedded sources that would have been filtered out by requiring a sub-millimeter detection. In Chameleon II, however, Kryukova et al. [48] excludes some of the objects found in Dunham et al. [59]. The net effect is that clusters reported in Kryukova et al. [48] tend to have have larger populations of low-luminosity sources [59]. Additional disagreement occurs because the two surveys assume different distances for a few of the shared clouds (i.e., for Perseus the former uses a distance of 230 pc and the later uses 250 pc). An order of magnitude luminosity discrepancy is evident between the two surveys for Chameleon II because

the selection criteria in Kryukova et al. [48] only has one of the three Chameleon II objects in Dunham et al. [59]. Both of the surveys likely suffer from incompleteness at low luminosities to some degree due to missing sources that are either very low-mass ($m_* \lesssim 0.2 M_\odot$, Offner and McKee 50) or very young and embedded ($L \leq 0.1 L_\odot$, e.g., Maureira et al. 173)

Given that a significant number of dim protostars could lie below the survey detection limits, we assume the reported number of sources in both cases is a lower limit that underestimates the true number by up to a factor of 2. This conservative completeness assumption encompasses sources that are either very low mass, e.g., $\lesssim 0.1 M_\odot$, or are undergoing a period of low accretion. Enoch et al. [174] cite a 50% completeness limit for the Bolocam 1.1 mm survey, and we use that as an upper limit in the error of the observed protostar number counts to account for incompleteness. Furthermore, while our derived PLF luminosity value is exact, the measured bolometric luminosities have some intrinsic uncertainties that are not reported.

Figure 3.4 shows the model predictions for the total cluster luminosity across three orders of magnitude in cluster size. We include predictions for the three different accretion models described above. The figure shows the mean total luminosity of the statistically sampled clusters, where dotted lines indicate the one and two σ deviations from the mean. These boundaries are slightly irregular since they are influenced somewhat by the statistical sampling of the mock clusters. For smaller clusters, a broader PMF creates a correspondingly large spread in the cluster luminosity. The spread decreases for large clusters as the PMF becomes well-sampled. For all three models, the total luminosity scales superlinearly with cluster size until $\mathrm{N}_* \approx 10^3$ when it approaches a linear scaling. For the TTC model, the bolometric luminosity is fit by:

$$\log L_{\mathrm{Bol}} = \begin{cases} 1.96 \cdot \log N_* + 0.18 & \log N_* < 2.78 \\ \log N_* + 5.63 & \log N_* \geq 2.78 \end{cases} \tag{3.27}$$

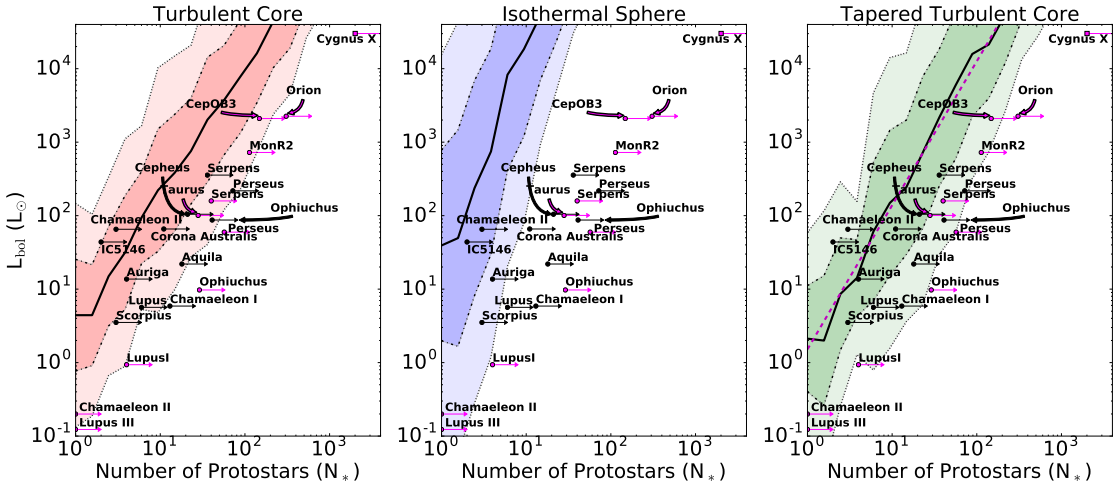

Figure 3.4. Total cluster luminosity as a function of the number of protostars for three different accretion histories. The black solid lines indicate the mean of the luminosity distributions, $\langle L \rangle$. The dark and light colored bands indicate the 1 and 2 σ spread of the distribution, respectively. The magenta dotted line is the best fit for the TTC model (Equation 3.27). The black data points indicate the sum of the bolometric luminosities for each cluster in Dunham et al. [59]. The pink circles show clusters from the Kryukova et al. [48] catalog and the pink square is Cygnus X from Kryukova et al. [172]. The arrows indicate that each of the points are likely lower limits to the actual number due to incompleteness at low luminosities.

Inspection of Figure 3.4 shows that the IS model agrees poorly with the data. It fails to match both the mean and the spread of observed luminosities of the low-mass clusters. However, both the tapered and non-tapered TC models are able to reproduce the observed spread quite well. This suggests that poor statistical sampling together with a significant range of underlying accretion rates is needed to explain the observational data. All the models appear to significantly over-predict the total luminosity of Cygnus X. However, the brightest sources are saturated in the MIPS 24 μm band, and their luminosities are under-estimated in the catalog (R. Gutermuth priv. comm.).

The TC model does a good job of representing the spread as a function of cluster size, but it over-predicts the luminosities of clusters with sizes $N_* = 10 - 100$, where observed data points fall outside the 2σ statistical sampling error. The TTC model

does exceptionally well in encapsulating the data from all the surveys. The majority of the observed cluster bolometric luminosities are included within the 2σ spread of the model predictions. All models over-predict the luminosities at the smallest cluster sizes. The discrepancy may be caused by several factors, such as completeness limits and differences in the physical parameters we assume, which we discuss in more detail in Appendix 3.7.1. As a result of this comparison, we adopt TTC as the fiducial accretion model for the analysis in the following sections.

While the total bolometric luminosity is an observable quantity and, thus, useful for evaluating the accuracy of PLF predictions, our PDR calculations require the strength of the FUV radiation field as an input. Since protostellar radiation is heavily reprocessed by the surrounding dusty envelope, it is not possible to directly measure the FUV component of the spectrum. Instead, our PLF models provide an approach to calculate the fraction of short-wavelength radiation. We use the approximation in Equation3.17 to calculate the FUV and ionizing luminosity for each protostar in a given cluster and then compute the total by summing over all protostars, i.e., $L_{\Delta E} = \sum_i L^i_{\Delta E}$.

Figure 3.5 shows the PLF model predictions for the total FUV luminosity as a function of cluster size. The TC and TTC models exhibit significant spread in the predicted FUV for modest cluster sizes due to stochastic sampling of intermediate and high-mass stars, which contribute most of the FUV radiation. The IS PMF is narrower, which produces slightly better sampling. The spread is magnified in the TC and TTC models, because they assume a broad range of accretion rates. At large cluster masses the luminosity spread diminishes for all three models. All accretion histories show a super-linear trend for small clusters, with the TTC model exhibiting the steepest dependence on cluster size:

$$\log L_{\rm FUV} = \begin{cases} 3.13 \cdot \log N_* - 2.73 & \log N_* < 2.42 \\ \log N_* + 4.84 & \log N_* \geq 2.42 \end{cases} \tag{3.28}$$

Figure 3.6 shows the total ionizing luminosity, which exhibits a similar trend to the FUV component. Stochastic sampling of the highest mass protostars (future O and B stars), which are the source of all ionizing radiation, creates larger scatter in the models. Because O stars dominate the budget of ionizing radiation, clusters with $N_* < 10^4$, which do not perfectly sample the high-mass end of the PMF, continue to exhibit a large amount of statistical variation. The steeper slope is due to the strong dependence of accretion rate on stellar mass and the higher peak accretion rates. The TTC model again exhibits the steepest dependence on cluster size:

$$\log L_{\rm ION} = \begin{cases} 5.4 \cdot \log N_* - 8.29 & \log N_* < 2.42 \\ \log N_* + 4.78 & \log N_* \geq 2.42 \end{cases} \tag{3.29}$$

Overall, the models predict that once star formation commences a substantial amount of FUV radiation permeates the natal cloud. For lower-mass clusters the predicted amount of ionization is very small, while a substantial amount of ionizing luminosity is expected in the highest mass clusters, such as the ONC complex or Cygnus X. In all cases, *statistical sampling introduces significant variation, which could drive environmental differences in clouds forming clusters with similar sizes.*

3.4.2 Cloud Properties and Abundances

In this section, we use Model CM_1000D_1kms_1ξ to study the effects of internal embedded sources on the chemical distribution within a cloud. Figure 3.7 shows the abundance of H_2 and CO as a function of cloud depth and extinction (A_V), where $x/R = 0$ is the surface. At low A_V the models for all cluster sizes are similar since the

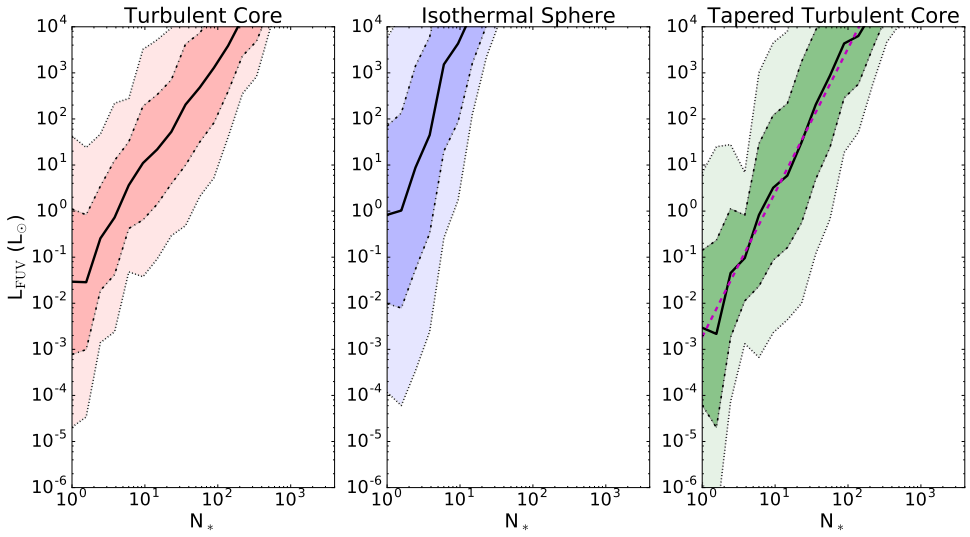

Figure 3.5. Cluster FUV luminosity versus the number of stars for three different accretion histories. The black solid lines indicate the mean of the cluster distributions. The dark and light colored bands indicate the 1 and 2 σ spread in the cluster luminosity. The magenta dotted line is the best fit for the TTC model (Equation 3.28)

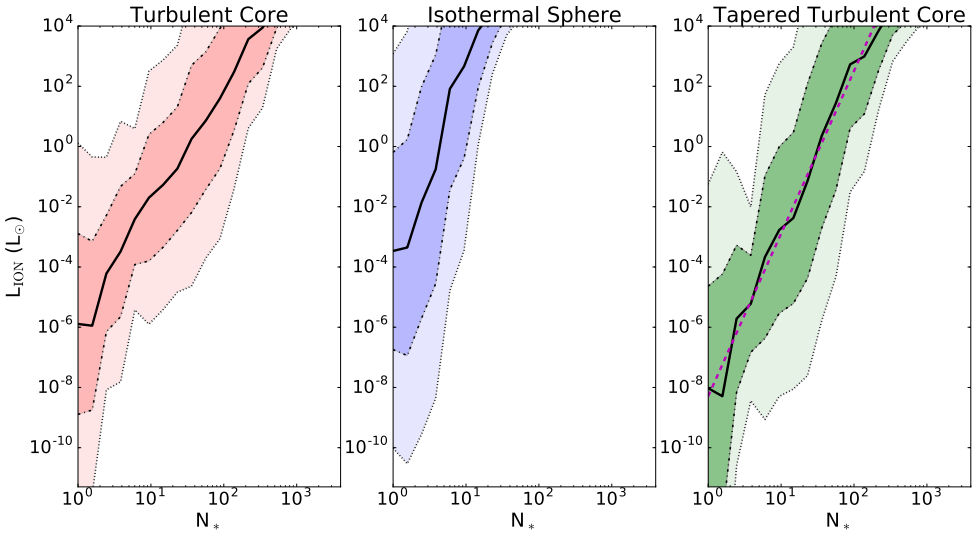

Figure 3.6. Cluster ionizing luminosity versus the number of stars for three different accretion histories. The black solid lines indicate the mean of the cluster distributions. The dark and light colored bands indicate the 1 and 2 σ spread of the distribution. The best linear fit to the means of the cluster distributions are annotated on the plot. The magenta dotted line is the best fit for the TTC model (Equation 3.29)

chemistry is dominated by the external radiation field. The H_2 abundances converge to ~ 0.5, which indicates that nearly all the H is in H_2.

The embedded FUV sources ($x/R = 1$) create a shell of H_2, which becomes progressively thinner with increasing cluster size. For $N_* = 10^6$, the H_2 shell is only $\sim$60% of the total cloud radius. In addition, the amount of CO is reduced even in the region that remains molecular. This is because the column density of material that provides self-shielding is much lower. Consequently, the embedded sources significantly alter the CO abundance profile compared to the typical 1D PDR model. Without embedded sources, the CO abundance asymptotically approaches a value around 10^{-4} at high A_V. However, the model predicts that CO is effectively dissociated by $A_V \geq 7$ for all clusters. Increasing the cluster size from $N_* \sim 100 - 10^6$ causes 2 orders of magnitude difference in the CO abundance at $A_V = 4$.

Figure 3.8 shows the temperature structure of the cloud. 3D-PDR determines the temperature by balancing the heating and cooling as described above. Without embedded sources, the cloud cools to a temperature of 10 K when $A_V \geq 1$. The model results show that the embedded sources have a strong impact, heating the high A_V gas to hundreds of Kelvin. Comparing this temperature structure to the abundance profiles in Figure 3.7 indicates there is a large amount of warm CO. These temperatures lead to higher excitation, so more emission preferentially comes from higher rotational levels.

The far right panel of Figure 3.8 displays the CO abundance as a function of gas temperature. This phase diagram shows a tight correlation between gas hotter than approximately 50 K and decreasing CO abundance. At cold temperatures, the phase diagram is more complicated due to the formation and destruction of CO at various points in the cloud.

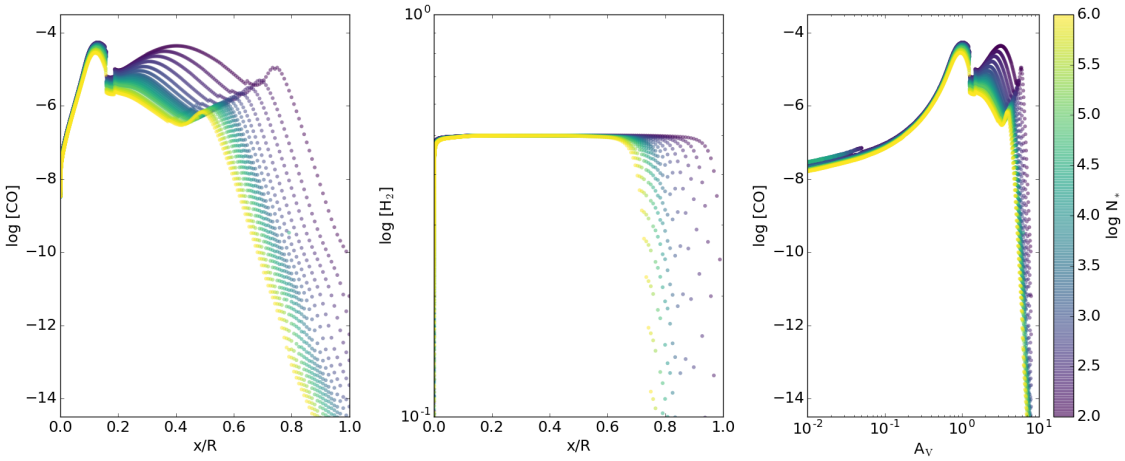

Figure 3.7. Left: Fractional abundance of CO versus distance into the cloud with R = 4.1 pc for model CM_1000D_1kms_1ξ. The coordinate, x, is measured such that $x = 0$ at the cloud surface. Middle: Fractional abundance of H_2 as a function of distance into the cloud. Right: Fractional abundance of CO versus A_V. The color indicates the number of stars in the cluster, where purple corresponds to 100 stars and yellow corresponds to 10^6 stars.

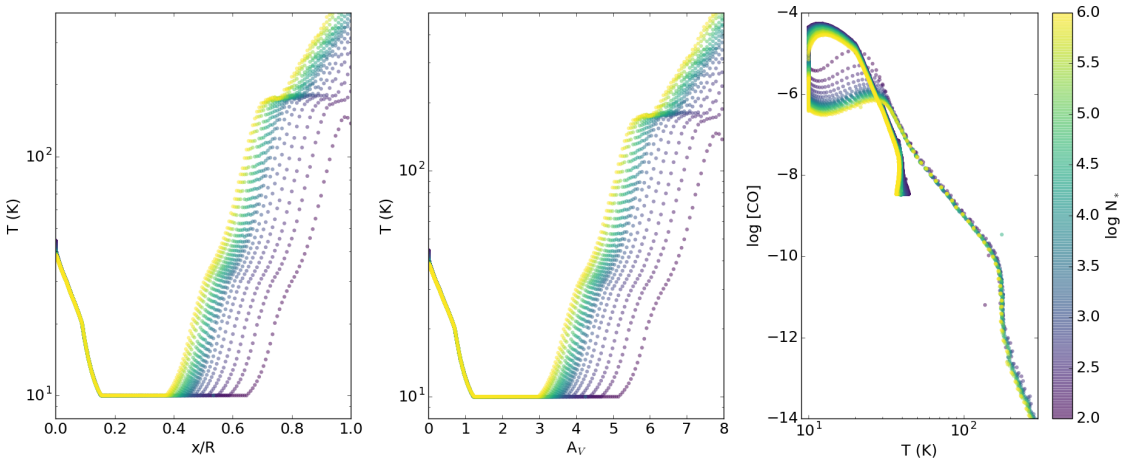

Figure 3.8. Left: Temperature as a function of distance with R = 4.1 pc for model CM_1000D_1kms_1ξ. The coordinate, x, is measured such that $x = 0$ at the cloud surface. Middle: Temperature as a function of A_V. Right: Phase plot showing the fractional abundance of CO versus gas temperature. The color indicates the number of stars in the cluster, where purple corresponds to 100 stars and yellow corresponds to 10^6 stars.

3.4.3 Variation of X_{CO}

In this section we investigate how changes in chemistry due to the presence of embedded sources impact the observed CO emission. We control for other factors including the cluster size, star formation efficiency, turbulent linewidth and gas density.

3.4.3.1 Cluster Size with Fixed Cloud Mass

We first consider the simplest cloud model, Model CM_1000D_1kms_1ξ, which holds the cloud mass fixed for all cluster sizes. Figure 3.9 shows the model predictions for X_{CO} as a function of the number of stars in the cluster. X_{CO} approaches 10^{20} cm^{-2} (K km s^{-1})$^{-1}$ for small cluster sizes but increases steeply for large clusters. The abundance and temperature profiles in Figures 3.7 and 3.8 show the cause of the increase. For a large number of stars, the amount of FUV radiation increases superlinearly reducing the shell of molecular gas and the column density of H_2. However, due to the high optical depth of the CO (1-0) line the intensity is dominated by emission near the surface of the cloud. While more CO is dissociated due to the embedded FUV radiation, the gas also exhibits higher temperatures. These competing factors cancel, producing only a factor 2 change in X_{CO} over four dex of N_*. This insensitivity to cluster size is encouraging, since it seems to suggest that X_{CO} is largely invariant. However, our model assumptions break down for large clusters when the stellar mass becomes much greater than the gas mass.

3.4.3.2 Cluster Size with Varying Cloud Mass

Figure 3.10 shows X_{CO} as a function of cluster mass, M_*, and the star formation efficiency, ε_g. Here, M_* is the total protostellar mass ($\Sigma_i^{N_*} m_i$). This figure shows the opposite trend to the constant mass model shown in Figure 3.9. For fixed values of the efficiency, X_{CO} drops by a factor of a few as the cluster mass increases by 4 dex. This mainly occurs as a result of assuming the molecular cloud is virialized. The corresponding larger linewidths increase the integrated CO intensity causing X_{CO} to

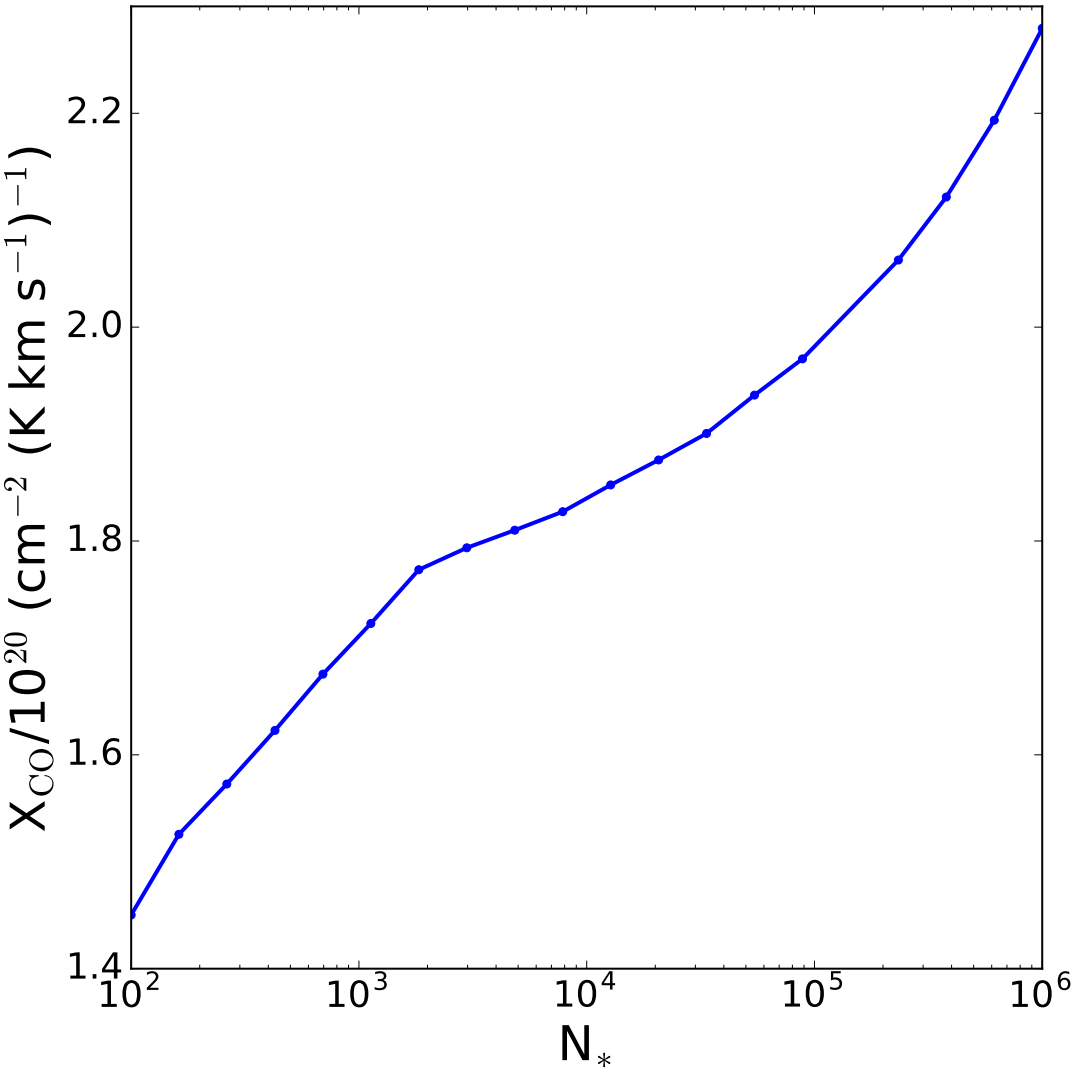

Figure 3.9. X_{CO} normalized by 10^{20} as a function of the number of stars, N_*, for model CM_1000D_1kms_1ξ.

decline. This model is more physically motivated than the simpler constant mass model; however, it shows that the gas-to-star conversion has a significant impact on the relationship between the column density and CO emission.

In Figures 3.10-3.14, the solid white contour indicates the average X_{CO} measured in the MW, $X_{CO} = 2 \times 10^{20}$ cm^{-2} (K km s^{-1})$^{-1}$, and the dotted white contours indicate the $\pm$ 30% error [36]. Our predicted X_{CO} are consistent with the measured MW values for a large fraction of the parameter space. If we further constrain to look at the region of parameter space encompassing measured star formation efficiencies (See below), the model is consistent for clusters between $N_* \approx 20$ - 10^4. The protostar surveys, mentioned above, span that range of cluster sizes for local star forming regions where X_{CO} measurements are best measured.

3.4.3.3 Star Formation Efficiency

An important consideration is the relative amount of mass in stars and gas as codified by the star formation efficiency, ϵ_g. Figure 3.10 shows X_{CO} increases with ϵ_g for fixed cluster mass. For large clusters, $X_{CO}(\epsilon_g)$ a factor of two difference over 1.5 dex of star formation efficiency. These clusters have gas masses sufficient for their optical depths to minimize the impact of the embedded feedback. Therefore, the CO line emission is not much affected by radiation feedback from the embedded cluster. The change for the largest clusters is due to the change in velocity dispersion. For smallest clusters, the change in X_{CO} with ϵ_g is a factor of four. For the smallest clusters, the increased sensitivity to the embedded clusters is due to the reduction in cloud optical depth. The trend here is driven by irradiation by the embedded clusters.

The white band in Figure 3.10 shows the measured star formation efficiencies from the Dunham et al. [59] survey of Gould Belt clouds. Within the band, a significant amount of the parameter space is consistent with the local Milky Way average X_{CO} (in white contours). Furthermore, X_{CO} is nearly constant for moderate cluster sizes, so

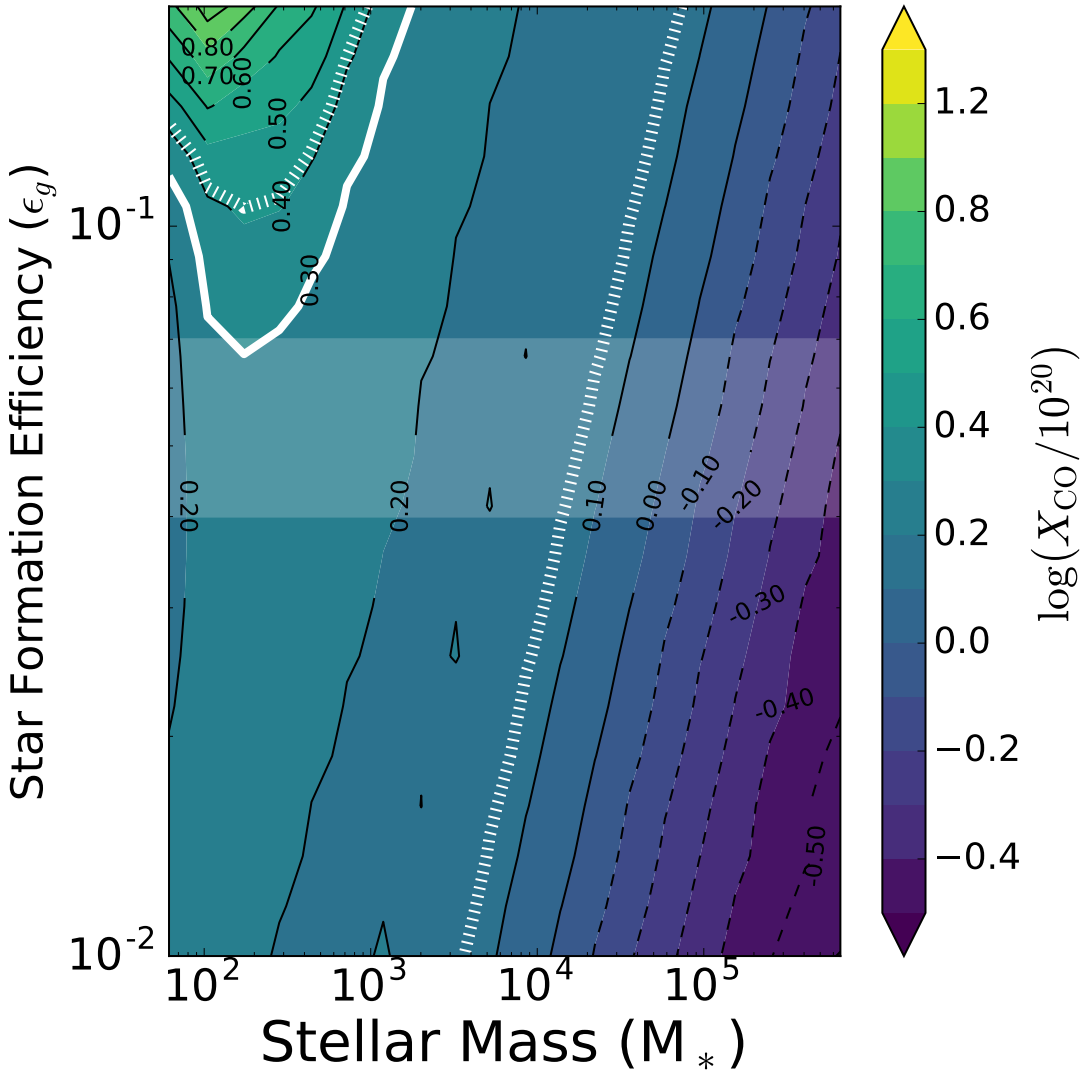

Figure 3.10. Contour plot of X_{CO} as a function of the final star cluster mass, M_*, and the efficiency, ε_g, for model CE_1000D_V_1ξ. The color scale indicates the logarithm of X_{CO} normalized by 10^{20}. The white solid contour is the typical Milky Way X_{CO} and the white dotted contours are the 30% error bars [36]. The horizontal white band marks the star formation efficiency estimated for local Gould Belt clouds [59].

our model predicts the Milky Way average is representative of local molecular clouds. The model also predicts $X_{\rm CO}$ decreases by a factor of 5-10 in the largest clusters due to the increase in turbulent linewidth.

3.4.3.4 Mean Gas Density

Molecular clouds have a range of mean densities. In this section, we explore the impact of the mean gas density on $\rm X_{CO}$. Model CE_500D_V_1ξ is the same model as the fiducial expect with $\rm n_H$ = 500 cm^{-3}. Figure 3.11 shows the same parameter space as the fiducial model shown in Figure 3.10. The lower density causes $\rm X_{CO}$ to increase over much of the parameter space. Lowering the density also reduces the column density (and thus the dust extinction) making photochemistry more important. However, changes in the amount of molecular hydrogen and the CO (1-0) emission compete and partially cancel. If there is a reduction in both, $\rm X_{CO}$ may increase but not by a large factor. In Figure 3.11 the overall trend remains the same as the fiducial model but is amplified for moderate and smaller clusters. There is no change for the largest clusters since they have sufficient mass such that changes in the interior abundances occur after the line has become opaque.

$\rm X_{CO}$ for small clusters is greatly amplified due to the lower dust extinction within the cloud. These clouds have significantly less CO emission compared to their $\rm H_2$ column density, i.e., they have a larger fraction of "CO-dark" gas [i.e. 113]. Typically, CO-dark clouds are assumed to have faint CO emission due to their low densities, but the gas here is CO deficient due to dissociation caused by the embedded sources. Consequently, the MW average values occupy only a narrow band across the parameter space. Within the range of typical star formation efficiencies, $\rm X_{CO}$ is only consistent for clusters with masses between 10^3 - 10^4 $\rm M_\odot$.

Prior work has also found that $\rm X_{CO}$ is sensitive to the gas density [28, 92]. Densities higher than 10^3 cm^{-3} make dust extinction more efficient, while lower densities

enhance the effect of embedded clusters since more of the cloud is influenced by photochemistry. Our models predict X_{CO} is most sensitive to density for clouds forming small clusters with high star formation efficiencies. However, this trend may not be evident in observations since diffuse clouds are less likely to form stars with high efficiencies.

3.4.3.5 Turbulent Velocity Dispersion

The turbulent velocity dispersion is an important factor in the calculated CO emission due to its influence on the line width and, hence, the optical depth. The line optical depth for a given line of sight is inversely proportional to the velocity dispersion. There is ample evidence that higher mass clouds have greater velocity dispersions and that many clouds are close to virial equilibrium [149]. Although a constant linewidth model is unphysical, it is useful to examine the importance of velocity information. In this section, we study the effects of the turbulent velocity dispersion by comparing model CE_1000D_V_1ξ to model CE_1000D_1kms_1ξ.

Figure 3.12 shows X_{CO} across the parameter space assuming a constant turbulent linewidth of 1 km/s. X_{CO} exhibits a similar trend to that of the constant mass model shown in Figure 3.9. A smaller turbulent velocity dispersion increases the line optical depth, which decreases the overall integrated line flux. The decline in flux, for the same H_2 distribution, increases X_{CO}. This completely reverses the trend illustrated in Figure 3.10. Thus, increasing velocity dispersion accounts for much of the decline in X_{CO} with increasing cloud mass, and the local velocity dispersion is essential to understanding trends in X_{CO}.

3.4.3.6 Cosmic Ray Ionization Rate

We investigate the effect of the cosmic ionization rate, ξ, which prior work indicates strongly influences X_{CO} [e.g., 154]. X_{CO} increases with ξ due to the increased destruction of CO and overall decline in the emission. Higher cosmic ray fluxes also

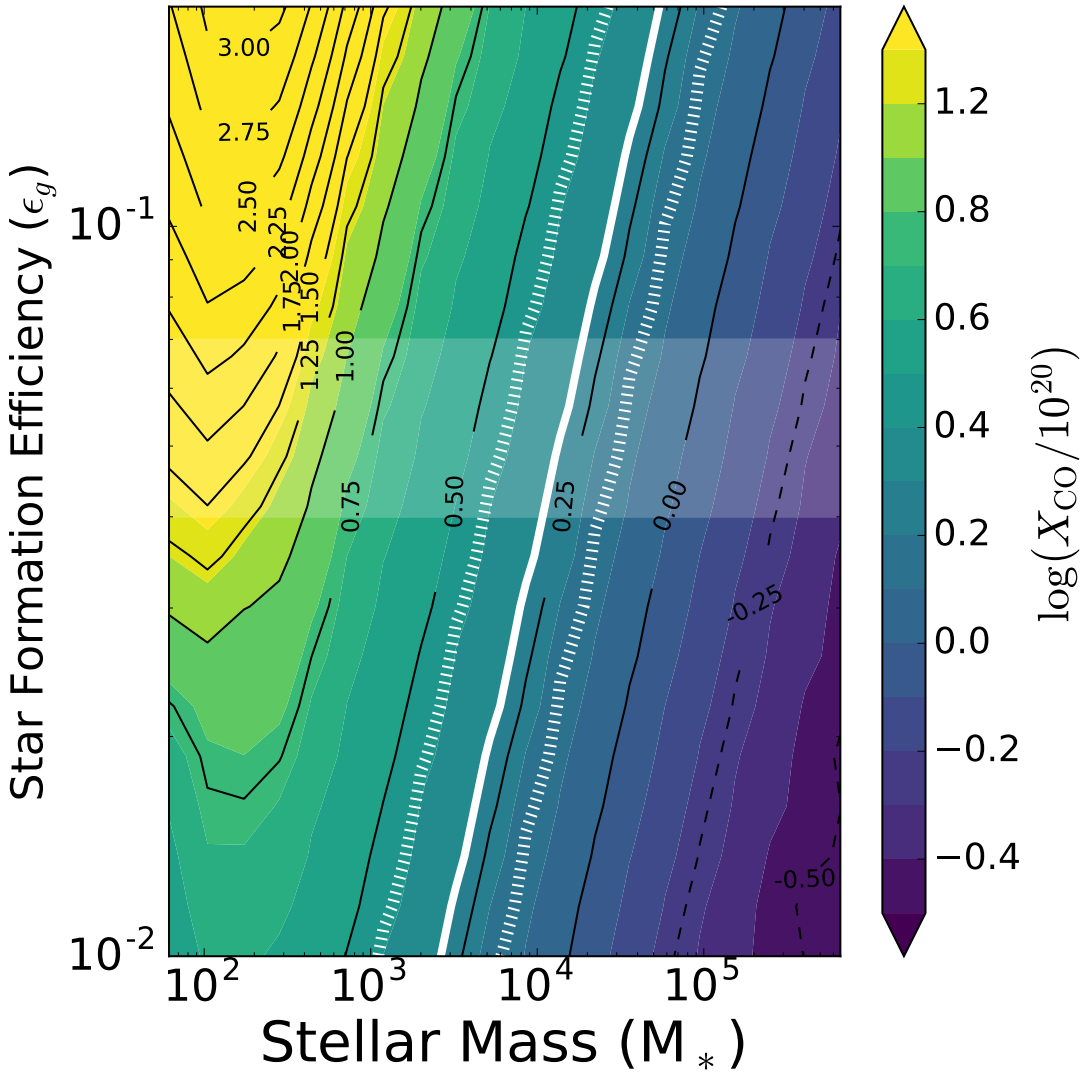

Figure 3.11. Same as Figure 3.10 but for model CE_500D_V_1ξ.

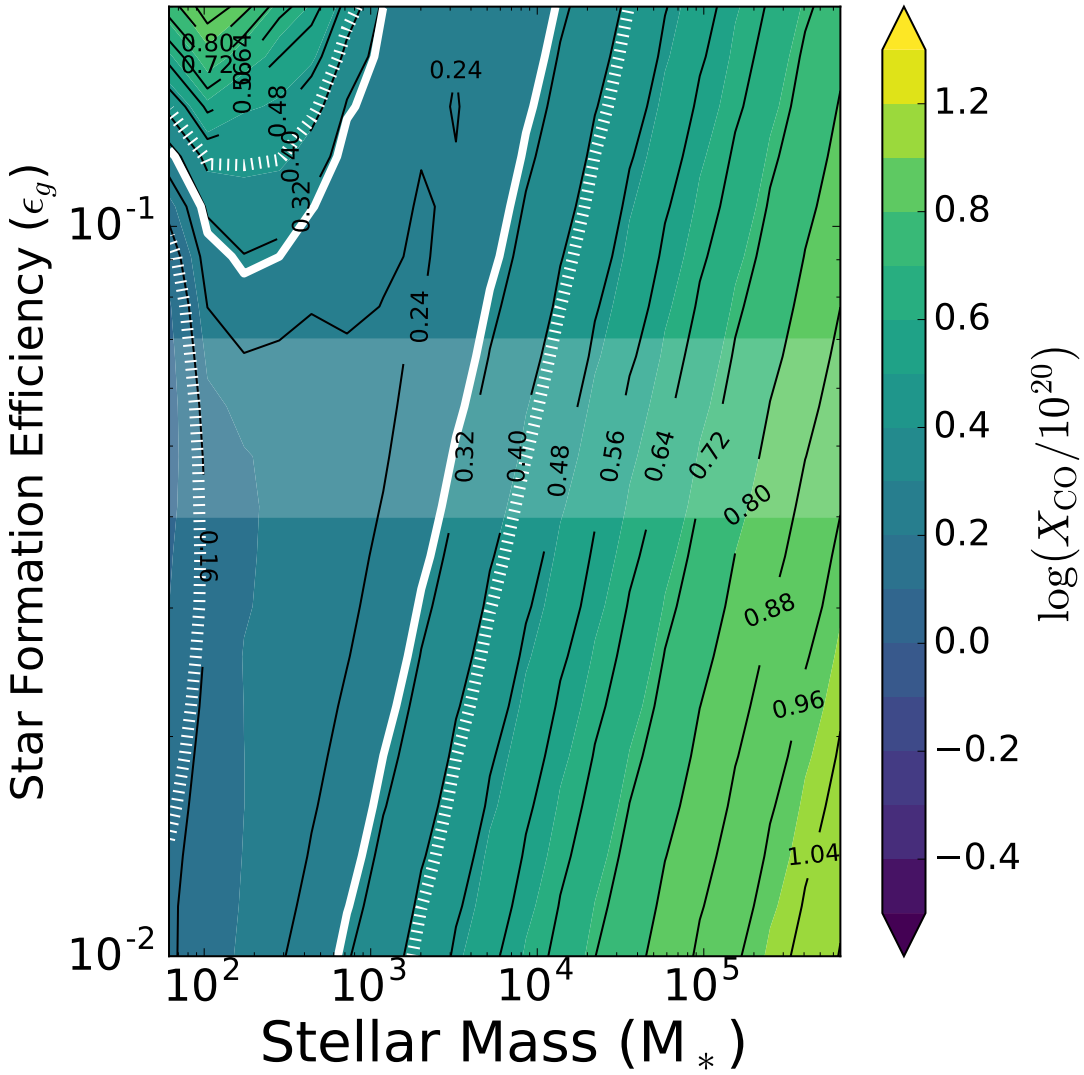

Figure 3.12. Same as Figure 3.10 for Model CE_1000D_1kms_1ξ.

lead to higher gas temperatures, which in principle could cause X_{CO} to decline. However, a value of $\xi = 100$ is not high enough to make cosmic ray heating the dominant heating mechanism throughout the whole cloud [28]. Model CE_1000D_V_100ξ adopts a cosmic ionization rate enhanced by a factor of 100 compared to the other models. An increase in the cosmic ray ionization rate is observed in environments with more star formation, such as those in ULIRGS [160] and towards the central molecular zone of the Milky Way [175].

Figure 3.13 shows X_{CO} for the enhanced cosmic ray ionization rate. The higher rate increases X_{CO} by a nearly constant value for all stellar masses. However, the overall trend remains, and the total spread is similar. Since X_{CO} increases, the fraction of the parameter space consistent with the measured Milky Way values declines.

3.4.3.7 Impact of Internal Sources

To constrain the impact of embedded sources, specifically, on X_{CO}, model CE_1000D_V_1ξ_NS excludes the star cluster FUV. Figure 3.14 shows Model CE_1000D_V_1ξ_NS with an external field only. Clusters with a mass greater than a few thousand solar masses show almost no difference in X_{CO} compared to the fiducial model with the inclusion on internal fields. Towards smaller clusters, the model without internal radiation shows an opposite trend. Without the internal FUV radiation, X_{CO} decreases towards small efficient clusters. Furthermore, X_{CO} decreases enough that the average MW value is no longer represented in the parameter space. The model values of X_{CO} within the local star formation efficiency band are only consistent with the lowest measured values.

The inclusion of internal FUV radiation increases X_{CO} for clusters within the sizes indicated in Figure 3.4 towards MW average values. Large clusters are relatively unaffected because the turbulent linewidth dominates over chemical effects. Embedded

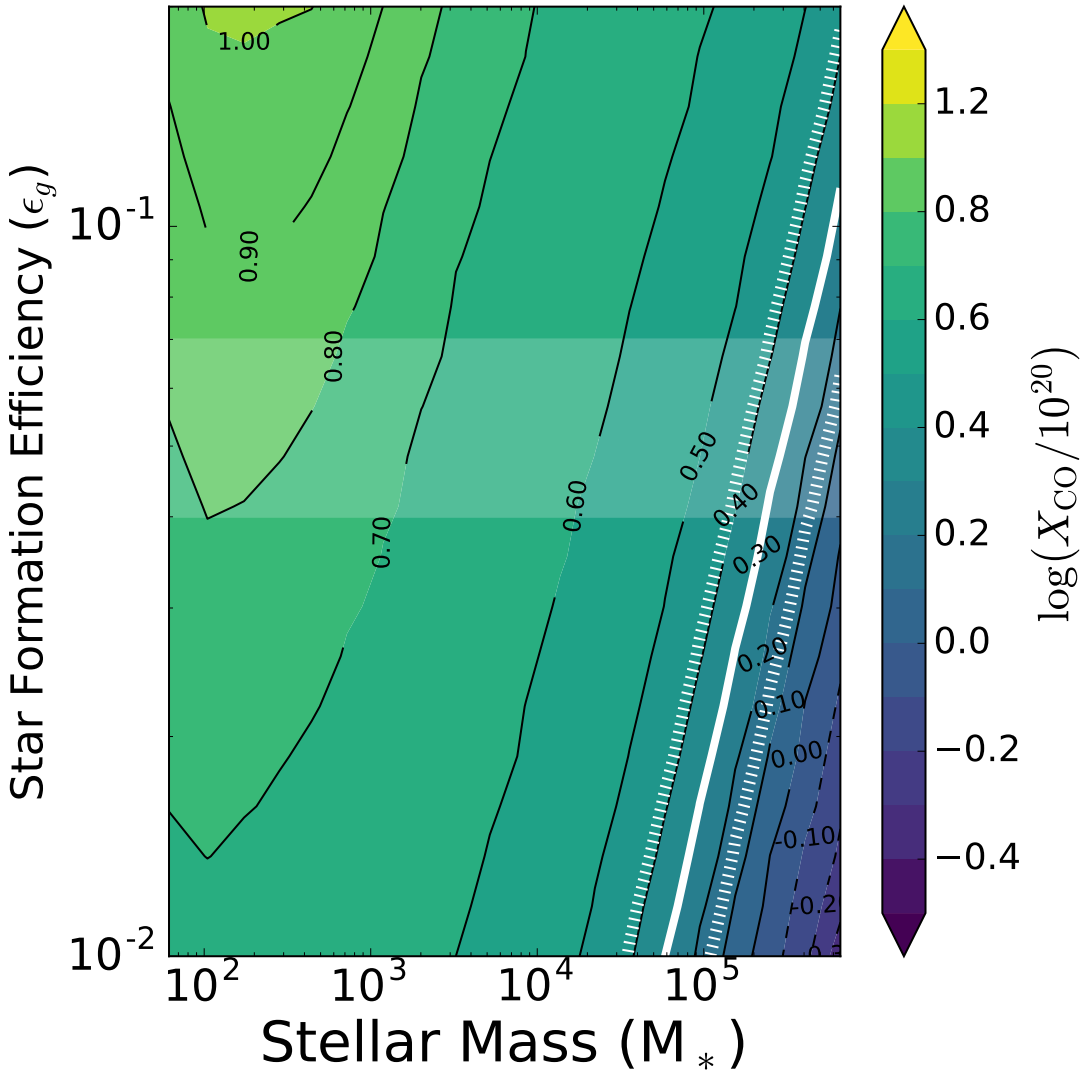

Figure 3.13. Same as Figure 3.10 for Model CE_1000D_V_100ξ.

photochemistry only affects the smaller clusters since CO emission is dominated by flux emitted closer to the surface.

Figure 3.15 shows the linear ratio of X_{CO} with embedded sources and without them. For most the parameter space, the embedded sources increase X_{CO} by 30-50%. For small efficient clusters, the change is up to a factor of 8, increasing rapidly towards clouds with smaller gas mass. For these clouds, X_{CO} would likely be time-dependent, evolving with the protostellar population.

3.5 Discussion

3.5.1 Implications for Unresolved Star-Formation in Extragalactic Sources

Measuring molecular gas mass in extragalactic sources relies on two dominant methods: dust observations in the infrared and sub-millimeter and CO emission. In the later case, the common procedure is to use some approximate conversion factor to calculate the total molecular gas mass within a galaxy. Molecular gas measurements for local galaxies have resolutions of tens to hundreds of parsecs [e.g. 176, 177]. Furthermore, many of the galaxies targeted are actively star-forming. Since the measured CO integrated flux is an average over the spatially larger star-forming regions, our results suggest embedded star formation must be taken into account.

Our model results show that for the largest clusters, there is little impact from the embedded FUV radiation and the conversion factor is instead dominated by the turbulent line width. However, for smaller clusters in the range of hundreds to thousands of stars, the embedded radiation has a clear effect. These smaller clusters have X_{CO} values factors of 3-10 larger than otherwise assumed without the embedded clusters. Furthermore, excluding embedded FUV sources will bias chemical models towards either lower densities, higher external radiation or higher cosmic ray fluxes. Our X_{CO} factors presented here are lower limits since our models are one-dimensional constant density slabs. Real clouds have significant structure and porosity, and the

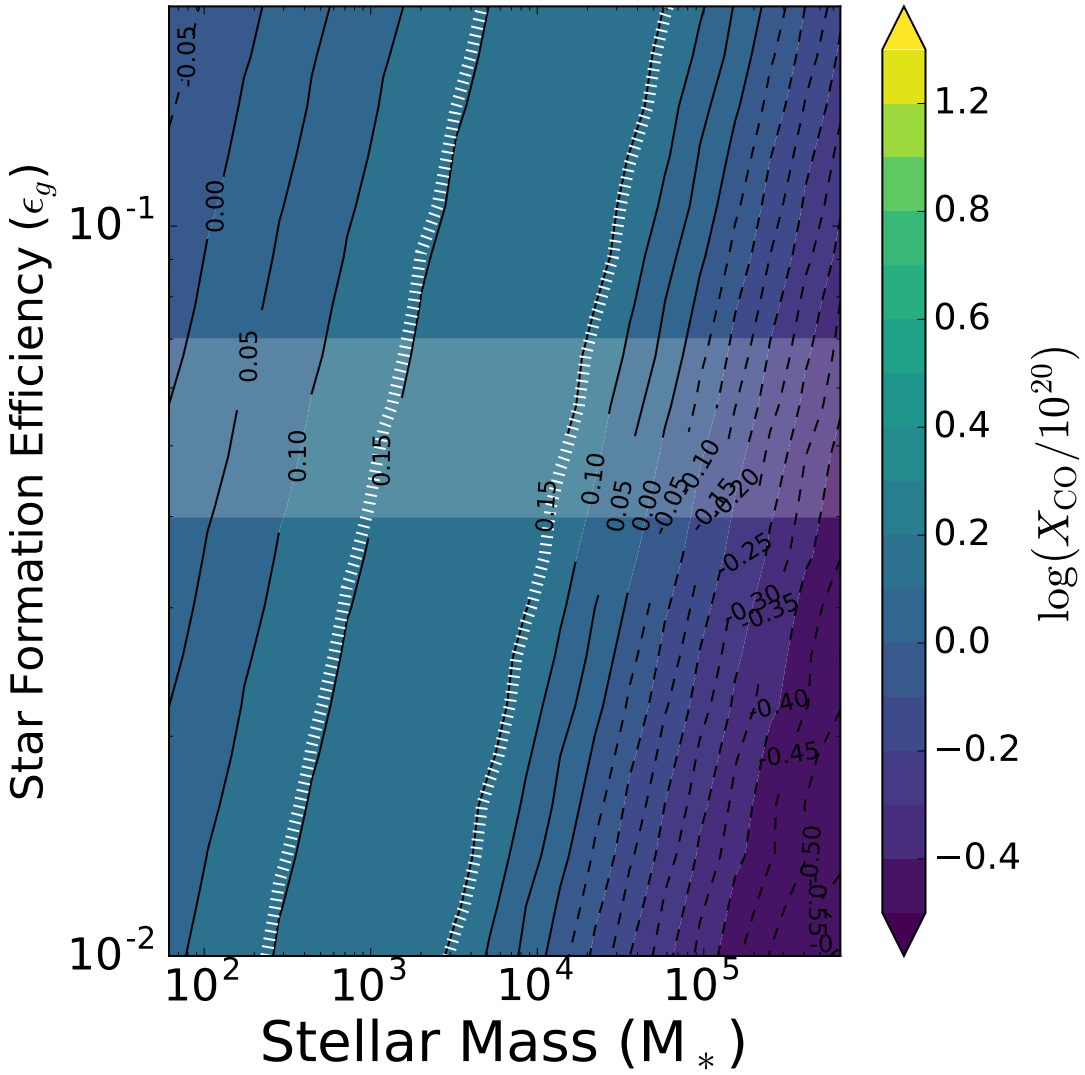

Figure 3.14. Same as Figure 3.10 except the internal FUV flux is not included in the chemistry modeling.

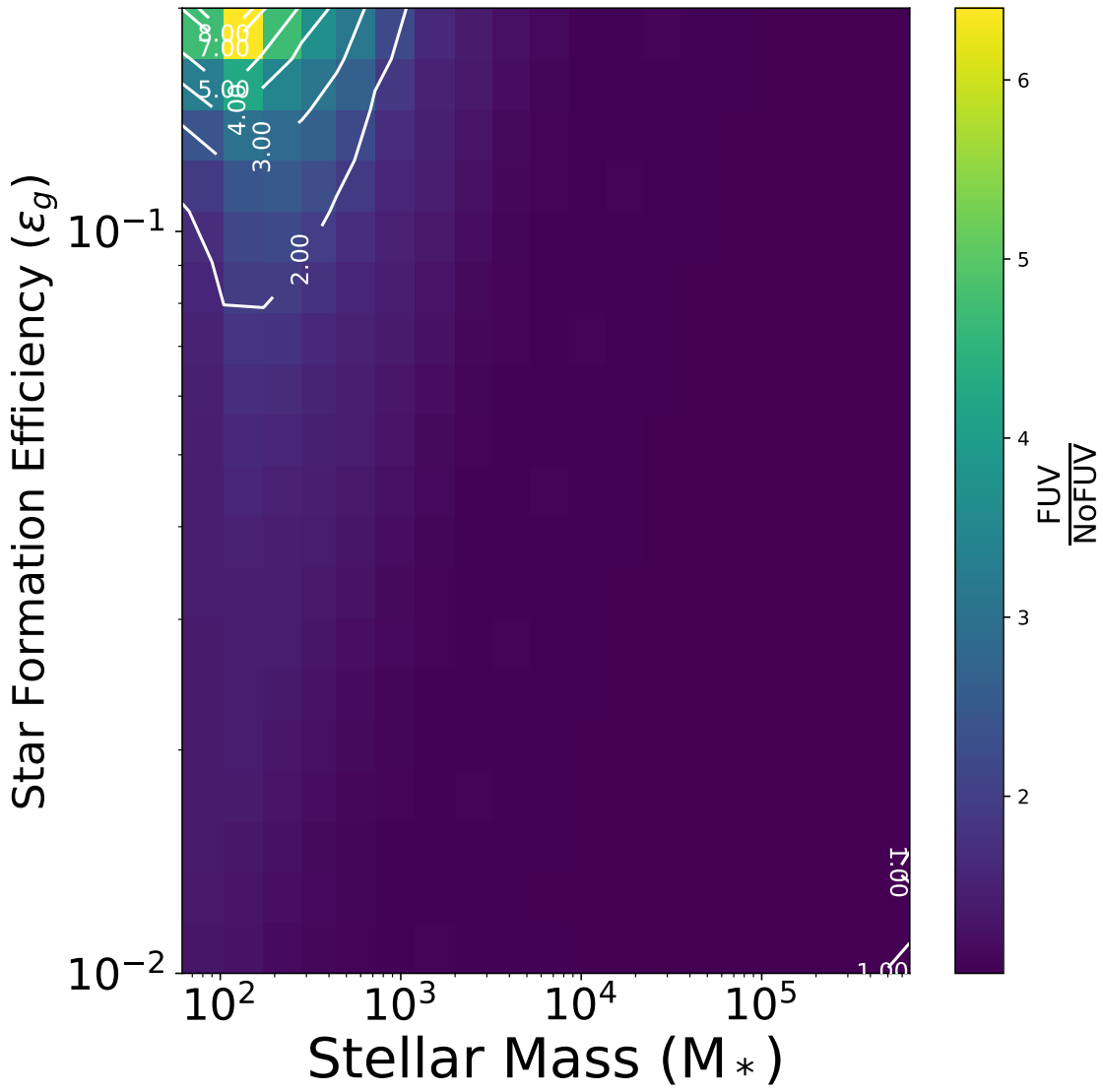

Figure 3.15. Ratio of X_{CO} calculated with the embedded protostellar FUV (model CE_1000D_V_1ξ) to X_{CO} calculated without (model CE_1000D_V_1ξ_NS).

embedded protostars are not tightly grouped into a central cluster but distributed throughout the cloud. Both of these effects would serve to increase the embedded FUV throughout the cloud, amplifying these trends.

Carbon monoxide has been measured in galaxies out to high redshifts using large single-dish integrated line measurements [e.g., 178]. At these redshifts, the star formation rate densities are typically much greater than present-day values [179]. These measurements are dominated by the brightest CO regions, which we predict inherently correspond to lower values of X_{CO}.

3.5.2 Implications for Dense Gas Tracers of Star Formation

Many molecular gas surveys use dense gas tracers to more directly measure the molecular gas undergoing star formation. Tracers such as HCN and HCO^+ are the most common alternatives to CO due to their relatively high abundances [e.g. 180, 181]. Ammonia (NH_3) is also readily observed in local galaxies [e.g. 182], even though it is associated with dense gas and has a low abundance, because it has a low critical density. Optically thin isotopologues of CO such as ^{13}CO and $C^{18}O$ are often used for line ratio diagnostics [36]. Because they are optically thin, emission from these tracers is sensitive to the conditions of the high A_V gas, especially molecules such as NH_3 and HCN. Strong FUV radiation from embedded forming star clusters not only dissociates the molecules but heats the gas in the vicinity to hundreds of degrees. Therefore, our work underscores the importance of considering the embedded FUV when modeling optically thin emission from regions expected to have accreting protostars.

In some ways, this is not a novel conclusion. A variety of prior observational work has studied the evolution of gas chemistry near protostars XX, and observations of high-mass protostars, in particular show significant chemical time variation with protostellar evolution [i.e., 60, 183]. Our results build on the previously acknowledged importance of protostellar feedback to provide a framework for quantifying the impact

of feedback on chemistry at cloud scales in addition to the well-studied smaller scales of individual protostars.

3.5.3 X_{CO} Variation within Galaxies

A large number of surveys have studied X_{CO} variation within the MW. For example, Sodroski et al. [184] and Strong et al. [185] investigate the radial dependencies of X_{CO}. Both results, although using different methods, conclude that X_{CO} increases with radius. There are various possible explanations for this trend, Of particular import is the role of the turbulent linewidth and the mass surface density of clouds. In the center of the galaxy molecular clouds not only have larger masses on average but also larger column densities compared to clouds in the outer regions of the galaxy [186]. Furthermore, the overall galactic mass surface density decreases with radius in the MW except for a slight increase around 4 kpc. The star formation rate (SFR) surface density also generally decreases except for the same bump at 4 kpc [39]. Sodroski et al. [184] measure X_{CO} in the center of the MW to be $\log \frac{X_{CO}}{10^{20}} \approx -0.5$. Our work produces this value for large inefficient star-forming molecular clouds, especially those subject to a strong cosmic ray flux. The outer galactic values in Sodroski et al. [184] are between $\frac{X_{CO}}{10^{20}} \approx 0.6 - 1.0$, which are represented in our parameter space by small to intermediate molecular clouds for a mean density of 10^3 cm^{-3} or smaller star-forming clouds with a mean density of 500 cm^{-3}.

Similar trends are observed in other nearby galaxies. Sandstrom et al. [187] measured X_{CO} using high resolution *Herschel* maps of 26 nearby disk galaxies. The survey showed that nearly all galaxies exhibit a decrease in X_{CO} in their inner regions. For example, NGC 6946 is a nearby disk galaxy around 7 Mpc away and one of the galaxies included in Sandstrom et al. [187]. NGC 6946 has also been shown to have a radially decreasing molecular gas and SFR surface density [39]. The model parameter space used in this work has a mass surface density that increases from the upper

left corner to the lower right corner. Furthermore, Sandstrom et al. [187] finds the average central $\log \frac{X_{CO}}{10^{20}} \approx -0.5 - 0.2$ consistent with large star-forming molecular clouds in this work. We find that when embedded sources are included we replicate the trends between molecular gas surface density and X_{CO} in NGC 6947. We stress, however, that this trend does not appear without the FUV radiation from embedded star formation.

3.5.4 Comparison to Other Astrochemistry Studies

Bell et al. [28] used the UCL-PDR code[3] [27] to perform a parameter study of X_{CO} as a function of A_V. This cannot be directly related to a cloud integrated X_{CO}, but rather to the cloud average A_V, but the trends are similar. Bell et al. [28] show that in high-density environments X_{CO} is only weakly affected by the impinging UV field with X_{CO} decreasing slightly over 5 orders of magnitude of increasing field. The trend reverses at low A_V where slight increases in the FUV field significantly increase X_{CO}. In our study, the external field is fixed while the internal field is increased, and we find low A_V gas is relatively unaffected by the embedded sources.

Narayanan et al. [151] studied the effect of galaxy mergers on X_{CO}. They compared simulations of quiescent star forming discs with merging starburst systems and found that the local variation within the galaxy is a smooth function of metallicity. However, starburst systems, which have much higher SFRs, exhibit a lower X_{CO} factor. They attributed the lower value to an increase in temperature caused by heating from young high-mass stars and larger gas velocity dispersions. This is in good agreement with our model, where the inclusion of FUV radiation from embedded star formation systematically increases the temperature locally, while more massive, turbulent clouds have lower X_{CO}.

[3] 3D-PDR extends UCL-PDR to 3D, so the underlying approaches are very similar.

Recently, Clark and Glover [152] performed simulations to study how X_{CO} varied with SFR. They fixed bulk properties such as the total mass and initial turbulent field and varied environmental factors that are thought to correlate with star formation rate. They linearly increased the external FUV field and cosmic ray ionization rate with the assumed star formation [160]. They found X_{CO} increases with star formation rate, contrary to other studies. In fact, their models are similar to our constant mass model, CM_1000D_1kms_1ξ, (Figure 3.9) and constant velocity model CE_1000D_1ks_1ξ (Figure 3.12), in which X_{CO} also increases with cluster mass. Here, this is due to the rapid photodissociation of CO, such that the clouds become CO-deficient or rather "CO-faint". The constant mass model is also represented in our constant efficiency models by using a fixed cluster mass and increasing the efficiency. X_{CO} increases as a function of star formation efficiency in all of our CE models. Our results show the same qualitative trends as Clark and Glover [152] when considering models that keep bulk hydrodynamic properties fixed. Keeping the velocity dispersion constant as the star formation activity increases leads to an increasing X_{CO} as a function of star formation activity.

Previous theoretical studies probed the star formation rate by changing the external environment. Higher SFR clouds are bathed in stronger FUV fields and in some cases [152, 153] experience higher cosmic ray ionization. The cosmic-ray ionization rate also correlates with the supernova rate and thus the SFR. The result of the scaling between the supernova rate and the SFR creates the linear scalings, $\chi \sim \chi_0 \times$ SFR and $\xi \sim \xi_0 \times$ SFR, where χ_0 and ξ_0 are the MW ISRF and cosmic ray ionization rate. The scalings of the impinging FUV radiation and cosmic ray flux with the SFR apply for galactic-wide studies where a galaxy-averaged SFR is used. On smaller scales these correlations do not hold due to the star formation activity becoming more stochastic.

3.6 Summary and Conclusions

This paper presents an approach coupling a semi-analytic protostellar cluster model with a PDR code to study of the effects of FUV stellar feedback on the natal physical and chemical environment of molecular clouds. We create a semi-analytic model to calculate cluster luminosities as a function of the number of protostars. We calculate the total, far-ultraviolet and ionizing luminosities for three different accretion models: Isothermal Sphere (IS), Turbulent Core (TC) and Tapered Turbulent Core (TTC) using the Protostellar Luminosity Function (PLF) formalism. We compare the model predictions against observations of three different surveys [48, 59, 172] and find our results for the TTC model fit the observations well. We present fits to the model predictions for the different luminosities as a function of cluster size summarized below for the TTC model:

$$\log L_{\rm Bol} = 1.96 \cdot \log N_* + 0.18 \quad \text{if } \log N_* < 2.78 \tag{3.30a}$$

$$\log L_{\rm FUV} = 3.13 \cdot \log N_* - 2.73 \quad \text{if } \log N_* < 2.42 \tag{3.30b}$$

$$\log L_{\rm ION} = 5.4 \cdot \log N_* - 8.29 \quad \text{if } \log N_* < 2.42 \tag{3.30c}$$

with the equations becoming linear after the indicated break.

We use the photodissociation region (PDR) code 3D-PDR to model the chemistry of molecular clouds hosting forming embedded star clusters assuming two different physical models: a constant mass model, where the cloud contains a fixed 10^4 $M_\odot$ of gas, and a constant efficiency model where the total gas mass scales with the cluster mass and the star formation efficiency parameter. Using the constant mass model, we study the chemical and physical effects of the embedded FUV radiation in detail. We find that the embedded FUV flux significantly increases the temperature of the

high A_V gas, raising the temperature to hundreds to thousands of degrees Kelvin deep within the cloud. Furthermore, we find that increasing the cluster mass creates a thinner shell of H_2 and CO, reducing the amount of CO by orders of magnitude, even at the $A_V = 1$ surface.

We calculate X_{CO} as a function of cluster mass for both physical models. The constant mass model, which also assumes a constant velocity dispersion, has an X_{CO} that increases with cluster mass. However, the increase is small: only a factor of 2 increase over four orders of magnitude in cluster mass. In contrast, the constant efficiency models show the opposite trend. In these models, the velocity dispersion is calculated assuming the cloud is in virial equilibrium. We find that X_{CO} decreases with higher cluster masses, although there is a slight increase for higher efficiencies due to their lower column densities. Altogether, the trends over four orders of magnitude in cluster mass and two orders of magnitude in star formation efficiency amount to a 1.5 dex variation in X_{CO}. Most of the parameter space is consistent with the measured MW values, and we find that including feedback from embedded clusters improves the agreement with observations.

We also investigate the effect of three different parameters on X_{CO} for the constant efficiency model. We calculate X_{CO} using mean gas densities of $n_H = 500$ cm^{-3} and $n_H = 1000$ cm^{-3}. We find that the qualitative trend remains the same, although for the lower density cloud the dispersion is over three dex over the whole parameter space. Reducing the density increases the typical X_{CO}, decreasing the agreement with the average MW value. We also fix the velocity dispersion at 1 km s^{-1}. In this case, the trend reverses. The reversal indicates that a main contributor to X_{CO} variation is the velocity dispersion typical of clouds with large clusters, which has the largest impact on the line optical depth. Finally, as shown by prior studies changing the cosmic ray ionization rate has a large impact on X_{CO}. Increasing the cosmic ray ionization rate

by a factor of 100 increases $X_{\rm CO}$, but the overall trend with efficiency and cluster mass does not change.

Finally, we show *that the internal physical and chemical structure of the PDR is altered by the presence of FUV radiation from embedded forming star clusters, with $X_{\rm CO}$ increasing by a factor of a nearly ten for smaller clusters.* High-optical depth in the CO(1-0) line reduces – but does not eliminate – the dependence of $\rm X_{CO}$ on the embedded (or impinging) FUV flux. We expect the change in internal physical structure has a more significant impact on optically thin tracers. The embedded flux causes an order of magnitude increase in the internal gas temperature and significantly reduces the total molecular gas column density. Other factors not considered in this work, including cloud sub-structure and a more distributed stellar population, will likely have a large impact – both on $X_{\rm CO}$ and the cloud temperature distribution. We will explore these factors in future work using hydrodynamic simulations.

3.7 Appendix

3.7.1 Model Variations

In this appendix, we revisit Figure 3.10 and discuss the impact of our accretion model assumptions. Our fiducial model, TTC, agrees well with observations of larger clusters, but it over-predicts the luminosities of some of the smaller clusters. This disagreement mainly applies to cluster data from Kryukova et al. [48], since these include a larger number of low-luminosity sources.

There are several possible explanations for this discrepancy. First, our luminosity formalism could be inaccurate. The model includes several tunable factors, including the accretion coefficient, $\dot{m}_0$ and the fraction of accretion energy radiated away, $f_{\rm acc}$. The former parameter depends on local physical parameters such as the column density or temperature, which vary from region to region. The latter parameter is uncertain since it depends on pre-main sequence model assumptions and the out-

flow/wind launching mechanism [188, 189]. However, $f_{\rm acc}$ is estimated to be between 0.5 and 1, which is a relatively narrow range of uncertainty. A more significant uncertainty is the choice of protostellar radii. These are debated to factors of two, although some authors have argued that the initial radii are largely independent of stellar mass [188, 190] and the evolution is insensitive to the accretion history [188].

A more comprehensive concern is the form of the accretion model, which may be incorrect. The TC model was formulated for massive stars ($M \gtrsim 10\ M_\odot$) and may simply not represent smaller clusters, which are dominated by lower mass stars. To address this, Offner and McKee [50] proposed the two-component turbulent core model (2CTC), which allows for lower mass cores in which turbulent pressure is comparable to or smaller than the thermal pressure. However, this hybrid formalism shifts the peak of the PMF and PLF to slightly higher masses and luminosities, respectively; adopting tapered 2CTC in lieu of TTC would increase disagreement between the models and observations of small clusters. Alternatively, the competitive accretion (CA) model, as adapted by Offner and McKee [50], predicts lower typical luminosities. In fact, Kryukova et al. [48] found that the CA model exhibited the best agreement with their data. However, this model would produce an overall shift to lower luminosities, potentially reducing the agreement between the models and higher mass clusters.

A final possibility is that accretion may be variable or episodic [191, and references therein]. One way to account for episodic accretion is by modifying $f_{\rm acc}$. If $f_{\rm epi}$ is the fraction of mass accreted during episodic events, then the effective $f_{\rm acc}$ can be written [50]:

$$f_{\rm acc,eff} = f_{\rm acc}\,(1 - f_{\rm epi}) \tag{3.31}$$

Note that this formulation implicitly assumes that accretion bursts are rare and short-lived. In this case, episodic events are likely absent in small statistical samples, such as those representative of Gould Belt clouds. Through comparisons with mean

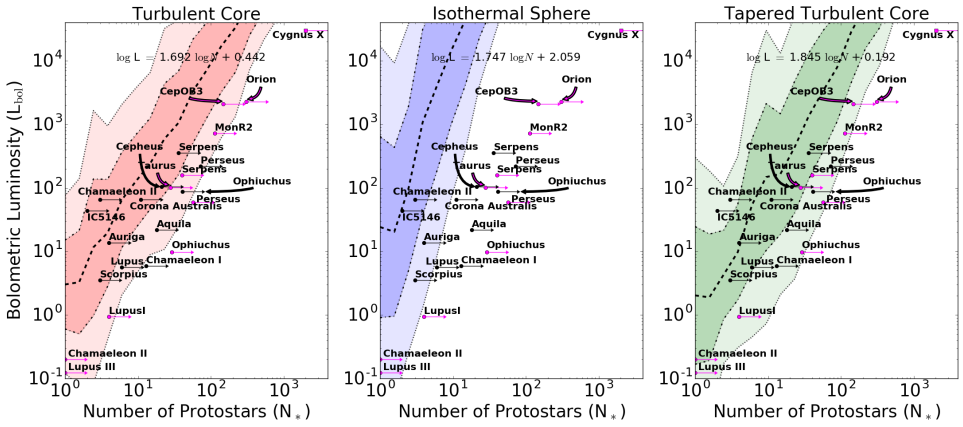

Figure 3.16. Total cluster luminosity versus the number of protostars in the galaxy for three different accretion histories assuming $f_{\rm acc} = 0.5$. The black solid lines indicate the mean of the luminosity distributions. The dark and light colored bands indicate the 1 and 2 σ spread of the distribution. The black data points indicate the sum of the bolometric luminosities for each cluster in Dunham et al. [59]. The pink circles show clusters from the Kryukova et al. [48] catalog and the pink square is Cygnus X from the Kryukova et al. [172]. The best fit to the mean total luminosity is annotated on each plot.

protostellar luminosities in local regions Offner and McKee [50] suggested an effective value of $f_{\rm acc} = 0.56$. Figure 3.16 shows the bolometric luminosity predictions for our three accretion models with $f_{\rm acc,eff} = 0.5$. This value corresponds to $f_{\rm epi} = \frac{1}{3}$. The total luminosities are lower, and more moderately sized clusters fall within the 2σ bounds. In fact, some degree of episodic accretion could explain why discrepancies appear with smaller clusters but not more massive ones: more massive clusters are sufficiently well-sampled to include some bursts.

In conclusion a great deal of uncertainty underlies protostellar accretion. Different models may produce degenerate results as noted by Dunham et al. [42], and additional constraints are needed to converge on the most accurate model.

3.7.2 Tapering Parameter

McKee and Offner [162] adopts tapered accretion histories with a general form of

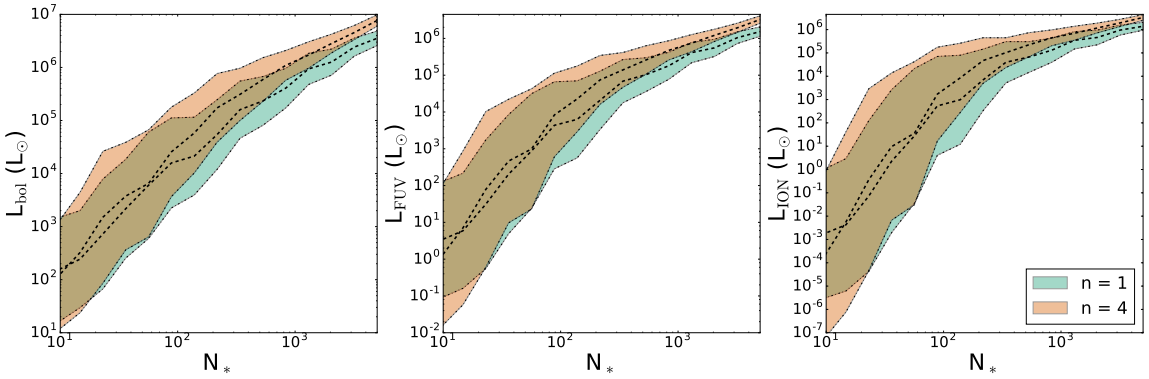

Figure 3.17. Cluster luminosity as a function of the number of protostars in the cluster for the $n = 1$ and $n = 4$ tapering models. The left panel is the bolometric luminosity, the center is the FUV luminosity and the right is the ionizing luminosity.

$$\dot{m} = \dot{m}_1 \left(\frac{m}{m_f}\right)^j {m_f}^{j_f} \left[1 - \left(\frac{t}{t_f}\right)^n\right], \tag{3.32}$$

where n defines how steeply the accretion tapers. In this work, we use $n = 1$, such that the formation time of stars is twice that of stars with untapered accretion. Recent magneto-hydrodyamic simulations of isolated star-forming cores by Offner and Chaban [68] indicate $n = 4$. Figure 3.17 shows the cluster luminosities as a function of the number of protostars for both the $n = 1$ and $n = 4$ tapering cases. For smaller clusters the luminosities are similar within the spread. For larger clusters the $n = 4$ clusters are brighter by a factor of few. The exact form of the accretion history is poorly constrained by observations [42], although there is some support for steeper tapering for protostars in Orion [192]. Given the spread of bolometric luminosities, a much larger statistical sample of clusters would be needed to better constrain the tapering parameter, n.

3.7.3 Time Dependence and Main Sequence Stars

Star formation within a cloud is not instantaneous and is likely spread over a few million years [193]. Thus, for a given cloud the first forming stars will be on the main sequence (MS) by the time the last generation of protostars appears. Here, we

assume that star formation occurs at a steady state and that all the stellar objects contributing to the total luminosity are still protostars. However, this is an approximation, which is most accurate for young clusters less than $\sim$ 1 Myr old. In this appendix we investigate the impact of an additional population of MS stars on the total bolometric luminosity.

Fletcher and Stahler [194] modeled evolving star clusters assuming an IS accretion model and followed the populations of both protostars and MS stars. This naturally produces a time dependent cluster luminosity. For our work, this suggests an additional degree of freedom for $X_{\rm CO}$: the cluster age. Since stars with different star masses have different formation times, this implies that not only the number but the mass distribution of MS stars is a strong function of age and the accretion model. At early times, however, most of the cluster members are still protostars. To assess the impact of MS stars on the cluster luminosities, we generate mock clusters where instead of sampling from the bivariate PMF we draw the populations from the IMF, i.e., we assume all the stars are on the MS. The luminosities and radii of the MS stars are from Tout et al. [165]. Such clusters represent an idealized case where star formation has recently ended. For comparison, we also generate mock clusters with twice as many stars but where half of the population are protostars sampled from the bivariate PMF and the other half are MS stars. This approximates clusters at an intermediate time of their formation.

Figure 3.18 shows the mean cluster bolometric luminosity as a function of the number of cluster members. Clusters composed entirely of MS stars have lower luminosities compared to their protostar counterparts. This is especially true for small clusters, where accretion luminosity dominates. Larger clusters composed of $\rm N_*$ protostars and $\rm N_*$ MS stars have luminosities that are higher by a factor of two. This difference is driven by the dominance of higher mass stars, whose internal luminosity exceeds their accretion luminosity. Therefore, assuming the clusters we model are

relatively young, we expect a secondary MS population to have minimal impact on our conclusions for small clusters. In contrast, our models may underestimate the true luminosities of large clusters that are somewhat advanced in star formation by a factor of $\sim$2.

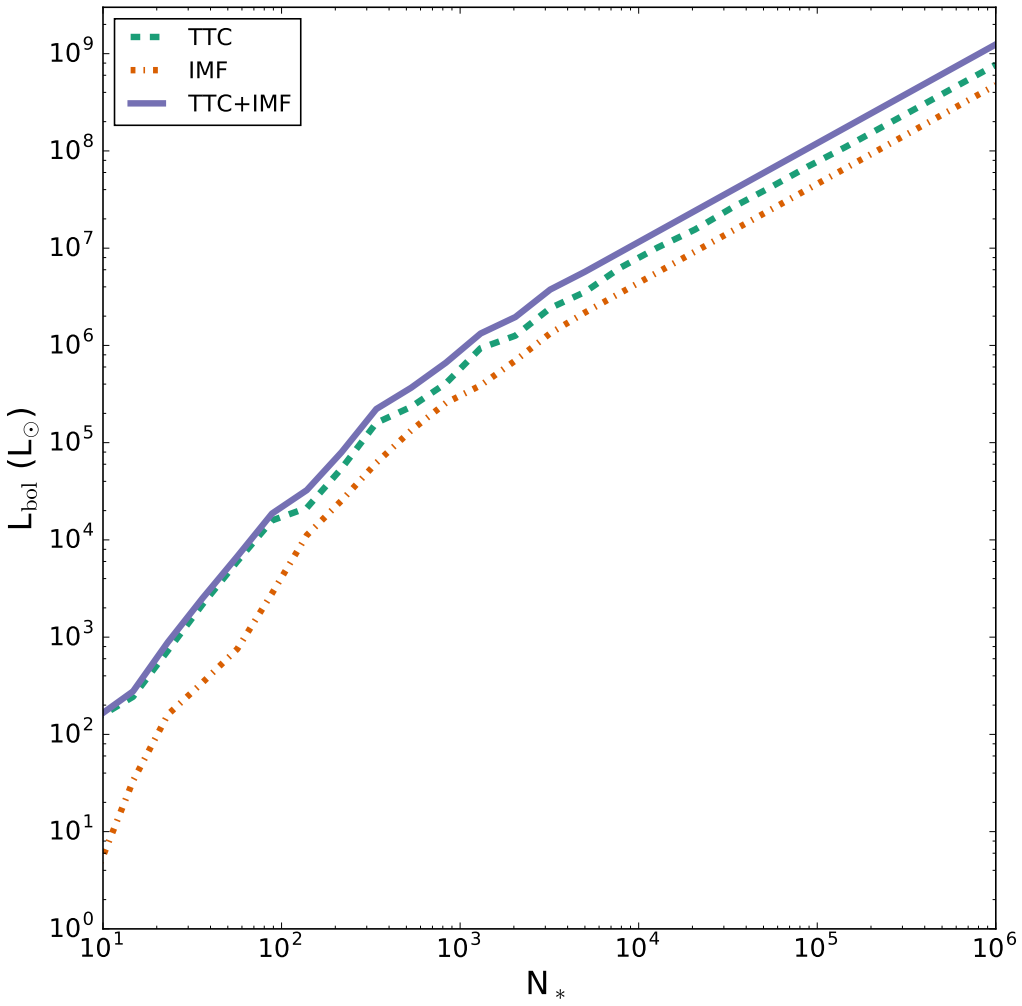

Figure 3.18. Total cluster luminosity as a function of the number of members in the cluster. The blue dashed line is the mean luminosity for the TTC model, the orange dashed-dot line for the IMF model and the solid purple line for the IMF+TTC combined model.

CHAPTER 4

EXPLORATION OF COSMIC-RAY ACCELERATION IN PROTOSTELLAR ACCRETION SHOCKS AND A MODEL FOR IONIZATION RATES IN EMBEDDED PROTOCLUSTERS

This chapter[1] focuses on investigating the potential for protostars to accelerate cosmic rays in their accretion shocks. The cosmic ray models presented in this chapter will be used in astrochemical models in later chapters.

4.1 Abstract

We construct a model for cosmic ray acceleration from protostellar accretion shocks and calculate the resulting cosmic ray ionization rate within star-forming molecular clouds. We couple a protostar cluster model with an analytic accretion shock model to calculate the cosmic ray acceleration from protostellar surfaces. We present the cosmic ray flux spectrum from keV to GeV energies for a typical low-mass protostar. We find that at the shock surface the spectrum follows a power-law trend across 6 orders of magnitude in energy. After attenuation, the spectrum at high energies steepens, while at low energies it is relatively flat. We calculate the cosmic ray pressure and cosmic ray ionization rate from relativistic protons at the protostellar surface and at the edge of the core. We present the cosmic ray ionization rate for individual protostars as a function of their instantaneous mass and final mass. The protostellar cosmic ray ionization rate is $\zeta \approx 0.01 - 1$ s^{-1} at the accretion

[1]These results are based on research published by Gaches and Offner [81] and is reproduced with permission from the AAS.

shock surface. However, at the edge of the core, the cosmic ray ionization rate drops substantially to between $\zeta \approx 10^{-20}$ to 10^{-17} s^{-1}. There is a large spatial gradient in the cosmic ray ionization rate, such that inner regions may experience cosmic ray ionization rates larger than the often assumed fiducial rate, $\zeta = 3 \times 10^{-17}$ s^{-1}. Finally, we calculate the cosmic ray ionization rate for protostellar clusters over 5 orders of magnitude of cluster size. We find that clusters with more than approximately 200 protostars produce a higher cosmic ray ionization rate within their natal cloud than the fiducial galactic value.

4.2 Introduction

Cosmic rays (CRs) are one of the fundamental constituents of interstellar matter, along with ordinary matter, radiation and magnetic fields. Within molecular clouds, CRs are a primary driver of the complex chemistry in dense molecular gas [195]. CRs, mostly relativistic protons, are the dominant source of ionization in molecular gas where ultraviolet radiation cannot penetrate. At the temperatures and densities of molecular clouds, ion-neutral reactions make up the most efficient pathways [83, 196]. Within molecular clouds, CR chemistry follows largely from the rapid formation of H_3^+:

$$\mathrm{CR} + \mathrm{H_2} \rightarrow \mathrm{H_2^+} + \mathrm{e^-} + \mathrm{CR'}$$

$$\mathrm{H_2^+} + \mathrm{H_2} \rightarrow \mathrm{H_3^+} + \mathrm{H},$$

where the CR' is the initial CR after the interaction. Following the formation of $\mathrm{H_3^+}$, more complex molecules form via the generic reaction

$$\mathrm{X} + \mathrm{H_3^+} \rightarrow \mathrm{HX^+} + \mathrm{H_2}$$

Observationally important molecules such as $\mathrm{N_2H^+}$ and $\mathrm{HCO^+}$ are created through this pathway.

CRs are introduced into the chemistry through the CR ionization rate (CRIR), ζ, which gives the rate of ionization per H (ζ(H)) or per H_2 ($\zeta(H_2)$). In this work, we focus on $\zeta(H_2)$, which we hereafter refer to as ζ. Observations of diffuse clouds find $\zeta \approx 10^{-16}$ s^{-1} from measurements of both H_3^+ and H_3O^+ [169, 170], and measurements near supernova remnants show even higher ζ [197]. Nearby supernova and winds from higher mass star are typically used to explain the CRIR in diffuse clouds [198]. Molecular clouds are expected to have a lower CRIR from energy losses due to gas interactions, and various screening mechanics are expected to reduce ζ with increasing gas column density [171].

Recent observational evidence has shown indirect evidence that the CRIR within protoplanetary disks (PPDs) and envelopes may be significantly greater than what would be expected with only Galactic CRs [80, 199]. It is not possible to detect CRs directly from embedded sources. Instead, the CRIR is inferred using various chemical signatures, often HCO^+ and N_2H^+. Ceccarelli et al. [86] used measurements of N_2H^+ and HCO^+ towards OMC-2 FIR 4, an intermediate mass protocluster and found $\zeta \approx 10^{-14}$ s^{-1}. Podio et al. [87] measured similar molecular ions towards the L1157-B1 shock, near the low-mass protostar L1157-mm, and found $\zeta = 3 \times 10^{-16}$ s^{-1}, which is inconsistent with the fiducial value from galactic sources if the CR flux is attenuated while penetrating into the cloud [171]. The inferred spread and uncertainties in measured ζ are quite large [88].

In this work, we focus on the early stages of star formation when the protostar is still accreting much of its mass. Padovani et al. [200, 201] show that the magnetic fields in dense cores can screen externally produced CRs. Furthermore, Cleeves et al. [202] studied 2D models of Class II PPDs and found that the T-Tauri wind was able to diminish the external CR flux by orders of magnitude. If CRs are screened in such a way, the higher values mentioned in the studies above indicate that locally accelerated CR may be important in star-forming regions.

Within the solar system, there is also ample evidence that the young Sun produced high energy ($\geq$ 10 MeV) CRs. Measurements of short lived radio nuclei such as ^{10}Be and ^{26}Al indicate an over abundance in the early solar system [203]. One possible explanation requires the interaction of dust particles with highly energetic CRs – whether from galactic sources [204] or from the proto-Sun [205, 206]. If we consider the Sun a typical stellar object, it is likely many early stellar systems are bathed in highly energetic particles. In low-mass star-forming regions, like the Taurus Molecular Cloud, protostellar sources may be more important since there is a lack of supernova from the local star formation.

Theoretical studies of CR acceleration in protostars show that CR particles can be accelerated to MeV and GeV energies, both in their accretion shocks at the protostellar surface and within the jet shocks [80, 199]. For typical protostars, however, the unattenuated protostellar surface CR flux is a factor of 10^4 greater than the unattenuated flux produced by shocks associated with jets [80]. Given that T Tauri stars exhibit enhanced stellar activity, Rab et al. [207] and Rodgers-Lee et al. [208] adopted a scaled-up version of the solar spectrum and predicted a substantial increase in CR ionizations in protoplanetary disks.

A self-consistent treatment of the shock properties, which fully determine the CR spectrum and CRIR, and the CR physics is currently lacking. In the prior theory work, somewhat arbitrary assumptions are made about either the CR spectrum or the properties of the shock. In this work, we couple analytic models for protostar accretion histories and accretion shocks to produce self-consistent CR flux spectra for individual protostars and proto-clusters from high-energy protons accelerated at the protostellar surface.

We organize the paper as follows. In §4.3 we describe the analytic formalism of the protostars, the method for generating mock protostar clusters, and the CR physics. In §4.4 we show the results of the model calculations and present CR spectra, pres-

sures and ionization rates for individual protostars and the CRIR from protostellar clusters. In §4.5 we discuss parameter variations and comparisons to observations. We summarize our results in §4.6.

4.3 Methods

4.3.1 Protostar Cluster Model

In this section we briefly summarize the Protostellar Mass Function (PMF) formalism of McKee and Offner [162] that we adopt. The PMF describes the underlying distribution of protostellar masses with the assumption of an accretion history, $\dot{m}$, and a final initial mass function (IMF), Ψ. We assume a truncated Chabrier IMF [51], where we denote the upper truncation mass m_u. The bi-variate number density of protostars within a cluster is

$$d^2N_p = N_p\psi_{p2}(m, m_f)d\ln m d\ln m_f, \tag{4.1}$$

where N_p is the number of protostars in the cluster, ψ_{p2} is the bi-variate PMF, m is a protostar's current mass and m_f is the expected final mass. McKee and Offner [162] showed that for a steady star formation rate

$$\psi_{p2}(m, m_f) = \frac{m\Psi(m_f)}{\dot{m}\langle t_f\rangle}, \tag{4.2}$$

where t_f is the time it takes to form a star with mass m_f and

$$\langle t_f\rangle = \int_{m_\ell}^{m_u} d\ln m_f \Psi(m_f) t_f(m_f). \tag{4.3}$$

Following Gaches and Offner [148], we adopt the Tapered Turbulent Core (TTC) accretion history [50, 164]:

$$\dot{m}_{\rm TTC} = \dot{m}_{\rm TC} \left(\frac{m}{m_f}\right)^{1/2} {m_f}^{3/4} \left[1 - \left(\frac{m}{m_f}\right)^{1/2}\right]^{1/2} \quad M_\odot \text{ yr}^{-1}, \tag{4.4}$$

This model produces higher accretion rates for higher mass stars and smaller accretion rates as protostars approach their final mass. McKee and Tan [164] adopt

$$\dot{m}_{\rm TC} = 3.6 \times 10^{-5} \Sigma_{\rm cl}^{3/4} \quad M_\odot \text{ yr}^{-1} \tag{4.5}$$

where $\Sigma_{\rm cl}$ is the surface density given in units of g cm^{-2} for a star-forming clump. The formation time t_f is

$$t_f = \frac{4}{\dot{m}_{\rm TC}} {m_f}^{1/4}. \tag{4.6}$$

4.3.2 Cluster Generation and Statistical Sampling

We model clusters with different sizes and star formation efficiencies following Gaches and Offner [148]. Given a cluster with N_* protostars, the total mass is well-approximated by $M_* \approx \langle m \rangle N_*$. We denote the efficiency, $\epsilon_g = \frac{M_*}{M_{\rm gas}}$. We approximate a cloud as a uniform density sphere with radius, $R = \left(\frac{3M_{\rm gas}}{4\pi\rho}\right)^{1/3}$, where $\rho = \mu_{\rm M} m_{\rm H} n$, n is the gas number density, and $\mu_{\rm M}$ is the mean molecular weight for cold molecular gas. The gas surface density is $\Sigma_{\rm cl} = \frac{M_g}{\pi R^2}$, which sets $\dot{m}_{\rm TTC}$ for the cluster.

We generate mock clusters following the method in Gaches and Offner [148]. We directly draw N_* (m, m_f) pairs from the bi-variate PMF using the conditional probability method. First, we marginalize ψ_{p2} over the final mass, m_f, yielding $\Psi(m)$. The one-dimensional distribution is sampled using the inversion method. We use the m samples to calculate the one-dimensional conditional probability: $\Psi(m_f|m) = \frac{\psi_{p2}(m=m, m_f)}{\Psi(m=m)}$. In this work, we generate $N_{\rm cl}$, mock clusters when calculating cluster-wide statistics (such as the total cluster CRIR) to reduce statistical noise.

4.3.3 Accretion Shock Model

The protostellar accretion shock occurs at the protostellar surface, r_*. The shock front is assumed to be stationary, and the shock velocity is taken to be near free-fall

$$v_{\rm s} = \sqrt{\frac{2Gm}{r_*}} = 309 \left(\frac{m}{0.5 M_\odot}\right)^{0.5} \left(\frac{r_*}{2R_\odot}\right)^{-0.5} \ {\rm km\,s^{-1}} \tag{4.7}$$

where r_* is the protostellar radius calculated using the model presented in Offner and McKee [50]. In the strong shock regime, the shock temperature is

$$T_s = \frac{3}{16}\frac{\mu_{\rm I} m_{\rm H}}{k} v_s^2 = 1.302 \times 10^6 \left(\frac{\mu_{\rm I}}{0.6}\right) \left(\frac{v_s}{309\,{\rm km\,s^{-1}}}\right)^2 \ {\rm K} \tag{4.8}$$

where $\mu_{\rm I}$ is the mean molecular weight for ionized gas. The accretion onto the protostar is thought to occur in columns following the magnetic field lines [209]. Within these flows, the shock can be treated as planar and vertical, such that the shock front normal is parallel to the field lines. The density of the accreted material is given by the accretion rate and the filling fraction of the accretion columns on the surface of the protostar. The shock density is then

$$\begin{aligned} \rho_s &= \frac{\dot{m}}{A v_s} = 8.387 \times 10^{-10} \left(\frac{\dot{m}}{10^{-5}\,{\rm M_\odot\,yr^{-1}}}\right) \left(\frac{f}{0.1}\right)^{-1} \times \\ &\quad \left(\frac{r_*}{2\,{\rm R_\odot}}\right)^{-2} \left(\frac{v_s}{309\,{\rm km\,s^{-1}}}\right)^{-1} \ {\rm g\,cm^{-3}} \end{aligned} \tag{4.9}$$

where A is the area of the accretion columns, $A = 4\pi f r_*^2$, and f is the filling fraction. We adopt a constant value of $f = 0.1$, which reflects the high accretion rates typical of protostars. However, we note that the filling fraction likely depends on accretion rate and time, and thus, $f > 0.1$ for very young protostars and declines during the protostellar phase [209]. The number density of the shock is $n_s = \frac{\rho_s}{\mu_{\rm I} m_{\rm H}}$, where we assume the gas is fully ionized fully [209], and we use $\mu_{\rm I} = 0.6$ for a fully ionized gas.

4.3.4 Cosmic Ray Model

4.3.4.1 Cosmic Ray Spectrum

The physics of CR acceleration has been relatively well understood for decades [i.e., 210, 211]. First-order Fermi acceleration, also known as Diffusive Shock Acceleration (DSA), can work in jet shocks and protostellar accretion shocks to produce high-energy CRs [80]. Under this mechanism, CR protons gain energy every time they pass across the shock. If the flow is turbulent, magnetic field fluctuations scatter these protons back and forth across the shock many times allowing them to continuously gain energy. However, several important conditions must be met for DSA to occur. The flow must be supersonic and super-Alfvénic for there to be sufficient magnetic fluctuations. The acceleration rate must be greater than the collisional loss rate, the wave dampening rate, and the rate of diffusion in the transverse direction of the shock. Finally, the acceleration time must be shorter than the timescale of the shock. Each of these timescale conditions limits the energy at which the CRs can be accelerated (as discussed below and in Appendix 4.7.1). We verify that all of these conditions are met throughout our parameter space [see also 80].

We describe in detail the relevant physics for accretion shocks in Appendix 4.7.1 following Padovani et al. [80]. Here we give a brief summary of the model. First-order Fermi acceleration leads to a power-law momentum distribution, $f(p)$, where

$$f(p) \propto p^{-q}. \tag{4.10}$$

The physical quantity of most interest in this work is the CR flux spectrum, $j(E)$. The flux spectrum is related to the accelerated number density spectrum, $\mathcal{N}(E)$ by:

$$j(E) = \frac{v(E)\mathcal{N}(E)}{4\pi} \ \text{(particles GeV}^{-1}\ \text{cm}^{-2}\ \text{s}^{-1}\ \text{sr}^{-1}) \tag{4.11}$$

where $v(E)$ is the velocity as a function of energy in the the relativistic limit. The number density spectrum is related to the more fundamental momentum distribution

$$\mathcal{N}(E) = 4\pi p^2 f(p) \frac{dp}{dE} \quad (\text{particles GeV}^{-1}\ \text{cm}^{-3}), \tag{4.12}$$

where the momentum distribution power-law index, q, depends on the underlying shock properties. The flux spectrum is defined between an energy range, $E_{\rm inj} < E < E_{\rm max}$, where $\rm E_{inj}$ is the injection energy scale of thermal CR particles and $\rm E_{max}$ is the maximum energy possible for acceleration to be efficient. $\rm E_{inj}$ depends on the strength of the shock and the hydrodynamic properties, such that stronger shocks and stiffer equations of state lead to an injection energy increase. $\rm E_{max}$ is determined by a combination of the magnetic field, the ionization fraction, and the shock acceleration efficiency. It is important to note that as long as $\rm E_{max} > 1$ GeV, any additional increases only weakly affects our results below. We are mainly interested in the effects of ionization produced by CRs, which is dominated by CRs with energies between 100 MeV and 1 GeV [197]. Higher energy CRs are important to understand and characterize gamma rays or similar high-energy phenomena.

Neutral gas is not only ionized by the primary CRs. Electrons produced by CR ionization can have sufficient energy to cause additional ionizations. We account for secondary electron ionizations following Ivlev et al. [212], which we discuss in detail in Appendix 4.7.2. We ignore the effects of primary electron acceleration. Electrons couple more strongly to the magnetic field and have a significantly lower mass than protons resulting in a maximum energy orders of magnitude below that of protons [80].

The most uncertain parameters are the magnetic field, B, and the shock efficiency parameter, η. The latter represents the fraction of particles accelerated from the thermal population. Before selecting the fiducial values, we explore the impact of each on the results. The magnetic field at the surface of a protostar has not been

Table 4.1. Model Parameters.

Parameter	Fiducial Value	Range
$\mu_{\rm I}$	0.6 (ionized)	
$\mu_{\rm M}$	2.8 (neutral molecular)	
ρ (§4.3.2)	$10^3 \mu {\rm m}_H$ cm^{-3}	
$\Sigma_{\rm cl}$	1.0 g cm^{-2}	
f	0.1	0.1 - 0.9
B	10 G	10 G - 1 kG
η	10^{-5}	10^{-5} - 10^{-3}

Notes. Values for the parameters we assume in the model, and the ranges we discuss in §4.5

accurately measured. Theoretical studies of Class II/T-Tauri stars predict a surface magnetic field of a few Gauss to 1 kG [213]. We vary η between 10^{-5} and 10^{-3} and find that the CRIR scales linearly with η and changes $E_{\rm max}$ by factors of a few. However, a value of $\eta = 10^{-3}$ is an extreme case. We fix $B = 10$ G and $\eta = 10^{-5}$ following Padovani et al. [80]. Table 4.1 summarizes our fiducial physical parameters. We discuss the effects of varying these parameters in §4.5.

4.3.4.2 Cosmic Ray Interactions and Ionization Rate

The CRIR from protons and secondary electrons as a function of gas column density is

$$\zeta(N) = 2\pi \int \left[j(E,N)\sigma_p^{\rm ion}(E) + j_e^{\rm sec}(E,N)\sigma_e^{\rm ion}(E) \right] dE, \tag{4.13}$$

where $j(E,N)$ is the CR flux at energy E after traveling through the column density, N, and $\sigma_k^{\rm ion}$ is the ionization cross section [171]. Krause et al. [214] proposed relativistic corrections to the $p - {\rm H}_2$ ionization cross sections, applicable when $E > 1$ GeV. We confirmed that the correction factor to the cross section has no impact on our results due to the small population of GeV CRs. Therefore, we use the non-relativistic cross section for simplicity. At the shock, the CRIR is expected to be considerable. However, as CRs propagate away from the protostars they undergo two different processes: energy losses due to collisions with matter and geometric dilution.

The former directly modifies the spectrum's shape, since the energy loss is not a grey process (with respect to energy). The latter reduces the overall flux. We use the formalism of Padovani et al. [171] to account for the energy losses from interactions with matter. The loss function is defined by

$$L(E) = -\frac{dE}{dN(\mathrm{H_2})}. \tag{4.14}$$

We can calculate the new energy, E_k, after losses as a function of the initial energy, E_0 for a specific column density, $N(\mathrm{H_2})$:

$$N(\mathrm{H_2}) = n(\mathrm{H_2})\left[R(E_0) - R(E_k)\right] \tag{4.15}$$

with the range, $R(E)$, defined as

$$R(E) = \frac{1}{n(\mathrm{H_2})}\int_0^E \frac{dE}{L(E)}. \tag{4.16}$$

The attenuated spectrum is calculated assuming the number of particles is conserved:

$$j'(E_k, N(\mathrm{H_2})) = j(E_k, N=0)\frac{L(E_0)}{L(E_k)} \tag{4.17}$$

Equation 4.17 only takes into account interactions with matter. However, the CRs are generated by a point source, so we must also take into account the spatial dilution of the flux. This is in contrast to Padovani et al. [171] who consider a plane parallel slab geometry. We account for the spatial dilution by modifying the attenuated flux as:

$$j(E_k, N(\mathrm{H_2})) = j'(E_k, N(\mathrm{H_2}))\left(\frac{R_*}{(R_* + r(N))}\right)^a, \tag{4.18}$$

where $r(N(\mathrm{H_2})$ is the radius at which the gas has column density $N(\mathrm{H_2})$, and a is the power-law index for how fast the flux is diluted. A full solution of the CR transport

equation is needed to properly determined a. However, we take $a = 2$, corresponding to free streaming, as a lower limit for the CRIR, which is a common assumption [e.g. 207, 215]. Observations of ions in protostellar envelopes may be able to constrain the transport further, primarily whether they undergo free streaming ($a = 2$) or diffusive ($a = 1$) transport. We discuss the implications of different transport regimes in §4.5.1.4.

The H_2 column density, $N(H_2)$, from the embedded protostar to the edge of the core is the final piece needed to relate the protostellar feedback to the natal cloud environment. We use the McKee and Tan [164] model describing protostellar accretion from a turbulent core to calculate appropriate column densities. For a dense core embedded in a turbulent star-forming clump, the envelope column density and core radius are given by:

$$\Sigma_{\rm core} = 1.22\Sigma_{\rm cl} \tag{4.19}$$

$$N(H_2)_{\rm core} = \frac{\Sigma_{\rm core}}{\mu_{\rm M} m_{\rm H}} \tag{4.20}$$

$$R_{\rm core} = 0.057\Sigma_{cl}^{-\frac{1}{2}} \left(\frac{m_f}{30\,{\rm M}_\odot}\right)^{\frac{1}{2}}\ {\rm pc}, \tag{4.21}$$

where $\Sigma_{\rm cl}$ is the surface density of the embedding clump, which is the normalization factor in $\dot{m}_{\rm TTC}$, and $N(H_2)$ is the H_2 column density.

Our cluster results do not depend on an assumed density profile. However, we adopt a density profile to calculate how the CRIR changes within a protostellar enveloped (See §4.4.2.1). We calculate the radius for a given column density by assuming a polynomial density distribution, $n(r) = n_s \left(\frac{R_{\rm core}}{r}\right)^{-\kappa_\rho}$, where n_s is the number density at the surface of the core and $\kappa_\rho = \frac{3}{2}$ is motivated by McKee and Tan [164]. The column density as measured from the protostar follows from $N_{\rm H_2}(r) = N({\rm H_2})_{\rm core} - \int_r^{R_{\rm core}} n(r)dr$. Inversion results in $r(N({\rm H_2})) = \left(\frac{2n_s R_{\rm core}^{\frac{3}{2}}}{N({\rm H_2})_{\rm core} - 2n_s R_{\rm core} - N({\rm H_2})}\right)^2$.

The total CRIR produced by a forming star cluster is calculated by:

$$\zeta(N_*) = \sum_{i}^{N_*} \int \left[j_i(E, N_i)\sigma_p^{\rm ion}(E) + j_{i,e}^{\rm sec}(E, N_i)\sigma_e^{\rm ion}(E) \right] \, dE, \tag{4.22}$$

where N_i is the H_2 column density from the protostar to the surface of the core.

4.4 Results

4.4.1 Dependence on Protostellar Mass

4.4.1.1 Flux Spectrum

The CR spectrum of protostars is an observational unknown. The unattenuated spectrum is impossible to constrain because CRs quickly interact with matter, both neutral, in the form of excitations and ionizations, and ionized, through Coulomb interactions. Since protostars are embedded within their natal envelope, their radiation is heavily re-processed by the surrounding dust. Current observations cannot differentiate between the CRs accelerated by Galactic sources and the Sun versus protostellar sources. Previous studies of young stellar objects have therefore used scaled versions of the local solar spectrum [207, 208]. In this section, we present predictions for the CR flux spectrum both at the protostellar surface and at the edge of its core.

Figure 4.1 shows the CR spectrum generated by the accretion shock for a protostar with an instantaneous mass $m = 0.5$ $M_\odot$ as a function of its final mass taking into account both protons and secondary electrons assuming $\Sigma_{\rm cl} = 1.0$ g cm^{-2}. The unattenuated spectrum shows a clear power-law behavior with an index of -1.9. In the strong shock regime, the index in Equation 4.10 asymptotically approaches $q = 4$. The energy spectrum scales as $p^2 f(p)$, such that $j(E) \propto p^{-2}$ [198], which is consistent with our result. The unattenuated spectrum is well described as a product of an efficient strong shock at the protostellar surface. We note that the final mass dependence acts largely to scale the spectrum through the accretion rate.

The injection energy of 1 keV corresponds to an ionized plasma with a temperature of roughly 1.5×10^6 K. The proton spectrum shows that the maximum energy weakly scales with the final mass of the protostar (or the accretion rate). The spectrum tapers to $q = 3.0$ at high energies due to the acceleration inefficiency at such relativistic speeds. The energy corresponding to the turnover for all spectra, $E \approx 1$ GeV, is the transition where $E = m_p c^2$. The secondary electron spectrum likewise shows qualitatively similar behavior.

The attenuated spectrum in Figure 4.1 shows very different behavior. Interactions with the dense core greatly alter the shape of the spectrum, and the radial distance traveled significantly reduces the flux. Short-ward of 1 GeV, ionizations and excitations effectively flatten the spectrum and shift higher energy CRs to lower energies. Losses due to pions are minimal due to the lack of CRs above 10 GeV. From 100 MeV to 1 GeV the proton flux spectrum exhibits a power-law index of $q = 2.5$.

The secondary electron spectrum shows similar features from collisional losses. However, the interactions of higher energy CRs enhances the secondary electron spectrum such that there are significantly more lower energy electrons. At $E = 1$ keV for every CR proton there are 10^4 secondary electrons due to the interactions of higher energy CRs, which are less affected by collisional losses.

Figure 4.2 shows the maximum energy of CR protons as a function of protostellar mass and final mass and the dominant constraint on acceleration. We find for protostars with $m > 1$ $M_\odot$, CR protons have maximum energies greater than 10 GeV. Only protostars with $M < 0.1$ $M_\odot$ have sub-GeV maximum energies. The maximum energy for solar and supersolar mass protostars is a constant $E_{max} = 17$ GeV. This behavior changes at the transition between different acceleration constraints. CR acceleration in subsolar mass protostars is constrained by upstream diffusion. In this process, CRs are lost by diffusion upstream at the shock, thus inhibiting the maximum possible energy. At greater masses, the constraint is set by interactions with

neutral gas near the shock. The collisional timescale becomes less than the time to accelerate CRs with $E > 17$ GeV.

The attenuated spectrum is only weakly affected by the cluster mass surface density, $\Sigma_{\rm cl}$ (Equation 4.19 and 4.5). While a drop by a factor of 10 in $\Sigma_{\rm cl}$ produces a reduction by a similar factor in the unattenuated spectrum, the lower column results in a decline of a factor of only a few in the attenuated spectrum. It is also important to note that the unattenuated spectrum here is from the protostellar surface, while previous theoretical models have calibrated their CR spectrum from terrestrial or space-based measurements [207, 208] and correct for geometric attenuation. However, it is difficult to correct for the effects of matter interactions.

4.4.1.2 Cosmic Ray Pressure

In order to properly model protostellar cores and to describe their dynamical state, various pressures must be taken into account. We calculate the CR pressure, $P_{\rm CR}$, from the energy flux spectrum:

$$P_{\rm CR} = \frac{4\pi}{3} \int p(E) j(E) dE, \tag{4.23}$$

where $p(E)$ is the relativistic momentum. Figure 4.3 shows the CR pressure across the parameter space of instantaneous mass, m, and final mass, m_f, assuming $\Sigma_{\rm cl} = 1.0$ g cm^{-2}. The unattenuated CR pressure is of order 1 dyne cm $^{-2}$ for most of the parameter space. There is a discrete change in the pressure at 3 $M_\odot$ caused by the similarly discrete radius change (itself brought on by a change in the internal structure of the protostar [50]). The pressure, in general, increases with mass. The maximum occurs when $m \approx 10$ $M_\odot$ and $m_f = 100$ $M_\odot$. The attenuated spectrum shows a significant decrease in the pressure: by 13 orders of magnitude. The gradient inverts and the highest CR pressures occur towards the $m = m_f$ boundary and towards the highest (m, m_f). This is due to the change in the radius of the core. For a given final

instantaneous mass, the core is physically smallest when the final mass is smallest. The discrete change at 3 $M_\odot$ is still apparent, although it is less significant.

The ratio of the CR pressure to the kinetic pressure is an important test of the model. Figure 4.4 shows the ratio $P_{\rm CR}/P_{\rm kin}$ across the (m, m_f) parameter space. We compare the unattenuated CR pressure to the ram pressure of the accreting matter, $P_{\rm kin} = \rho_s v_s^2$. Across the parameter space, $P_{\rm CR}$ is approximately a millionth of the kinetic pressure. Therefore, it is negligible compared to the accretion, as expected. The important kinetic pressure for the attenuated CR pressure is the surrounding molecular cloud turbulent pressure, $P_{\rm kin} = \Phi_{\rm core}\Phi_s G\Sigma_{\rm cl}^2$ with $\Phi_{\rm core} = 2$ and $\Phi_s = 0.8$ following McKee and Tan [164]. The maximum value of the ratio throughout the parameter space is only $P_{\rm CR}/P_{\rm kin} \approx 10^{-6}$. The CR pressure of CRs leaving the core is negligible to the dynamics of the surrounding molecular cloud as expected.

4.4.2 Cosmic Ray Ionization Rates

4.4.2.1 Single Protostar

The CRIR is one of the key parameters of any astrochemical model, controlling the ionization fraction of gas with $A_V >$ a few, where the external FUV cannot penetrate. Figure 4.5 shows the CRIR, ζ, as a function of (m, m_f) for a single protostar. The same discrete jump at $3_\odot$ appears due to the radius discontinuity discussed in §4.4.1.2.

The unattenuated CRIR, near the protostellar surface, is incredibly high. Most of the parameter space exhibits $\zeta = 0.1 - 1$ s^{-1}. This value serves as an initial condition to scale the CRIR throughout the protostellar core. The attenuated CRIR, on the right side of Figure 4.5, shows much more modest values. The attenuated CRIR at the surface of the core varies between $10^{-17} - 10^{-19}$ s^{-1}. The reduction is due in part to the radial dilution (decreasing the overall flux) and the collisional losses (moving 100 MeV - 1 GeV protons to lower energies ionize less efficiently). At the surface of the core, the CRIR produced by an individual protostar becomes comparable to the

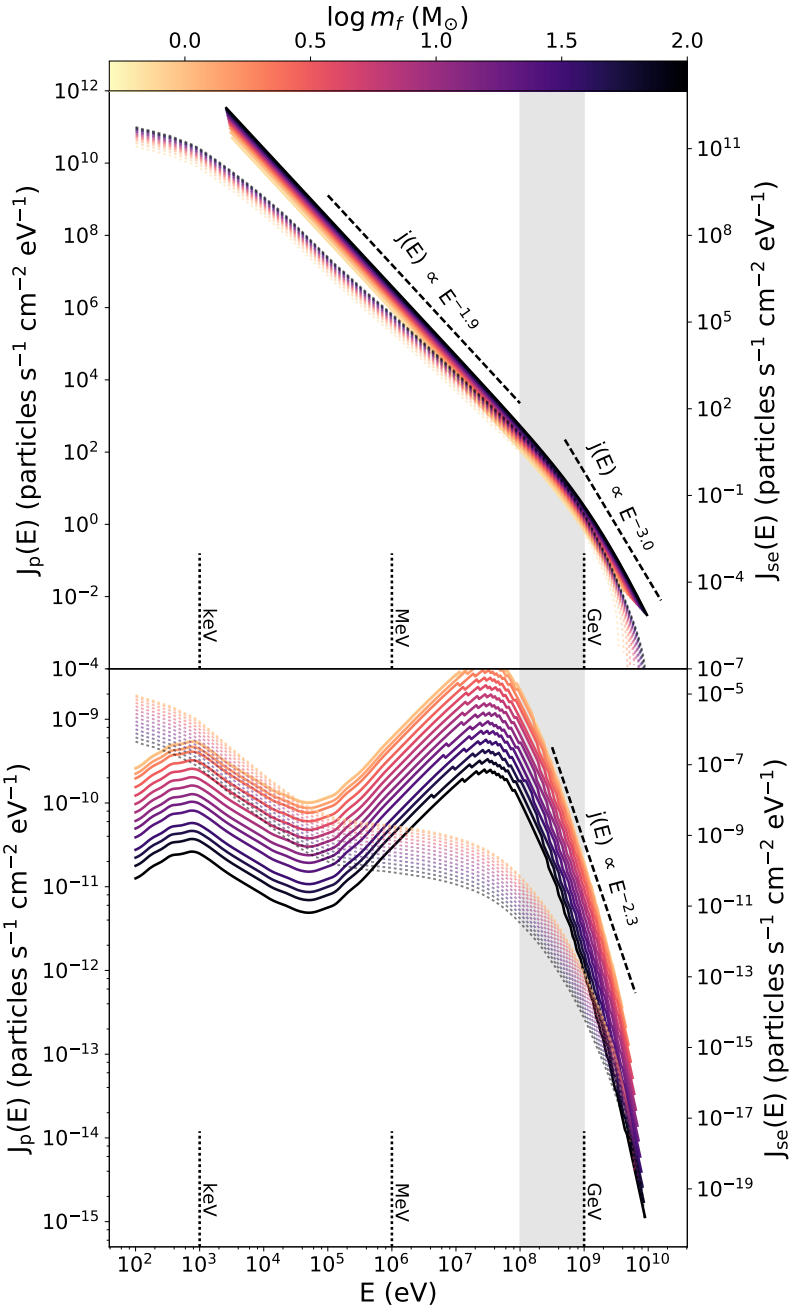

Figure 4.1. Proton (solid) and secondary electron (dotted) CR flux spectrum as a function of energy for a $m = 0.5$ $M_\odot$ protostar. The color indicates the final mass, m_f, of the protostar. The vertical grey band shows the dominant energy range for ionization. Power-law fits to various parts of the spectra are presented as the dashed lines and annotations. Top: Unattenuated flux at the protostellar accretion shock surface. Bottom: Attenuated flux at the edge of the core. We set $\Sigma_{\rm cl} = 1.0$ g cm^{-2}.

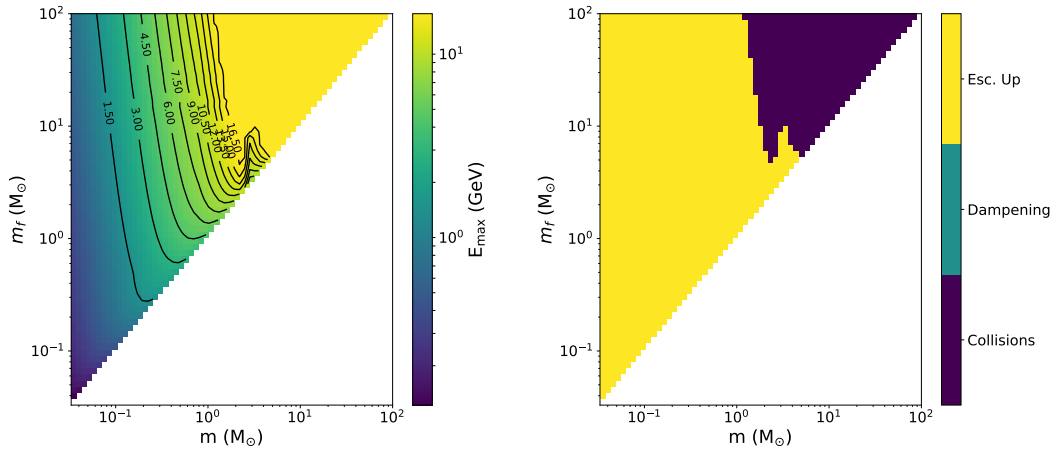

Figure 4.2. Left: Maximum energy of proton CRs in units of GeV as a function of instantaneous mass, m, and final mass, m_f. Right: The dominant constraint on acceleration as a function of (m, m_f), where "Esc. Up" refers to upstream escape diffusion, "Dampening" refers to wave dampening and "Collisions" refers to interactions with H_2. We adopt the fiducial parameters: $B = 10$ G, $\eta = 10^{-5}$ and $f_{acc} = 0.1$.

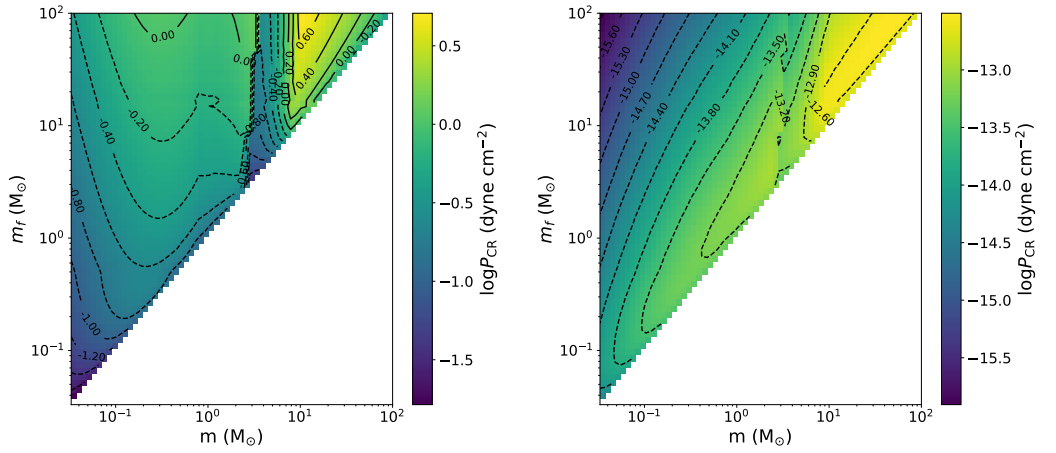

Figure 4.3. Log cosmic ray pressure as a function of mass and final mass in units of dyne cm^{-2}. Left: Unattenuated cosmic ray pressure. Right: Attenuated cosmic ray pressure including matter interactions and geometric dilution. We set $\Sigma_{cl} = 1.0$ g cm^{-2}.

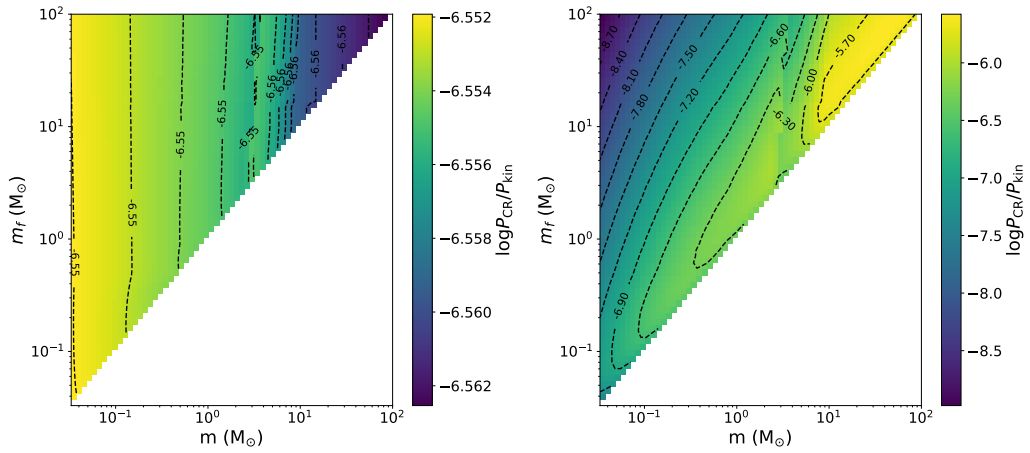

Figure 4.4. Log Ratio of CR pressure to kinetic pressure as a function of mass and final mass. Left: Unattenuated cosmic ray pressure, where the ram pressure is $P_{\rm kin} = \rho_s v_s^2$. Right: Attenuated cosmic ray pressure including matter interactions and geometric dilution, where the ram pressure is $P_{\rm kin} = \Phi_{\rm core}\Phi_s G\Sigma_{\rm cl}^2$. We set $\Sigma_{\rm cl} = 1.0$ g cm^{-2}.

attenuated external CRIR [171]. Therefore, it is likely that in star-forming clouds, gas near embedded protostars may be equally affected by external and internal CR sources.

There is a large difference between the unattenuated and the attenuated CRIR: 17 orders of magnitude. Figure 4.6 shows the CRIR as a function of column density for a protostar with $m = 0.5$ M$_\odot$ and $m_f = 1.0$ M$_\odot$ as the solid black line. There is a near power-law behavior showing a 6 dex decrease in ζ with a 5 dex decrease in $N(\rm H_2)$. The column density is a proxy for the distance from the central protostar. As such, different molecules used to constrain ζ may suggest very different values of ζ depending on what radial surface they trace.

Figures 4.1- 4.6 assume a fixed value of $\Sigma_{\rm cl} = 1$ g cm^{-3}. $\Sigma_{\rm cl}$ has a linear relationship with the unattenuated CRIR. A decline of a factor of 10 in $\Sigma_{\rm cl}$ incurs a similar factor of 10 decrease in the unattenuated ζ and $\rm P_{CR}$ due to the decrease in the accretion rate through $\dot{m}_{\rm TC}$. However, there is a much weaker dependence of $\Sigma_{\rm cl}$ on the attenuated

CRIR and CR pressure. The core radius depends on $\Sigma_{\rm cl}^{\frac{1}{2}}$ and the core molecular column density $N(\mathrm{H}_2)$ scales linearly with $\Sigma_{\rm cl}$. Together, these factors result in only a factor of a few decrease in ζ and $P_{\rm CR}$ with an order of magnitude decrease in $\Sigma_{\rm cl}$. We present $\zeta(N)$ for the whole (m, m_f) space and for different values of $\Sigma_{\rm cl}$ in an interactive online tool [2].

4.4.2.2 Protostellar Cluster Cosmic Ray Ionization Rate

We have so far presented results for individual protostars within their natal core. However, molecular clouds form many stars simultaneously. We have shown in §4.4.2.1 that at the protostellar core surface, the CRIR can be on par with the attenuated external CRIR. This suggests it is important to consider both CRIR components in order to understand cloud chemistry in forming clusters.

Figure 4.7 shows the attenuated CRIR due to all the embedded protostars in a cluster. The size of the points indicates the number of protostars and the color of the points indicates the assumed star formation efficiency, which impacts the result through $\Sigma_{\rm cl}$. Figure 4.7 represents 400 mock clusters covering a large range of (N_*, ϵ_g). The error bars indicate the 1σ spread due to sampling the bi-variate PMF. For $N_* > 500$, the error bars are smaller than the data points due to more complete sampling of the bi-variate PMF.

The two parameters, ϵ_g and N_*, produce opposite trends in the CRIR. A reduction in ϵ_g leads to a higher Σ, thus causing a greater CRIR. However, this effect is sublinear - a dex change in ϵ_g leads to less than a dex change in the cluster CRIR. The CRIR depends more strongly on N_* than ϵ_g. Increasing N_* leads to a slightly super-linear increase in ζ due to the inclusion of more high-mass protostars.

We fit $\zeta(N_*, \epsilon_g)$ with a two-dimensional linear function in log space, which represents the model results well:

---

[2] `http://protostarcrs.brandt-gaches.space`

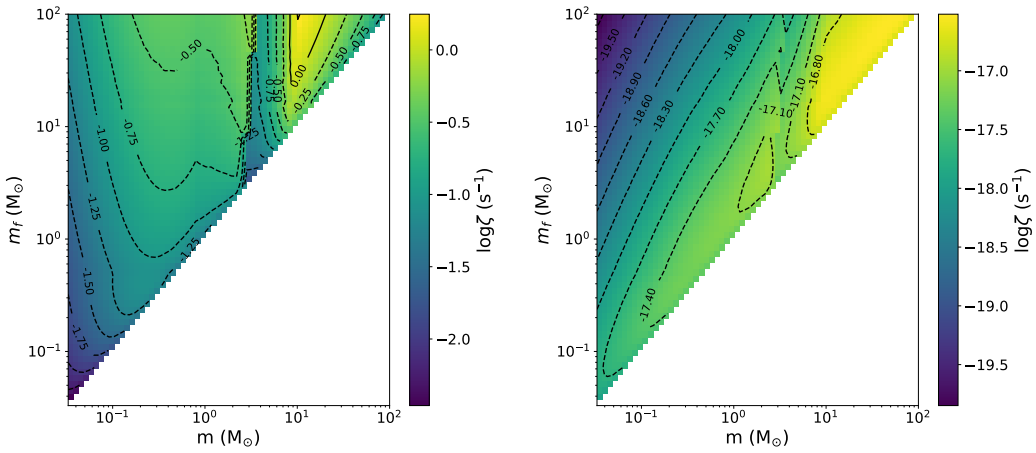

Figure 4.5. Log cosmic ray ionization rate as a function of protostellar mass and final mass. Left: Cosmic ray ionization rate at the accretion shock. Right: Attenuated cosmic ray ionization rate at the edge of the protostellar core including matter interactions and geometric dilution. We set $\Sigma_{\rm cl} = 1.0$ g cm^{-2}.

$$\log \zeta = -0.24 \log \epsilon_g + 1.24 \log N_* - 19.56. \tag{4.24}$$

We plot this function on Figure 4.7 as the dashed lines, and we add lines of constant N_* for reference. For clusters with $N_* >$ few hundred protostars, the CRIR due to embedded protostars is *greater* than the typically assumed fiducial rate of $\zeta_0 = 3 \times 10^{-17}$ s^{-1}, which is shown as the gray solid line.

4.5 Discussion

4.5.1 Variations of Physical Parameters

There are 3 key unknowns in our model: the protostellar magnetic field, B, the accretion flow filling fraction, f and the shock efficiency parameter, η. We discuss the uncertainties and impact of each below.

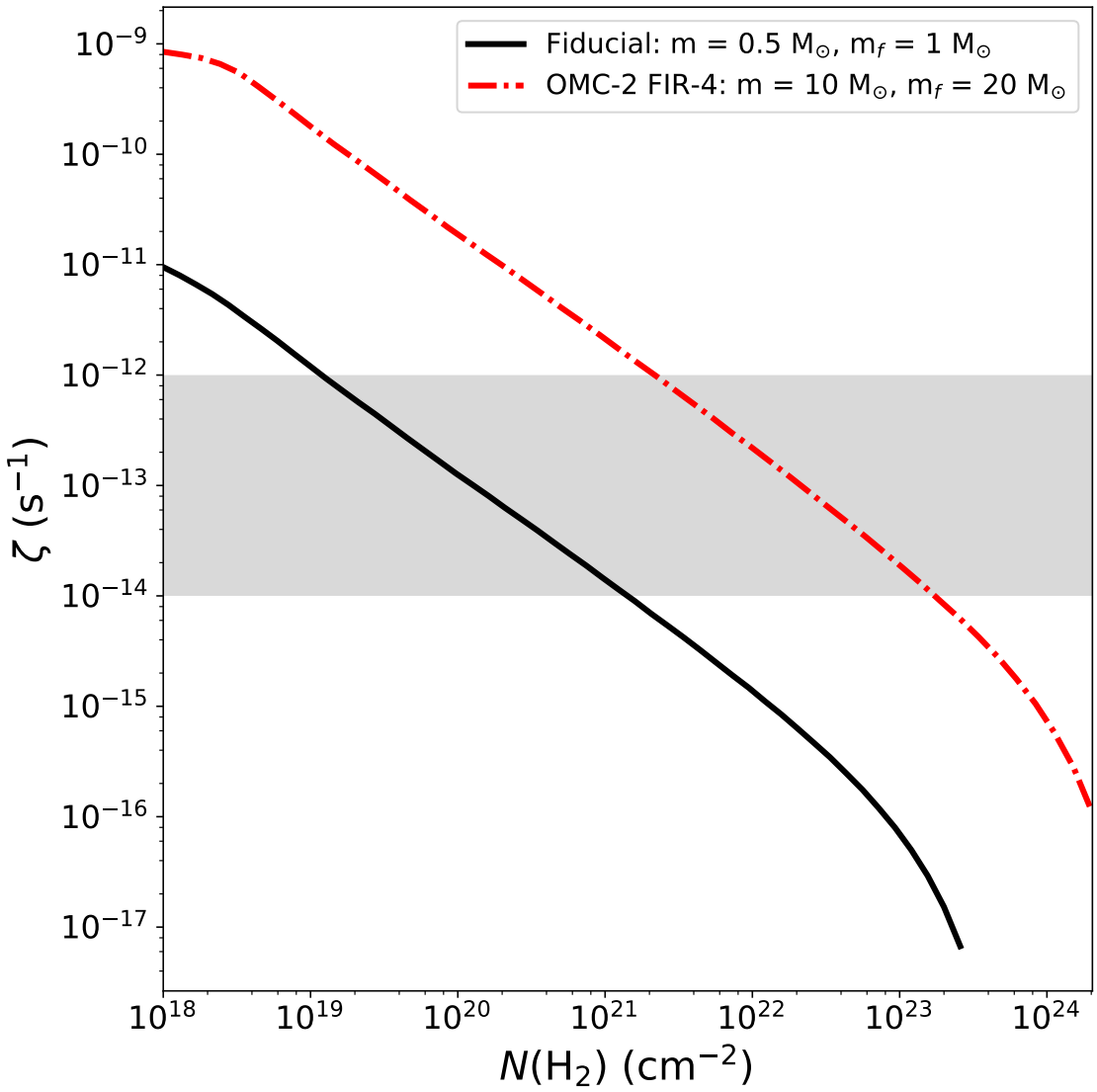

Figure 4.6. Cosmic ray ionization rate as a function of column density for a single protostar. The solid black line represents a protostar with instantaneous mass $m = 0.5$ M$_\odot$ and final mass $m_f = 1$ M$_\odot$ using the fiducial values in Table 4.1. The dashed-dot red line represents a protostar with instantaneous mass $m = 10$ M$_\odot$ and final mass $m_f = 20$ M$_\odot$ with $\Sigma_{\rm cl} = 8$ g cm^{-2}. The grey box represents the order of magnitude range of ζ measured in OMC-2 FIR 4 by Ceccarelli et al. [86].

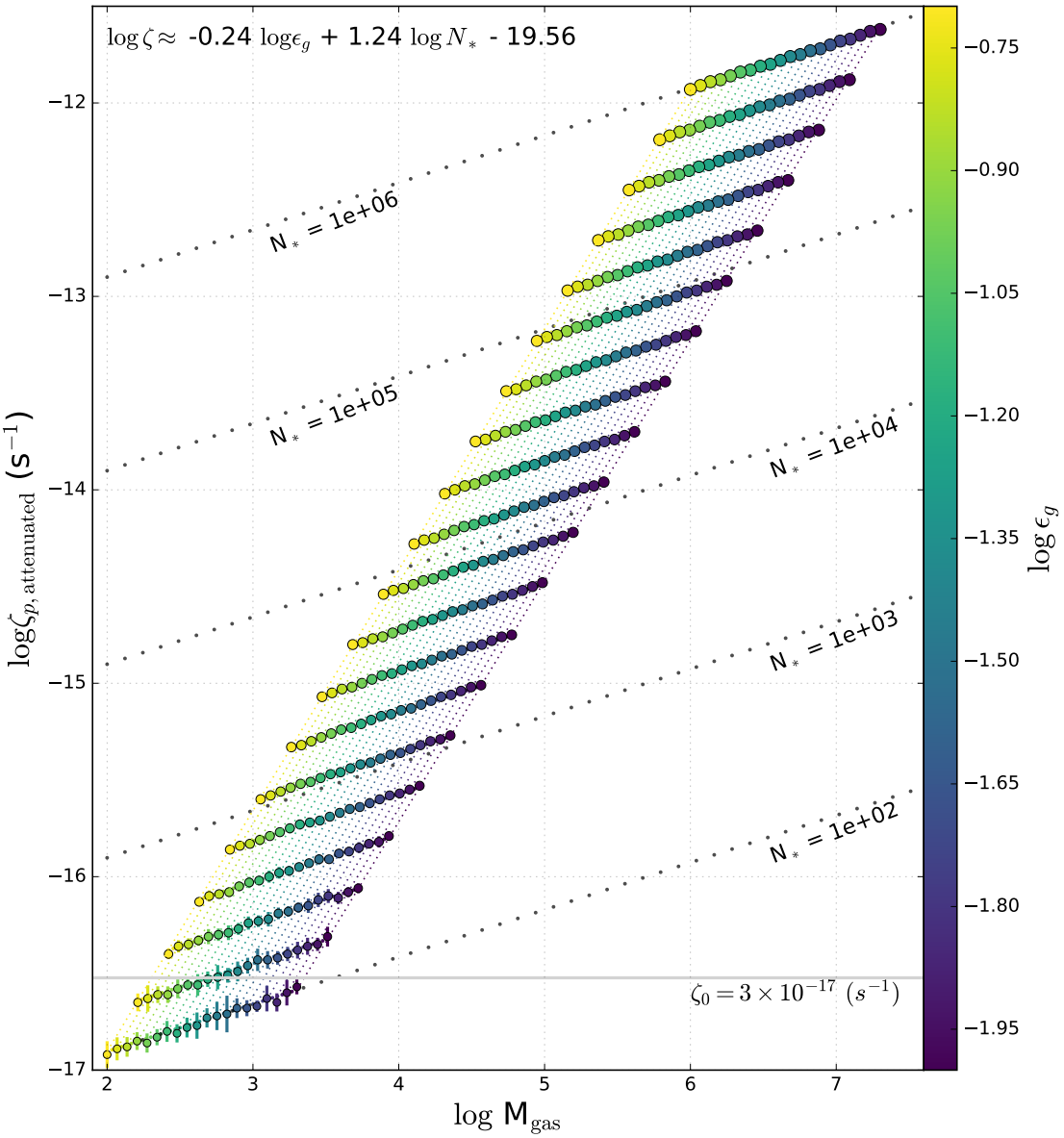

Figure 4.7. Attenuated cosmic ray ionization rate as a function of number of protostars in the cluster, star formation efficiency and gas mass. Error bars indicate the $\pm 1\sigma$ spread. Point size and color indicate N_* and ϵ_g, respectively. The gray horizontal line indicates the fiducial value $\zeta_0 = 3 \times 10^{-17}$ (s^{-1}). Dotted black lines show lines of constant N_*. A two-dimensional fit of $\log \zeta(N_*, \epsilon_g)$ is annotated in the top left corner.

4.5.1.1 Magnetic Field Strength

The magnetic field strength at the protostellar surface is not well constrained. Typically, it is thought to range between a few Gauss and 1 kG. In our fiducial model, we assume $B = 10$G. However, this is on the smaller end of the possible range. The magnetic field plays a dominant role in setting the maximum energy due to wave dampening. Wave dampening is very sensitive to the magnetic field. A small increase in the magnetic field leads to significantly more dampening of self-produced Alfvén waves by the CRs, described in detail in Appendix 4.7.1. The dampening criterion in Equation 4.34 depends on B^{-4}; a factor of hundred difference in magnetic field strength yields a substantial change in this criterion.

We recalculated the CR spectrum and CRIR for the (m, m_f) parameter space with B = 1 kG. Figure 4.8 shows the maximum energy and acceleration constraints as a function of (m, m_f). We find that there are swaths of the parameter space where the shock density, temperature and velocity are such that wave dampening becomes the dominant constraint in acceleration. Figure 4.8 shows that in these regions E_{max} is reduced to 50-100 MeV significantly below the GeV energy scale in our fiducial model. This has relatively little effect on the unattenuated CRIR. However, for high column densities, the collisional losses are sufficient to significantly reduce the high CR flux. Therefore, there are regions within the (m, m_f) parameter space where the attenuated CRIR will be negligible due to wave dampening. These regions only account for a few percent of the parameter space ,i.e. mainly low-mass protostars, so that our cluster results are largely independent of the assumed magnetic field strength.

4.5.1.2 Accretion Flow Filling Fraction

The accretion flow filling fraction, f, directly influences the shock density as $n \propto f^{-1}$. Our fiducial model assumes $f = 0.1$. However, Class 0 sources, which likely have higher accretion rates, may undergo more spherical accretion. We investigate the

effect of increasing the shock filling fraction to $f = 0.9$. Figure 4.9 shows the maximum energy and acceleration constraint mechanisms for $f = 0.9$. The behavior is very similar to the fiducial values in Figure 4.2, although the region where the acceleration is constrained by matter interactions is smaller and pushed towards higher masses. We find that a factor of 9 increase in f leads to a factor of 3-4 decrease in $E_{\max}$ for protostars with masses below 3 $M_{\odot}$. The maximum energy for the rest of the parameter space remains above 10 GeV. For this higher filling fraction, we find a factor of 9 decrease in the unattenuated and attenuated CRIR due to a change in the normalization of $f(p)$ (see Equation 4.10).

While variation in the filling fraction leads to a respectively linear change in the CRIR, in a cluster environment higher f values for young sources may cancel with lower values exhibited by older sources, whose accretion has declined.

4.5.1.3 Shock Efficiency Parameter

The shock efficiency parameter, η, which describes the fraction of thermalized protons that are accelerated to relativistic speeds, is also poorly constrained. We assume $\eta = 10^{-5}$ for the fiducial model following Padovani et al. [80]. The normalized CR pressure, $\tilde{P}_{\rm CR} = \frac{P_{\rm CR}}{\rho_s v_s^2}$, depends linearly on η (see Appendix 4.7.1 for details). Stronger CR pressure, in relation to the shock ram pressure, decreases the effectiveness of wave dampening. As such, the maximum energy is constrained mainly by interactions with neutral gas. Figure 4.10 shows the maximum energy and acceleration constraints for $\eta = 10^{-3}$. We find that the maximum energy for the whole parameter space is approximately 17 GeV. A 2 dex increase in η leads to a 2 dex increase in the unattenuated and attenuated CRIR, i.e., ζ depends linearly on η. Consequently, uncertainties in η lead to large uncertainties in the expected CRIR. However, evidence for CRs with energies greater than 10 GeV would be an indication of a higher η.

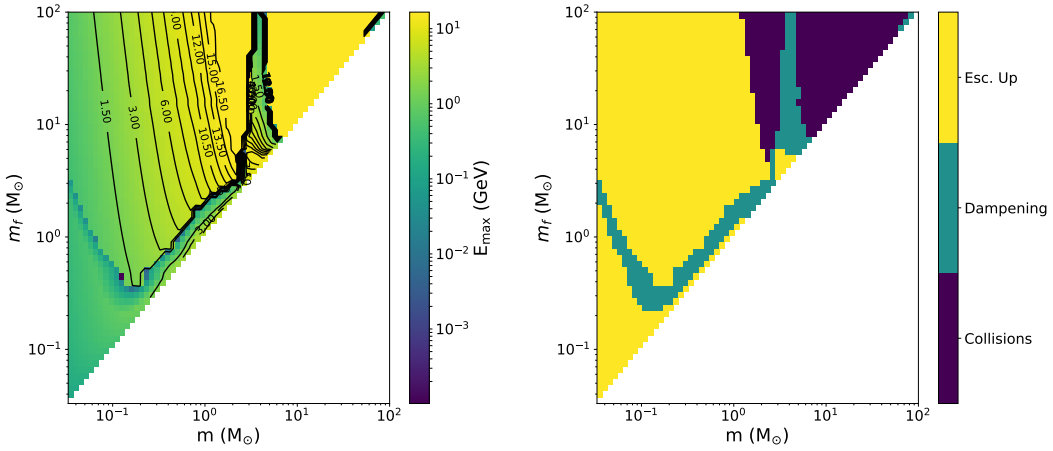

Figure 4.8. Same as Figure 4.2 but with B = 1 kG.

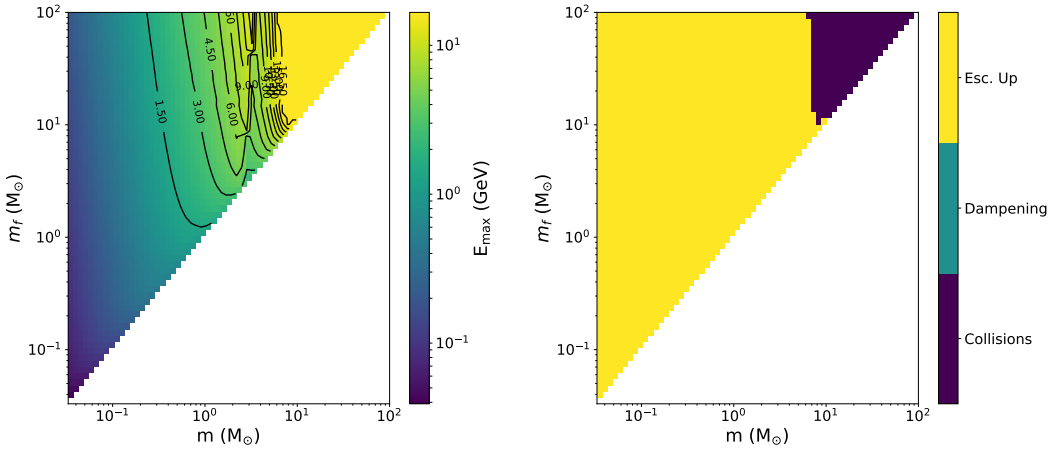

Figure 4.9. Same as Figure 4.2 but with $f_{\rm acc} = 0.9$.

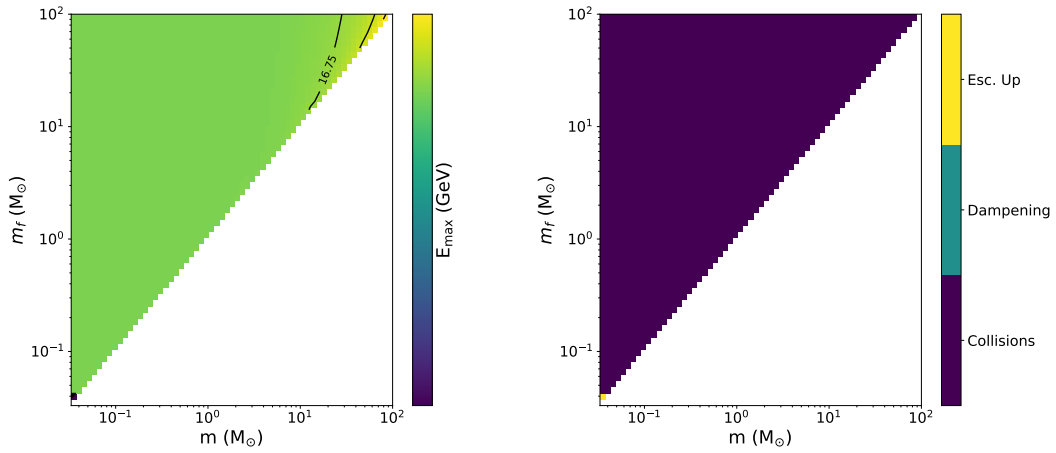

Figure 4.10. Same as Figure 4.2 but with $\eta = 10^{-3}$.

4.5.1.4 Transport Parameter

How CRs are transported through a protostellar core from its central protostar has not been modeled in detail. Transport of CRs is determined by factors relating to the gas density, magnetic field configuration, diffusion coefficients and cosmic ray energy [200, 208]. Figure 4.11 shows a comparison between the two limiting cases of transport through the core for a subsolar Class 0 protostar. The CRIR is five orders of magnitude higher in the diffusive regime than the free streaming. At the edge of the core, the CRIR is $\zeta = 10^{-11}$ s^{-1}. Balancing cosmic ray heating, $\Gamma_{\rm cr}$, with atomic and molecular line cooling, given by Goldsmith [216], predicts temperatures of $T > 10^3$ K for densities of $n = 10^3$ cm^{-3} and a CRIR $\zeta = 10^{-11}$ s^{-1}. Such temperatures at the core edge are inconsistent with observations. However, $\zeta = 10^{-17}$ s^{-1}, the case of free-streaming, produces temperatures of $T \approx 10$ K. Observations of molecular ions can measure the CRIR in the outer regions of cores, constraining the transport mechanism. We discuss this in §4.5.2

The case of transport in protostellar disks is much more complicated. The transport through the disk strongly depends on assumptions about the magnetic field mor-

phology [217]. In contrast, protostellar core magnetic fields are thought to exhibit an hour glass morphology [218, 219]. Such a morphology will allow free streaming, although not fully isotropically.

4.5.2 Comparison with Observations

Directly measuring the CR flux from embedded protostars is not possible. However, the CRIR can be constrained through modeling the radio and sub-millimeter emission from molecular ions. There have been several recent observations towards embedded protostars, which have attempted to constrain the CRIR.

Ceccarelli et al. [86] measured HCO^+, $H^{13}CO^+$ and N_2H^+ emission towards OMC-2 FIR 4. OMC-2 FIR 4 is a protocluster within the Orion Molecular Cloud (OMC) at a distance of 420 pc which contains a few low- and intermediate-mass protostars, a total mass of 30 $M_\odot$ and luminosity of 10^3 $L_\odot$ [220, 221, 222]. They modeled the chemistry using a two zone model: a warm inner region and a cold envelope. The inner region, at a radius of 1,600 AU, is well fit by a CRIR of $\zeta = 6 \times 10^{-12}$ s^{-1}, while the outer envelope, at a distance of 3,700 AU, has a CRIR of $\zeta = 4 \times 10^{-14}$ s^{-1}. They use a power-law CR flux spectrum, f(E) $\propto E^p$, with p between -4 and -2.5. The central compact source in OMC-2 FIR 4 is thought to be an early stage Class 0 protostar, with a mass around 10 $M_\odot$ [222, 223]. To compare with their results, we assume that this source dominates the CR flux and bolometric luminosity. Figure 4.5 shows that for a 10 $M_\odot$ protostar, the CRIR is fairly insensitive to the final mass. Figure 4.6 shows the inferred CRIR with a protostar of $(m, m_f) = (10, 20)$ $M_\odot$ and $\Sigma_{\rm cl} \approx 8.0$ g cm^{-2} following the column density measurements of López-Sepulcre et al. [222]. We show $\zeta \approx 10^{-12} - 10^{-14}$ between column densities of $2 \times 10^{21} - 2 \times 10^{23}$ cm^{-2}. Therefore, our model is consistent with the enhanced CRIR measured towards OMC-2 FIR 4 from CRs accelerated by the central protostar's accretion shock. Under these assumptions, $\zeta > 10^{-14}$ at column densities $N(H_2) < 3 \times 10^{23}$ cm^{-2}. The elevated

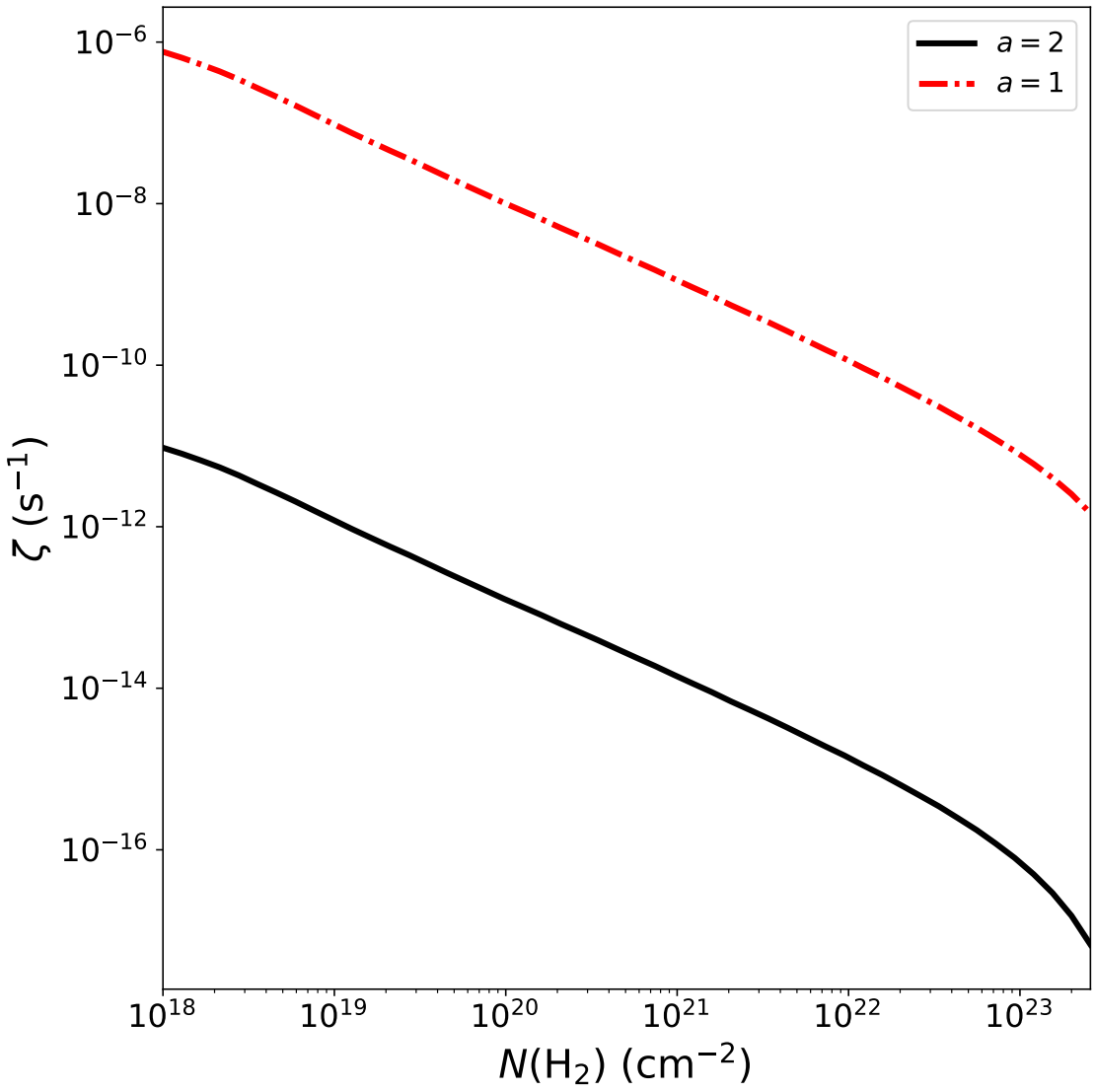

Figure 4.11. Cosmic ray ionization rate as a function of column density from a single protostar. The solid black line indicates free-streaming transport with $a = 2$. The dashed-dotted red line shows the case for diffusive transport. The parameters assumed for the plot are $m = 0.5$ M$_\odot$, $m_f = 1.0$ M$_\odot$ and $\Sigma_{\rm cl} = 1$ g cm^{-2}.

CRIR in OMC-2 FIR 4 has been similarly inferred from HC_3N and HC_5N [224] and c-C_3H_2 [89]. The observed CRIR towards OMC-2 FIR 4 is consistent with the free streaming approximation in §4.3.4.2.

Favre et al. [88] expanded the work of Ceccarelli et al. [86] with a survey of Class 0 protostars spanning low to intermediate masses. They use high J transitions of HCO^+ and N_2H^+ to measure the ratio HCO^+/N_2H^+ to infer the CRIR. They assume a fixed temperature of 40 K and density of 2.5×10^5 cm^{-3}. They could not confirm a systematically higher CRIR in embedded Class 0 sources due to large errors in converting the molecular emission to an abundance. For many sources, the full Spectral Line Energy Distribution (SLED) of HCO^+ and N_2H^+ are not observed, and some sources are not detected in N_2H^+. However, Favre et al. [88] show that the ratio does not depend strongly on the luminosity of the protostar. In our results, we find that the parameter space for protostars between 0.1 $M_\odot$ and 3 $M_\odot$ exhibits a relatively flat ζ dependence. One caveat is that not all sources have all molecular lines detected so the emission may trace different column density surfaces. We show in Figure 4.6 that this could result in orders of magnitude difference in ζ. This makes it difficult to constrain the absolute value of ζ without constraining the radial surfaces and temperatures, as done in Ceccarelli et al. [86].

Cleeves et al. [225] measured the total ionization rate towards TW Hya, which is an evolved Class II protostar. They found $\zeta_{\rm CR} < 10^{-19}$ s^{-1}, which is discrepant with our results. However, TW Hya has $\dot{m} \approx 10^{-9}$ $M_\odot$ yr^{-1} [226]. Our results focus on Class 0 and Class I protostars, which are still accreting from their envelope. Therefore, we would not expect CR acceleration to be efficient in this system.

4.6 Summary

We present self-consistently derived CR spectra and CRIRs for protostars and protoclusters from accretion shocks at the protostellar surfaces. We combine a CR

model [80] with analytic accretion history models. We find that protostars are efficient accelerators of protons from energies between keV to GeV scales. The energy losses due to diffusion escape and collisional losses inhibit acceleration of CRs to TeV scales, indicating that gamma radiation would not be present. Furthermore, the CR flux spectrum is consistent with an ideal supersonic, super-Alfvénic shock with $j(E) \propto E^{-2}$. Collisional losses due to envelope gas interactions and geometric dilution substantially decrease the CR flux at the edge of the envelope such that the spectrum at lower energies flattens.

We quantify the CR pressure and the importance of this pressure to the kinetic pressure and find that the CR pressure is minimal, confirming that it need not be included in a virial analysis of cores.

We present the CRIR for protostars for a broad range of instantaneous and final protostellar masses. Protostellar accretion shocks are efficient accelerators of CRs, producing $\zeta > 10^{-12}$ s^{-1} in the inner region of their envelopes and disks. Towards the edge of the envelope, ζ drops to 10^{-17} s^{-1}. However, within the natal molecular cloud, this rate is still greater than that due to external CR sources if collisional losses are accounted for [171]. We present the results from this paper over an extended parameter space in an online interactive tool (See Footnote 1). *We conclude individual protostars may dominate the high extinction gas ionization in their natal cloud.*

We calculate ζ for protoclusters as a function of the number of constituent protostars, N_*, and star formation efficiency, ϵ_g. We find that protoclusters with $N_* \gtrsim$ a few hundred exhibit ζ greater than the often assumed value of $\zeta_0 = 3 \times 10^{-17}$. Large protoclusters, such as those within the OMC, will accelerate CRs and provide $\zeta > 10^{-16}$ within their natal cloud. We fit the protocluster results with a two dimensional linear function, Equation 4.24, showing a sub-linear trend with ϵ_g and a superlinear trend with N_*:

$$\zeta \propto \epsilon_g^{-0.24} N_*^{1.24} \tag{4.25}$$

The dispersion in this relation is incredibly small due to the flatness of $\zeta(m, m_f)$. This elevated CR flux should be considered in models of protoclusters. We will explore the impact of protostellar CRs on cloud chemistry in future work.

4.7 Appendix

4.7.1 Cosmic Ray Spectrum Physics

CRs can be accelerated to near relativistic speeds in strong shocks. We use the CR model from Padovani et al. [80] and couple it to the protostellar accretion shock model described in §4.3. Throughout this section, β and γ are used as proxies of energies, with $E = \gamma m_p c^2$ and $\gamma = \frac{1}{\sqrt{1-\beta^2}}$. The CRs are assumed to be accelerated in a Bohm-type diffusion shock. The momentum distribution of the CRs from first order Fermi acceleration is

$$f(p) = f_0 \left(\frac{p}{p_{\rm inj}} \right)^{-q}, \tag{4.26}$$

where f_0 is a normalization constant, p is the momentum of the CR, $p_{\rm inj}$ is the injection momentum and q is the power-law index. The power-law index is related to the shock compression factor, r, by $q = \frac{3r}{r-1}$. The distribution is defined between momenta $p_{\rm inj} < p < p_{\rm max}$, where $p_{\rm max}$ is the maximum CR momentum. The energy distribution of the shock-accelerated CRs is

$$\mathcal{N}(E) = 4\pi p^2 f(p) \frac{dp}{dE} \quad (\text{particles GeV}^{-1}\ \text{cm}^{-3}) \tag{4.27}$$

and the CR flux emerging from the shock surface is

$$j(E) = \frac{v(E)\mathcal{N}(E)}{4\pi} \quad (\text{particles GeV}^{-1}\ \text{cm}^{-2}\ \text{s}^{-1}\ \text{sr}^{-1}). \tag{4.28}$$

The values for $p_{\rm inj}$, $p_{\rm max}$ and r come from the underlying shock properties. For the compression factor, r, we use the hydrodynamic strong shock result

$$r = \frac{(\gamma_{ad}+1)\mathcal{M}_s^2}{(\gamma_{ad}-1)\mathcal{M}_s^2+2}, \tag{4.29}$$

where γ_{ad} is the adiabatic index and $\mathcal{M}_s = \frac{v_s}{c_s}$ is the sonic Mach number for the shock flow. $\mathcal{M}_s \approx 2$ at the protostellar accretion shock due to the high temperatures of the gas. The injection momentum, $p_{\rm inj}$ is related to the thermal pressure by

$$p_{\rm inj} = \lambda p_{\rm th} = \lambda m_p c_{s,d}, \tag{4.30}$$

where $c_{s,d} = \frac{v_s}{r}\sqrt{\gamma_{ad}(r-1)}$ is the downstream sound speed, m_p is the proton mass, and the parameter λ depends on the shock efficiency η:

$$\eta = \frac{4}{3\sqrt{\pi}}(r-1)\lambda^3 e^{-\lambda^2}. \tag{4.31}$$

Protostellar accretion is thought to proceed via flow along the magnetic field lines in columns connecting the disk and protostar [209]. Therefore, we assume the shock front normal is parallel to the magnetic field lines. The coefficients for upstream and downstream diffusion, k_u and k_d respectively, under a parallel shock are equal, $k_u = k_d$. The upstream diffusion coefficient is calculated in Padovani et al. [80]:,

$$\begin{aligned} k_u = \frac{2}{\tilde{P}_{CR}}\frac{V_A}{v_s} = 4\times10^{-2}\left(\frac{v_s}{10^2\ \mathrm{km\ s^{-1}}}\right)^{-1}\times \\ \left(\frac{n_H}{10^6\ \mathrm{cm^{-3}}}\right)^{-0.5}\left(\frac{B}{10\ \mu\mathrm{G}}\right)\left(\frac{\tilde{P}_{CR}}{10^{-2}}\right)^{-1}. \end{aligned} \tag{4.32}$$

Berezhko and Ellison [227] calculates $\tilde{P}_{\rm CR}$ as a function of the injection and maximum momentum. Under the approximation that $p_{\rm max} >> p_{\rm inj}$ (which is reasonable, since $\mathrm{E_{max}} \propto$ GeV and $\mathrm{E_{inj}} \propto$ keV), $\tilde{P}_{CR} = \eta r \left(\frac{c}{U}\right)^2 \tilde{p}_{\rm inj}^{a}\left(\frac{1-\tilde{p}_{\rm inj}^{b}}{2r-5}\right)$, where $\tilde{p} = p/(m_p c)$, $a = \frac{3}{r-1}$, and $b = \frac{2r-5}{r-1}$. The maximum energy is derived by considering different limits of the CR propagation.

As CRs propagate through neutral gas, they undergo various kinds of interaction. CRs can excite electronic excitations and cause ionizations, with CRs with energies between 100 MeV and 1 GeV dominating the H_2 ionization. Furthermore, at GeV and higher energies, they can lose energy by pion production, resulting in gamma radiation. These losses are encoded in the loss function, $L(E)$. The maximum energy possible due to collisional losses is found when the acceleration rate equals the loss rate:

$$\beta \left[\frac{L(E)}{10^{-25}\ \mathrm{GeV\ cm^2}}\right] = 3.4\frac{k_u^{\alpha}(r-1)}{r[1+r(k_d/k_u)^{\alpha}]}\times \left(\frac{v_s}{10^2\ \mathrm{km\ s^{-1}}}\right)^2 \left(\frac{n_s}{10^6\ \mathrm{cm^{-3}}}\right)^{-1} \left(\frac{B}{10\ \mu\mathrm{G}}\right), \tag{4.33}$$

where β (and γ) are relativistic proxies for the energy. We use the loss function $L(E)$ from Padovani et al. [171]. When neutral and ionized media are mixed, the self-generated CR wave fluctuations can be damped, decreasing the efficacy of their acceleration. The energy upper limit due to this wave damping is found by requiring that the acceleration rate is shorter than the dampening loss rate:

$$\gamma\beta^2 = 8.8\times10^{-5}\tilde{\mu}^{-1}\Xi(1-x)^{-1}\left(\frac{v_s}{10^2\ \mathrm{km\ s^{-1}}}\right)^3 \times \left(\frac{T_s}{10^4\ K}\right)^{-0.4}\left(\frac{n_s}{10^6\ \mathrm{cm^{-3}}}\right)^{-0.5}\left(\frac{B}{10\ \mu G}\right)^{-4}\left(\frac{\tilde{P}_{CR}}{10^{-2}}\right), \tag{4.34}$$

where

$$\Xi = \left(\frac{B}{10\ \mu G}\right)^4 + 1.4\times10^{12}\tilde{\mu}^2\gamma^2\beta^2x^2\left(\frac{T}{10^4\ K}\right)^{0.8}\left(\frac{n_s}{10^6\ \mathrm{cm^{-3}}}\right)^3$$

and $\tilde{P}_{CR} = \frac{P_{CR}}{n_s m_{\mathrm{H}} U^2}$ is the fraction of the shock ram pressure that goes into the CR acceleration. CRs will diffuse out in the transverse direction of the shock. If the accretion is purely spherical, this diffusion could not happen. However, if the accretion flows along columns of gas, then this loss mechanism is taken into account.

The maximum energy due to upstream escape, $E_{esc,u}$, is set by requiring that the escape rate is slower than the acceleration rate:

$$\gamma\beta^2 = 4.8\mathscr{M}k_u^{\alpha}\tilde{\mu}^{-1}\left(\frac{v_s}{10^2 \text{ km s}^{-1}}\right)\left(\frac{B}{10\ \mu G}\right), \tag{4.35}$$

where $\mathscr{M} = \frac{\epsilon r_*}{10^2 \text{AU}}$ and $\epsilon = 0.1$ [228]. The maximum CR energy, $E_{\max}$

$$E_{\max} = \min(E_{\text{loss}}, E_{\text{damp}}, E_{\text{esc,u}}) \tag{4.36}$$

and the maximum momentum, $p_{\max}$

$$p_{\max}c = \sqrt{E_{\max}^2 - (m_p c^2)^2} \tag{4.37}$$

4.7.2 Secondary Electron Ionizations

Secondary electron ionizations can occur when the left over electron due to H_2 ionization has an energy greater than the H_2 ionization potential. We follow the prescription by Ivlev et al. [212] to calculate the secondary electron flux and ionization rate. The secondary electron flux is given by:

$$j_{\text{e}}^{\text{sec}}(E) = \frac{E}{L(E)} \int_{E+I(\text{H}_2)}^{\infty} j(E')\frac{d\sigma_p^{\text{ion}}}{dE}(E, E')dE', \tag{4.38}$$

where I(H_2) = 15.6 eV, $L(E)$ is the collisional loss function and $\frac{d\sigma_p^{\text{ion}}}{dE}$ is the proton-H_2 ionization differential cross section. We use the differential cross section from Glassgold and Langer [229]:

$$\frac{d\sigma_p^{\text{ion}}}{dE}(E, E') = \frac{\sigma_0(E')}{1 + \left(\frac{E'}{J}\right)^2}, \tag{4.39}$$

where $\sigma_0(E) = \frac{\sigma_p^{\rm ion}(E)}{J}\left[\tan^{-1}\frac{E-I(\rm H_2)}{J}\right]^{-1}$ is the total proton-H_2 ionization cross section, and J = 7 eV [229]. The total proton-H_2 ionization cross section is

$$\begin{aligned}
\sigma_p^{\rm ion} &= (\sigma_l^{-1} + \sigma_h^{-1})^{-1} \\
\sigma_l(E) &= 4\pi a_0^2 C x^D \\
\sigma_h(E) &= 4\pi a_0^2 [A\ln(1+x) + B] x^{-1},
\end{aligned}$$

where $x = m_e E_p / m_p \mathrm{I(H)}$, I(H) = 13.598 eV, A = 0.71, B = 1.63, C = 0.51, and D = 1.24 [171, 230]. When calculating the H_2 ionization rate due to secondary electrons, we use the electron-H_2 ionization cross section:

$$\begin{aligned}
\sigma_e^{\rm ion} &= 8\pi a_0^2 \left(\frac{\mathrm{I(H)}}{\mathrm{I(H_2)}}\right)^2 F(t)G(t) \\
F(t) &= \frac{1-t^{1-d}}{d-1}\left[\left(\frac{2}{1+t}\right)^{d/2}\frac{1-t^{1-d/2}}{d-2}\right] \\
G(t) &= \frac{1}{t}\left(A_1 \ln t + A_2 + \frac{A_3}{t}\right),
\end{aligned}$$

where t = $E_e/\mathrm{I(H_2)}$ and we adopt $d = 2.4$, $A_1 = 0.72$, $A_2 = 0.87$ and $A_3 = -0.6$ [171, 231].

In principle, this process can be repeated as a cascade. However, such higher order effects will not significantly affect our results compared to other model assumptions.

CHAPTER 5

THE ASTROCHEMICAL IMPACT OF COSMIC RAYS IN PROTOCLUSTERS I: MOLECULAR CLOUD CHEMISTRY

This chapter[1] introduces an extended astrochemical code which includes cosmic ray attenuation in-situ. This astrochemical code utilizes user-defined cosmic ray spectra and computes the cosmic ray ionization rate locally rather than a globally constant rate. We use this code to quantify the impact of different cosmic ray models on molecular cloud chemistry.

5.1 Abstract

We present astrochemical photo-dissociation region models in which cosmic ray attenuation has been fully coupled to the chemical evolution of the gas. We model the astrochemical impact of cosmic rays, including those accelerated by protostellar accretion shocks, on molecular clouds hosting protoclusters. Our models with embedded protostars reproduce observed ionization rates. We study the imprint of cosmic ray attenuation on ions for models with different surface cosmic ray spectra and different star formation efficiencies. We find that abundances, particularly ions, are sensitive to the treatment of cosmic rays. We show the column densities of ions are under predicted by the "classic" treatment of cosmic rays by an order of magnitude. We also test two common chemistry approximations used to infer ionization rates.

[1]These results are based on research published in Gaches et al. [232] and is reproduced with permission from the AAS.

We conclude that the approximation based on the H_3^+ abundance under predicts the ionization rate except in regions where the cosmic rays dominate the chemistry. Our models suggest the chemistry in dense gas will be significantly impacted by the increased ionization rates, leading to a reduction in molecules such as NH_3 and causing H_2-rich gas to become [C II] bright.

5.2 Introduction

Molecular cloud dynamics and chemistry are sensitive to the ionization fraction. The chemistry of molecular clouds is dominated by ion-neutral reactions [196] and thus controlled by the ionization fraction. The gas (kinetic) temperature of a typical molecular cloud with an average H-nucleus number density of $n \approx 10^3\,\mathrm{cm}^{-3}$ is approximately 10 K for cosmic-ray ionization rates $\zeta \lesssim 10^{-16}\,\mathrm{s}^{-1}$ [154, 161], thus rendering neutral-neutral reactions inefficient. Ionization in molecular clouds is produced in three difference ways: UV radiation, cosmic rays (CRs), and X-Ray radiation. Ultraviolet radiation, from external O- and B-type stars and internal protostars, does not penetrate very far into the cloud due to absorption by dust. However, cosmic rays, which are relativistic charged particles, travel much further into molecular clouds and dominate the ionization fraction when $A_V \geq 5\,\mathrm{mag}$ [195, 233, 234]. CR-driven chemistry is initiated by ionized molecular hydrogen, H_2^+ [83]. The ion-neutral chemistry rapidly follows:

$$\mathrm{CR} + \mathrm{H_2} \rightarrow \mathrm{H_2^+} + \mathrm{e^-} + \mathrm{CR'}$$

$$\mathrm{H_2^+} + \mathrm{H_2} \rightarrow \mathrm{H_3^+} + \mathrm{H},$$

where CR′ is the same particle as CR but with a lower energy. The ejected electron from the first reaction can have an energy greater than the ionization potential of H_2 and thus cause further ionization. Once H_3^+ forms, more complex chemistry follows, thereby creating a large array of hydrogenated ions:

$$X + H_3^+ \rightarrow [XH]^+ + H_2.$$

Both HCO^+ and N_2H^+, important molecules used to map the dense gas in molecular clouds, form this way with X being CO and N_2, respectively. These species are also used to constrain the cosmic ray ionization rate (CRIR) [i.e., 86, 235]. OH^+ and H_nO^+ are also formed this way through H_3^+ and H^+ [236]. In addition, at low column densities ($A_V < 1\,\mathrm{mag}$), which is typical of the boundaries of molecular clouds), the non-thermal motions between ions and neutrals may overcome the energy barrier of the reaction

$$C^+ + H_2 \rightarrow CH^+ + H,$$

leading to an enhancement of the CO column density [237, 238] and a shift of the HI-to-H_2 transition to higher A_V [239].

The ionization fraction controls the coupling of the magnetic fields to the gas, influencing non-ideal magnetohydrodynamic (MHD) effects such as ambipolar diffusion [41]. These non-ideal effects can play a significant role in the evolution in the cores and disks of protostars. On galactic scales, numerical simulations have shown that CRs can help drive large outflows and winds out of the galaxy [e.g., 240]. Our study focuses on the impact of CRs on Giant Molecular Cloud scales which is typically not resolved fully in such simulations.

There have been a plethora of studies modeling the impact of CRs on chemistry and thermal balance [i.e., 28, 154, 235, 241, 242, 243]. However, in these studies, and the vast majority of astrochemical models, the CRIR is held constant throughout the cloud, despite the recognition that CRs are attenuated and modulated while traveling through molecular gas [15, 82, 171, 217]. Galactic-CRs, thought to be accelerated in supernova remnants or active galactic nuclei, are affected by hadronic and Coulombic energy losses and screening mechanisms that reduce the flux with increasing column density [244, 245, 246]. The modulation of CRs has not previously been included

within astrochemical models of molecular clouds due to the difficulty in calculating the attenuation and subsequent decrease in the CRIR [16, 247].

Given that CRs are thought to be attenuated, it is expected that the ionization rate should decline within molecular clouds. However, recent observations do not universally show a lower ionization rate. Favre et al. [88] inferred the CRIR towards 9 protostars and found a CRIR consistent with the rate inferred for galactic CRs. The OMC-2 FIR 4 protocluster, hosting a bright protostar, is observed to have a CRIR 1000 higher than the expected rate from galactic CRs [86, 89, 224]. Gaches and Offner [81] show that this system can be modeled assuming the central source is accelerating protons and electrons within the accretion shocks on the protostar's surface. In general, accreting, embedded protostars may accelerate enough CRs to cancel the effect of the attenuation of external CRs at high column densities, producing a nearly constant ionization rate throughout the cloud [80, 81].

Typical accretion shocks and shocks generated by protostellar jets satisfy the physical conditions necessary to accelerate protons and electrons [80, 81]. Accretion shocks in particular are a promising source of CRs since they are strong, with velocities exceeding 100 km/s and temperatures of millions of degrees Kelvin [209]. Gaches and Offner [81] calculated the spectrum of accelerated protons in protostellar accretion shocks and the attenuation through the natal core assuming that the CRs free-stream outwards. These models suggest that clusters of a few hundred protostars accelerate enough CRs into the surrounding cloud to exceed the ionization rate from Galactic CRs.

In this study, we explore the effects of protostellar CRs on molecular cloud chemistry by employing the model of Gaches and Offner [81]. We implement an approximation for CR attenuation into the astrochemistry code 3D-PDR [30] to account for CR ionization rate gradients. We investigate the signatures of a spatially varying

ionization rate. We further explore the impact of protostellar CR sources and their observable signatures.

The layout of the paper is as follows. In §5.3 we present the CR and protostellar models and describe the implementation of CR attenuation into 3D-PDR. We discuss our results in §5.4. Finally, in §5.5 we create observational predictions and compare them to observations.

5.3 Methods

5.3.1 Protocluster Model

We generate protoclusters following the method of Gaches and Offner [148], where the model cluster is parameterized by the number of stars and gas surface density, N_* and $\Sigma_{\rm cl}$, respectively. These parameters are connected to the star formation efficiency $\varepsilon_g = M_*/M_{\rm gas}$, where $M_{\rm gas}$ is related to $\Sigma_{\rm cl}$ following McKee and Tan [164] $\Sigma_{\rm cl} = \frac{M_{\rm gas}}{\pi R^2}$, where the cloud radius, R, is determined from the density distribution (See §5.3.3). We model protoclusters with surface densities in the range $0.1 \leq \Sigma_{\rm cl} \leq 10$ g cm^{-2} and with a number of stars in the range $10^2 \leq N_* \leq 10^4$. In this parameter space, we always consider $\varepsilon_g \leq 25\%$.

We generate $N_{\rm cl} = 20$ protoclusters for each point in the parameter space and adopt the average CR spectrum for the chemistry modeling. We use the Tapered Turbulent Core (TTC) accretion history model [50, 164], where the protostellar core is supported by turbulent pressure and accretion is tapered to produce smaller accretion rates as the protostellar mass, m, approaches the final mass, m_f. Gaches and Offner [148] showed the TTC model is able to reproduce the bolometric luminosities of observed local protoclusters.

5.3.2 Cosmic Ray Model

We brielfy summarize the CR acceleration and propagation model in Gaches and Offner [81] and refer the reader to that paper for more details. We assume CRs are accelerated in the accretion shock near the protostellar surface. Accreting gas is thought to flow along magnetic field lines in collimated flows with the shock at the termination of the flow. We assume the shock velocities are comparable to the free-fall velocity at the stellar surface. Following Hartmann et al. [209], we assume fully ionized strong shocks with the shock front perpendicular to the magnetic field lines. We adopt a mean molecular weight $\mu_I = 0.6$ and a filling fraction of accretion columns on the surface, $f = 0.1$.

We calculate the CR spectrum under the Diffusive Shock Acceleration (DSA) limit, also known as first-order Fermi acceleration [e.g., reviewed in 248, 249, 250]. Under DSA, the CR momentum distribution is a power-law, $f(p) \propto p^{-q}$, where q is related to the shock properties. We attenuate the CR spectrum through the protostellar core following Padovani et al. [171]. Padovani et al. [217] presented updated attenuation models for surface densities up to 3000 g cm^{-2}, but the results remain unchanged for the surface of concern in this work. The core surface density and radius for a turbulence-supported core are [164]:

$$\Sigma_{\rm core} = 1.22\Sigma_{\rm cl} = 0.122\,{\rm g\,cm^{-2}} \left(\frac{\Sigma_{\rm cl}}{0.1\,{\rm g\,cm^{-2}}}\right) \tag{5.1a}$$

$$\begin{aligned} N({\rm H_2})_{\rm core} &= \frac{\Sigma_{\rm core}}{\mu_M m_H} \\ &= 3\times10^{22}\,{\rm cm^{-2}} \left(\frac{\Sigma_{\rm core}}{0.122\,{\rm g\,cm^{-2}}}\right)\left(\frac{2.4}{\mu}\right) \end{aligned} \tag{5.1b}$$

$$\begin{aligned} R_{\rm core} &= 0.057\Sigma_{\rm cl}^{-\frac{1}{2}} \left(\frac{m_f}{30\ M_\odot}\right)^{\frac{1}{2}} \quad {\rm pc} \\ &= 0.104\,{\rm pc} \left(\frac{\Sigma_{\rm cl}}{0.1\,{\rm g\,cm^{-2}}}\right)^{-\frac{1}{2}} \left(\frac{m_f}{10\,{\rm M_\odot}}\right)^{\frac{1}{2}}, \end{aligned} \tag{5.1c}$$

where $\mu_M = 2.4$ is the mean molecular weight for a molecular gas. We calculate the total protocluster CRIR by summing over the N_* attenuated CR spectra.

5.3.3 Density Structure

We assume the molecular cloud density is described by an inverse power law

$$n(r) = n_0 \left(\frac{R}{r}\right)^2, \tag{5.2}$$

where R is the cloud radius and n_0 is the number density with an inner radius of 0.1 pc. The r^{-2} dependence matches the solution for isothermal collapse [163]. We take $n_0 = 100$ cm^{-3}, corresponding to a gas regime in which the cloud is expected to be mostly molecular under typical conditions. The radius is set by constraining the total surface density by $\Sigma_{\rm cl}$ as defined:

$$\int_{R_c}^{R} n(r)dr = \frac{\Sigma_{\rm cl}}{\mu_M m_H}, \tag{5.3}$$

where R_c is the inner radius delineating the transition between the molecular cloud and protostellar core. The turbulent-linewidth, σ, of a cloud with density profile $n(r) \propto r^{-2}$ and a virial α parameter is [251]:

$$\sigma = \left(\frac{GM^2\alpha}{3\mu_M m_H \bar{n} V R}\right)^{\frac{1}{2}}, \tag{5.4}$$

where $\bar{n}$ is the volume-averaged density from $n(r)$, G is the gravitational constant, and $V = \frac{4}{3}\pi R^3$ is the volume of the molecular cloud. We take $\alpha = 2$ for our fiducial model [149].

Table 5.1. Atomic Abundances

Species	Abundance Relative to H
H	1.0
He	0.1
C	1.41×10^{-4}
N	7.59×10^{-5}
O	3.16×10^{-4}
S	1.17×10^{-5}
Si	1.51×10^{-5}
Mg	1.45×10^{-5}
Fe	1.62×10^{-5}

Notes. Atomic abundances adopted from Sembach et al. [167].

5.3.4 Chemistry with Cosmic Ray Attenuation

We use a modified version of the 3D-PDR astrochemistry code[2] introduced in Bisbas et al. [30]. 3D-PDR solves the chemical abundance and thermal balance in one-, two- and three-dimensions for arbitrary gas distributions. The code can be applied to arbitrary three dimensional gas distributions, such as post-processing simulations [112, 116, 252]. Here, we use the code in one dimension to model a large parameter space. We adopt the McElroy et al. [18] UMIST12 chemical network containing 215 species and approximately 3,000 reactions. We assume the gas is initially composed of molecular H_2 with the rest being atomic with abundances from Sembach et al. [167] shown in Table 5.1. Cooling is included from line emission, which is mainly due to carbon monoxide at low temperatures and forbidden lines of [OI],[CI] and [CII] at higher temperatures. Heating is due to dissipation of turbulence, photoelectric heating of dust from far-ultraviolet emission, H_2 fluorescence and CR heating of gas. We use a temperature floor of 10 K. Previously, 3D-PDR included CRs via a single global CRIR parameter. See Bisbas et al. [30] for more technical details.

[2]The code can be downloaded from `https://uclchem.github.io`, including the new modifications presented in this paper.

We modify 3D-PDR to account for CR attenuation through the cloud. Currently, our implementation is restricted to one-dimensional models where we assume spherical symmetry. 3D-PDR calculates the CRIR from $N_{\rm SRC}$ CR sources. The user provides a CR spectrum for any number of sources and whether it is external (incident at the surface) or internal (originating at the cloud center). In 1D, the fluxes are defined on either surface of the domain. The flux due to external sources is attenuated while the point sources are assumed to radiate isotropically; both are attenuated and spatially diluted. The spectra are attenuated after every update of the molecular abundances to keep the amount of H_2 for interaction losses self-consistent. 3D-PDR stores the initial CR flux in $N_{\rm ene}$ bins and self-consistently calculates ζ from all sources across the domain. Point sources require a user-set radial scaling factor, r_s, and a transport parameter, a. For our model results, we set $r_s = R_C$ to represent the core radius. Point source CR spectra, $j(E, r)$, are attenuated by the H_2 column density [171] and diluted by the radial distance following

$$j(r) \propto \left(\frac{r_s}{r + r_s} \right)^a , \tag{5.5}$$

to approximate the effects of transport. Solving the transport equations for Galactic transport problems has been done with specialized codes, such as GALPROP [253] and DRAGON2 [246]. Fully solving the steady-state transport equations are beyond the scope of this work but will be investigated in the future.

In our study, we include two CR flux sources. First, we include the internal protostellar clusters discussed above. We set the radial scaling $r_s = R_C = 0.1$ pc, which is approximately the size of a protostellar core. Second, we include an external isotropic CR flux to model interstellar CRs. We follow Ivlev et al. [212] and parameterize the external flux as

$$j_{\rm ext} = C \frac{E^\alpha}{(E + E_0)^\beta} \quad (\text{particles eV}^{-1}\ \text{cm}^{-2}\ \text{s}^{-1}\ \text{sr}^{-1}). \tag{5.6}$$

We use their "low" model ($\mathcal{L}$), with $C = 2.4 \times 10^{15}$, $E_0 = 650$ MeV, $\alpha = 0.1$ and $\beta = 2.8$ and their "high" model ($\mathcal{H}$), with $C = 2.4 \times 10^{15}$, $E_0 = 650$ MeV, $\alpha = -0.8$ and $\beta = 1.9$. The $\mathcal{L}$ model is a direct extrapolation of the Voyager-1 data [254], while the $\mathcal{H}$ is a maximal model to correct for any possible effects of the solar magnetic field. The CRIR is calculated by integrating the spectrum multiplied by the H_2 cross section:

$$\zeta_p = 2\pi \int j(E)\sigma_i(E)dE, \tag{5.7}$$

where the factor of 2π accounts for irradiating the 1-D surface on one side and $\sigma_i(E)$ is the H_2 ionization cross section with relativistic corrections [214]. The code allows for an arbitrary number of energy bins, $N_{\rm bins}$, for input CR spectrum. We compared the CRIR for bin sizes ranging from $N_{\rm bin} = 4$ to 1000 and found that $N_{\rm bins} > 40$ only produces changes in the CRIR at the 1% level. We do not fully solve for primary or secondary electrons. Therefore, we multiply the proton CRIR by $\frac{5}{3}$ to account for the electron population [255, 256].

Our fiducial parameters for the study are shown in Table 5.2. Table 5.3 shows the full suite of models we adopt. The model names describe the included physics: L/H denotes using the $\mathcal{L}/\mathcal{H}$ (Low/High) external spectrum, NI denotes no internal sources, DI denotes internal sources with $a = 1$ (diffusive transport), RI denotes internal sources with $a = 2$ (rectilinear transport) and NA denotes no internal sources or CR attenuation. We study the impact of these parameters in §5.4.

5.4 Results

5.4.1 Cosmic Ray Spectrum

Our modified 3D-PDR code requires as an input the flux of CR protons for any number of sources. As a result, the CR proton flux and CRIR throughout the spatial domain become outputs rather than inputs. Figure 5.1 shows an example CR spectrum for a molecular cloud with $\Sigma_{\rm cl} = 0.75$ g cm^{-2} and $N_* = 750$ using the

Table 5.2. Model Parameters

Parameter	Definition	Fiducial Value
$\mu_{\rm I}$	Reduced gas mass	0.6 (ionized)
$\mu_{\rm M}$	Reduced gas mass	2.4 (neutral molecular)
n_0	Density at edge of cloud	10^2 cm^{-3}
$N_{\rm src}$	Number of CR Sources	2
$N_{\rm bins}$	Number of CR spectrum bins	40
a	CR transport parameter	1
r_s	Scaling radius for CR flux	0.1 pc
α	Cloud virial parameter	2

Table 5.3. Models examined. L/H denotes Low/High external spectrum, NI denotes no internal sources, DI denotes internal sources with $a = 1$ (diffusive transport), RI denotes internal sources with $a = 2$ (rectilinear transport) and NA denotes no internal sources or CR attenuation.

Name	Source Transport	Internal	External Field	Attenuation
LDI	r^{-1}	✓	$\mathcal{L}$	✓
LRI	r^{-2}	✓	$\mathcal{L}$	✓
LNI	...	...	$\mathcal{L}$	✓
LNA	...	...	$\mathcal{L}$	...
HNI	...	...	$\mathcal{H}$	✓
HDI	r^{-1}	✓	$\mathcal{H}$	✓

LDI model. The CR proton flux increases inside the cloud because of the embedded sources. The double peaked shape of the spectrum is due to peaks in the loss function from ionization and Coulomb losses. The inset shows the CRIR as a function of the position within the cloud. In this model, the ionization rate climbs nearly two orders of magnitude throughout the cloud with increasing proximity to the protostellar cluster.

5.4.2 Cosmic Ray Ionization Rate Models

A number of prescriptions have been used to calculate the CRIR from observed column densities of various tracer species [235, 257]. The inclusion of CR attenuation allows us to directly test the accuracy of these approximations. Our astrochemical models provide the abundances throughout the cloud and the local CRIR in-situ. We test two different prescriptions that are typically used for diffuse and dense gas, respectively, from Indriolo and McCall [257]. The first, and simplest, denoted as "Simple Electron Balance" (SEB), estimates the CRIR using only the abundance of H_3^+ and e^-:

$$\zeta = k_e n(\mathrm{e}^-) \frac{n(\mathrm{H_2})}{n(\mathrm{H_3^+})}, \tag{5.8}$$

where k_e is the H_3^+ electron-recombination rate and $n(\mathrm{e}^-)$, $n(\mathrm{H_2})$ and $n(\mathrm{H_3^+})$ are the densities of electrons, molecular hydrogen and H_3^+, respectively. The second approximation includes the destruction of H_3^+ with CO and O, which we denote the "Reduced Analytic" (RA) model:

$$\zeta = \frac{x(\mathrm{H_3^+})}{x(\mathrm{H_2})} n_H \left[k_e x(\mathrm{e}^-) + k_{\mathrm{CO}} x(\mathrm{CO}) + k_O x(\mathrm{O})\right] \times \left[1 + \frac{2k_3 x(\mathrm{e}^-)}{k_2 f(\mathrm{H_2})} + \frac{2k_4}{k_2}\left(\frac{1}{f(\mathrm{H_2})} - 1\right)\right], \tag{5.9}$$

where k_i are the reaction rate coefficients for the reactions in Table from Indriolo and McCall [257] (repeated in Table 5.4 below), x_i is the abundance of species i with respect to total hydrogen nuclei and $f(\mathrm{H_2}) = 2n(\mathrm{H_2})/n_H$ is the molecular hydrogen fraction.

Table 5.4. Reactions for Reduced Analytic H_3^+ Chemistry

Reaction	Rate Coefficient ($cm^3\ s^{-1}$)	Reference
$H_2^+ + H_2 \rightarrow H_3^+ + H$	$k_2 = 2.09 \times 10^{-9}$	[258]
$H_2^+ + e^- \rightarrow H + H$	$k_3 = 1.6 \times 10^{-8}(T/300)^{-0.43}$	[259]
$H_2^+ + H \rightarrow H_2 + H^+$	$k_4 = 6.4 \times 10^{-10}$	[260]
$H_3^+ + e^- \rightarrow$ products	$k_5 = k_e = -1.3 \times 10^{-8} + 1.27 \times 10^{-6} T_e^{-0.48}$	[261]
$H_3^+ + CO \rightarrow H_2 + HCO^+$	$k_6 = 1.36 \times 10^{-9}(T/300)^{-0.142} \exp 3.41/T$	[262]
$H_3^+ + CO \rightarrow H_2 + HCO^+$	$k_7 = 8.49 \times 10^{-10}(T/300)^{0.0661} \exp -5.21/T$	[262]
$H_3^+ + O \rightarrow H_2 + OH^+$	$k_8 = k_O = 1.14^{-9}(T/300)^{-0.156} \exp -1.41/T$	[262]

Notes. Equations 5.8 and 5.9 reactino rates where $k_{CO} = k_6 + k_7$ in Equation 5.9. We omit the Nitrogen reaction from [257] Table 3 since it is not in use by either approximation.

Figure 5.2 shows the calculated CRIR using the full model and the approximations in Equations 5.8 and 5.9 as a function of the H_3^+ abundance. We show the cases of four different CR models: LNA, LNI, LDI and HDI. The first model, LNA, is of particular importance since it represents the simplest one-dimensional PDR model. Observations typically assume 0D distribution, such that the ratio of column densities is equal to the ratio of the abundances. This makes a tacit assumption that the ionization rate is the same throughout the domain. We find that both approximations produce a large range of CRIRs – even when the input CRIR is fixed due to other effects impacting the chemistry, notably the influence of the external FUV radiation. *The SEB and RA approximation models systematically underestimate the CRIR and produce an artificial spread in the inferred CRIR.* When internal sources are included, we find that both approximations infer the CRIR reasonably well. When there are no internal sources, both approximations underestimate the CRIR by up to an order of magnitude and in general do not represent any real spread in the CRIR accurately.

5.4.3 Impact of Cosmic Ray Sources on Cloud Chemistry

We examine in detail two different CR models: the traditional LNA and the LDI model. Figure 5.3 shows the column densities of different species and density

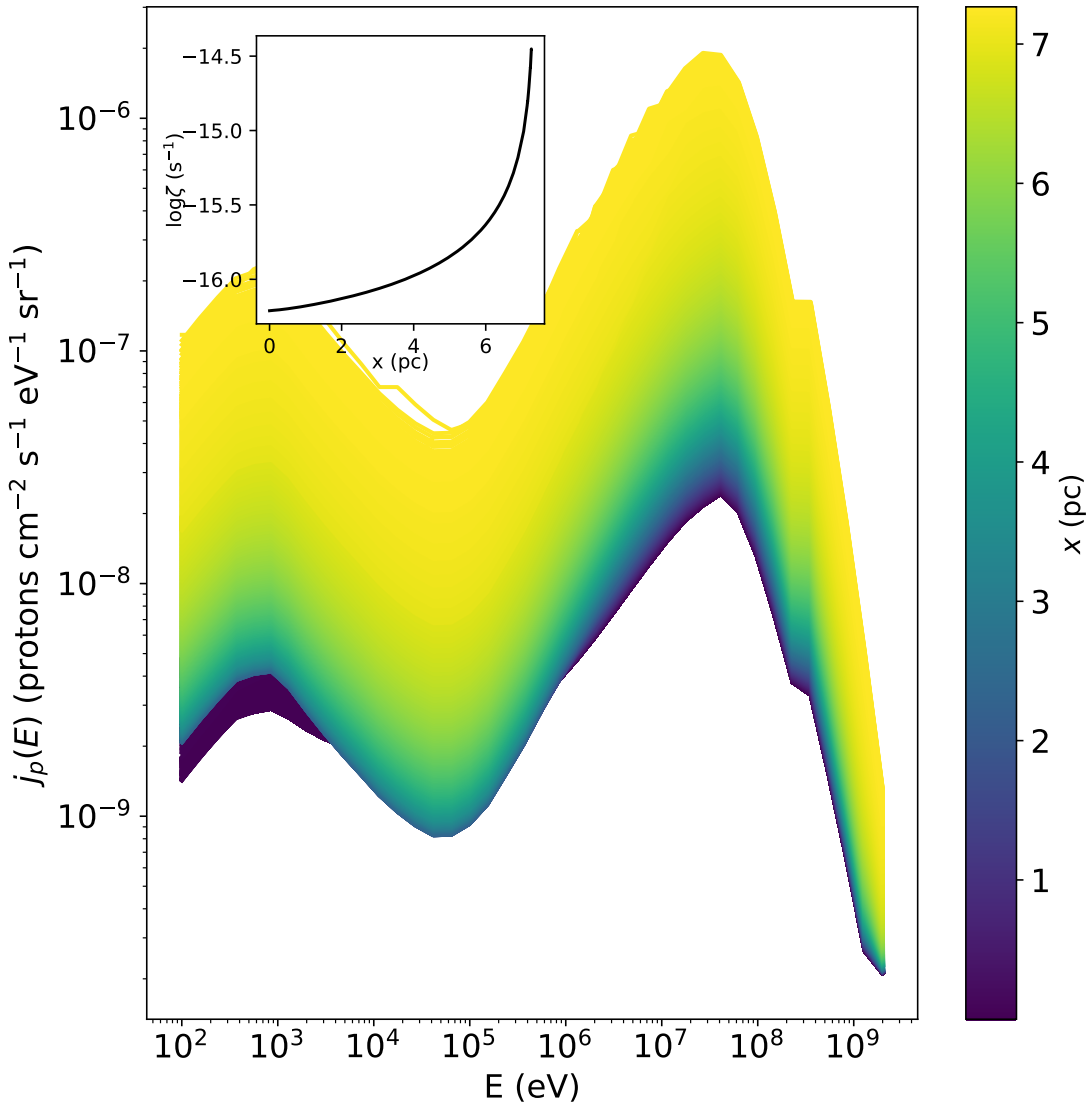

Figure 5.1. Proton cosmic ray spectrum with line color indicating position within the cloud for $\Sigma_{\rm cl} = 0.75$ g cm^{-2} and $\rm N_* = 750$ using the LDI CR model. Inset: Cosmic ray ionization rate versus position, x, into the cloud, where $x = 0$ is the cloud surface.

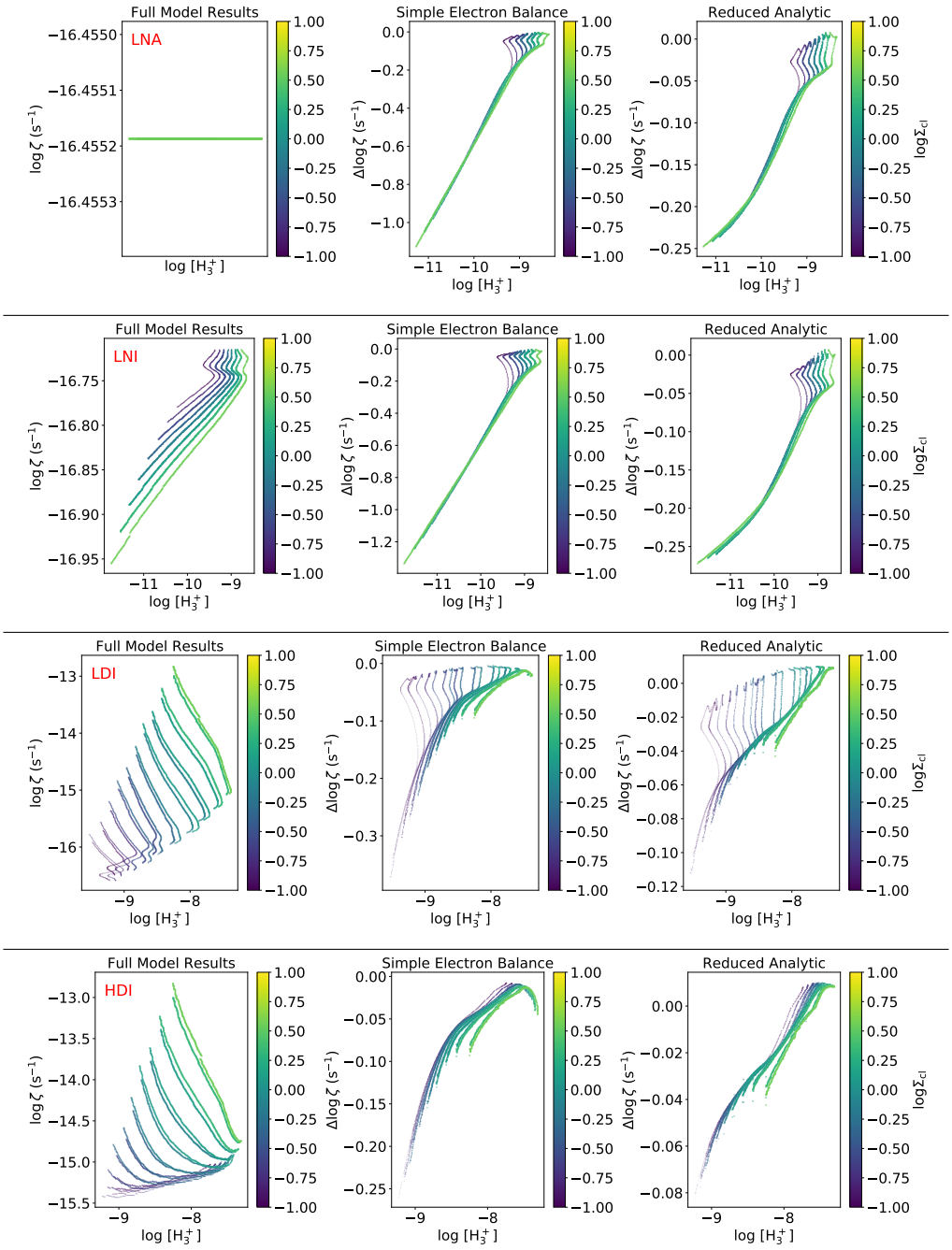

Figure 5.2. Left: Cosmic ray ionization rate as a function of H_3^+ abundance using the full astrochemical model results. Middle: Relative logarithmic error in ζ, $\Delta \log \zeta$, calculated using electron-balance approximation (Equation 5.8) and full astrochemical model. Right: Same as middle row but using the reduced analytic approximation (Equation 5.9). Color: Gas surface density, $\Sigma_{\rm cl}$ in g cm^{-2}. Models in descending order from the top are: LNA, LNI, LDI, HDI.

averaged temperature and CRIR for the LNA model as a function of $\Sigma_{\rm cl}$ and N_*. The total column density of each species increases with the gas surface density, $\Sigma_{\rm cl}$, and hence the total gas mass. Furthermore, we find across the whole parameter space that N(CO) > N(C) > N(C^+). This qualitative behavior is to be expected with no internal sources. Figure 5.4 shows the abundance profiles for the LNA model as a function of A_V into the cloud, $\Sigma_{\rm cl}$ and N_*. Since there are no embedded sources in this model, there is no difference between models of different N_*. The abundance profiles for C^+, C and CO exhibit the expected "layered" behavior [13]: C^+ is confined to the surface, C exists in a thin, warm layer and CO asymptotically approaches an abundance of $[CO/H_2] \approx 10^{-4}$. Similarly the abundance of NH_3 steadily increases into the cloud.

The abundance ratio $[HCO^+/N_2H^+]$ is sometimes used to infer the CRIR under the assumption the two molecules are co-spatial [i.e., 86]. We find that, while they share some local maxima, they are not completely co-spatial in agreement with the turbulent cloud study of Gaches et al. [90].Moreover, observations show that while they are not entirely co-spatial, there is overlap in the emission regions [i.e., 86, 88, 263, 264, 265, 266]. In particular, we show HCO^+ can exist at much lower A_V than N_2H^+. Due to similar critical densities however, the two molecules thermalize at nearly the same densities.

Figure 5.5 shows the column densities across the parameter space for the LDI model. Here we find a very different behavior compared to the LNA model shown in Figure 5.3, where the differences are especially pronounced for the more diffuse gas tracers. The column densities are no longer strictly functions of $\Sigma_{\rm cl}$ but depend on N_*. For large, massive star-forming regions (upper right corner in each panel), the gas becomes CO deficient and C rich while the bulk of gas remains molecular. Similarly, there is a slight increase in the column density of HCO^+ and N_2H^+ due to the increase in ionization. The qualitative trends exhibited by C^+, C, and marginally by HCO^+ and N_2H^+, follow that of the density-averaged CRIR, $\langle\zeta_\rho\rangle$.

The effect of an embedded protocluster is also visible in the abundance profiles. Figure 5.6 shows the abundance profiles for the LDI model. We find that CO only approaches abundances of 10^{-4} for clusters with little embedded star formation.For smaller mass clouds (i.e., smaller $\Sigma_{\rm cl}$), the C^+, C and CO abundance remains fairly unchanged compared to the LNA model. In the most massive clouds, the amount of CO at $A_V \leq 1$ is enhanced by an order of magnitude and reduced by an order of magnitude at $A_V \geq 5$. We further see a reduction in N_2H^+ at mid-A_V with an enhancement of HCO^+. Likewise the gas temperature exceeds $T > 30$ K for most of the clouds with $\Sigma_{\rm cl} > 0.25$ g cm^{-2}. As $A_V \rightarrow 10^3$, the differences between the molecular ion abundances is much less due to the greatly increased density compared to the surface of the cloud. The abundance of H_2 in the dense gas is unaffected by the increased CRIR.

We now statistically quantify the impact of different CR models on the six different molecules: C^+, C, CO, N_2H^+, HCO^+ and H_3^+. We investigate the H_3^+ column density because it is the simplest molecule that can be used to constrain the CRIR [83]. We calculate the column density logarithmic difference:

$$\Delta_s = \log \frac{N_{s,i}}{N_{s,\rm LNA}}, \tag{5.10}$$

with s representing the different species, and i the different CR models excluding the LNA model. Figure 5.7 shows violin plots representing the probability distribution of Δ_s using all clouds in the $(\Sigma_{\rm cl} - N_*)$ space. In all cases, CO is never enhanced but rather depleted. This is because the maximum abundance [CO] $= 10^{-4}$ is set by the C/O ratio. Our models generally increase the local CRIR, thereby dissociating the CO and reducing its abundance. We find very little difference between the LNI and LNA for all molecules except for N_2H^+ and HCO^+, which exhibit a 25% linear dispersion. This is caused by the impact of higher ionization rates towards the surface of the clouds. The HNI model,which has the highest overall CRIR at the surface, shows a

clear offset for the atomic and ionic species and a slight deficit for CO. In models LRI, LDI and HDI there is a significant dispersion in the column density difference, Δ_s, in all species. Figure 5.7 demonstrates that considerable care must be taken when modeling observed column densities of atomic or ionic species: the possible error, Δ_s, in the modeled column densities may be off by an order of magnitude depending on the transport of the cosmic rays and the amount of ongoing embedded star formation. The CRIR is not the only factor that leads to the creation of molecular ions, as typically assumed in observational studies. The abundances are influenced by the FUV flux, which is also enhanced by a central protocluster [148].

5.4.4 Abundance Ratio Diagnostics for the Cosmic Ray Ionization Rate

Line and abundance ratios of various tracers are often used to constrain the CRIR in dense gas. The species are typically assumed to be co-spatial (although as demonstrated in §5.4.3 that is not typically the case). We examine two different ratio diagnostics: global diagnostics using column densities and local diagnostics using the local abundance ratios and CRIRs.

Figure 5.8 shows three different column density ratios for the LNA, LNI and HNI models: $[HCO^+/N_2H^+]$, $[CO/C^+]$ and $[C/C^+]$. We find that the column density ratios in these cases increase monotonically with Σ_{cl}. The ratio of $[HCO^+/N_2H^+]$ is nearly constant, changing by less than a factor of two across two dex of Σ_{cl}. The HNI case shows a slightly different behavior with a slight local minimum in $[HCO^+/N_2H^+]$ at $\Sigma_{cl} = 6$ g cm^{-2}. The trends in these models are not due to changes in the CRIR but rather in the total amount of gas column. The $[CO/C^+]$ ratio shows a buildup of CO compared to C^+. This is to be expected in an externally irradiated model: C^+ remains consistently on the surface, while the amount of CO continues to build with Σ_{cl} with a proportional increase in the amount of dense gas. Similarly, the $[C/C^+]$ remains fairly constant since these species exist only in limited areas of A_V.

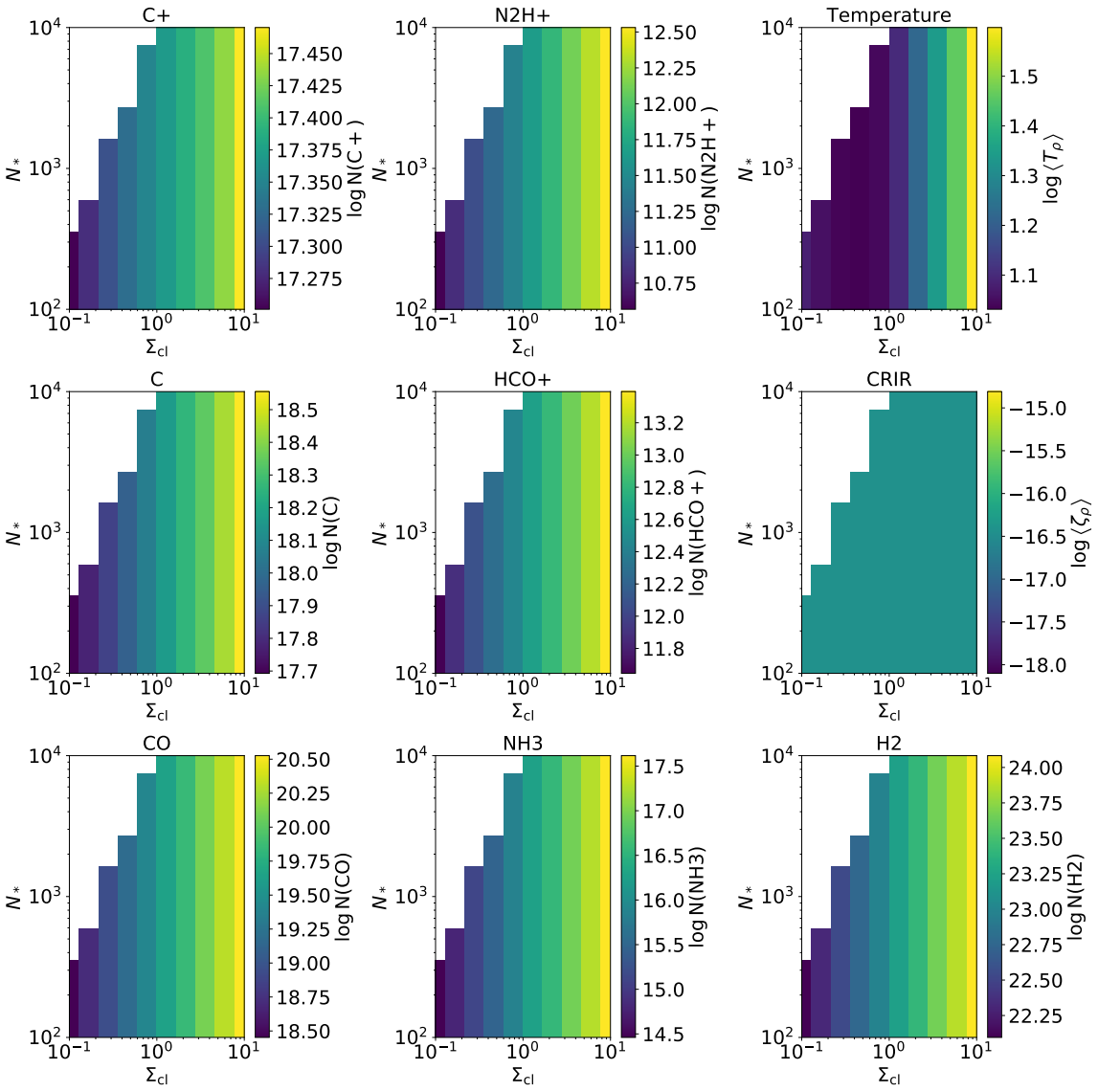

Figure 5.3. Column density of different molecular species as a function of the number of stars in the protocluster, N_* and the mass surface density, $\Sigma_{\rm cl}$ for the LNA model. The last 3 panels on the far right show the density averaged temperature, CRIR and the total gas column density.

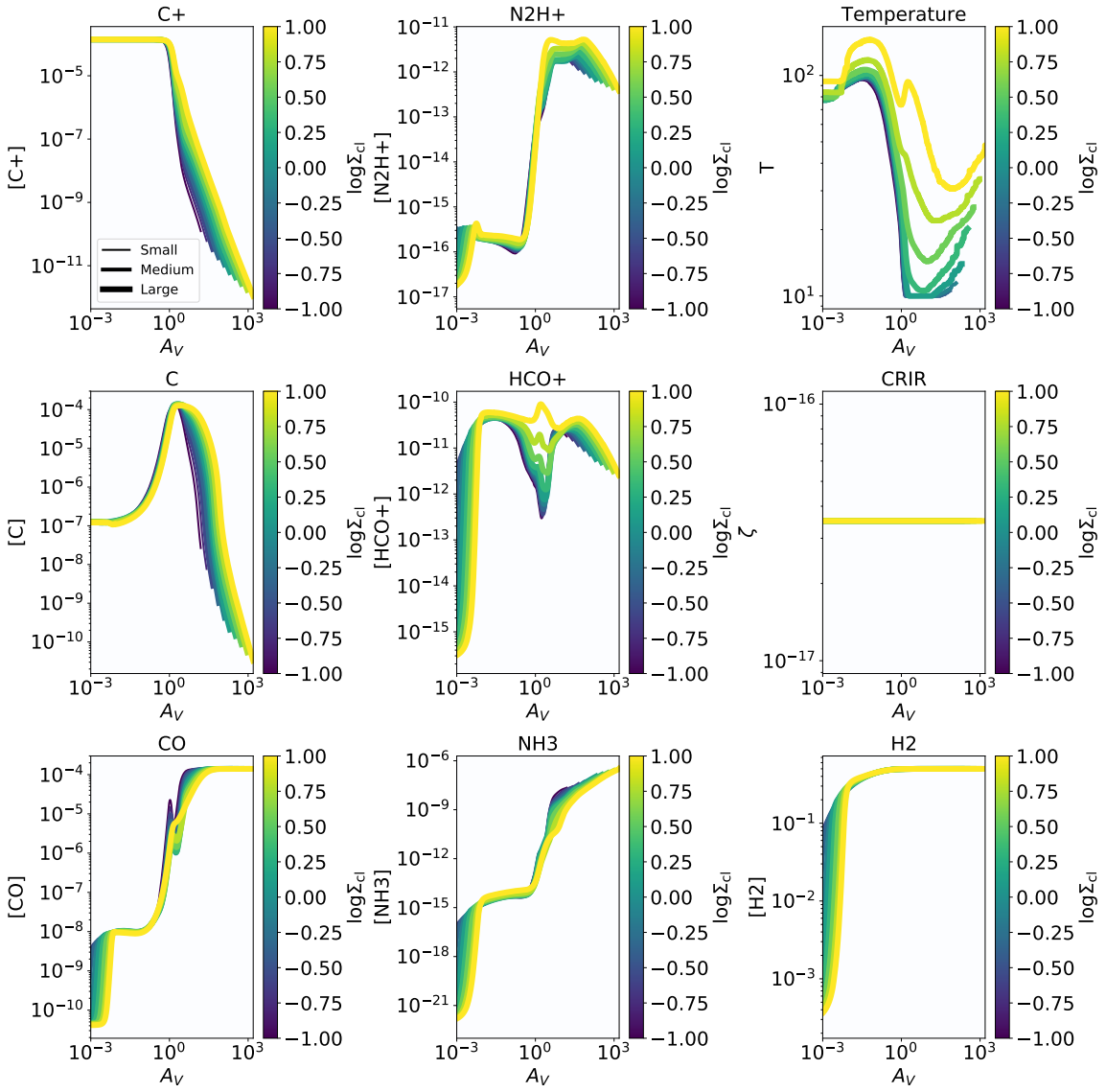

Figure 5.4. ,

for various molecular species, as a function of the visual extinction into the cloud, A_V, for the LNA model.] The abundances, [X], for various molecular species, as a function of the visual extinction into the cloud, A_V, for the LNA model. The top two panels on the right column show the temperature and CRIR as a function of the A_V. The colorbar indicates the gas surface density, $\Sigma_{\rm cl}$. The line width indicates the number of protostars in the cluster with "Small" = 10^2, "Medium" = 10^3 and "Large" = 10^4 protostars.

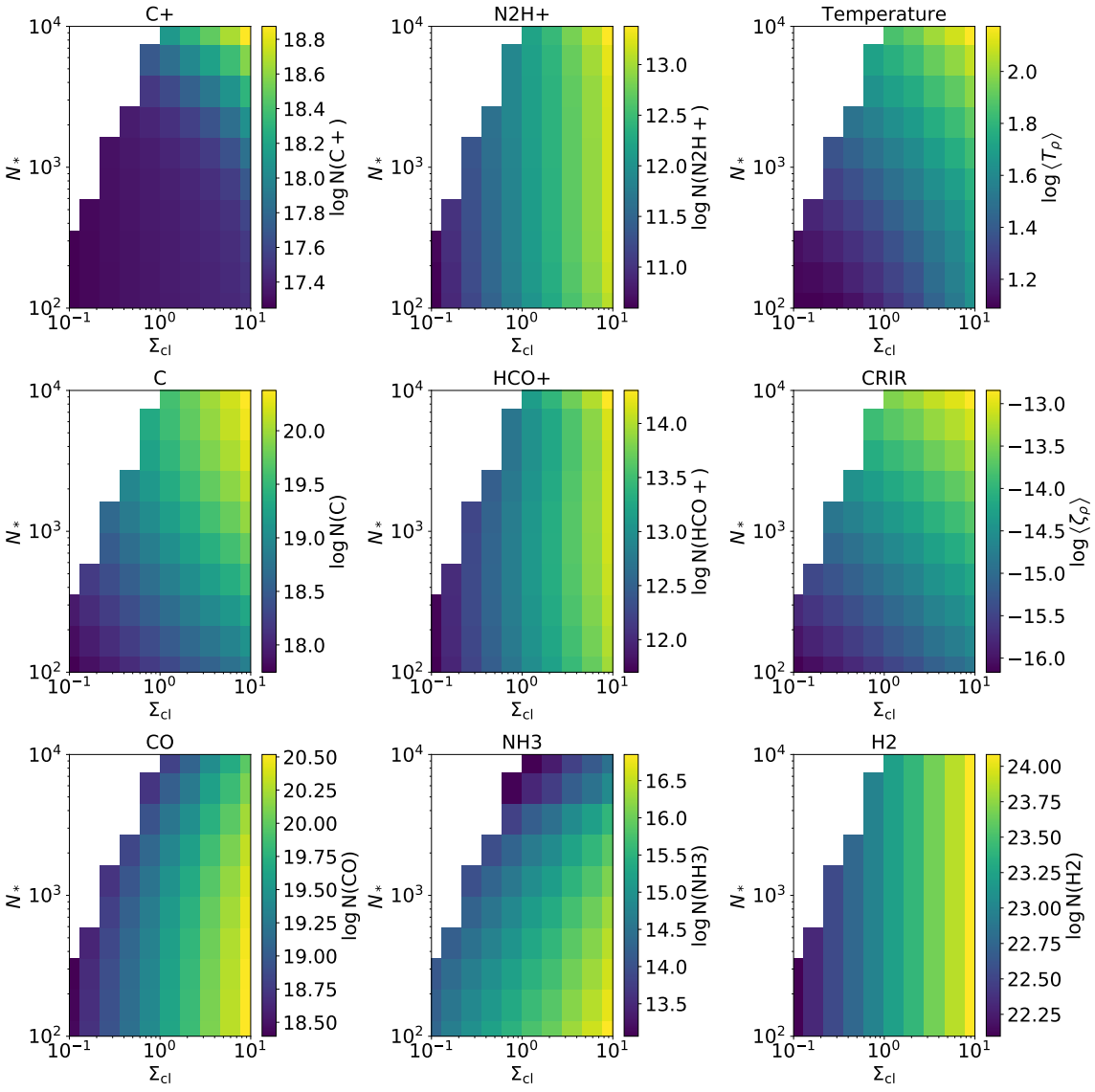

Figure 5.5. Same as Figure 5.3 but for model LDI.

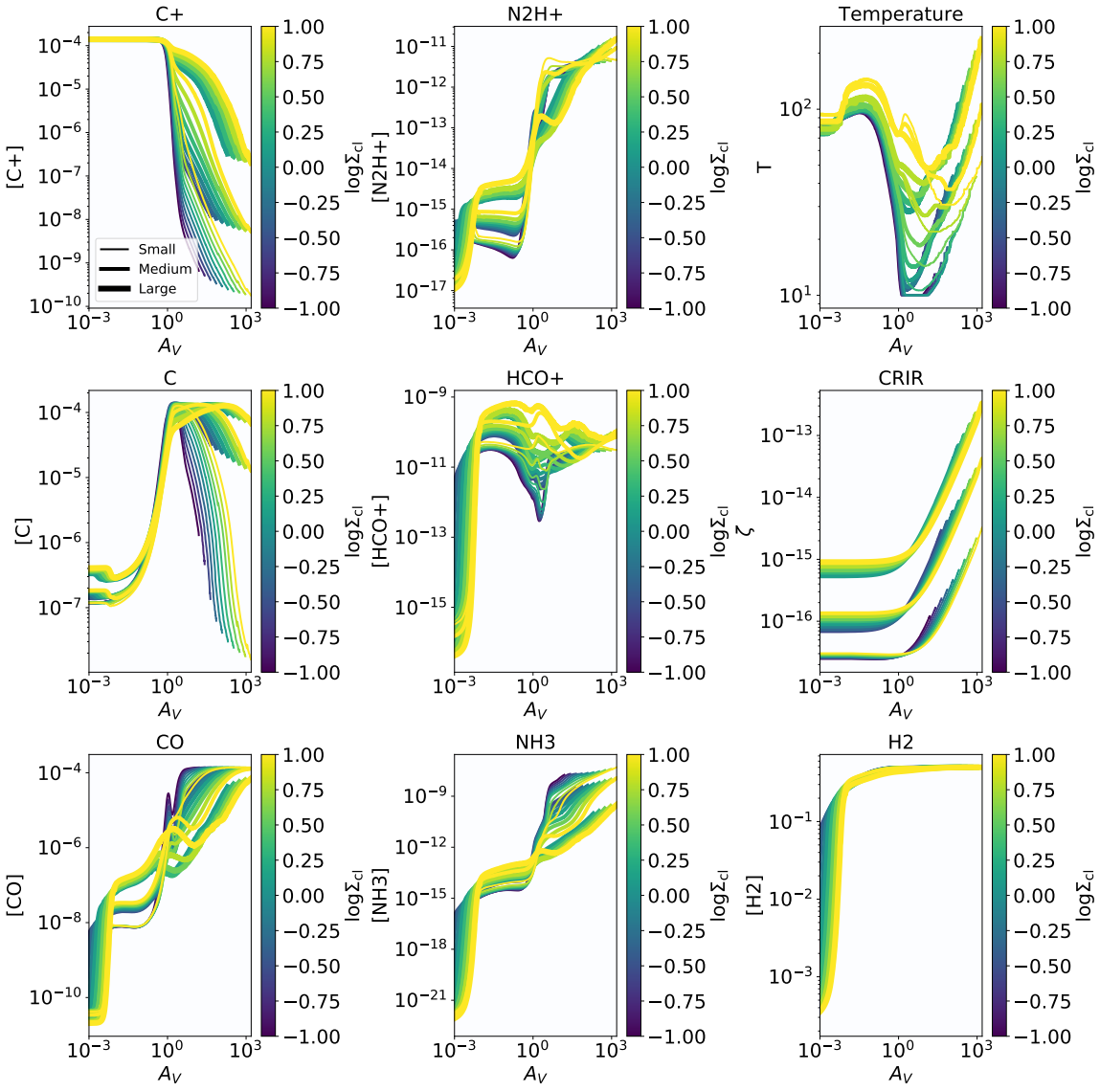

Figure 5.6. Same as Figure 5.4 but for model LDI.

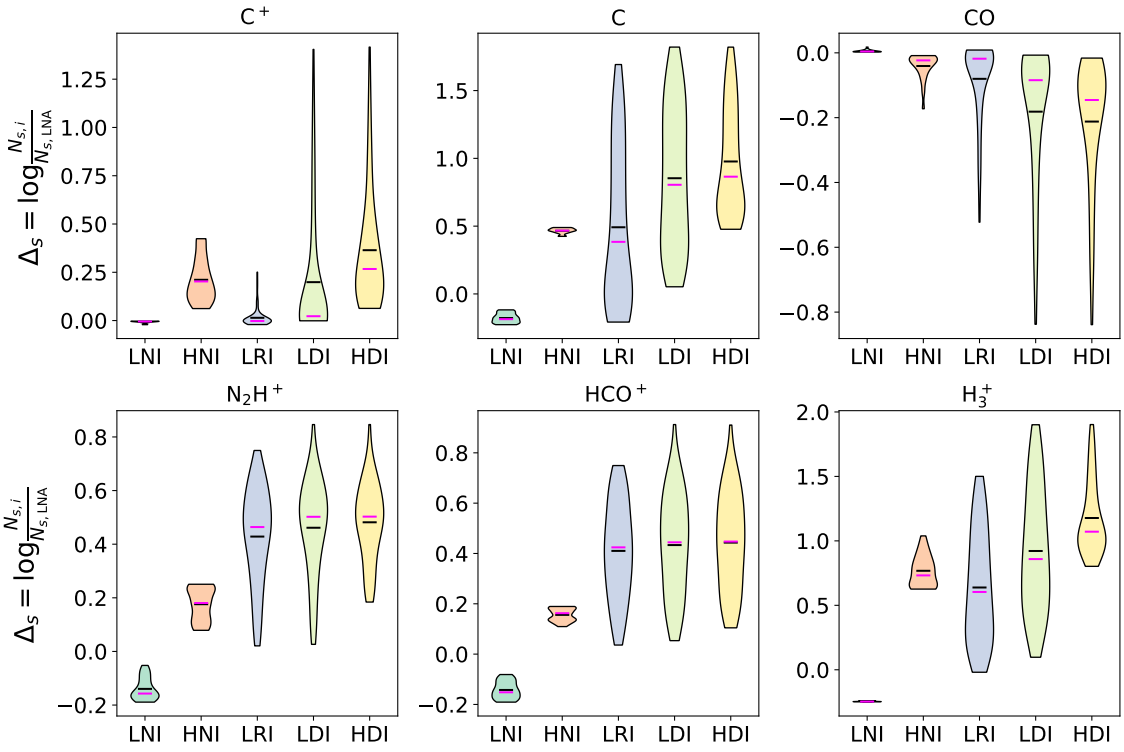

Figure 5.7. Logarithmic difference distribution, $\Delta_s = \log \frac{N_{\mathrm{s,i}}}{N_{\mathrm{s,LNA}}}$ comparing the difference in column density for molecular species, s, for five different cosmic ray models, $i \subset$ (LNI, HNI, LRI, LDI, HDI), compared to the LNA model. Distributions are generated using the model clouds across the (Σ_{cl} - N_*) parameter space. The black and magenta line indicate the mean and median, respectively.

Figure 5.9 shows the same column density ratios for three models including the embedded protoclusters: LRI, LDI and HDI. Here the trends are significantly more complicated. The $[HCO^+/N_2H^+]$ ratio still only varies by a factor of two throughout the parameter space, but it exhibits more complex behavior. The ratio decreases with Σ_{cl} and rises with N_* up to some maximum, with an additional increase in $[HCO^+/N_2H^+]$ for $N_* \approx 10^4$ for the LDI and HDI model. To understand this, we can look at the abundance profiles of the LDI model in detail in Figure 5.6. The abundance of HCO^+ increases with both with Σ_{cl} and N_* with the abundance profile flattening as a function of A_V for $\Sigma_{cl} > 1$ g cm^{-2}. For N_2H^+ the trends are separated by an A_V threshold at $A_V = 1$. At $A_V < 1$, the abundance of N_2H^+ increases like HCO^+, with Σ_{cl} and N_*. For $1 < A_V < 100$, the abundance of N_2H^+ is sensitive primarily to N_*. In high ionization environments, CO will be destroyed in the creation of HCO^+ due to interactions with H_3^+. These environments will also produce N_2H^+ which destroys CO to create HCO^+. This is likely the main driving cause in the abundance profiles: there is a reduction of CO and N_2H^+ in the dense more ionized gas, and an systematic increase in HCO^+. The $[CO/C^+]$ ratio increases monotonically across two orders of magnitude towards high Σ_{cl} and low N_*: cold gas is less ionized (lower right corner), so the amount of CO increases with respect to C^+. $[C/C^+]$ shows a different trend compared to $[CO/C^+]$. High ionization rates, in both the LDI and HDI models, have an increased $[C/C^+]$ in lower mass clouds hosting smaller clusters and a decreased $[C/C^+]$ at high Σ_{cl} compared to the LRI model. The $[C/C^+]$ ratio is nearly flat across the $\Sigma_{cl} - N_*$ parameter space in the HDI model. Clouds with fewer CRs and more gas shielding to the incident the FUV radiation have more C compared to C^+.

Observational measurements of ζ in dense gas typically use astrochemical modeling and local abundance ratios (See §5.5.2). Figure 5.10 plots the CRIR for models with $5\% \leq \varepsilon \leq 25\%$ as a function of different abundance ratios. A good CRIR indicator should exhibit a monotonic trend in response to changes in the CR flux. The

LNI model does not exhibit much change in the CRIR, so the local trends depend on density and radiative effects. In the HNI model, only the [HCO^+/CO] ratio exhibits a monotonic trend.

The models with sources show completely different abundance ratios because the dense gas is warmer and the ionization rates are higher. In all of these cases, the ratios are monotonic for $\Sigma_{\rm cl} \gtrsim 1$ g cm^{-2}. For $\Sigma_{\rm cl} \lesssim 1$ g cm^{-2} each exhibits a similar trend as in the NI model subsets. This demonstrates that these diagnostics only constrain regimes where the CRIR influences the chemistry more than radiative or other heating processes.

5.5 Discussion

5.5.1 Model Assumptions and Caveats

Our models require a variety of assumptions. First and most importantly, the models are one-dimensional and we assume protostars are clustered in the center. In reality, protostars are distributed throughout molecular clouds. Furthermore, the density distribution of molecular clouds is set by turbulence and is not a purely radial distribution. However, our results will hold qualitatively for the molecular gas around young, dense embedded clusters in molecular clouds, such as the central cluster in ρ Oph. Second, our chemical network does not include any gas-grain chemistry or freeze-out [see 18]. Therefore, we over-predict the CO abundance in regions where $n > 10^4$ cm^{-3} and $T \lessapprox 30$ K [267]. Comparing this criteria to the temperature profiles in Figure 5.6 shows the models with $\Sigma_{\rm cl} < 0.5$ g cm^{-2} and where $1 \leq A_V \leq 10$ are below the freeze-out temperature. When embedded sources are included, the densest gas heats to temperatures > 50 K. These temperatures lead to desorption from the grains, producing gas-phase CO: any CO-ice that formed before star formation occured would be evaporated back into the gas phase [268, 269].

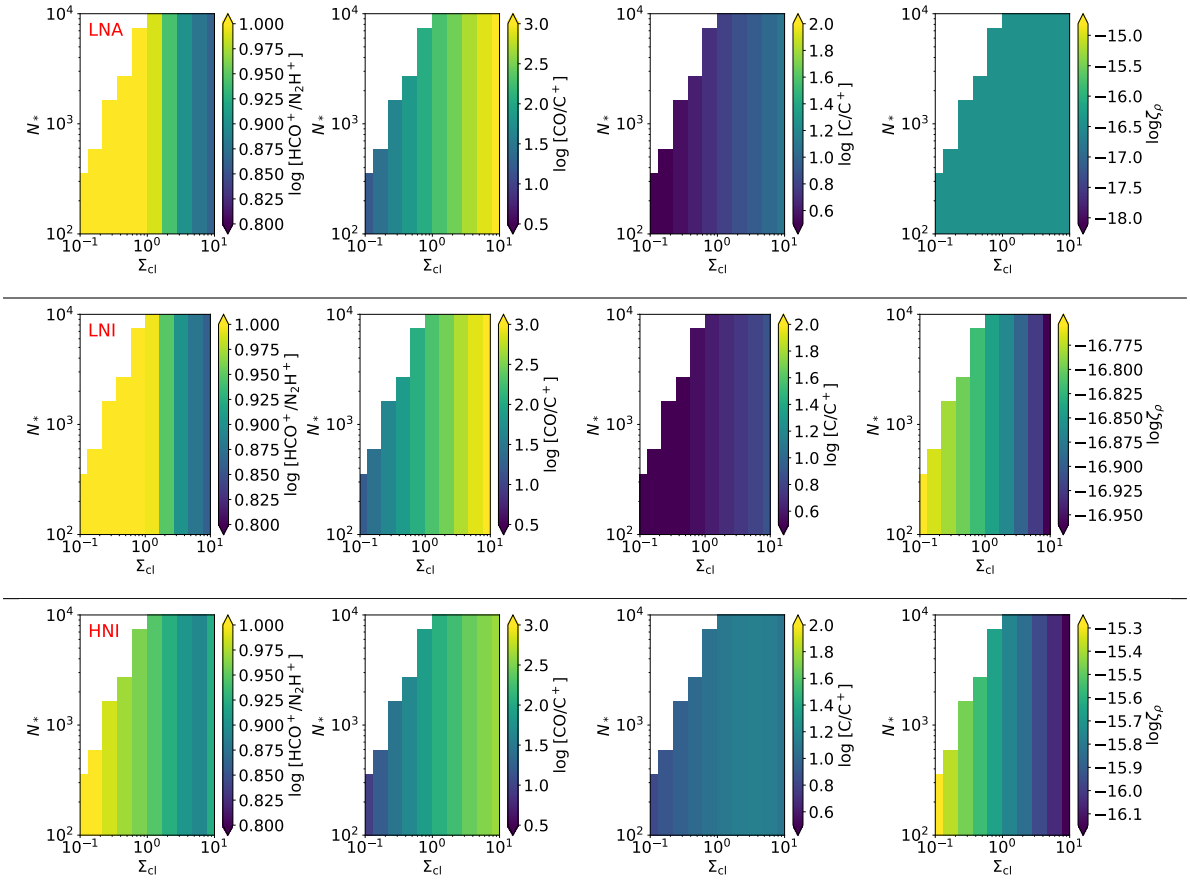

Figure 5.8. Abundance ratios versus $\Sigma_{\rm cl}$ and N_*. White contours and labels show the star formation efficiency $\varepsilon = M_*/M_{\rm gas}$. Far left: $[HCO^+]/[N_2H^+]$. Middle left: $[CO/C^+]$. Middle right: $[C/C^+]$. Far right: Density-weighted average cosmic ray ionization rate, $< \zeta_\rho >$. The models are in descending order from top: LNA, LNI, HNI. We use the same scales for the individual ratios in Figures 5.8 and 5.9 to facilitate comparison between models.

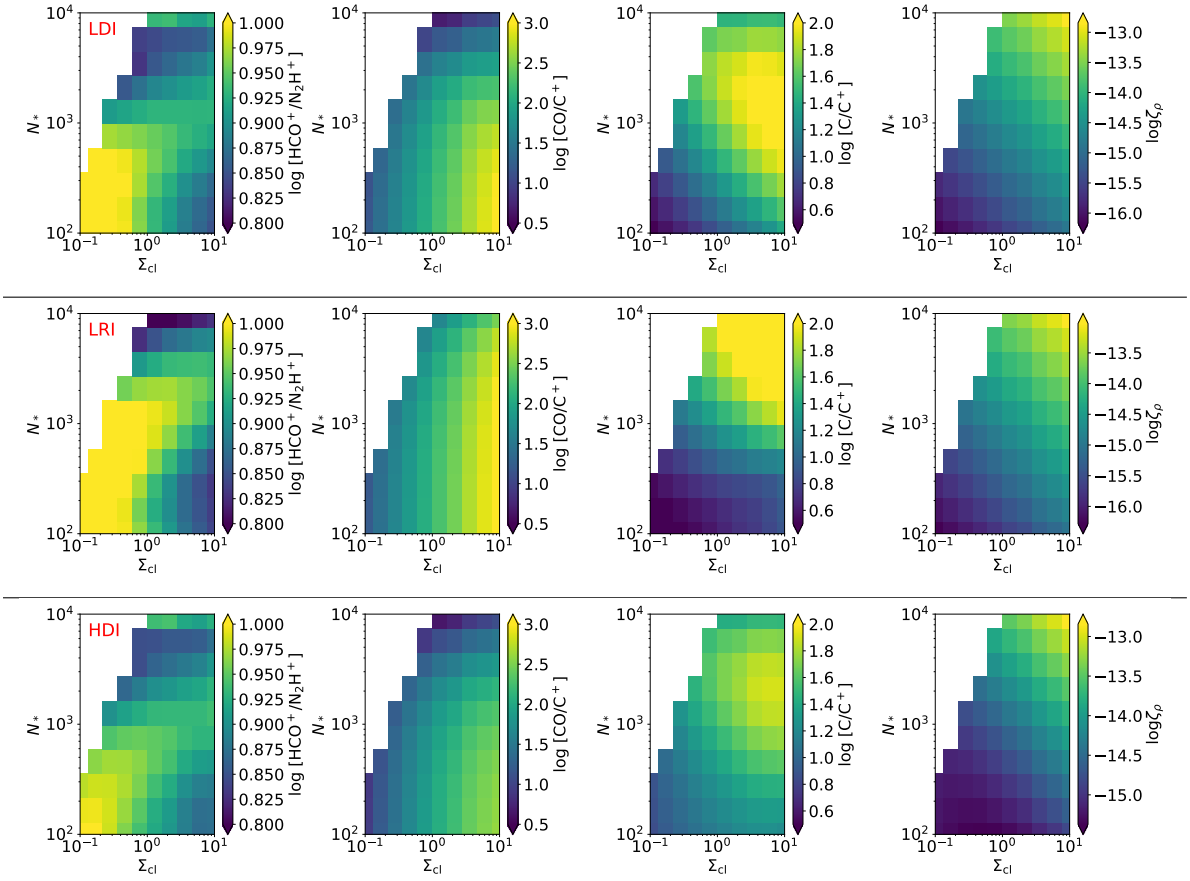

Figure 5.9. Abundance ratios versus $\Sigma_{\rm cl}$ and N_*. White contours and labels show the star formation efficiency $\varepsilon = M_*/M_{\rm gas}$. Far left: $[HCO^+]/[N_2H^+]$. Middle left: $[CO/C^+]$. Middle right: $[C/C^+]$. Far right: Density-weighted average cosmic ray ionization rate, $< \zeta_\rho >$. Models in descending order from top: LDI, LRI, HDI

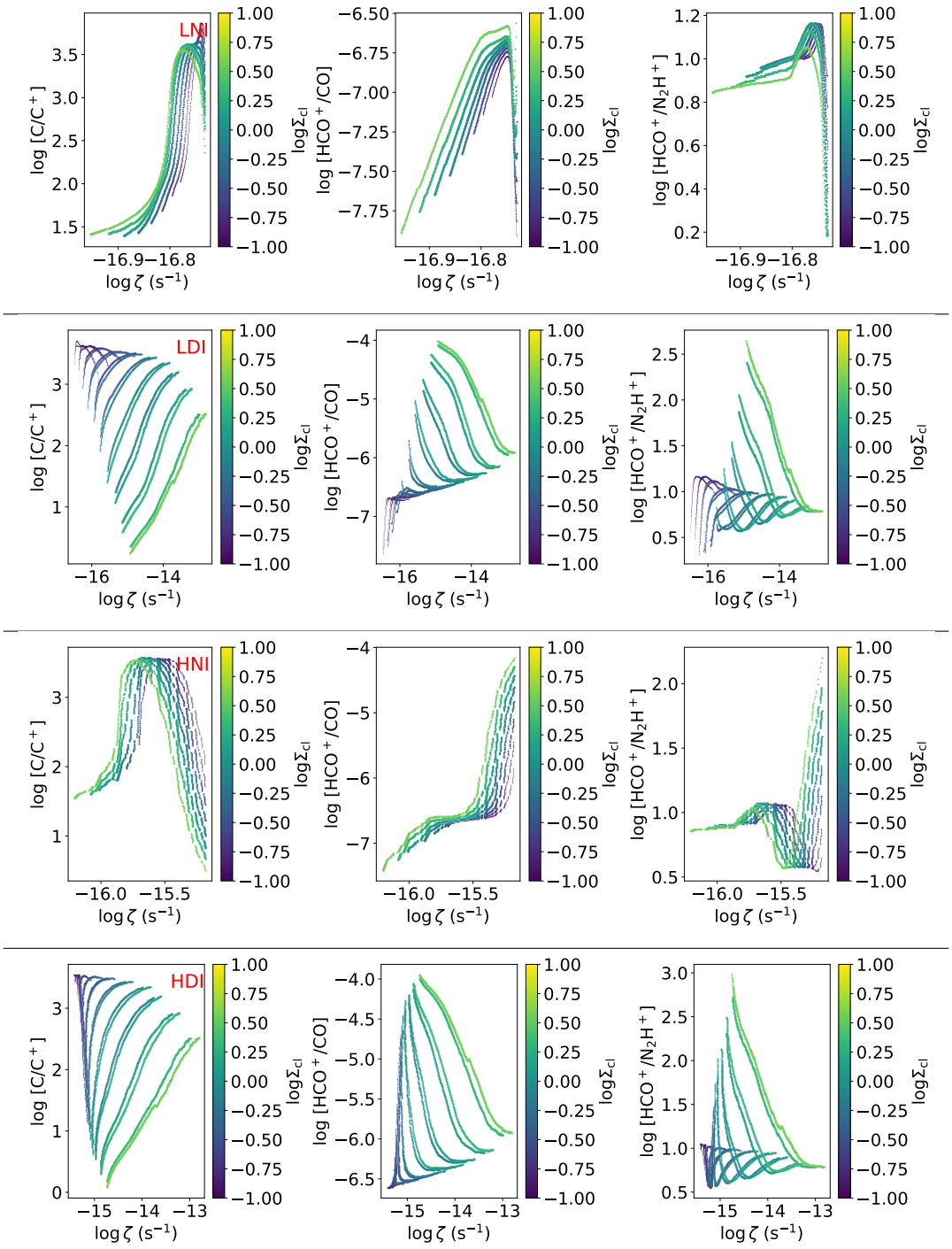

Figure 5.10. Cosmic ray ionization rate as a function of different abundance ratios. Left: C/C^+, middle: HCO^+/CO and right: HCO^+/N_2H^+. Models in descending order from top: LNI, LDI, HNI, HDI.

We do not fully solve the cosmic ray transport equations or the acceleration dynamics of protons in protostellar accretion shocks. We use analytic approximations to describe the acceleration of CRs at the protostellar shock and the transport out of both the parent core and cloud. Gaches and Offner [81] explore the changes in the CRIR for different transport regimes, shock efficiencies and magnetic fields. Differences in the protostellar magnetic field changes the maximum energy of the accelerated CRs but has little effect on the CRIR. However, the CRIR scales nearly linearly with the shock efficiency. Our results assume CR transport in the rectilinear regime through the core. More diffusive transport would produce higher temperatures at the surface of the core than observed. The details of the transport depend both on the magnetic field morphology and on the coupling between the particles and the field. In molecular clouds, turbulence is much stronger than in the cores allowing CRs to diffuse across magnetic field lines rather than streaming along them [15]. Conversely, if the particles are well-coupled their trajectories would follow the field lines, potentially producing asymmetries in the CR flux. The directionality imposed by the protostellar outflow could cause CR beaming in the outflow direction or simply advect the particles along with the outflow gas [208]. We assume CRs transport from their parent cores through the clouds by parameterizing the radial scaling by either diffusive ($1/r$) or free-streaming ($1/r^2$). We do not fully solve the transport equations, which has yet to be done for CRs propagating out of molecular clouds from internal sources.

5.5.2 Comparison to Observed CRIRs

Figure 5.11 shows the results from the different PDR models in Table 5.3 compared to four different observational surveys covering a range of $1 \leq A_V \leq 10^3$. The CRIR is one of the trickier astrochemical parameters to constrain from observations. Unfortunately, no universal method is applicable to all clouds conditions. Historically, there have been two main methods: absorption measurements of simple

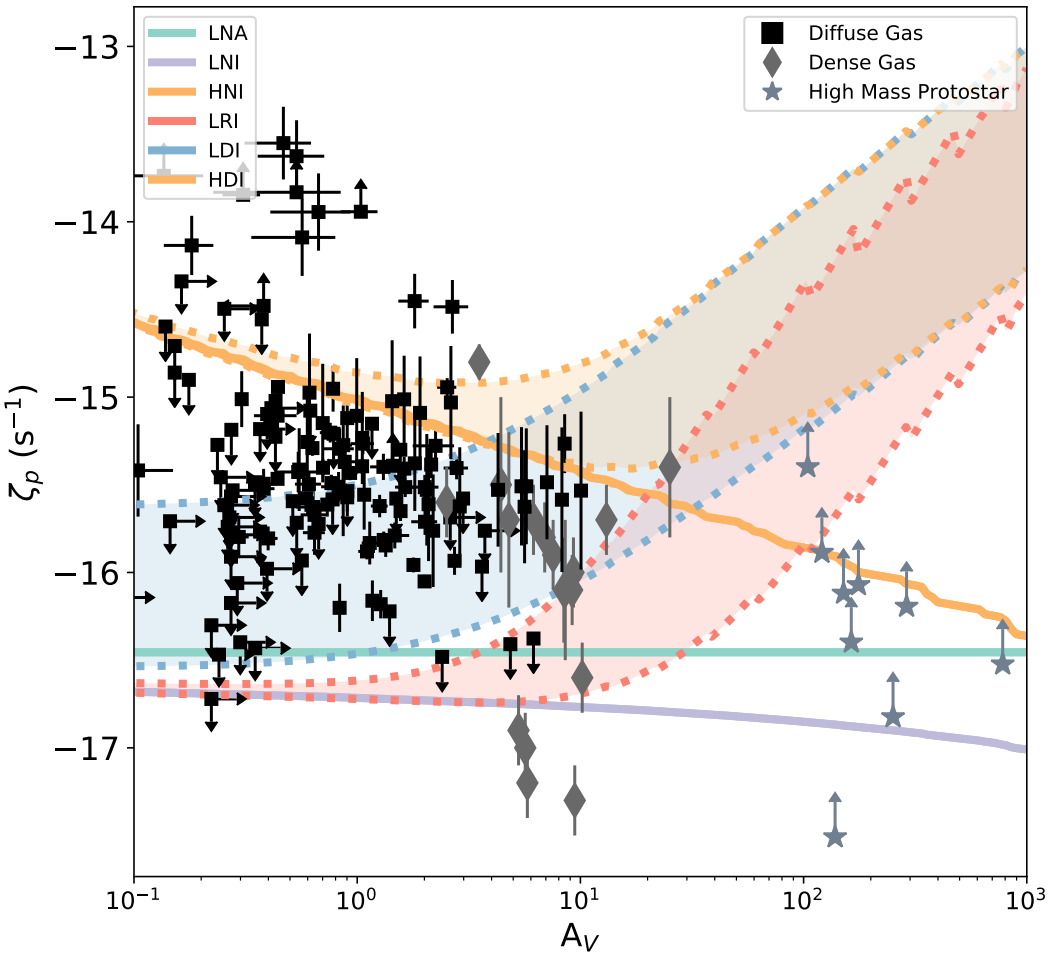

Figure 5.11. Cosmic ray ionization rate, ζ, versus A_V for the six different models in Table 5.3. The filled curves represent the 1σ spread from the models covering the ($\Sigma_{\rm cl}$ - N_*) parameter space. Squares represent diffuse gas measurements from Indriolo and McCall [257] and Indriolo et al. [170]. Diamonds represent dense gas measurements from Caselli et al. [235]. Crosses represent observations towards high-mass protostars from de Boisanger et al. [270], van der Tak and van Dishoeck [271].

ions, such as H_3^+ or OH^+, in the infrared or molecular line observations using key molecules in neutral-ion pathways along with astrochemical modeling. H_3^+ is typically thought to be among the best tracers of the CRIR due to its simple chemistry. However, H_3^+ is only observed in infrared absorption, limiting its use to sight lines with bright background sources. Indriolo and McCall [257] and Indriolo et al. [170] used H_3^+, H_2O^+ and OH^+ absorption to trace the CRIR in diffuse gas with $A_V < 1$ and found the CRIR in low A_V gas varies between 10^{-16} -10^{-14} s^{-1}. The gas at low A_V is particularly sensitive to external influences, motivating the need to model the chemistry with external CR spectra derived from examining the local galactic environment. The grouping of points at low A_V with high CRIR ($\zeta \geq 10^{-14}$ s^{-1}) are clouds in sight-lines towards the galactic center and thus in environments with extreme external particle irradiation. Caselli et al. [235] used a combination of HCO^+, DCO^+ and CO together with analytic chemistry approximations to infer the CRIR in 24 dense cores. Their observations exhibit a nearly bi-model distribution: some are clustered at $\zeta \lessapprox 10^{-17}\,s^{-1}$, while the majority are at $\zeta \approx 10^{-16}\,s^{-1}$. They infer the ionization rates using the abundance ratios of $[DCO^+/HCO^+]$ and $[HCO^+]/[CO]$ under 0D spatial assumptions and a reduced analytic chemical network. Finally, we include the CRIRs from the van der Tak and van Dishoeck [271] survey towards single high-mass protostars with the central protostar being massive enough to provide a bright background source for H_3^+ absorption. They find CRIRs scattered from 10^{-17} to 10^{-16} using an assumed H_3^+ abundance and density distribution. They find the observed H_3^+ column density increases with cloud distance, which can be explained by contamination from low-density clouds along the line of sight.

Our model results show good agreement with the inferred CRIRs from Indriolo and McCall [257], Indriolo et al. [170] and Caselli et al. [235]. We find the LDI model is able to replicate the spread in the CRIR. There are two main controlling factors for the CRIR in the clouds: the number of embedded sources and the cloud environment.

Embedded sources create a natural dispersion in ζ for different molecular cloud masses and star formation efficiencies. Without internal sources, there is no spread in our modeled CRIR as a function of column density. In order to represent the observations, the external CRIR must be increased instead for different regions. Local sources of CRs, such as nearby OB associations or supernova, contribute significantly to the CR flux at the cloud boundary. As the external CR flux is increased, the impact of attenuation also increases due to the rapid reduction in low energy CRs. Figure 5.11 shows that the impact of attenuation is different between the HNI and LNI models. For the LNI model, ζ changes by less than an order of magnitude across 4 orders of magnitude in A_V. Conversely, the HNI model CRIR decreases by 2 orders of magnitude due to an overall reduction in MeV-scale CRs. The HNI model over predicts the CRIRs measured in diffuse gas to CRIRs measured near high-mass protostars, excluding the galactic center sight-lines. However, the $\mathcal{H}$ spectrum is the maximal CR spectrum from Voyager-1 observations [212, 254]. The LNI and LNA models under-predict the observed CRIR for all but a few sight-lines. Thus, Figure 5.11 demonstrates that it is essential to consider the cloud environment and properly treat the CR physics and cloud density distributions. Models without attenuation only represent the CRIR within narrow ranges of A_V and not in the cloud interiors. Figure 5.11 also underscores that the low energy CR spectrum, which if often adopted in astrochemical modeling, is a poor fit to the majority of the observations.

5.5.3 Challenges for Deriving the CRIR from Chemical Diagnostics

There have been numerous attempts to find chemical diagnostics that are strong tracers of the CRIR [169, 170, 235, 257, 272, 273, 274]. Some of these, such as $[DCO^+]/[HCO^+]$, cannot be modeled with the current 3D-PDR version due to the lack of deuterium and isotopic chemistry. Most probes of the CRIR are based on the local abundance, which is difficult to directly ascertain from observations. The use of

column density ratios typically assumes the line emission observed between species is co-spatial. Figures 5.8 and 5.9 examine effects of CR physics on the [HCO^+/N_2H^+], [CO/C^+] and [C/C^+] column density ratio diagnostics. However, we find that none of these ratios are monotonically sensitive to the average CRIR, shown for the LDI model in Figure 5.5. The [CO/C^+] column density ratio is anti-correlated with the density-averaged CRIR because the amount of CO declines while the amount of C^+ increases in large, massive clusters.

Local abundance ratios are used for fitting observations with astrochemical models which assume the ratio of the column densities is equal to the ratio of the abundances [257]. These are constrained through the use of 0-D spatial models, where a single density, temperature and extinction are evolved over time. However, this ignores the physical structure of clouds, which have non-uniform density, temperature, FUV and, as we show here, CRIR distributions [90, 111, 116, 275, 276]. As Figure 5.10 shows, in models without internal sources, none of the abundance ratios are strong diagnostics. Furthermore, the range in the CRIR is small despite some large changes in each of the ratios. For models with internal sources, the CRs from embedded sources dominate the chemistry throughout the cloud. Here, we find the ratios of C/C^+ and HCO^+/CO are mostly monotonic with the CRIR. However, there is significant variation with $\Sigma_{\rm cl}$ and thus with the gas mass. The results signify that more careful physical and chemical modeling needs to be done to accurately constrain the CRIR in high-surface density, star-forming regions. The ratios are only a good diagnostic in regions where CRs dominate the thermo-chemistry.

Recently, Le Petit et al. [175] used H_3^+ absorption to infer the CRIR and physical conditions in the CMZ. They used a similar relation to Equation 5.8:

$$N(H_3^+) = 0.96\frac{\zeta L}{k_e}\frac{f}{2x_e}, \tag{5.11}$$

where k_e, f, and x_e have the same definition as in Equations 5.8 and 5.9 and L is the size of the cloud. They fit observed H_3^+ column densities with PDR models as a function of the gas density, n_H, and the size of the cloud, L. Most sight-lines are well fit using their method by clouds with densities $10 \leq n_H \leq 100$ cm^{-3} corresponding to $5 \lesssim L \lesssim 100$ pc. Our models suggest that these length scales would incur CR screening effects which would change the CRIR. Similarly, for the high density clouds, the energy losses will deplete MeV CRs and reduce the CRIR. In these cases, there is a further degeneracy in the $n_H - L$ plane resulting in an average decrease in the CRIR. The reduction would systematically produce model fits with lower densities to correct for the lower CRIR.

Rimmer et al. [277] used a similar hybrid approach, adopting a prescription for $\zeta(N)$ ad-hoc with the MEUDON PDR code [31] to model the Horsehead Nebula. They found their high $\zeta(N_H)$ model improved agreement over standard constant CRIR PDR prescriptions. However, their treatment of $\zeta(N)$ is static and fixed in time. The decoupling of CR attenuation and chemistry is only a good approximation if the abundance of neutral Hydrogen (H, H_2) does not change much in time, ensuring that the CR spectrum is constant in time. The new approach presented here will allow $\zeta(N)$ to be connected to the chemical time evolution.

5.5.4 Impact of Cosmic Ray Feedback on Cloud Chemistry

The *Herschel* Galactic Observations of Terahertz C+ (GOT C+) [278] survey mapped [C II] 158 μm emission over the whole galactic disk, providing the best constraint on where [C II] emission originates. Pineda et al. [278] found that nearly half of the [C II] emission originates from dense photon dominated regions with about another quarter of the emission from CO-dark H_2 gas. Clark et al. [279] performed synthetic observations of young simulated molecular clouds and found the majority of their [C II] emission originates from atomic-Hydrogen dominated gas. This dis-

crepancy was explained by the time evolution of molecular gas due to star formation and feedback. The results presented here provide an complementary explanation for the [C II]-bright molecular gas. When protoclusters become active, they accelerate CRs into the densest regions of molecular clouds. Figure 5.6 shows that high-mass protoclusters will lead to [C II]-bright H_2 dominated gas since CRs i) increase the gas temperature to values closer to the [C II] excitation temperature of 91.2 K, ii) increase the abundance of C^+ in dense gas due to the destruction of CO and iii) do not significantly alter the abundance of H_2.

In local star-forming regions, the lowest inversion transitions of ammonia, NH_3, have been widely used to map the dense gas cores within molecular clouds [i.e., 99, 280, 281, 282]. Ammonia remains optically thin, and while it does suffer from depletion, it's formation is enhanced in regions where CO freezes out [283] (although this effect is not included in our models). However, this also makes ammonia much more susceptible to local variations in the FUV radiation field, temperature and CRIR. Recently, the Green Bank Ammonia Survey (GAS) mapped all the Gould Belt clouds with $A_V > 7\,\mathrm{mag}$ [38]. The DR1 data show the line-of-sight averaged abundance, $X(NH_3) = N(NH_3)/N(H_2)$, exhibits a spread through molecular clouds. The spread could be caused by the porosity of molecular clouds allowing more FUV radiation into regions of dense gas. However, our 1D models also exhibit a variation in this abundance measurement for the models with internal sources (LRI, LDI and HDI). Figure 5.6 shows that ammonia is depleted in clusters exhibiting more embedded star formation by a couple of orders of magnitude. The abundance within the dense gas goes from 10^{-8} in small clusters to 10^{-10} in the largest. Furthermore, the gas also heats up leading to stronger emission in higher transitions, such as $NH_3(3,3)$. Redaelli et al. [284] examined the NH_3 GAS map of the Barnard 59 clump in more detail. They found that the abundance appears to drop in gas around the central central 0/1

protostar. The dust temperature shows a clear increase around the same source with a slight increase in the ammonia excitation temperature.

5.5.5 Impact of Cosmic Ray Feedback on Chemistry in Dense Cores

Protostars are observed to be dimmer than classic collapse models predict, i.e., the "Protostellar Luminosity Problem" [42]. One possible solution is that accretion is strongly episodic [50, 285, 286]. Although our models assume steady-state accretion, we can infer the impact of large bursts of accretion on cloud chemistry. An accretion burst leads to a stronger accretion shock, which in turn produces higher energy CRs and a higher CRIR. The CRIR increase in the dense gas then raises the temperature. The higher temperatures, whether caused by radiative or CR heating, lead to several different chemical effects. First, molecules frozen onto dust grains will evaporate, both by thermal desorption [287] and CR-induced desorption [288], into the gas phase. Second, the increase of the CRIR will increase the ionization fraction leading to a chain of ion-neutral reactions following H_3^+. Finally, the elevated radiative and CR flux may be strong enough to destroy some molecules. Jørgensen et al. [269] and Frimann et al. [289] showed that episodic accretion can cause the sublimation of CO-ice and explain the excess $C^{18}O$ emission observed near protostars. Intuitively, a burst a CRs will lead to a reaction chain: H_3^+ is created, thereby leading to the destruction of CO to form HCO^+. However, the increase in CRs will provide a large population of free electrons which recombine with HCO^+ to form CO. HCO^+ also interacts with water and other dipole neutrals (in the case of water, the reaction leads to the formation of CO and protonated water). HCO^+ is observed to be depleted near protostars that have undergone episodic accretion [268]. Ices sublimated by an accretion burst will cause a more active gas-phase chemistry and lead to an increase in carbon-chain molecules in molecular clouds as well as increase gas-phase CO in the dense gas where it would otherwise freeze-out. Overall, the addition of CRs magnifies the effect of an

accretion burst. Temperatures increase beyond that expected from radiative heating alone. This suggests that a smaller change in accretion rate may be needed to produce the observed chemical changes.

5.5.6 Implications for Comparing Data and Models

Synthetic observations of hydro-dynamic simulations are a vital tool for comparing theoretical predictions to observations. The synthetic observations may treat the chemistry in different ways: from assuming a constant abundance of some molecule to post-processing simulations with an astrochemical code or using the reduced-network chemistry from the hydrodynamic simulation [see review by 290]. These synthetic observations are used to gauge how well the simulations correspond to the observed universe. As such, it is paramount to ensure that all astrochemical parameters are as accurate as possible. Radiation-MHD simulations can provide the density and temperature at every point [e.g., 61]. Simulations also now often include FUV radiation and optical depth calculations using packages such as Fervent [291], TreeRay [292] and Harm^2 [293]. These methods can provide the FUV radiation and/or optical depth into the cloud. Our results, here, show that the H_2 optical depth into the cloud should be considered when calculating the appropriate CRIR for post-processing. Typically, the CRIR is held constant throughout the entire simulation domain, which will lead to systematic differences in the simulation line emission.

5.6 Conclusions

We implement cosmic-ray attenuation in the public astrochemistry code 3D-PDR. The implementation uses the H_2 column density from the chemistry to attenuate the CR spectra. We couple the code to the protostellar CR models from Gaches and Offner [81], which solve for the total attenuated protocluster CR spectrum as a function of the cloud surface density, $\Sigma_{\rm cl}$, and number of constituent protostars, N_*.

We present one-dimensional astrochemical models for molecular clouds with a wide range of $\Sigma_{\rm cl}$ and N_*. We compare the abundance distributions for a low external CR spectrum, representing an extrapolation of the Voyager-1 data, and a high external CR spectrum, representing a maximal correction for solar influences. Our model results show that CRs originating from the accretion shocks of protostars affect the chemistry of the surrounding molecular cloud. We conclude the following:

- Models with no sources or attenuation cannot explain observed CRIRs. Models with no internal sources but a higher ($\mathcal{H}$) external spectrum (HNI) match the observed CRIRs, although it may under-predict the CRIRs inferred for high-mass protostars. We find that a model using the commonly adopted spectrum with internal sources (LDI) matches both the low and mid A_V observations of ζ and the observed spread.

- CRs accelerated by protostellar accretion shocks significantly alter the Carbon chemistry in star-forming clouds. The amount of neutral and ionized Carbon increases in the dense gas as the number of protostars increases. Models with embedded sources (LDI, LRI, HDI) increase the amount of C, HCO^+ and NH_3 at lower A_V and decrease the abundance of CO and NH_3 at higher A_V. Overall, models including internal sources (LDI, LRI and HDI) exhibit a higher abundance of HCO^+ and H_3^+ with $\Sigma_{\rm cl}$ and N_*.

- Approximations that use H_3^+ and C-based tracers to estimate the CRIR systematically under-predict the CRIR unless CRs are the dominant source of ionization. The Reduced Analytic Approximation, which uses the abundances of H_3^+, CO and O,always produces more accurate values of the CRIR, highlighting the importance of obtaining accurate oxygen and carbon monoxide abundances within molecular clouds.

- Ions are systematically under produced using the canonical CRIR while CO is over produced. Internal sources created a dispersion in the distribution of column densities by driving more active ion-neutral chemistry deep within molecular clouds.

- Models using the low external CR spectrum ($\mathcal{L}$) and/or no internal sources of CRs under estimate the H_3^+ column density by a order of magnitude or more.

- Internally-accelerated CRs will naturally lead to molecular gas which become CO-deficient but [C II]-bright, particularly for high surface density molecular clouds hosting large clusters.

- Including CR attenuation in PDR models will help break the degeneracy in astrochemical modeling between the density, CRIR and FUV radiation.

As protoclusters grow in constituent numbers, the impact on the chemistry is amplified, greatly so if CRs diffuse out of molecular clouds rather than stream. Comparison to observed CRIRs suggest the external CR spectrum, attenuation and internal sources are important for modeling the chemistry of molecular clouds. However, the current uncertainties are large due to lack of observational data that can simultaneously constrain the density, FUV radiation and CRIR on molecular cloud scales. Observations to constrain the CRIR within dense gas necessitate multi-line data, to independently determine the temperature as in e.g., [86], and multi-species data, to act as astrochemical diagnostics as in e.g., [235]. The 3D-PDR CR attenuation FORTRAN module can be included in any FORTRAN astrochemistry code.

CHAPTER 6

THE ASTROCHEMICAL IMPACT OF COSMIC RAYS IN PROTOCLUSTERS II: CO-TO-H_2 CONVERSION FACTOR

This chapter[1] focuses on the CI-to-H_2 and CO-to-H_2 conversion factors and the impact different cosmic ray models have on them.

6.1 Abstract

We utilize a modified astrochemistry code which includes cosmic ray attenuation in-situ to quantify the impact of different cosmic-ray models on the CO-to-H_2 and CI-to-H_2 conversion factors, $X_{\rm CO}$ and $X_{\rm CI}$. We consider the impact of cosmic rays accelerated by accretion shocks, and we show that in clouds with star formation efficiencies greater than 2% have $X_{\rm CO} = (2.5 \pm 1) \times 10^{20}$ cm^{-2}(K km s^{-1})$^{-1}$, consistent with Milky Way observations. We find that changing the surface cosmic ray ionization rate from the canonical $\zeta \approx 10^{-17}$ to $\zeta \approx 10^{-16}$ s^{-1} reduces $X_{\rm CO}$ by 0.2 dex for clusters with surface densities below 3 g cm^{-2}. $X_{\rm CI}$ has been proposed as an alternative to $X_{\rm CO}$ due to its accessibility and brightness at high redshifts. Our canonical models exhibit $X_{\rm CI} \geq 4 \times 10^{21}$ cm^{-2} (K km s^{-1})$^{-1}$. However, the inclusion of internal sources leads to 1.2 dex dispersion in $X_{\rm CI}$ ranging from $2 \times 10^{20} < X_{\rm CI} < 4 \times 10^{21}$ cm^{-2} (K km s^{-1})$^{-1}$.

[1]These results are based on Gaches et al. (2019, sub.)

6.2 Introduction

Studying the properties of molecular clouds is crucial to understand star formation [39]. The dominant constituent of molecular clouds is molecular hydrogen, (H_2), which is a perfectly symmetric molecule, rendering it largely invisible at the typical temperatures of molecular clouds. While observable in ultraviolet absorption against background sources, it can only be detected via emission in environments where the gas is excited to temperatures above a few hundred Kelvin. The second dominant species is neutral helium which remains inert in molecular clouds. Therefore, observational studies of molecular clouds largely rely on tracer species, namely emission from dust and molecules. The most important of these tracers is carbon monoxide (CO) [36]. CO has a relatively high abundance, canonically [CO/H_2] $\approx 10^{-4}$ [14], making it the most abundant molecule after H_2 . The small dipole moment allows it's rotational transitions to be easily excited at the cold temperatures of molecular clouds. A crucial CO observable is the J = (1-0) rotational transition at 115.27 GHz.

It is common for the emission of the lowest rotational transition of CO to be used to measure the total molecular gas [36]. This is encoded in CO-to-H_2 conversion factor, $X_{\rm CO}$, and the related quantity $\alpha_{\rm CO}$. $X_{\rm CO}$ is defined as:

$$X_{\rm CO} = \frac{N(\rm H_2)}{W_{\rm CO}(J = 1 - 0)}, \tag{6.1}$$

where $N(\rm H_2)$ is the H_2 column density in cm^{-2} and $W_{\rm CO}(J = 1 - 0)$ is the CO flux in K km s^{-1}. The fiducial Milky Way (MW) value is $X_{\rm CO,MW} = 2 \times 10^{20}$ cm^{-2} (K km s^{-1})$^{-1}$ [36]. This conversion factor has been used to estimate gas mass in local, resolved studies of MCs and the molecular gas mass in high redshift galaxies [e.g. the COLDz survey 294]. A significant number of studies, both observational and theoretical, have been devoted to measuring, modeling or applying $X_{\rm CO}$. Prior work shows it varies with density, metallicity [28, 92, 153, 155, 295], cosmic ray (CR) ionization rate (CRIR) [28, 113, 152, 154, 295, 296, 297] and the radiation field

[28, 92, 113, 148, 152, 153, 155, 295, 298]. Previously, Gaches and Offner [148] found that far ultraviolet radiation feedback from forming stars can reproduce the higher $X_{\rm CO}$ values measured towards diffuse star-forming clouds in the outer galaxy.t

Traditional one-dimensional photo-dissociation region (PDR) models have long predicted that neutral carbon will exist only in a thin transitional layer between ionized carbon and CO [14]. However, observations show that forbidden line emission from neutral carbon covers similar spatial extents as CO [e.g. 135, 137, 299]. It is posited that forbidden line emission from neutral carbon is a good tracer of the gas mass [110, 111, 112, 295]. Synthetic observations of hydrodynamic simulations show that $X_{\rm CI}$ has a smaller dispersion than $X_{\rm CO}$ within a molecular cloud and is a better tracer in low metallicity gas which tends to become CO-dark [111, 112, 295]. Observational studies using $X_{\rm CI}$ as a tracer of gas mass performs as well as $X_{\rm CO}$ [299]. $X_{\rm CI}$ is defined analogously to $X_{\rm CO}$:

$$\mathrm{X_{CI}} = \frac{\mathrm{N(H_2)}}{\mathrm{W(CI)}_{609\,\mu\mathrm{m}}} \ \ \mathrm{cm^{-2}\,(K\,km\,s^{-1})^{-1}} \tag{6.2}$$

where $W(\mathrm{CI})_{609\,\mu\mathrm{m}}$ is the integrated flux at 609 μ m.

Gaches et al. [232] (hereafter Paper I) presented a modified astrochemical code which includes CR attenuation in-situ. Paper I included CRs accelerated by accreting, embedded protostars and CR attenuation in one-dimensional astrochemical models of molecular clouds. We used the code to study the impact of changing the CR spectrum due to differing galactic environments and the effects of embedded CR sources for a subset of species including CO, HCO^+ and N_2H^+ and tested various prescriptions for constraining the CRIR. We found that ions are enhanced and neutrals are depleted in dense gas due to embedded CRs. Carbon chemistry is substantially altered depending on the assumed CR model: CRs produced by embedded sources create a significant reservoir of atomic carbon, mostly neutral, in dense gas. Embedded CRs reduce the amount of CO in clouds and warm the gas to over 30 K. In this letter we investigate

the impact of the above effects on $X_{\rm CI}$ and $X_{\rm CO}$. In §5.3 we describe the methods used in this paper. In §5.4 we present the results and discuss the implications for observations.

6.3 Methods

We use the same astrochemical models from Paper I and summarize the methodology here. See Paper I for further details.

We generate synthetic protoclusters assuming the Tapered Turbulent Core [50] accretion model following the method described in Gaches and Offner [148]. We directly sample from the bi-variate protostellar mass distribution using the method of conditional probabilities. Each molecular cloud is described by a gas surface density and number of constituent protostars, $\Sigma_{\rm cl}$ and N_*, respectively. We only consider models where the star formation efficiency, $\varepsilon_g = M_*/M_{\rm gas} \leq 50\%$.

We calculate the accelerated proton spectrum due to accretion shocks for each star in the protocluster. CR protons are assumed to be accelerated via Diffuse Shock Acceleration (DSA) [reviewed by 211, 250] near the surface of the protostar. DSA predicts a power law spectra in momentum space, $j(p)$, with an injection momentum, $p_{\rm inj}$, set by the shock gas temperature and a maximum energy constrained by collisional energy losses and upstream diffusion [81]. The CR flux spectrum is

$$j(p) = j_0 \left(\frac{p}{p_{\rm inj}} \right)^{-a}, \tag{6.3}$$

where j_0 is the normalization constant calculated from the total shock energy and efficiency, and a is set by the shock compression factor. We find that the maximum proton energy is typically between 1 - 10 GeV [81]. We attenuate the CRs by the gas surface density out of each protostellar core, $\Sigma_{\rm core} = 1.22\Sigma_{\rm cl}$, following Padovani et al. [171]. We assume the CRs within the core free-stream outwards since shallower

attenuation produces too much CR heating in the core (see Gaches and Offner 81). CRs may also be attenuated by the accretion flow (Offner et al. 2019, sub.), although we do not include this in the model. The total number of CRs escaping into a natal molecular cloud embedding a protocluster is the sum of the CRs accelerated by the individual protostars and then attenuated into the surrounding gas: $j_{\rm cluster}(E) = \sum_i^{N_*} j_i(E)$.

We embed the protoclusters in the center of one-dimensional molecular clouds with a density profile, $n(r) = n_0(R/r)^2$. We set the outer density to $n_0 = 100$ cm^{-3}, and the radius, R is determined by the total column density, $\mu m_H N(R) = \Sigma_{\rm cl}$. We utilize a modified version of the photo-dissociation region astrochemistry code 3D-PDR described in Paper I[2], which includes CR attenuation in-situ. The astrochemistry code uses CR spectra at the surfaces of the gas model as inputs, rather than a global CRIR. It is not known exactly how CRs transport through molecular clouds. Therefore, we consider two different transport regimes: diffusive (1/r) and rectilinear (1/r^2). We use the two external CR spectra from Ivlev et al. [212]: a model that extrapolates the Voyager 1 data, $\mathcal{L}$, and one that attempts to account for modulation from interstellar gas, $\mathcal{H}$.

We also consider the impact of FUV radiation, and we irradiate the external surface of the molecular cloud with the interstellar radiation field from Draine [119]. We model the chemistry with the gas-phase UMIST12 network [18], which includes 215 species and several thousand reactions. The network does not include gas-grain reactions, freeze-out or any desorption processes. We consider the six different CR models listed in Table 3.2.

3D-PDR calculates the CO line-integrated emissivity, ϵ, for the J-ladder from J=0 to J=41 assuming non-local thermodynamic equilibrium and the CI 609 μm emissivity

[2]The code is public at `https://uclchem.github.io/3dpdr.html`

Table 6.1. Models examined. L/H denotes Low/High external spectrum, NI denotes no internal sources, DI denotes internal sources with $a = 1$ (diffusive transport), RI denotes internal sources with $a = 2$ (rectilinear transport) and NA denotes no internal sources or CR attenuation.

Name	Source Transport	Internal	External Field	Attenuation
LDI	r^{-1}	✓	$\mathcal{L}$	✓
LRI	r^{-2}	✓	$\mathcal{L}$	✓
LNI	...	...	$\mathcal{L}$	✓
LNA	...	...	$\mathcal{L}$	...
HNI	...	...	$\mathcal{H}$	✓
HDI	r^{-1}	✓	$\mathcal{H}$	✓

using an escape probability method to account for the line opacity. We calculate the line flux from the emissivity:

$$I = \frac{1}{2\pi} \int_0^R \epsilon \, dz \quad (\mathrm{erg\,s^{-1}\,cm^{-2}\,sr^{-1}}), \tag{6.4}$$

with

$$W = \frac{1}{10^5} \frac{c^3}{2 k_b \nu^3} I \quad (\mathrm{K\,km\,s^{-1}}), \tag{6.5}$$

where c is the speed of light, k_b is Boltzmann's constant and ν is the line frequency. We calculate the H_2 column density from the astrochemical models

$$N(\mathrm{H_2}) = \int_0^R x(\mathrm{H_2})\, n_H \, dz, \tag{6.6}$$

where $x(H_2)$ is the abundance of H_2 and n_H is the gas density. Finally, we compute X_{CO} using Equation 6.1.

6.4 Results and Discussion

We present the results from the astrochemical models on the CO-to-H_2 and CI-to-H_2 conversion factors here. A more general discussion on the astrochemical impact of CRs accelerated within protoclusters is presented in Paper I.

6.4.1 Effect of Cosmic Rays on $X_{\rm CO}$

Figure 6.1 shows the CO-to-H_2 conversion factor as a function of $\Sigma_{\rm cl}$ and ε_g for four of the CR models in Table 3.2. We plot $X_{\rm CO}$ normalized to the fiducial MW value $X_{\rm MW} = 2 \times 10^{20}$ [36]. The behavior of $X_{\rm CO}$ changes significantly with the assumed CR model. $X_{\rm CO}$ varies only as function of $\Sigma_{\rm cl}$ for models without internal sources, LNI and HNI. There is a 0.2 dex offset in $X_{\rm CO}$ between the LNI and HNI models for $\Sigma_{\rm cl} < 3$ g cm^{-2} owing to increased temperatures at low A_V in model HDI. The decline in $X_{\rm CO}$ at higher $\Sigma_{\rm cl}$ is the result of a larger turbulent line width because of two cooperating effects. First, there is a higher temperature due to the increasing importance of turbulent heating. Second, the turbulent linewidth produces brighter optically thick CO emission.

In models with CRs that attenuate diffusively, LDI and HDI, $X_{\rm CO}$ becomes a sensitive function of ε_g, losing much of the dependence on $\Sigma_{\rm cl}$. $X_{\rm CO}$ is reduced by up to 0.5 dex due to embedded sources with the lowest values occurring for the highest star formation efficiencies. It is important to emphasize that CRs from embedded sources do little to reduce the overall amount of H_2 [Paper I]. However, they cause two effects which act to decrease $X_{\rm CO}$. First, while they reduce the amount of CO in deeply embedded regions of the cloud, they cause an enhancement of CO in low A_V gas. Second, the increased CRIR leads to a higher temperature making the CO emission brighter overall.

CR and FUV feedback from star formation external to the molecular cloud can be modeled by scaling their intensity linearly with the star formation rate (SFR) [160]. This is motivated by the relationship between the supernova rate and the SFR and implicitly assumes that CRs are mainly accelerated in supernova shocks. Clark and Glover [152] used these relations to model how the SFR affects $X_{\rm CO}$ in simulated molecular clouds. They found that $X_{\rm CO}$ increases with the SFR if the cloud properties remain fixed. The increase of $X_{\rm CO}$ with SFR is very weak if the

density of the cloud scales with the SFR. Bisbas et al. [154] modeled the effect of enhanced CRs on the [CO/H_2] ratio, emulating different environments. They show that [CO/H_2] decreases substantially with an increase in the CRIR. By construction, these models only account for variations in the external CR flux and neglect CRs accelerated within protoclusters due to accretion, jets or stellar winds.

6.4.2 Effect of Cosmic Rays on $X_{\rm CI}$

Forbidden line emission from neutral carbon is a possible tracer for molecular gas, as discussed above. Figure 6.2 shows $X_{\rm CI}$ as a function of $\Sigma_{\rm cl}$ and ε_g. $X_{\rm CI}$ shows the same qualitative trends as $X_{\rm CO}$, although it is more sensitive to the CRIR: a spread of 1.2 dex in $X_{\rm CI}$ and 0.5 dex in $X_{\rm CO}$ for the LDI model.. The canonical model, LNA, exhibits a maximum value of $X_{\rm CI} \geq 4 \times 10^{21}$ cm^{-2} (K km s^{-1})$^{-1}$. Models using the high, $\mathcal{H}$, spectrum, HNI and HDI, exhibit a 0.2-0.8 dex reduction in $X_{\rm CI}$ compared to LNI and LDI, respectively.

The increased CRIR throughout the cloud causes atomic carbon to exist outside a thin transition layer. Atomic carbon is formed in the dense gas through the destruction of CO by He^+:

$$\mathrm{He} + \mathrm{CRP} \rightarrow \mathrm{He}^+ + \mathrm{e}^-$$

$$\mathrm{He}^+ + \mathrm{CO} \rightarrow \mathrm{He} + \mathrm{O} + \mathrm{C}^+$$

with neutral carbon forming from recombination of C^+. Neutral carbon is also the result of direct dissociation of neutral molecules by CR protons and CR-generated photons. This enhancement leads to a reduced $X_{\rm CI}$. Embedded sources cause $X_{\rm CI}$ to decrease by over an order of magnitude across two orders of magnitude increase in the star formation efficiency.

Neutral carbon emission is easily observable at high redshifts due to the line shifting to millimeter wavelengths. Starburst galaxies have higher SFRs producing

extreme environments and more CO-dark gas [113, 295]. Thus, at high redshifts and in galaxies undergoing starbursts, CI may become an optimal tracer of molecular gas.

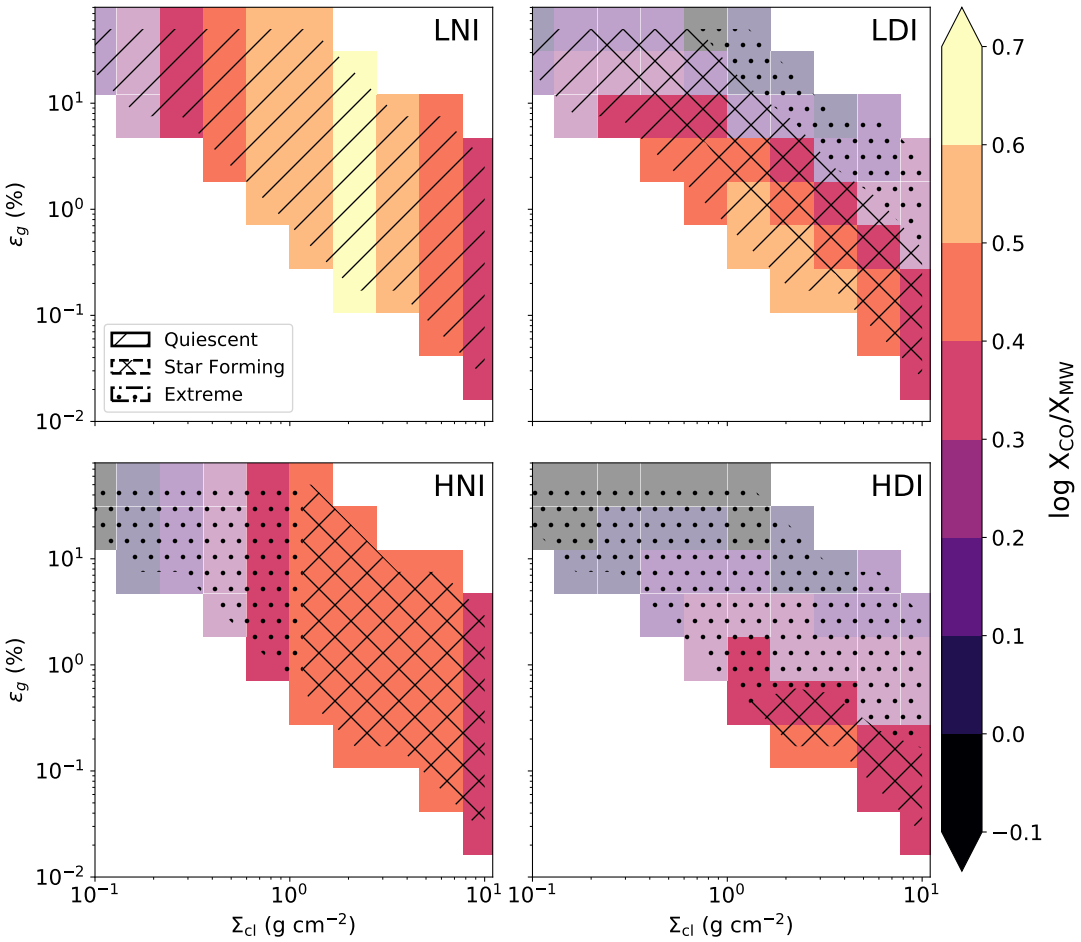

Figure 6.1. Color shows $\log X_{\rm CO}/X_{\rm MW}$ where $X_{\rm MW} = 2 \times 10^{20}$ cm^{-2} (K km s^{-1})$^{-1}$ as a function of gas surface density, $\Sigma_{\rm cl}$, and star formation efficiency, ε_g. White shaded cells show regions where $\rm X_{CO}$ is consistent with Milky Way observations, $-0.3 \geq \log X_{\rm CO}/X_{\rm MW} \leq 0.3$. The hatched regions indicate different cosmic-ray environments, where we define $\langle\zeta\rangle_x$, the spatially-averaged CRIR, $\langle\zeta\rangle_x < 10^{-16}$ as "quiescent", $10^{-16} < \langle\zeta\rangle_x < 10^{-15}$ as "star forming" and $\langle\zeta\rangle_x > 10^{-15}$ as "extreme."

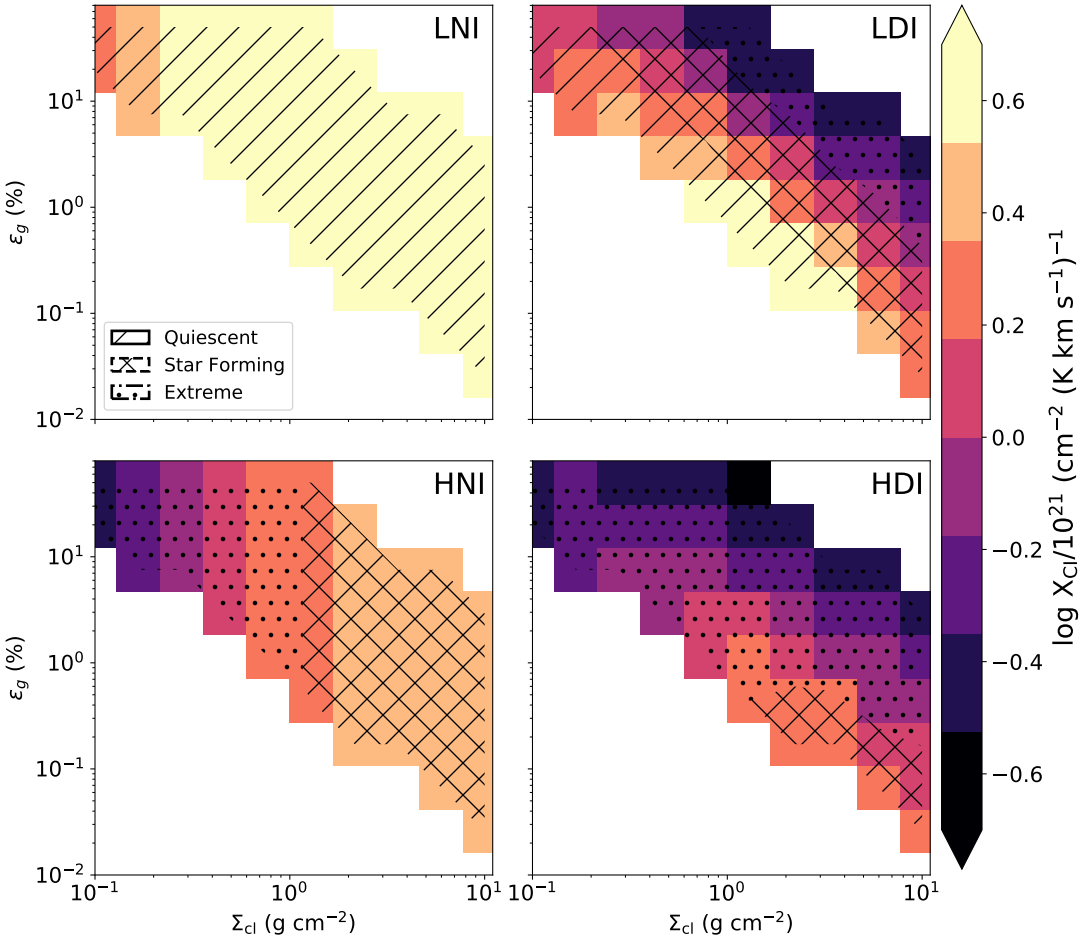

Figure 6.2. Same as Figure 6.1 but for $\log X_{\rm CI}/10^{-21}$.

6.4.3 Statistical Trends

Figure 5.7 statistically summarizes the impact of the various CR models on $X_{\rm CI}$ and $X_{\rm CO}$. The violin plots show the distribution of the logarithmic difference between $\rm X_i$ as calculated with the canonical model, LNA, and each of the CR models in Table 3.2 using the clouds across the $\Sigma_{\rm cl}-\varepsilon_g$ space as samples. These distributions represent the impact on $X_{\rm CO}$ when CR attenuation or embedded sources are neglected. We find

very little deviation in $X_{\rm CO}$ for the LNI model compared to the LNA model. The HNI model shows that $X_{\rm CO}$ will be over-estimated by 0.15 dex in calculations using the often-assumed CRIR of $\zeta \approx 10^{-17}$ s^{-1}. CRs from embedded sources, which propagate via diffusion, decrease $X_{\rm CO}$ for all clouds. Furthermore, there is a substantial spread due to variation with the number of protostars, N_*. The HDI model logarithmic difference exhibits a dispersion of 0.3 dex, similar to the spread derived from MW observations [36]. If CRs from embedded sources transport via free-streaming there is no impact on $X_{\rm CO}$ because the CRIR is lower and dominated by the CRs originating from external sources rather than internal.

The $X_{\rm CI}$ distributions in the left panel of Figure 5.7 show much greater sensitivity to the CR model assumptions. Models that differ from the often-assumed canonical models show, on average, a 0.5 dex change in $X_{\rm CI}$. $X_{\rm CI}$ decreases by 0.5 dex in model HNI, for massive and inefficient star forming regions. Embedded CRs lead to more drastic effects on $X_{\rm CI}$ than on $X_{\rm CO}$. In the case of a "Quiescient" CR environment, CRs from embedded sources have a larger impact on $X_{\rm CI}$. The inclusion of CRs from embedded sources in extreme star-forming environments, represented by HDI, reduces $X_{\rm CI}$ by nearly a dex compared to the canonical model.

6.4.4 Comparisons to Galactic-scale Observations

The hatching in Figure 6.1 denotes different CR environments: "Quiescent" regions with $\langle\zeta\rangle_x < 10^{-16}$ s^{-1}, "Star Forming" regions with $10^{-16} < \langle\zeta\rangle_x < 10^{-15}$ s^{-1} and "Extreme" regions with $\langle\zeta\rangle_x > 10^{-15}$ s^{-1} where $\langle\zeta\rangle_x$ is the spatially-averaged CRIR. These labels are motivated by observational surveys which show the majority of pointings through diffuse gas have $10^{-15} < \zeta < 10^{-16}$ s^{-1}. Low A_V observations where $\zeta > 10^{-15}$ s^{-1} are primarily sight-lines towards the galactic center [170, 257].

There have been numerous observational studies measuring $X_{\rm CO}$ in different environments within the MW and other galaxies [see 36, and citations within]. Remark-

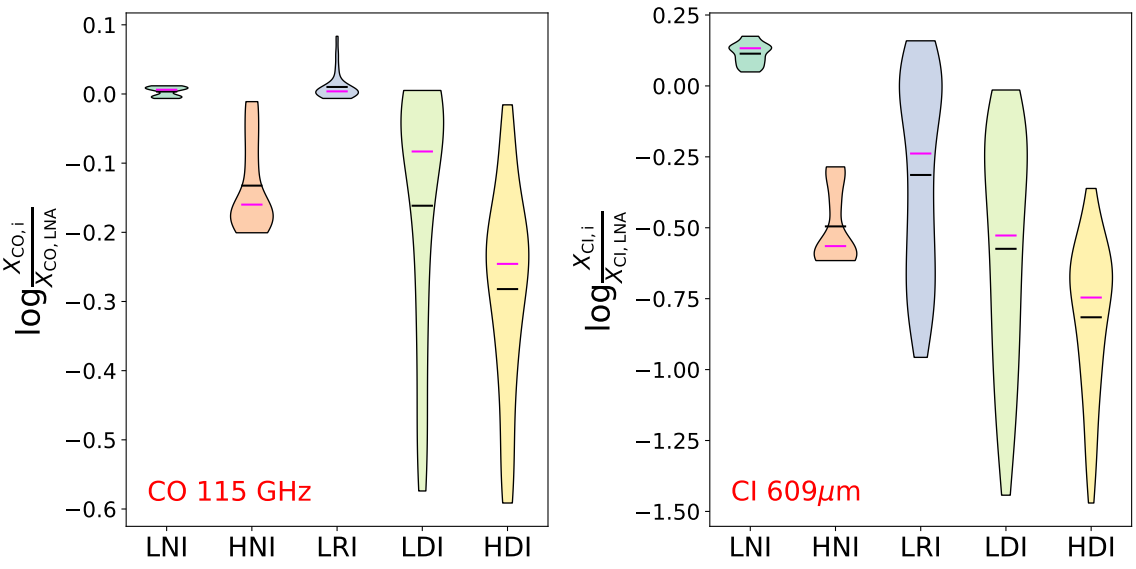

Figure 6.3. Logarithm of the ratio of X_{CO} and X_{CI} for a given cosmic-ray model $i \subset$ (LNI, HNI, LRI, LDI, HDI) compared to model LNA. Black line indicates the mean. Magenta line indicates the median.

ably, in the MW and many of the Local Group galaxies, X_{CO} is relatively constant on kpc scales. The consistency of X_{CO} in the MW and Local Group can be explained by similar molecular cloud properties due to star-formation feedback [155]. There is a general trend in star-forming galaxies of low values of X_{CO} towards the center and larger values in the outer disk [187]. The white shading in Figure 6.1 shows where X_{CO} is consistent with the MW average value and spread. Models without embedded sources, LNI and HNI, are only consistent with the MW value for $\Sigma_{cl} < 0.2$ g cm^{-2} and $\Sigma_{cl} < 0.6$ g cm^{-2}, respectively. Models with high surface density and low star formation efficiency, similar to clouds in the galactic center, exhibit a decreased X_{CO} compared to clouds with $\Sigma \approx 1$ g cm^{-2}. The introduction of embedded sources makes the consistency with the MW much better. Nearly all clouds in the LDI model with $\varepsilon > 2\%$ and 85% of parameter space in the HDI model is consistent with the MW average value. *Thus, embedded CRs act in a way to regulate X_{CO} to keep it constant.*

$X_{\rm CO}$ is observed to be lower in starburst galaxies [300, 301, 302, 303]. Our models show that $X_{\rm CO}$ always decreases towards regions of more extreme CR environments. Environmental changes, which occur in higher redshift galaxies due to enhanced supernova rates, will also decrease $X_{\rm CO}$ and $X_{\rm CI}$. In starburst galaxies, which have a high star formation rate, this decrease could be compounded by embedded CR sources.

6.4.5 Summary

We found in Paper I that the inclusion of embedded sources and CR attenuation make the CRIR variable throughout the cloud. In this paper, we investigate the impact of different external CR fluxes and the inclusion of embedded sources on the CO-to-H_2 and CI-to-H_2 conversion factors. We find that differences in the CR flux from changes in the external environment and embedded star formation alter $X_{\rm CI}$ and $X_{\rm CO}$ significantly. External environment changes reduce $X_{\rm CO}$ only by 0.2 dex, within the measured spread of $X_{\rm CO}$ in the MW [36]. The difference in $X_{\rm CI}$ is more pronounced: an order of magnitude reduction for the lowest surfaced densities. The inclusion of embedded sources removes the strong dependence of $X_{\rm CO}$ and $X_{\rm CI}$ on $\Sigma_{\rm cl}$ and reduces the conversion factors by 0.6 and 1.2 dex, respectively. Embedded sources act in a way to regulate $X_{\rm CO}$ and keep it more constant as a function of $\Sigma_{\rm cl}$ and ε_g. Our models with embedded sources are consistent with the observed MW value and deviation of $X_{\rm CO,MW} = 2 \times 10^{20} \pm 0.3$ dex cm^{-2} (K km s^{-1})$^{-1}$ for all models with $\varepsilon_g > 2\%$. Observations of the CRIR in diffuse gas in the MW show that the average CRIR, $\langle\zeta\rangle \approx 10^{-16}$, represented by the high models. Our models with this external CRIR and ongoing star formation, represented by HDI, are consistent with the MW observed value and deviation for 85% of the parameter space. Our models reproduce the trends of a decreasing $X_{\rm CO}$ towards more extreme CR environments, such as those observed in the galactic center, the high redshift universe and starburst

galaxies. Our results motivate the inclusion of CR physics and the possibility of cosmic-ray feedback from internal sources when modeling $X_{\rm CO}$ and $X_{\rm CI}$.

CHAPTER 7

THE THREE-DIMENSIONAL DISTRIBUTION OF FAR ULTRAVIOLET RADIATION IN PROTOCLUSTERS

This chapter focuses on presenting the preliminary results of a simulation of the formation of a cluster of protostars including far ultraviolet radiation transfer. The chapter introduces the ray tracing formalism developed to calculate the attenuation of external fields.

7.1 Introduction

Molecular clouds are the sites of star formation, tying their evolution to processes which govern the formation of planets to galaxies [39]. The dynamics of molecular clouds are dominated by a combination of turbulence, gravity and magnetic fields [41]. The therodynamics, however, is mediated by radiation and chemistry. Molecular line emission acts as the primary coolant, with emission from carbon monoxide (CO) providing cooling down to tens of degrees Kelvin. Gas is heated through a combination of processes: photoelectric heating from ultra-violet emission, cosmic ray heating, and exothermic chemical reactions [13]. The temperature of the gas, though, controls the chemistry through temperature-dependent rate coefficients. Modeling both the dynamics and the thermodynamics self-consistently is paramount to understand the long-term evolution of the molecular phase of the interstellar gas.

Molecular clouds are filled with radiation across the electromagnetic spectrum. Radiation with energy greater than 13.6 eV is strong enough to ionize hydrogen and renders molecular gas atomic [13, 72]. The origin of ionizing radiation is mainly high

mass stars, particular O and B stars. Ionizing radiation sets the transition from warm atomic gas to cold neutral gas. Molecular clouds near extreme environments, such as galactic centers, black holes and/or supernova remnants, are also immersed in x-ray radiation [304]. Radiation this energetic ionizes molecules and atoms. Hard radiation sources influence the boundary between atomic and molecular gas.

In studies of photo-dissociation regions (PDRs), radiation with energies between 5 eV and 13.6 eV, the far ultraviolet (FUV), is of utmost importance. Photons with energies from 5 - 11 eV photoionize dust grains liberating electrons, providing photoelectric heating to the gas. Photons with energies between 11 eV and 13.6 eV are particularly important for the dissociation of H_2. It is difficult to directly dissociate H_2 since it lacks a dipole moment. However, if H_2 undergoes an electron excitation, it can decay into an unbound ground state. The excitation is a line process: only specific energies of light can excite the electrons. As a consequence, H_2 self-shields: H_2 deeper embedded in a cloud is shielded by the gas closer to the surface which absorbs the necessary wavelengths around excitation energies. The self-shielding process is sensitive to the velocity and density distribution of the gas [305, 306].

There have been numerous numerical prescriptions to model the density distributions of molecular clouds. The simplest models are one-dimensional. These models allow the use of large chemical networks and more sophisticated treatments of the FUV radiation [31, 306]. One dimensional models can either be semi-infinite and uniform in density [e.g. 154, 306] or impose a finite density structure [e.g. 232, 307]. The next step in sophistication is the use of clumpy [e.g. 107] or fractal structure [e.g. 75, 161, 308]. These structures are meant to mimic the porosity of molecular clouds which allow FUV radiation to penetrate further in than constant-density models allow. Finally, hydrodynamic simulations provide an accurate representation of the density and velocity structure of molecular clouds. These simulations can be post-processed with an astrochemical code utilizing large networks [116]. Chemistry

can also be included in-situ, although this restricts the chemical models to smaller, reduced networks [e.g. 26, 79, 240, 309].

There are two main algorithms for solving the radiative transfer and column densities: ray tracing and monte carlo. Ray tracing utilizes rays which are propagated through the domain and accumulate the opacity and/or column density. Background radiation fields can be treated with simple approaches, such as the six-ray method [309], or more sophisticated approaches utilizing the HEALPIX package [120], such as TREECOL [275]. Ray tracing is also done to quickly solve the radiation from point sources, using methods such as adaptive ray tracing [293, 310] or tree-based solvers, such as TREERAY [292]. Monte-Carlo solvers make up the other main class of algorithms, where photon packets are emitted from sources of radiation and utilize Monte-Carlo sampling for the propagation and absorption of photons [e.g. 311, 312].

Once the star formation process is underway, embedded regions in molecular clouds are illuminated by protostars. The radiation from protostars comes from two main sources: accretion onto the protostar and internal energy. The accretion luminosity is the result of the conversion of gravitational energy to thermal,

$$L_{\rm acc} = f_{\rm acc}\frac{GM\dot{M}}{R} \tag{7.1}$$

where $f_{\rm acc}$ is the fraction of converted gravitational energy, M and R are the mass and radius of the protostar, respectively, and $\dot{M}$ is the accretion rate. Protostars also have internal energy sources depending on their evolutionary stage, predominantly Kelvin-Helholtz and Deuterium burning. For modest accretion rates, intermediate-mass stars become bright in the FUV. These protostars will act as internal FUV lamps creating PDRs in dense gas far from the surface of the molecular cloud. The accretion luminosity dominates for lower mass stars while internal energy dominates for high mass protostars [50, 60].

In this paper, we explore the distribution of FUV radiation from an external field and internal sources using three-dimensional hydrodynamic simulations. In §7.3, we describe our numerical methods for the hydrodynamic simulations and radiation computation. We introduce an adaptive six-ray approach to calculate the column density from the external radiation field. In §7.3 we will present test problems and preliminary results of a protocluster simulation.

7.2 Methods

We perform the hydrodynamic calculations using the ORION2 magneto-hydrodynamics code [114, 115]. ORION2 is an adaptive mesh refinement (AMR) code which utilizes a second order Godunov scheme [313]. The full set of magneto-hydrodynamic equations are

$$\frac{\partial \rho}{\partial t} = -\nabla \cdot (\rho \mathbf{v}) + \sum_i \dot{M}_{w,i} W_w(\mathbf{x} - \mathbf{x_i}) \tag{7.2}$$

$$\frac{\partial (\rho \mathbf{v})}{\partial t} = -\nabla \cdot \left(\rho \mathbf{v}\mathbf{v} - \frac{1}{4\pi}\mathbf{B}\mathbf{B} \right) - \nabla P - \rho \nabla \phi + \sum_i \dot{\mathbf{p}}_{w,i} W_w(\mathbf{x} - \mathbf{x_i}) \tag{7.3}$$

$$\frac{\partial \rho e}{\partial t} = -\nabla \cdot \left[(\rho e + P)\mathbf{v} - \frac{1}{4\pi}\mathbf{B}(\mathbf{v} \cdot \mathbf{B}) \right] - \rho \mathbf{v} \cdot \nabla \phi + \dot{\mathcal{E}}_{w,i} W(\mathbf{x} - \mathbf{x_i}) \tag{7.4}$$

$$\frac{\partial \rho_t}{\partial t} = -\nabla \cdot (\rho_t \mathbf{v}) + \sum_i \dot{M}_{w,i} W_w(\mathbf{x} - \mathbf{x_i}) \tag{7.5}$$

$$\frac{\partial B}{\partial t} = \nabla \times (\mathbf{v} \times \mathbf{B}) \tag{7.6}$$

$$\nabla^2 \phi = 4\pi G \rho + 4\pi G \sum_i M_i \delta(\mathbf{x} - \mathbf{x_i}) \tag{7.7}$$

$$\frac{dM_i}{dt} = -\dot{M}_{w,i} + \dot{M}_{\mathrm{acc},i} \tag{7.8}$$

$$\frac{d\mathbf{x}_i}{dt} = \frac{\mathbf{p}_i}{M} \tag{7.9}$$

$$\frac{d\mathbf{p}_i}{dt} = -M_{w,i} \nabla \phi - \mathbf{p}_i \tag{7.10}$$

Equations 7.2 - 7.4 describe the conservation of mass, momentum and energy, respectively and equation 7.5 describes the evolution of the tracer field used to track

the matter injected by protostellar outflows. ORION2 solves the Poisson equation, equation 7.7, using a multi-grid solver [115]. We close the equations by assuming the gas is effectively isothermal, such that the energy density is $e = \frac{1}{2}v^2 + \frac{P}{(\gamma-1)\rho}$, where $\gamma = 1.0001$. Equations 7.8 - 7.10 describe the evolution of the sink mass, position and momentum, respectively[118].

Our simulations cannot resolve the jet launching radius since this is typically a few solar radii away from the protostar's surface [64]. We therefore adopt the outflow model of Matzner and McKee [314] where sink particles loose gas through bipolar collimated jets. Mass, momentum and energy are deposited from the jet onto the rest of the rest of the grid according to a weight function, W_w [315].

We refine our grids based on the Truelove criterion[114]

$$\rho < \rho_J = J^2 \frac{\pi c_s^2}{G \delta x_l^2} \tag{7.11}$$

where c_s is the sound speed, δx_l is the grid resolution at level l and we adopt $J = 0.125$. Sink particles are created when the Truelove criterion is violated in cells on the maximum AMR level.

ORION2 has been modified to include radiation from embedded sources utilizing a hybrid ray tracing scheme [62]. We include a modified ray tracing scheme to allow the use of external radiation fields, discussed in detail below.

7.2.1 Source Radiation

Once star formation is underway, the molecular cloud becomes illuminated from the embedded protostars. Radiation from protostars has two contributions: the accretion luminosity and internal energy sources. We focus on radiation at FUV energies. The protostellar mass, radius and internal luminosity evolve following models which account for different stages, including pre-collapse and Deuterium burning phases [61]. We use equation 7.1 to calculate to accretion luminosity, where the mass and radius

are provided by the evolution model [61]. We assume the accretion and protostellar components emit as blackbodies, so that each have a defined radiation temperature, i.e.,

$$L_{\rm tot} = 4\pi R_*^2 \sigma (T_{\rm acc}^4 + T_*^4) \tag{7.12}$$

where $\rm T_{acc}$ and $\rm T_*$ are the radiation temperature for each component. Figure 7.1 shows the tabulated fraction of the luminosity at FUV energies as a function of blackbody temperature. The FUV fraction becomes high in the temperature range of 11,000 - 70,000 Kelvin. The total FUV luminosity is

$$L_{\rm FUV} = f_{\rm FUV,acc}(T_{\rm acc}) L_{\rm acc} + f_{\rm FUV,*}(T_*) L_* \tag{7.13}$$

Here we briefly describe the ray tracing scheme utilized for point sources, HARM^2, and refer the reader for further details to Rosen et al. [62]. We use a single frequency bin, between 5 eV $\leq h\nu \leq$ 13.6 eV, although the method is generalized for an arbitrary number. Rays are emitted from the source using an angular distribution from the HEALPIX package [120], with each ray subtending a solid angle $\Omega_{\rm ray}$ and direction $\mathbf{n}$. The solid angle the ray subtends is defined by the number of pixels $N_{\rm pix} = 4\pi/\Omega_{\rm ray}$. The initial luminosity of each ray is $L_{\rm ray,i}(0) = L_i/N_{\rm pix}$ and is solved along the ray via the transfer equation

$$\frac{\partial L_{\rm ray,i}}{\partial r} = -\kappa_i L_{\rm ray,i}, \tag{7.14}$$

where r is the distance from the point source and κ_i is the absorption coefficient. The equation is solved by discretizing the ray positions at cells in the hydrodynamic mesh. When a ray passes through a cell with number density, n, and segment length, Δl, the luminosity is decreased by

$$\Delta L_{\rm ray,i} = L_{\rm ray,i}(1 - e^{-\tau_i}) \tag{7.15}$$

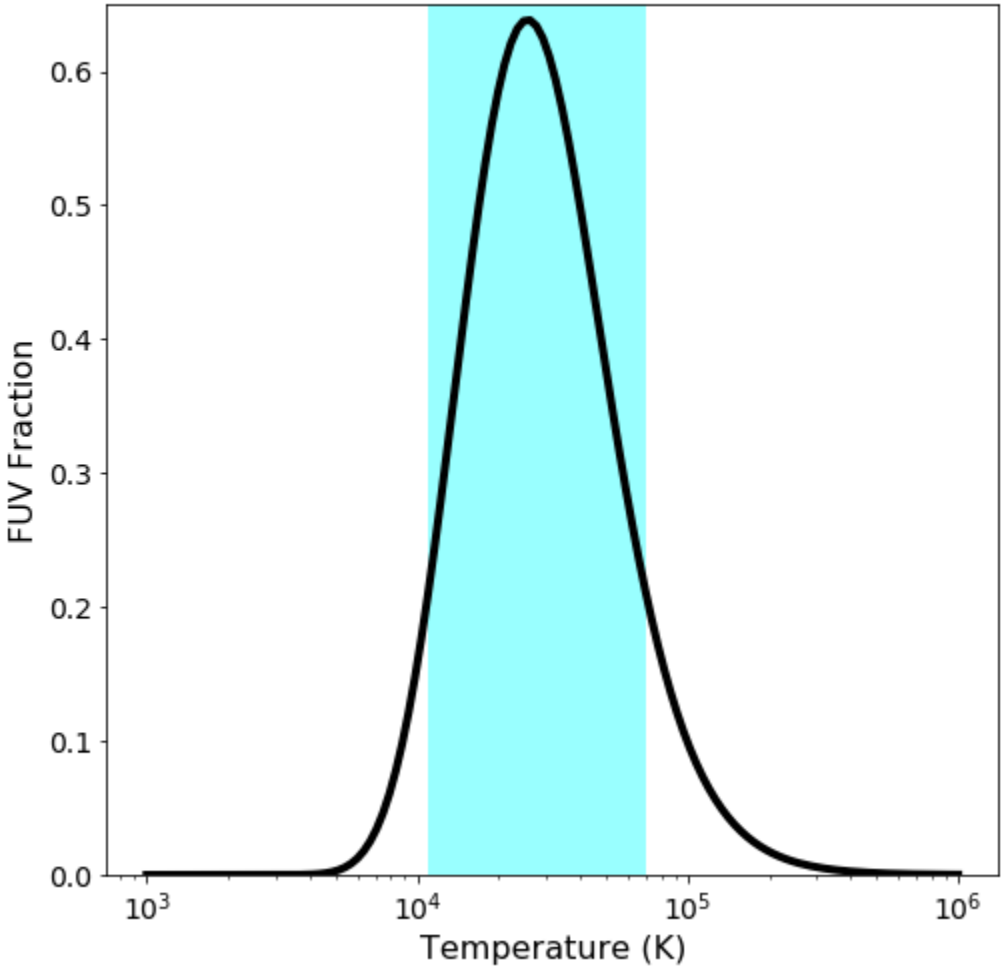

Figure 7.1. The fraction of blackbody radiation at FUV energies versus temperature. The blue band shows the temperature range where the FUV fraction is maximal.

where $\tau_i = \tau_0 A_{\mathrm{V},0} n \Delta l$, $\tau_0 = 3.02$ and $A_{\mathrm{V},0} = 6.29 \times 10^{-22}$ cm^2. Furthermore, we keep track of the gas column accumulated along the ray, $N_{\mathrm{ray,i}} = \sum_k n_k \Delta l_k$, where n_k and Δl_k are the number density and segment length from cell k along the ray path.

We initially choose $N_{\mathrm{pix}}(0) = 12$ at the lowest HEALPIX level, with $N_{\mathrm{pix}}(j) = 12 \times 4^l$ pixels at HEALPIX level j. The scheme is adaptive to allow for higher resolution across the computational domain. Rays are divided into 4 child-rays when the

condition

$$\frac{\Omega_{\rm cell}}{\Omega_{\rm ray}} = \frac{N_{\rm pix}(j)}{4\pi}\left(\frac{\Delta x}{r}\right)^2 < \Phi_c \tag{7.16}$$

is violated, where Δx is the cell size and Φ_c defines the minimum number of rays required to go through a cell. When the ray splits, the luminosity of each child-ray is $L_{\rm ray,i}(j+1) = L_{\rm ray,i}(j)/4$. The total column density accumulated along each ray is passed to the child-ray. We store the FUV flux from each ray in the cell on the hydrodynamic mesh. The FUV flux is calculated from the ray luminosity, direction vector and angle it enters the cell according to

$$F_{\rm ray,i} = (\mathbf{n}\cdot\hat{\mathbf{r}})\frac{L_{\rm ray,i}}{\Delta x^2}, \tag{7.17}$$

where $\mathbf{n}$ is the vector in the direction of the ray and $\hat{\mathbf{r}}$ is the unit vector normal to the cell face where the ray crosses. We terminate the ray when $F_{\rm ray,i} < 0.01$ Draine.

7.2.2 Background Radiation

Molecular clouds are externally irradiated by light from stars dispersed throughout the galaxy. The FUV component of this radiation is crucial in astrochemical studies since it controls the HI-H_2 transition. We utilize a six-ray approach similar to that adopted in Glover and Mac Low [309]. In typical six-ray approaches [e.g. 26, 309], the total column density is calculated from each cell outward in the positive and negative cardinal directions. This approach naturally scales with the number of cells. We modify the HARM^2 adaptive ray tracing scheme discussed above to create an adaptive six-ray algorithm.

The adaptive six-ray algorithm uses a modified ray tracing algorithm to propagate the external radiation field, $F_{\rm bkg}$. Rays are emitted from the six domain faces along their inward normal vectors, $\hat{n}_{\rm face}$, such that the rays point to the cell centers. The

flux along the ray, $F_{\rm ray}$ is initialized such that $F_{\rm ray,i}(0) = F_{\rm bkg}$, where $F_{\rm bkg}$ is the external FUV flux. The flux is attenuated along the ray such that

$$\Delta F_{\rm ray,i} = F_{\rm ray,i}(1 - e^{-\tau}) \tag{7.18}$$

similarly to Equation 7.15. If there is no AMR, every cell will be crossed by six rays, one from each cardinal direction. When there is AMR, the rays must be split to ensure that every cell has the appropriate six rays crossing through it. We do not utilize the splitting criterion from the HARM^2 scheme and instead split the ray if the ray encounters an AMR level, k, which is greater than the ray level, j. When this condition is met, the ray is split into four child-rays and the ray level increased. The flux of the child-rays is increased, $F_{\rm ray,i}(j+1) = 4 \times F_{\rm ray,i}(j)$ to conserve flux and the gas column is passed directly to the child-rays. When rays encounter lower AMR levels their flux is similarly reduced by a factor of 4 to conserved flux. The total gas column in each ray direction is stored in the hydrodynamic mesh. However, the column must be weighted following

$$N_{\rm col,\hat{n}} = \sum_i \left(\frac{1}{4}\right)^{(j-k)} N_{\rm col,i}. \tag{7.19}$$

The weighting is necessary because without ray merging, if a cell is not on the highest level grid, it may have more than six rays crossing through it. The column-density weighting ensures that the amount of gas column accumulated along the cardinal directions is correct.

The adaptive six-ray approach is very fast since it scales with $\mathcal{O}(N^{2/3})$ rays rather than $\mathcal{O}(N)$. However, the speed comes at a significant disadvantage in angular resolution. The approach will tend to underestimate the column density (and thus overestimate the flux) when the volume filling fraction of dense gas is small [309]. In a highly turbulent structure, such as before the gas has had much time to collapse,

we expect the lack of angular resolution will not lead to a significant overestimation of the flux.

7.2.3 Simulation Setup

We set up a simulation to model the formation of a cluster of protostars. We initialize the simulation with a uniform density and perturb the gas with a randomized velocity field for two crossing times. The random field follows a flat power spectrum between wavenumbers $k = 1...2$ corresponding to physical size scales $L/2 < x < L$. Perturbing the gas for two crossing times better ensures a properly developed turbulent power spectrum [74]. We normalize the velocity perturbations with a velocity dispersion following the line-width size relation [41, 149]. We use the virial parameter to derive the total gas mass from the velocity dispersion [e.g. 251]:

$$\alpha_{\rm vir} = \frac{5\sigma^2 R}{GM}, \tag{7.20}$$

where $R = L/2$ and L is the size of the simulation domain. The initial magnetic field is configured to be uniform in the +z direction with a magnitude defined from the thermal plasma beta, $\beta_{\rm th} = 8\pi\rho c_s^2/B_0^2$. Our fiducial simulation has a resolution of 512^3 covering a volume of (10 pc)^3 with $\alpha_{\rm vir} = 2$, $T_{\rm gas} = 10$ K and $\beta = 20$. After the initial driving phase, we turn on self-gravity to allow the cloud to collapse while continuing the driving. The simulation includes protostellar feedback from outflows and FUV radiation, as described above. The external FUV radiation field is chosen to be the Draine field [119], $F_0 = 2.72 \times 10^{-3}$ erg cm^{-2} s^{-1}.

7.3 Results

7.3.1 Test Problems

We perform three different tests to ensure the accuracy of the source and background radiation transfer: single source, single-sided external and a shadow test. For

all three test problems, we impose a fixed mesh refinement where the level 1 grid covers the inner 50% and the level 2 grid covers the inner 25%. We repeat the calculation for different maximum levels of refinement to check convergence.

7.3.1.1 Single Source

The single source test problem consists of a single radiation point source in the center of the domain with a fixed luminosity, $L_* = 2L_\odot$. The point source is surrounded by gas with a uniform density. For this test problem we turn off attenuation, such that the flux is exactly $F(r) = L/(4\pi r^2)$. The ORION2 code requires the sink particle to be on the highest level grid available, so we center the fixed mesh refinement on the point source.

Figure 7.2 shows the results of the test using an area factor $\Phi_c = 4$ for maximum grid levels up to two. The radiation field attenuation from the source shows good convergence as the number of levels is increased. In all cases, the ray tracing reproduces the r^{-2} profile exactly towards large radii. There are a couple of bumps in the profile which correspond to radii where the rays split. These artifacts are small and a consequence of the adaptive ray-splitting.

7.3.1.2 Single-sided Background Field

The single-sided background field test is the simplest physical test of the six-ray implementation. We irradiate a single side of a uniform density domain with an external field equal to the Draine field [119]. We perform the test up to a maximum grid level of 2 and include the attenuation of the FUV radiation due to dust. Figure 7.3 shows the result of the test comparing the numerical results to the analytic solution $F(x) = F_0 e^{-\tau_0 A_{V,0} n_0 x}$. The numerical solution matches the analytic prediction in all cases confirming the flux along each ray is properly solved.

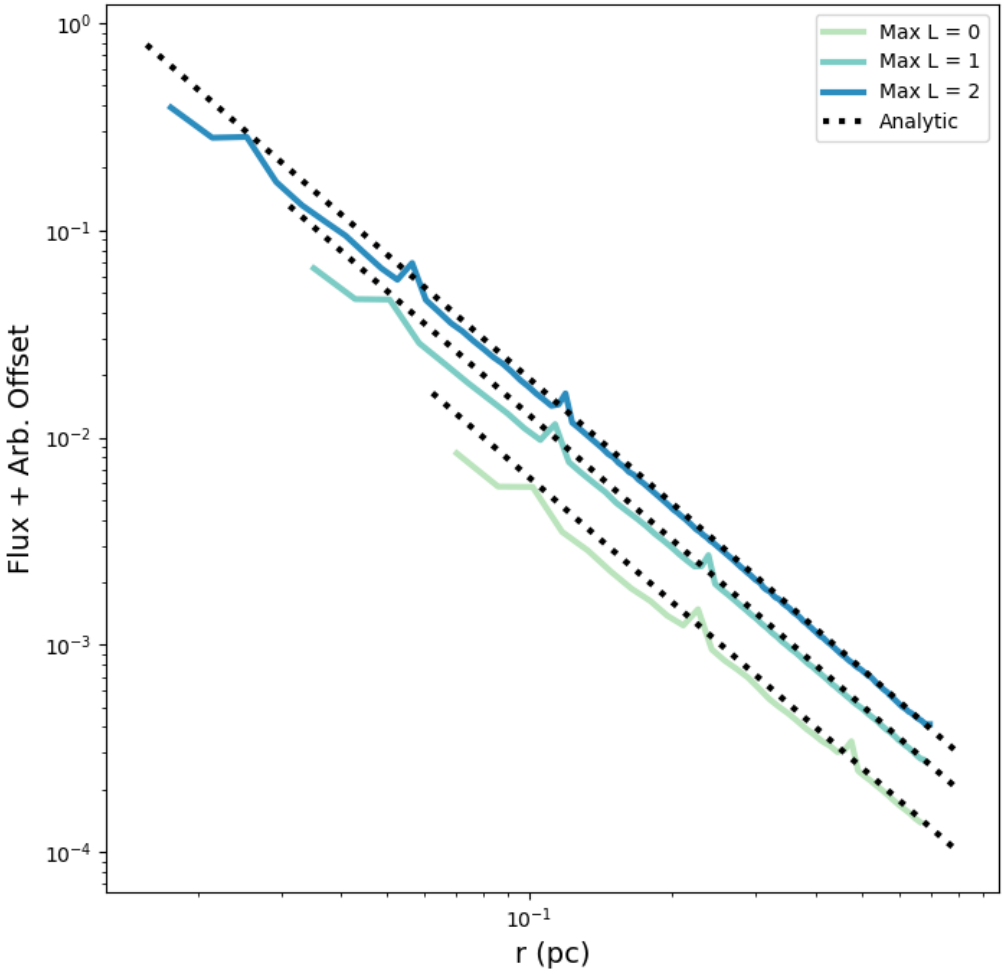

Figure 7.2. Flux from a single source as a function of radius. Solid lines show the results with the color denoting the maximum grid level. The dotted line shows the analytic $1/r^2$ solution.

7.3.1.3 Shadow Test

The density distributions of molecular clouds are not homogeneous. There structure is highly complex with many under-dense and over-dense regions. We perform a test to check the effect of high density regions. We initialize the domain with a uniform density of $n = 100$ cm^{-3} with a blob of density $n_b = 5000$ cm^{-3} offset in

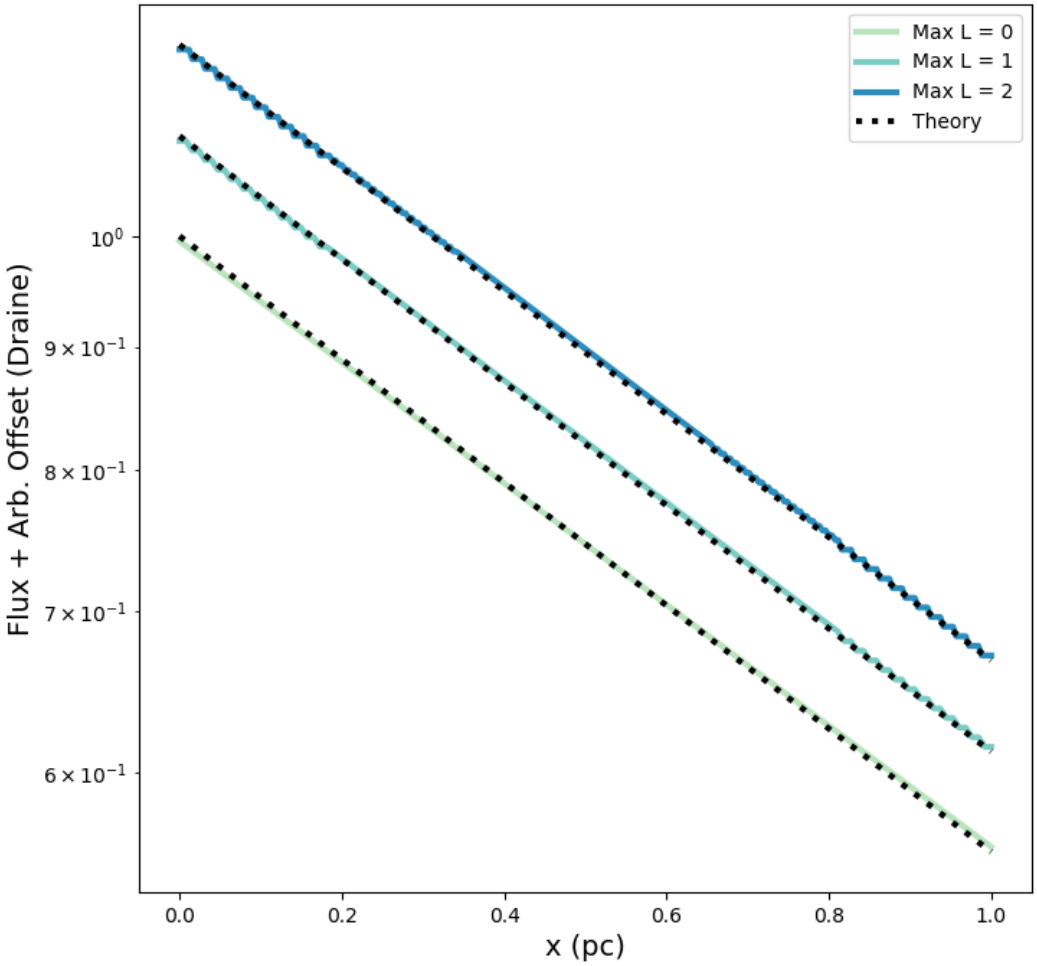

Figure 7.3. Flux from the external radiation field as a function of distance from the surface. Line color denotes the maximum grid level. Dotted line shows the analytic solution.

the x- and y-direction by 0.2 pc and a radius of 0.15 pc. We irradiate the blob with a central source with luminosity $L = 2L_{\odot}$ and a single-sided background radiation field of 1 Draine. Figure 7.4 shows the result of the test up to a maximum level of 2, using the same fixed mesh refinement as before. In all cases, the attenuation due to the high-density blob produces the appropriate shadowing. White regions in the

figure are locations where the rays were terminated due to the radiation field being attenuated below a hundredth of the Draine interstellar radiation field [119].

7.3.2 Cluster Simulation

In this section, we present preliminary results from our cluster simulation. Figure 7.5 shows the evolution of the cloud as a function of time. The initial time before collapse, 0.01 t_{ff}, where $t_{\rm ff} = \left(\frac{3\pi}{32G\rho}\right)^{1/2}$ is the free-fall time, shows a highly turbulent density distribution. As gravity takes over, the distribution because much more peaked in dense cores and filaments with most of the protostars forming in filament hubs.

Figure 7.6 is a postage-stamp plot showing the density distribution around the 36 most massive protostars at 0.25 $t_{\rm ff}$. The highest mass protostar in the simulation is 3.35 $M_\odot$. The protostars are still highly embedded in their natal cores, with peak densities around the protostar of 10^6 cm^{-3}. It is important to note that the physical resolution of the simulation is 4000 AU. Therefore, we are not properly resolving protostellar cores and disks. The super-solar mass protostars exhibit local structures which are highly complex since they are forming in clustered environments. The density distributions do not show cavities forming from the protostellar jets, so the density immediately surrounding the protostar is higher than expected.

Orion2 enables the use of tracer fields to track feedback gas originating from sources, in this case prototstellar jets. Figure 7.7 shows the same protostars as Figure 7.6 but shows the distribution of gas ejected in the outflows. We find that the tracer fields largely do not exhibit the expected bipolar outflows. The low resolution is likely the main culprit: since the accretion flow is not resolved, the net angular momentum is changing significantly as a function of time. As such, the sink particle is spinning around randomly injecting outflow material isotropically. This would explain why the outflow cavities are not apparent in the density distributions in Figure 7.6. The

FUV radiation, however, primarily escapes from cavities carved out by winds and jets. Therefore, the majority of the source radiation is being completely absorbed within a few cells of the protostar. At the resolution of the simulation, a ray traversing the first cell from the protostar would encounter a column density of 6×10^{22} cm^{-2}, already greatly attenuating the radiation. Higher resolution simulations, whether by focusing on a smaller domain or more levels of refinement, are needed to properly model the FUV radiation from sources. We focus the rest of our discussion on the FUV radiation from an external field.

Before the onset of star formation, and in regions far from forming protoclusters, the FUV radiation will be dominated by the externally-irradiated field. The middle and left panels of Figure 7.5 show the time evolution of the line-of-sight averaged FUV radiation and A_V, respectively. As expected, the most central regions exhibit small FUV irradiation. However, this is not necessarily correlated with the highest density regions. There are regions with high column density near the boundary of the cloud which, despite having a high density, are irradiated by a stronger radiation field than similar high-rdensity regions regions in the center of the domain.

The line-of-sight averaged A_V represents the *three-dimensional* A_V from the surface of the domain. However, observations do not have access to this information: they are constrained to the column density along the line of sight. Figure 7.8 investigates the correlation between the column density and the line-of-sight averaged FUV radiation. While the majority of the points appear to be clustered in a peak along $F \propto e^{-N}$, there is a large amount of spread. Nearly all regions with low column exhibit high FUV radiation. However, towards higher column densities there is a large dispersion: there are many regions of high column density experiencing radiation. There is effectively no variation with time: the main effect causing the dispersion is the turbulence structure of the molecular cloud. Our results show there is significant

error in using column densities across the plane of the sky into an estimation of the FUV radiation.

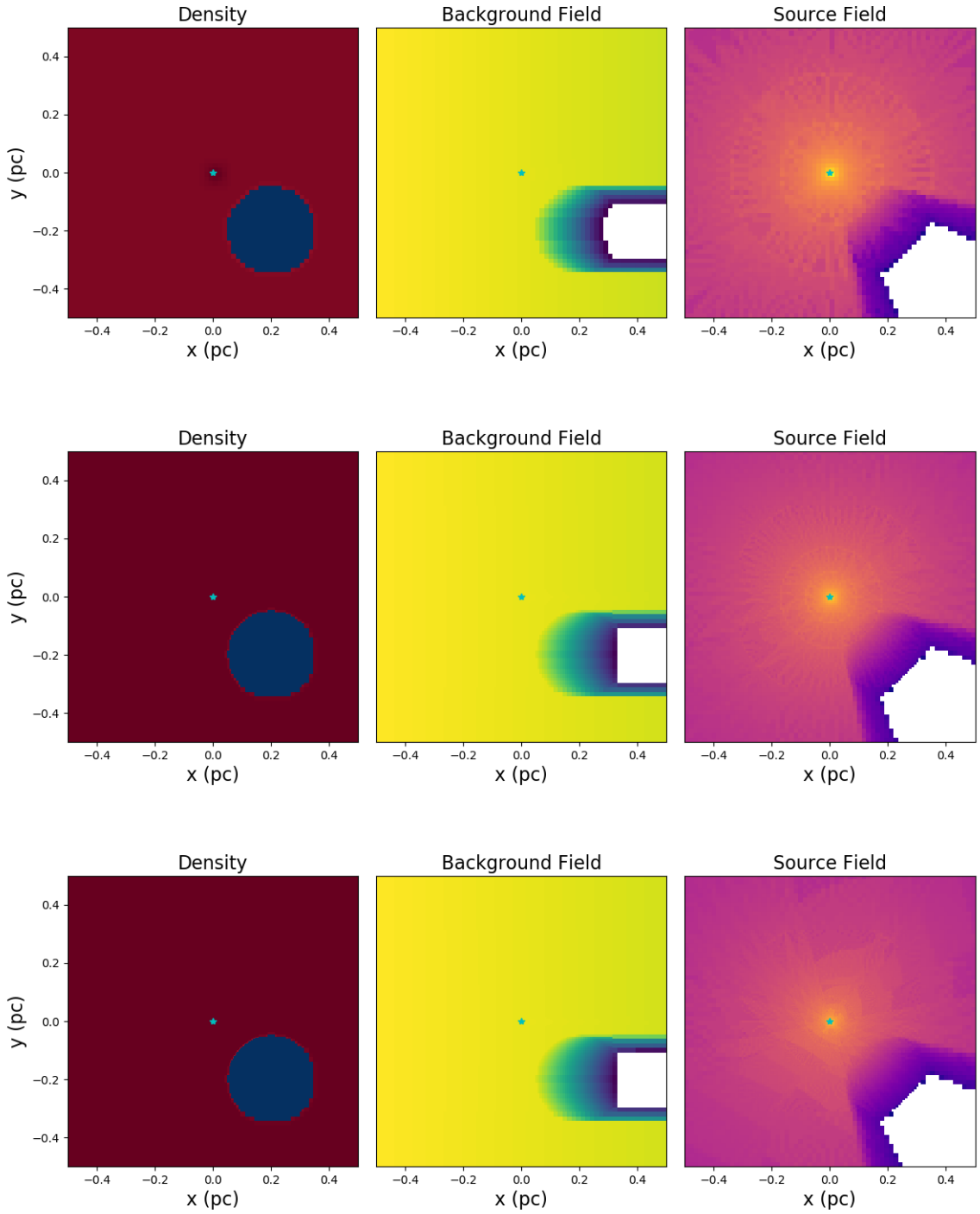

Figure 7.4. Results from the shadow test. Left: Density distribution showing the high density blob offset from center. Middle: Background radiation field from a single-sided radiation field. Right: Radiation field from a source located in the center of the domain. The rows are in increasing order from top to bottom of the maximum level, with the top, middle and bottom panels representing a maximum level of 0, 1 and 2.

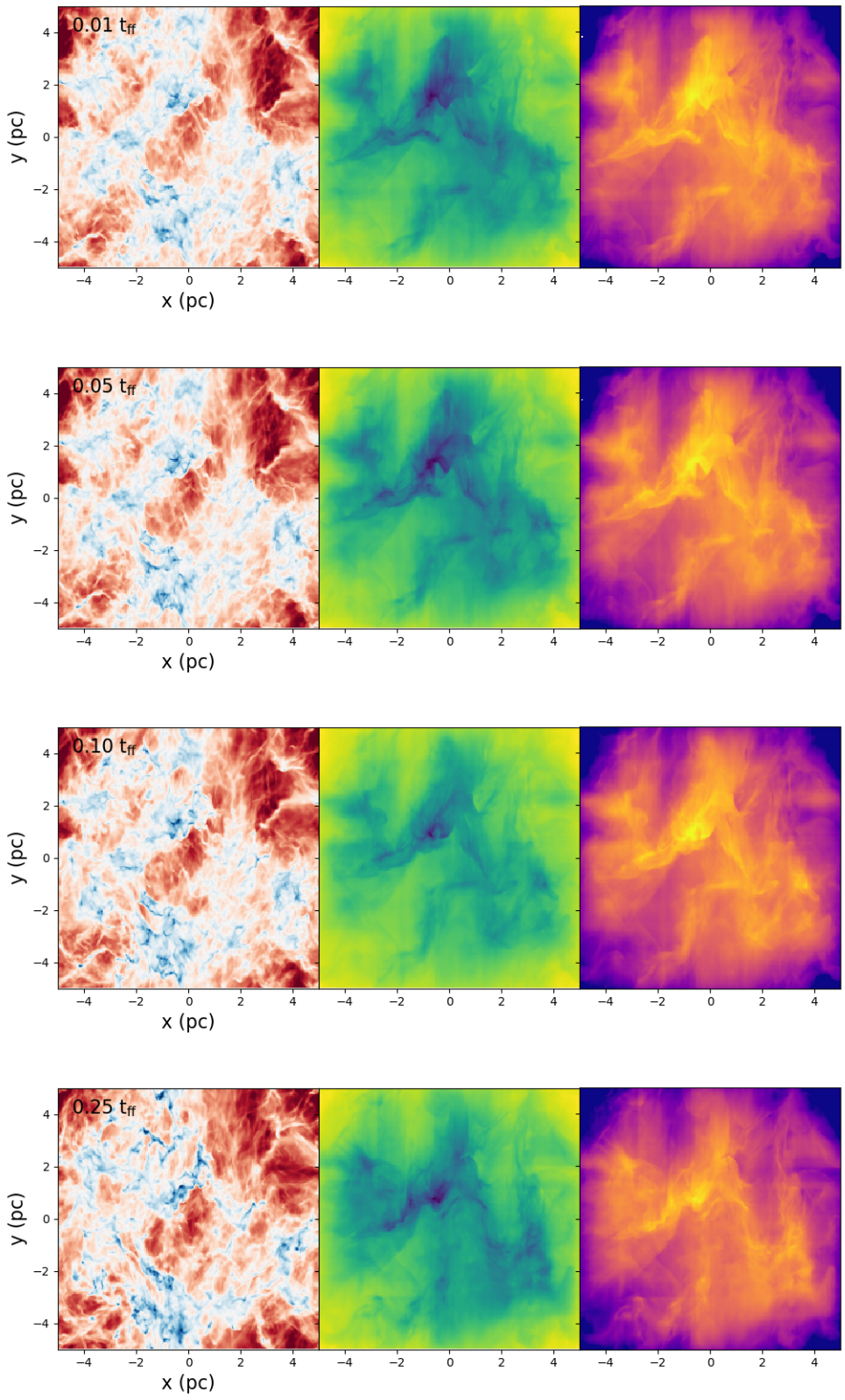

Figure 7.5. Evolution of the column density, average line-of-sight FUV field, and extinction (A_V) on the left, middle and right, respectively. The annotation denotes how much of a free-fall time has elapsed.

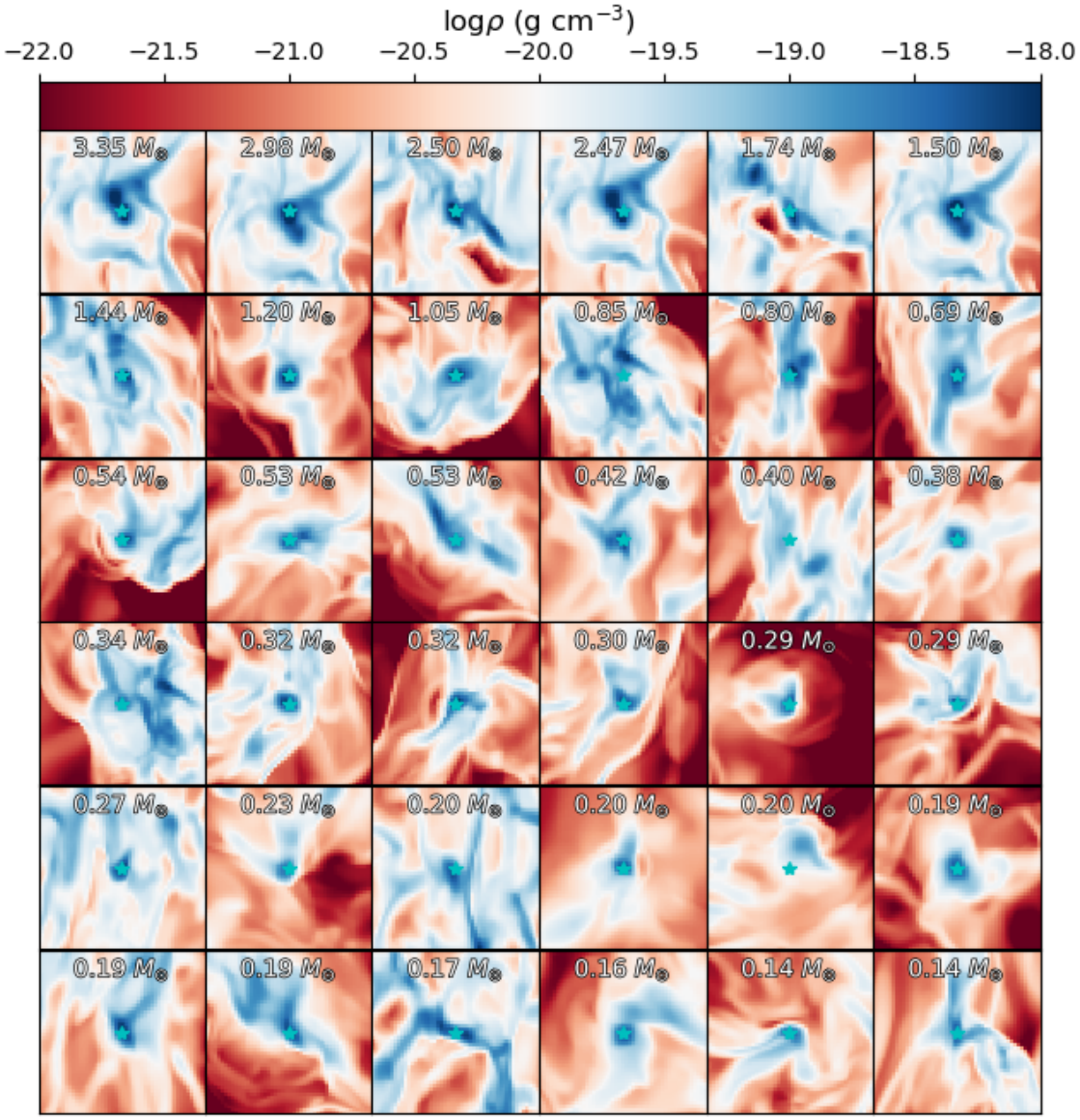

Figure 7.6. The distribution of gas, ρ, around the 36 most massive protostars in the cluster shown as a slice along the z-direction. Annotated text shows the mass of the protostar.

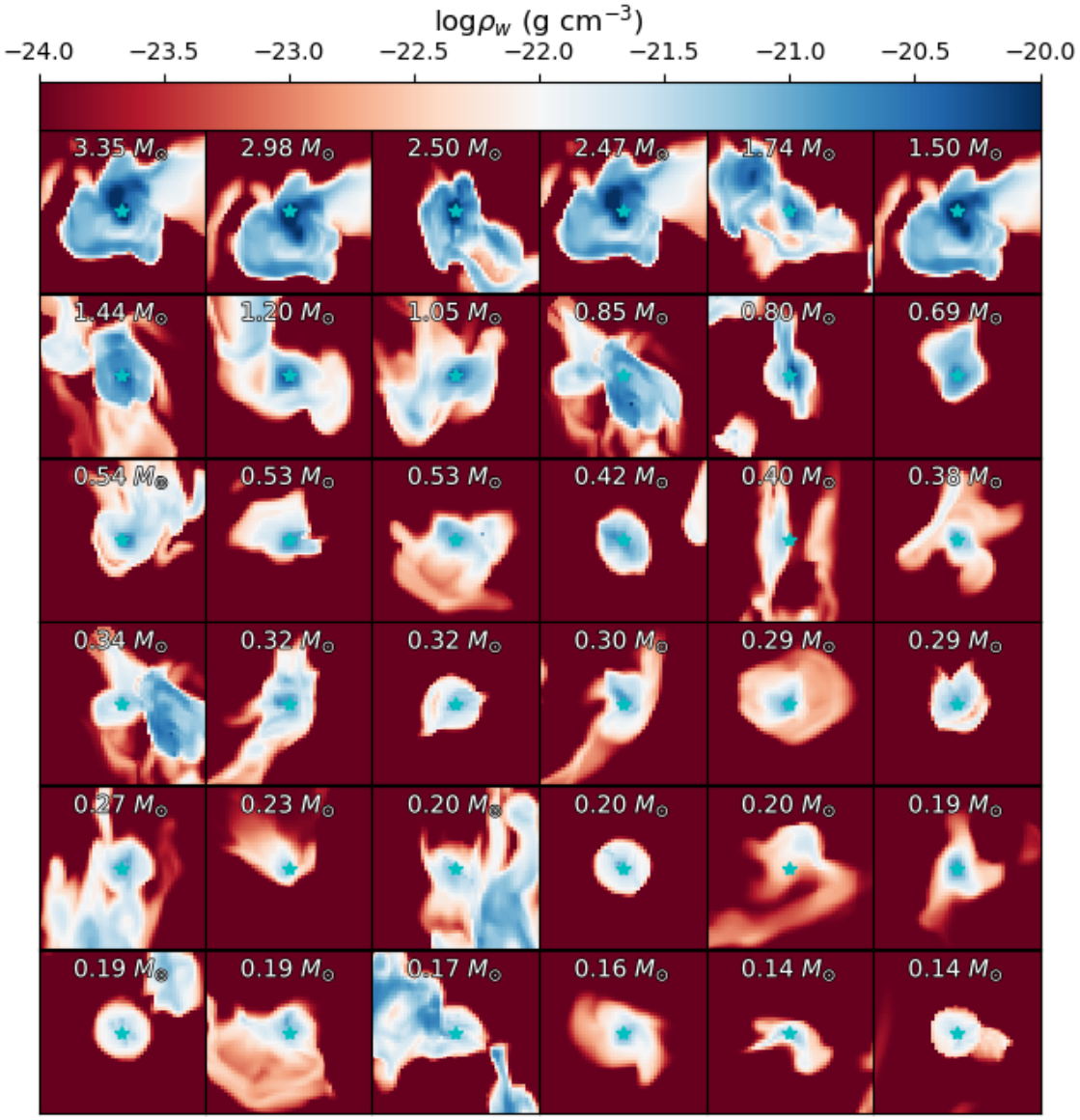

Figure 7.7. The distribution of gas ejected from protostellar outflows, ρ_w, for the 36 most massive protostars in the cluster. Annotated text shows the mass of the protostar.

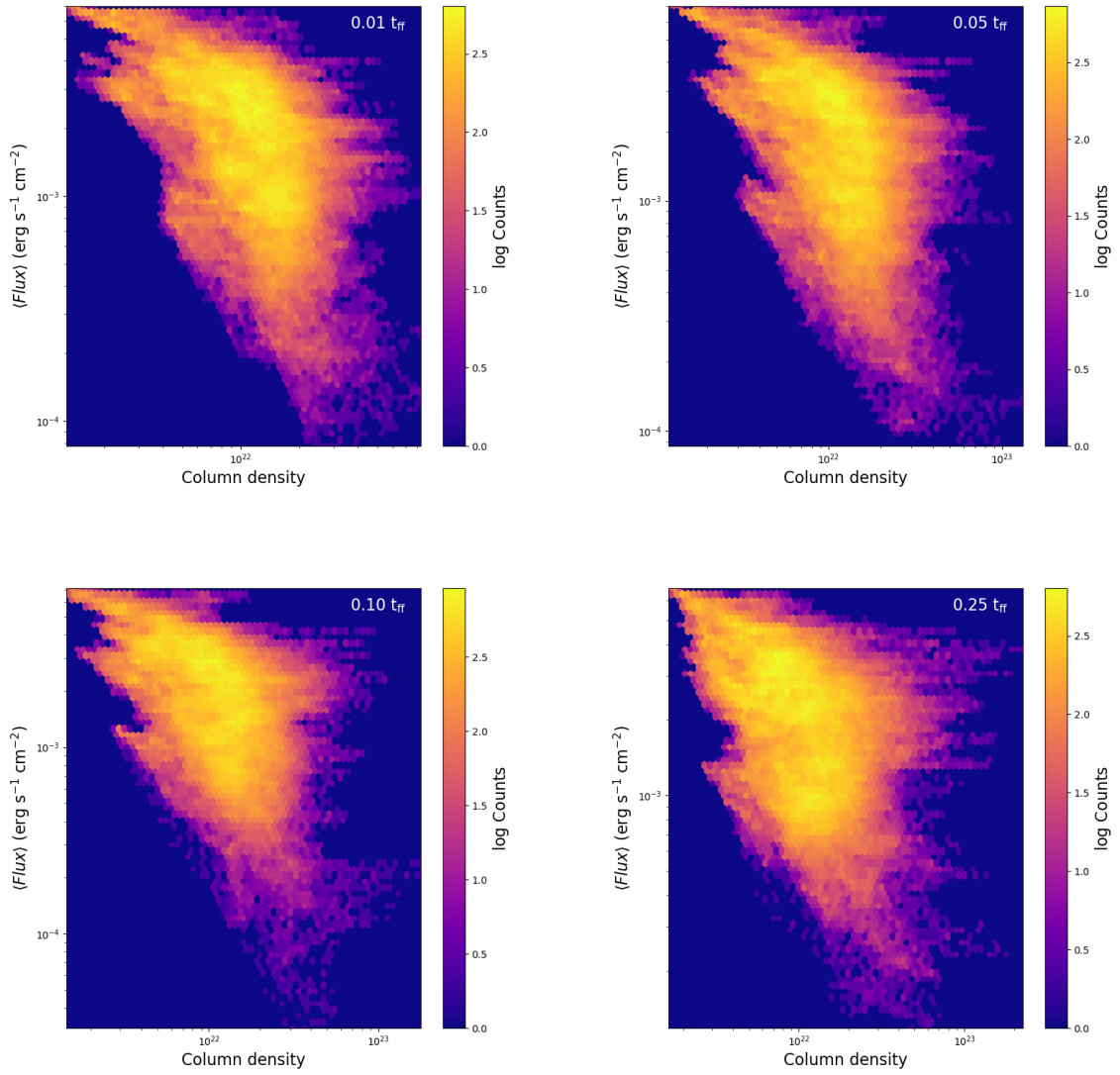

Figure 7.8. Line-of-sight averaged FUV flux versus column density. Hex-cell color denotes the number of points in the cell. Subplots show time evolution with 1%, 5%, 10% and 25% on the top-right, top-left, bottom-right and bottom-left.

CHAPTER 8

FUTURE WORK

8.1 Summary of the Dissertation

This dissertation focuses on quantifying the impact of various stellar feedback processes on the chemistry of their natal molecular cloud complexes. The results from Chapter 4 have led to two public web applications: PROTOSTAR-CRS[1] allows the user to explore the protostellar cosmic ray spectrum across the entire physical range of protostellar masses and CRGEN[2] allows the user to define their own protostellar parameters, accretion rate and column density profile to compute the accelerated proton and electron spectrum and attenuation on the fly. Finally, the last part of the thesis led to the develop of an extension to the astrochemistry code, 3D-PDR, that includes cosmic ray attenuation in-situ, which is public on Github[3]. The work presented in the dissertation has led to four papers accepted for publication[4] in the Astrophysical Journal (ApJ) with one paper submitted for publication to the Astrophysical Journal Letters (ApJ).

In Chapter 2, we present the results of an astrostatistics study of the inferred turbulence properties observed using different tracers. We use the spectral correlation function (SCF), which is a two point correlation function for spectra, to measure the turbulence properties of a simulated molecular cloud. We utilized a hydrodynamic

[1]http://protostarcrs.brandt-gaches.space/

[2]http://crgen.brandt-gaches.space/

[3]https://uclchem.github.io/3dpdr.html

[4]Gaches and Offner [81], Gaches et al. [90], Gaches and Offner [148], Gaches et al. [232]

simulation which was post-processed with a three-dimensional astrochemistry code producing the spatial distribution of over 200 molecular and atomic species. We performed synthetic observations for a subset of important species for studying molecular cloud dynamics. We found that the turbulence properties inferred through the SCF change drastically according to the species used. Our analysis shows that applying realistic observational noise and beam size convolution is necessary to compare simulations to observations. We concluded that species separated into three different density tracers, according to the slope of the SCF: diffuse (C^+, OH^+, C, CO, and CN), intermediate (CS, HCN, HNC, OH, HCO^+ and SiO) and dense (H_2CO, N_2H^+, NH_3, H_2CS and SO).

In Chapter 3, we construct semi-analytic models to generate synthetic protoclusters, calculate their luminosity properties and couple their far ultraviolet (FUV) feedback to molecular cloud chemistry. We calculate the bolometric, FUV and ionizing luminosity for clusters hosting between 10 and 10^6 protostars. We find that the Tapered Turbulent Core (TTC) accretion model best represents the bolometric luminosity of observed protoclusters. We couple the FUV radiation from these synthetic protoclusters to one-dimensional astrochemical models covering a wide range of molecular cloud gas surface densities and star formation efficiencies. We find that the dense gas thermo-chemistry is significantly altered by the cluster FUV radiation, heating the gas to a hundred degrees Kelvin. We quantify the impact of protostellar FUV radiation on the CO-to-H_2 conversion factor and conclude that it is necessary to replicate the high conversion factors found in diffuse star-forming regions.

In Chapter 4, we model the acceleration of cosmic rays in the accretion shocks of protostars self-consistently using semi-analytic accretion and shock models. We find that protostars can accelerate cosmic rays protons to energies of 1-20 GeV, with the primary constraints on their maximum energy being energy losses, diffusion losses and magnetic field wave dampening. We calculate the cosmic ray ionization rate

from cosmic rays which are able to escape their natal cores and show that solar-analogue protostars will provide increased ionization throughout their cores. Our models are able to replicate the increased ionization rate observed in the intermediate-mass protocluster OMC-2 FIR 4. Finally, we calculate the total cosmic ray ionization rate from clusters of protostars and show that clusters hosting more than a few hundred protostars are able to provide enough cosmic rays to compete with external galactic sources.

In Chapter 5, we implement a novel astrochemistry code which includes cosmic ray attenuation in-situ to quantify the impact of different cosmic ray models on the chemistry of molecular clouds. The new astrochemistry code allows the user to define the cosmic ray spectrum irradiating the external surface of the cloud rather than a globally constant cosmic ray ionization rate with the cosmic ray ionization rate now computed within the code locally at every point. We model star-forming molecular clouds hosting a wide range in numbers of protostars and including two different external cosmic ray spectra. We compare the cosmic ray ionization rate computed in our models to observational surveys and find that our models are reproduce the observed distribution. We show that the average cosmic ray ionization rate is on order of 10^{-16} s^{-1} rather than the canonical value of 10^{-17} s^{-1}. We directly test approximations used to infer the cosmic ray ionization rate from observations of molecular ions and find that the approximations are only valid locally in regions with a strong cosmic ray ionization rate and minimal irradiation by FUV radiation. We find that none of the column density ratios that are typically used are strongly sensitive to the cosmic ray ionization rate on molecular cloud scales.

The chemistry within molecular clouds is significantly altered due to embedded cosmic rays. The population of atomic carbon, both neutral and singly ionized, is greatly enhanced due to the increase in cosmic rays throughout the cloud. Neutral carbon no longer exists in a thin transitional layer and is instead found throughout the

cloud. The abundances of molecular ions, particularly N_2H^+ and HCO^+ are enhanced while neutral molecules, such as CO and NH_3 are significantly depleted. We conclude that including CR attenuation in PDR modeling using realistic cosmic ray spectra can help break the degeneracy found in astrochemical models between the density, cosmic ray ionization rate and FUV radiation.

In Chapter 6, we calculate the CO-to-H_2 and CI-to-H_2 conversion factors using the astrochemical models presented in Chapter 5. We show that embedded cosmic rays accelerated by protoclusters decrease both conversion factors. Models including embedded cosmic rays are consistent with the CO-to-H_2 conversion factor measured in the Milky Way for nearly all models with star formation efficiencies greater than a few percent. Embedded cosmic rays act to regulate the CO-to-H_2 conversion factor by keeping the total CO brightness constant. Protocluster cosmic rays do not significantly alter the amount of molecular Hydrogen, and although they dissociate carbon monoxide, they increase the gas temperature such that the total brightness of carbon monoxide is relatively constant. We find that the CI-to-H_2 conversion factor is incredibly sensitive to the assumed cosmic ray model. There is a large dispersion in the CI-to-H_2 conversion factor as a function of gas surface density and star formation efficiency.

Finally, in Chapter 7, we present preliminary results of a giant molecular cloud simulation hosting a protocluster. We introduce a novel adaptive six-ray algorithm to calculate the column density attenuating external radiation fields. The novel approach scales faster than the traditional approach and allows for rapid calculations in adaptive mesh refinement calculations with many levels. We show that the ray tracing algorithm accurately replicates the inverse power-law flux scaling for point sources and the analytic solution for one-sided irradiated models. We simulated a 16,000 $M_\odot$ molecular cloud including protostellar and external FUV radiation and protostellar outflows. We find that the resolution of the simulation is unable to properly resolve

the outflow cavities, disallowing any FUV from escaping the local protostellar environment. Observational studies of molecular clouds rely on using the line-of-sight column density as a proxy of the extinction from external radiation fields. We conclude that there is a significant dispersion in the average line-of-sight FUV radiation as a function of the column density. The use of column density as a proxy for the three-dimensional extinction may result in significant errors.

8.2 Orion2-Krome

Far ultra-violet radiation is of particular importance for the chemistry in molecular gas. Currently, in Orion2, the FUV radiation transfer is not directly coupled to the gas. Future developments of Orion2 will couple the hydrodynamic code to the microphysics package Krome[17][5]. Krome enables the user to define a chemical network and includes a wide range of thermodynamic physics, of particular importance is cooling due to the molecular line emission and heating from cosmic rays and far ultraviolet radiation. In order to properly model the chemistry, the far ultraviolet radiation must include self-shielding from molecular Hydrogen and carbon monoxide. We plan to implement an accurate self-shielding prescription using tabulated equivalent widths as a function of Doppler broadening and molecular hydrogen column density[316]. The ray tracing algorithm is easily expanded to include the necessary frequency bins to accomplish this. Once self-shielding is implemented, we will couple far ultraviolet radiation to the chemistry implemented in Orion2 through Krome.

Orion2-Krome will be used to perform simulations of protostellar cores and molecular clouds. The results of the simulations will be post-processed to generate predictions for the CI and CO radiation from star-forming molecular clouds. The simulations will also provide the density, temperature, far ultraviolet radiation and

[5]http://www.kromepackage.org

abundances of simple molecules throughout the domain. These will be used as inputs into 0-dimensional astrochemical codes that allow the inclusion of sophisticated gas-grain chemistry. The result of the post-processed chemistry will be the three-dimensional evolution of hundreds of molecules, from diatomic hydrides to complex organics.

8.3 High Energy Feedback

Molecular clouds are not just irradiated by far ultraviolet and ionizing ultraviolet radiation, but can also be immersed in high energy radiation such as x-rays and cosmic rays. Protostars have been shown to be x-ray bright during their Class I and II stages, and likely emit substantial x-rays at earlier times [317, 318]. Furthermore, nearby supernova increase the x-ray radiation impinging on the surface of molecular clouds from the hot plasma in the resulting shocks [319]. Currently, hydrodynamic simulations and astrochemical models of star-forming molecular clouds do not include embedded x-ray ionization sources. X-ray radiation from protostars will couple to the gas in a similar fashion as cosmic rays. We will include protostellar x-ray radiation and diffuse x-ray emission from supernova shocks in simulations of cluster formation and the collapse of isolated cores.

Cosmic rays are known to traverse through molecular gas in complex ways [15]. Cosmic rays undergo significant energy losses due to Coulomb interactions, ionizing interloping gas and pion production. Low energy cosmic rays couple to magnetic fields leading to streaming instabilities, mirroring, focusing, and anisotropic diffusion, with each effect being strongly dependent on the magnetic field strength. We plan to include magnetic field coupling to the cosmic ray transport implemented in Flash [240] to simulate protostellar cores and molecular clouds. Finally, the full cosmic ray transport equation can be solved in one-dimension numerically. Currently, the

expanded 3D-PDR includes cosmic ray attenuation only, which will be extended to solve the full transport equation.

The end stages of star formation feedback is typically considered to be supernova resulting from the deaths of high mass stars. However, the compact remnants, such as black holes and neutron stars, are bright in high energy radiation and accelerate cosmic rays. We will study the astrochemical impact of the feedback from compact objects with a blind line survey using the IRAM 30-meter radio telescope. We are targeting a Bok globule at a distance of 6 kpc which is back-irradiated by x-rays from the nearby microquasar Cygnus X-3 [320, 321]. We have been allocated 14 hours of time to do a blind line survey between 86 - 118 GHz, encompassing lines from simple molecules such as CO and CN, molecular ions, and a numerous complex organics and carbon-chain molecules.

BIBLIOGRAPHY

[1] T. M. Dame, Dap Hartmann, and P. Thaddeus. The Milky Way in Molecular Clouds: A New Complete CO Survey. *The Astrophysical Journal*, 547(2):792–813, Feb 2001. doi: 10.1086/318388.

[2] P. Swings and L. Rosenfeld. Considerations Regarding Interstellar Molecules. *The Astrophysical Journal*, 86:483–486, Nov 1937. doi: 10.1086/143880.

[3] A. McKellar. Evidence for the Molecular Origin of Some Hitherto Unidentified Interstellar Lines. *Publications of the Astronomical Society of the Pacific*, 52 (307):187, Jun 1940. doi: 10.1086/125159.

[4] W. S. Adams. Some Results with the COUDÉ Spectrograph of the Mount Wilson Observatory. *The Astrophysical Journal*, 93:11, jan 1941. doi: 10.1086/144237.

[5] Andrew M. Smith and Theodore P. Stecher. Carbon Monoxide in the Interstellar Spectrum of Zeta Ophiuchi. *The Astrophysical Journal*, 164:L43, Mar 1971. doi: 10.1086/180689.

[6] B. T. Soifer, R. C. Puetter, R. W. Russell, S. P. Willner, P. M. Harvey, and F. C. Gillett. The 4 - 8 micron spectrum of the infrared source W33 A. *The Astrophysical Journal*, 232:L53–L57, Aug 1979. doi: 10.1086/183035.

[7] J. H. Lacy, II Evans, Neal J., J. M. Achtermann, D. E. Bruce, J. F. Arens, and J. S. Carr. Discovery of Interstellar Acetylene. *The Astrophysical Journal*, 342: L43, Jul 1989. doi: 10.1086/185480.

[8] José Cernicharo, Javier R. Goicoechea, and Emmanuel Caux. Far-infrared Detection of C_3 in Sagittarius B2 and IRC +10216. *The Astrophysical Journal*, 534(2):L199–L202, May 2000. doi: 10.1086/312668.

[9] Brett A. McGuire. 2018 Census of Interstellar, Circumstellar, Extragalactic, Protoplanetary Disk, and Exoplanetary Molecules. *The Astrophysical Journal Supplement Series*, 239(2):17, Dec 2018. doi: 10.3847/1538-4365/aae5d2.

[10] A. G. G. M. Tielens, M. M. Meixner, P. P. van der Werf, J. Bregman, J. A. Tauber, J. Stutzki, and D. Rank. Anatomy of the Photodissociation Region in the Orion Bar. *Science*, 262(5130):86–89, Oct 1993. doi: 10.1126/science.262.5130.86.

[11] George R. Carruthers. Rocket Observation of Interstellar Molecular Hydrogen. *The Astrophysical Journal*, 161:L81, Aug 1970. doi: 10.1086/180575.

[12] R. W. Wilson, K. B. Jefferts, and A. A. Penzias. Carbon Monoxide in the Orion Nebula. *The Astrophysical Journal*, 161:L43, Jul 1970. doi: 10.1086/180567.

[13] B. T. Draine. *Physics of the Interstellar and Intergalactic Medium*. 2011.

[14] D. J. Hollenbach and A. G. G. M. Tielens. Photodissociation regions in the interstellar medium of galaxies. *Reviews of Modern Physics*, 71:173–230, January 1999. doi: 10.1103/RevModPhys.71.173.

[15] Reinhard Schlickeiser. *Cosmic Ray Astrophysics*. 2002.

[16] Valentine Wakelam, Herma M. Cuppen, and Eric Herbst. Astrochemistry: Synthesis and Modelling. *arXiv e-prints*, art. arXiv:1309.7792, Sep 2013.

[17] T. Grassi, S. Bovino, D. R. G. Schleicher, J. Prieto, D. Seifried, E. Simoncini, and F. A. Gianturco. KROME - a package to embed chemistry in astrophysical simulations. *Monthly Notices of the Royal Astronomical Society*, 439(3):2386–2419, Apr 2014. doi: 10.1093/mnras/stu114.

[18] D. McElroy, C. Walsh, A. J. Markwick, M. A. Cordiner, K. Smith, and T. J. Millar. The UMIST database for astrochemistry 2012. *Astronomy & Astrophysics*, 550:A36, feb 2013. doi: 10.1051/0004-6361/201220465.

[19] V. Wakelam, J. C. Loison, E. Herbst, B. Pavone, A. Bergeat, K. Béroff, M. Chabot, A. Faure, D. Galli, W. D. Geppert, D. Gerlich, P. Gratier, N. Harada, K. M. Hickson, P. Honvault, S. J. Klippenstein, S. D. Le Picard, G. Nyman, M. Ruaud, S. Schlemmer, I. R. Sims, D. Talbi, J. Tennyson, and R. Wester. The 2014 KIDA Network for Interstellar Chemistry. *The Astrophysical Journal Supplement Series*, 217(2):20, Apr 2015. doi: 10.1088/0067-0049/217/2/20.

[20] L. Reboussin, V. Wakelam, S. Guilloteau, and F. Hersant. Grain-surface reactions in molecular clouds: the effect of cosmic rays and quantum tunnelling. *Monthly Notices of the Royal Astronomical Society*, 440(4):3557–3567, Jun 2014. doi: 10.1093/mnras/stu462.

[21] O. Sipilä, P. Caselli, and J. Harju. Benchmarking spin-state chemistry in starless core models. *Astronomy & Astrophysics*, 578:A55, Jun 2015. doi: 10.1051/0004-6361/201424364.

[22] Maxime Ruaud, Valentine Wakelam, and Franck Hersant. Gas and grain chemical composition in cold cores as predicted by the Nautilus three-phase model. *Monthly Notices of the Royal Astronomical Society*, 459(4):3756–3767, Jul 2016. doi: 10.1093/mnras/stw887.

[23] L. Majumdar, P. Gratier, M. Ruaud, V. Wakelam, C. Vastel, O. Sipilä, F. Hersant, A. Dutrey, and S. Guilloteau. Chemistry of TMC-1 with multiply deuterated species and spin chemistry of H_2, H_2^+, H_3^+ and their isotopologues. *Monthly Notices of the Royal Astronomical Society*, 466(4):4470–4479, Apr 2017. doi: 10.1093/mnras/stw3360.

[24] David Quénard, Izaskun Jiménez-Serra, Serena Viti, Jonathan Holdship, and Audrey Coutens. Chemical modelling of complex organic molecules with peptide-like bonds in star-forming regions. *Monthly Notices of the Royal Astronomical Society*, 474(2):2796–2812, Feb 2018. doi: 10.1093/mnras/stx2960.

[25] R. P. Nelson and W. D. Langer. The Dynamics of Low-Mass Molecular Clouds in External Radiation Fields. *The Astrophysical Journal*, 482:796–826, June 1997. doi: 10.1086/304167.

[26] S. C. O. Glover, C. Federrath, M. M. Mac Low, and R. S. Klessen. Modelling CO formation in the turbulent interstellar medium. *Monthly Notices of the Royal Astronomical Society*, 404(1):2–29, May 2010. doi: 10.1111/j.1365-2966.2009.15718.x.

[27] T. A. Bell, S. Viti, D. A. Williams, I. A. Crawford, and R. J. Price. The chemistry of transient microstructure in the diffuse interstellar medium. *Monthly Notices of the Royal Astronomical Society*, 357:961–966, March 2005. doi: 10.1111/j.1365-2966.2005.08693.x.

[28] T. A. Bell, E. Roueff, S. Viti, and D. A. Williams. Molecular line intensities as measures of cloud masses - I. Sensitivity of CO emissions to physical parameter variations. *Monthly Notices of the Royal Astronomical Society*, 371:1865–1872, oct 2006. doi: 10.1111/j.1365-2966.2006.10817.x.

[29] F. D. Priestley, M. J. Barlow, and S. Viti. Modelling the ArH^+ emission from the Crab nebula. *Monthly Notices of the Royal Astronomical Society*, 472(4): 4444–4455, Dec 2017. doi: 10.1093/mnras/stx2327.

[30] T. G. Bisbas, T. A. Bell, S. Viti, J. Yates, and M. J. Barlow. 3D-PDR: a new three-dimensional astrochemistry code for treating photodissociation regions. *Monthly Notices of the Royal Astronomical Society*, 427:2100–2118, dec 2012. doi: 10.1111/j.1365-2966.2012.22077.x.

[31] Franck Le Petit, Cyrine Nehmé, Jacques Le Bourlot, and Evelyne Roueff. A Model for Atomic and Molecular Interstellar Gas: The Meudon PDR Code. *The Astrophysical Journal Supplement Series*, 164(2):506–529, Jun 2006. doi: 10.1086/503252.

[32] M. Röllig, V. Ossenkopf, S. Jeyakumar, J. Stutzki, and A. Sternberg. [CII] 158 μm emission and metallicity in photon dominated regions. *Astronomy & Astrophysics*, 451(3):917–924, Jun 2006. doi: 10.1051/0004-6361:20053845.

[33] G. J. Ferland, K. T. Korista, D. A. Verner, J. W. Ferguson, J. B. Kingdon, and E. M. Verner. CLOUDY 90: Numerical Simulation of Plasmas and Their Spectra. *Publications of the Astronomical Society of the Pacific*, 110(749):761–778, Jul 1998. doi: 10.1086/316190.

[34] G. Shaw, G. J. Ferland, N. P. Abel, P. C. Stancil, and P. A. M. van Hoof. Molecular Hydrogen in Star-forming Regions: Implementation of its Microphysics in CLOUDY. *The Astrophysical Journal*, 624(2):794–807, May 2005. doi: 10.1086/429215.

[35] F. F. S. van der Tak, J. H. Black, F. L. Schöier, D. J. Jansen, and E. F. van Dishoeck. A computer program for fast non-LTE analysis of interstellar line spectra. With diagnostic plots to interpret observed line intensity ratios. *Astronomy & Astrophysics*, 468(2):627–635, Jun 2007. doi: 10.1051/0004-6361:20066820.

[36] A. D. Bolatto, M. Wolfire, and A. K. Leroy. The CO-to-H_2 Conversion Factor. *Annual Review of Astronomy and Astrophysics*, 51:207–268, aug 2013. doi: 10.1146/annurev-astro-082812-140944.

[37] N. A. Ridge, J. Di Francesco, H. Kirk, D. Li, A. A. Goodman, J. F. Alves, H. G. Arce, M. A. Borkin, P. Caselli, J. B. Foster, M. H. Heyer, D. Johnstone, D. A. Kosslyn, M. Lombardi, J. E. Pineda, S. L. Schnee, and M. Tafalla. The COMPLETE Survey of Star-Forming Regions: Phase I Data. *Astronomical Journal*, 131:2921–2933, June 2006. doi: 10.1086/503704.

[38] Rachel K. Friesen, Jaime E. Pineda, co-PIs, Erik Rosolowsky, Felipe Alves, Ana Chacón-Tanarro, Hope How-Huan Chen, Michael Chun-Yuan Chen, James Di Francesco, Jared Keown, Helen Kirk, Anna Punanova, Youngmin Seo, Yancy Shirley, Adam Ginsburg, Christine Hall, Stella S. R. Offner, Ayushi Singh, Héctor G. Arce, Paola Caselli, Alyssa A. Goodman, Peter G. Martin, Christopher Matzner, Philip C. Myers, Elena Redaelli, and GAS Collaboration. The Green Bank Ammonia Survey: First Results of NH_3 Mapping of the Gould Belt. *The Astrophysical Journal*, 843(1):63, Jul 2017. doi: 10.3847/1538-4357/aa6d58.

[39] R. C. Kennicutt and N. J. Evans. Star Formation in the Milky Way and Nearby Galaxies. *Annual Review of Astronomy and Astrophysics*, 50:531–608, September 2012. doi: 10.1146/annurev-astro-081811-125610.

[40] J. C. Tan, M. T. Beltrán, P. Caselli, F. Fontani, A. Fuente, M. R. Krumholz, C. F. McKee, and A. Stolte. Massive Star Formation. *Protostars and Planets VI*, pages 149–172, 2014. doi: 10.2458/azu_uapress_9780816531240-ch007.

[41] C. F. McKee and E. C. Ostriker. Theory of Star Formation. *Annual Review of Astronomy and Astrophysics*, 45:565–687, sep 2007. doi: 10.1146/annurev.astro.45.051806.110602.

[42] M. M. Dunham, A. M. Stutz, L. E. Allen, N. J. Evans, II, W. J. Fischer, S. T. Megeath, P. C. Myers, S. S. R. Offner, C. A. Poteet, J. J. Tobin, and E. I. Vorobyov. The Evolution of Protostars: Insights from Ten Years of Infrared Surveys with Spitzer and Herschel. *Protostars and Planets VI*, pages 195–218, 2014. doi: 10.2458/azu_uapress_9780816531240-ch009.

[43] Ralf S. Klessen, Mark R. Krumholz, and Fabian Heitsch. Numerical Star-Formation Studies - A Status Report. *Advanced Science Letters*, 4(2):258–285, Feb 2011. doi: 10.1166/asl.2011.1207.

[44] Christoph Federrath. On the universality of interstellar filaments: theory meets simulations and observations. *Monthly Notices of the Royal Astronomical Society*, 457(1):375–388, Mar 2016. doi: 10.1093/mnras/stv2880.

[45] Ph. André, V. Könyves, D. Arzoumanian, and A. Roy. Molecular filaments and the origin of the IMF. *Memorie della Societa Astronomica Italiana*, 88:521, Jan 2017.

[46] Planck Collaboration, P. A. R. Ade, N. Aghanim, M. I. R. Alves, M. Arnaud, D. Arzoumanian, M. Ashdown, J. Aumont, C. Baccigalupi, A. J. Band ay, R. B. Barreiro, N. Bartolo, E. Battaner, K. Benabed, A. Benoît, A. Benoit-Lévy, J. P. Bernard, M. Bersanelli, P. Bielewicz, J. J. Bock, L. Bonavera, J. R. Bond, J. Borrill, F. R. Bouchet, F. Boulanger, A. Bracco, C. Burigana, E. Calabrese, J. F. Cardoso, A. Catalano, H. C. Chiang, P. R. Christensen, L. P. L. Colombo, C. Combet, F. Couchot, B. P. Crill, A. Curto, F. Cuttaia, L. Danese, R. D. Davies, R. J. Davis, P. de Bernardis, A. de Rosa, G. de Zotti, J. Delabrouille, C. Dickinson, J. M. Diego, H. Dole, S. Donzelli, O. Doré, M. Douspis, A. Ducout, X. Dupac, G. Efstathiou, F. Elsner, T. A. Enßlin, H. K. Eriksen, D. Falceta-Gonçalves, E. Falgarone, K. Ferrière, F. Finelli, O. Forni, M. Frailis, A. A. Fraisse, E. Franceschi, A. Frejsel, S. Galeotta, S. Galli, K. Ganga, T. Ghosh, M. Giard, E. Gjerløw, J. González-Nuevo, K. M. Górski, A. Gregorio, A. Gruppuso, J. E. Gudmundsson, V. Guillet, D. L. Harrison, G. Helou, P. Hennebelle, S. Henrot-Versillé, C. Hernández-Monteagudo, D. Herranz, S. R. Hildebrand t, E. Hivon, W. A. Holmes, A. Hornstrup, K. M. Huffenberger, G. Hurier, A. H. Jaffe, T. R. Jaffe, W. C. Jones, M. Juvela, E. Keihänen, R. Keskitalo, T. S. Kisner, J. Knoche, M. Kunz, H. Kurki-Suonio, G. Lagache, J. M. Lamarre, A. Lasenby, M. Lattanzi, C. R. Lawrence, R. Leonardi, F. Levrier, M. Liguori, P. B. Lilje, M. Linden-Vørnle, M. López-Caniego, P. M. Lubin, J. F. Macías-Pérez, D. Maino, N. Mandolesi, A. Mangilli, M. Maris, P. G. Martin, E. Martínez-González, S. Masi, S. Matarrese, A. Melchiorri, L. Mendes, A. Mennella, M. Migliaccio, M. A. Miville-Deschênes, A. Moneti, L. Montier, G. Morgante, D. Mortlock, D. Munshi, J. A. Murphy, P. Naselsky, F. Nati, C. B. Netterfield, F. Noviello, D. Novikov, I. Novikov, N. Oppermann, C. A. Oxborrow, L. Pagano, F. Pajot, R. Paladini, D. Paoletti, F. Pasian, L. Perotto, V. Pettorino, F. Piacentini, M. Piat, E. Pierpaoli, D. Pietrobon, S. Plaszczynski, E. Pointecouteau, G. Polenta, N. Ponthieu, G. W. Pratt, S. Prunet, J. L. Puget, J. P. Rachen, M. Reinecke, M. Remazeilles, C. Renault, A. Renzi, I. Ristorcelli, G. Rocha, M. Rossetti, G. Roudier, J. A. Rubiño-Martín, B. Rusholme, M. Sandri, D. Santos, M. Savelainen, G. Savini, D. Scott, J. D. Soler, V. Stolyarov, R. Sudiwala, D. Sutton, A. S. Suur-Uski, J. F. Sygnet, J. A. Tauber, L. Terenzi, L. Toffolatti, M. Tomasi, M. Tristram, M. Tucci, G. Umana, L. Valenziano, J. Valiviita, B. Van Tent, P. Vielva, F. Villa, L. A. Wade, B. D. Wandelt, I. K. Wehus, N. Ysard, D. Yvon, and A. Zonca. Planck intermediate results. XXXV. Probing the role of the magnetic field in the formation of structure in molecular clouds. *Astronomy & Astrophysics*, 586:A138, Feb 2016. doi: 10.1051/0004-6361/201525896.

[47] K. M. Menten, M. J. Reid, J. Forbrich, and A. Brunthaler. The distance to the Orion Nebula. *Astronomy & Astrophysics*, 474(2):515–520, Nov 2007. doi: 10.1051/0004-6361:20078247.

[48] E. Kryukova, S. T. Megeath, R. A. Gutermuth, J. Pipher, T. S. Allen, L. E. Allen, P. C. Myers, and J. Muzerolle. Luminosity Functions of Spitzer-identified Protostars in Nine Nearby Molecular Clouds. *Astronomical Journal*, 144:31, August 2012. doi: 10.1088/0004-6256/144/2/31.

[49] B. Reipurth, C. J. Clarke, A. P. Boss, S. P. Goodwin, L. F. Rodríguez, K. G. Stassun, A. Tokovinin, and H. Zinnecker. Multiplicity in Early Stellar Evolution. In Henrik Beuther, Ralf S. Klessen, Cornelis P. Dullemond, and Thomas Henning, editors, *Protostars and Planets VI*, page 267, Jan 2014. doi: 10.2458/azu_uapress_9780816531240-ch012.

[50] S. S. R. Offner and C. F. McKee. The Protostellar Luminosity Function. *The Astrophysical Journal*, 736:53, July 2011. doi: 10.1088/0004-637X/736/1/53.

[51] G. Chabrier. The Initial Mass Function: From Salpeter 1955 to 2005. In E. Corbelli, F. Palla, and H. Zinnecker, editors, *The Initial Mass Function 50 Years Later*, volume 327 of *Astrophysics and Space Science Library*, page 41, January 2005. doi: 10.1007/978-1-4020-3407-7_5.

[52] S. S. R. Offner, P. C. Clark, P. Hennebelle, N. Bastian, M. R. Bate, P. F. Hopkins, E. Moraux, and A. P. Whitworth. The Origin and Universality of the Stellar Initial Mass Function. In Henrik Beuther, Ralf S. Klessen, Cornelis P. Dullemond, and Thomas Henning, editors, *Protostars and Planets VI*, page 53, Jan 2014. doi: 10.2458/azu_uapress_9780816531240-ch003.

[53] Deepak Raghavan, Harold A. McAlister, Todd J. Henry, David W. Latham, Geoffrey W. Marcy, Brian D. Mason, Douglas R. Gies, Russel J. White, and Theo A. ten Brummelaar. A Survey of Stellar Families: Multiplicity of Solar-type Stars. *The Astrophysical Journal Supplement Series*, 190(1):1–42, Sep 2010. doi: 10.1088/0067-0049/190/1/1.

[54] Gaspard Duchêne and Adam Kraus. Stellar Multiplicity. *Annual Review of Astronomy and Astrophysics*, 51(1):269–310, Aug 2013. doi: 10.1146/annurev-astro-081710-102602.

[55] John J. Tobin, Marina Kounkel, Stella Offner, Patrick Sheehan, Doug Johnstone, S. Thomas Megeath, Kaitlin M. Kratter, Ian Stephens, Zhi-Yun Li, Sarah Sadavoy, Leslie Looney, Joel Green, Rob Gutermuth, Will Fischer, Michael M. Dunham, and Yao-Lun Yang. Astro2020 Science White Paper: The Formation and Evolution of Multiple Star Systems. *arXiv e-prints*, art. arXiv:1904.08442, Apr 2019.

[56] Paolo Padoan and Åke Nordlund. The Stellar Initial Mass Function from Turbulent Fragmentation. *The Astrophysical Journal*, 576(2):870–879, Sep 2002. doi: 10.1086/341790.

[57] Stella S. R. Offner, Kaitlin M. Kratter, Christopher D. Matzner, Mark R. Krumholz, and Richard I. Klein. The Formation of Low-mass Binary Star Systems Via Turbulent Fragmentation. *The Astrophysical Journal*, 725(2):1485–1494, Dec 2010. doi: 10.1088/0004-637X/725/2/1485.

[58] Kaitlin M. Kratter, Christopher D. Matzner, Mark R. Krumholz, and Richard I. Klein. On the Role of Disks in the Formation of Stellar Systems: A Numerical Parameter Study of Rapid Accretion. *The Astrophysical Journal*, 708(2):1585–1597, Jan 2010. doi: 10.1088/0004-637X/708/2/1585.

[59] M. M. Dunham, H. G. Arce, L. E. Allen, N. J. Evans, II, H. Broekhoven-Fiene, N. L. Chapman, L. A. Cieza, R. A. Gutermuth, P. M. Harvey, J. Hatchell, T. L. Huard, J. M. Kirk, B. C. Matthews, B. Merín, J. F. Miller, D. E. Peterson, and L. Spezzi. The Luminosities of Protostars in the Spitzer c2d and Gould Belt Legacy Clouds. *Astronomical Journal*, 145:94, April 2013. doi: 10.1088/0004-6256/145/4/94.

[60] M. R. Krumholz, M. R. Bate, H. G. Arce, J. E. Dale, R. Gutermuth, R. I. Klein, Z.-Y. Li, F. Nakamura, and Q. Zhang. Star Cluster Formation and Feedback. *Protostars and Planets VI*, pages 243–266, 2014. doi: 10.2458/azu_uapress_9780816531240-ch011.

[61] S. S. R. Offner, R. I. Klein, C. F. McKee, and M. R. Krumholz. The Effects of Radiative Transfer on Low-Mass Star Formation. *The Astrophysical Journal*, 703:131–149, September 2009. doi: 10.1088/0004-637X/703/1/131.

[62] Anna L. Rosen, Mark R. Krumholz, Christopher F. McKee, and Richard I. Klein. An unstable truth: how massive stars get their mass. *Monthly Notices of the Royal Astronomical Society*, 463(3):2553–2573, Dec 2016. doi: 10.1093/mnras/stw2153.

[63] A. Frank, T. P. Ray, S. Cabrit, P. Hartigan, H. G. Arce, F. Bacciotti, J. Bally, M. Benisty, J. Eislöffel, M. Güdel, S. Lebedev, B. Nisini, and A. Raga. Jets and Outflows from Star to Cloud: Observations Confront Theory. In Henrik Beuther, Ralf S. Klessen, Cornelis P. Dullemond, and Thomas Henning, editors, *Protostars and Planets VI*, page 451, Jan 2014. doi: 10.2458/azu_uapress_9780816531240-ch020.

[64] John Bally. Protostellar Outflows. *Annual Review of Astronomy and Astrophysics*, 54:491–528, Sep 2016. doi: 10.1146/annurev-astro-081915-023341.

[65] Zhi-Yun Li and Fumitaka Nakamura. Cluster Formation in Protostellar Outflow-driven Turbulence. *The Astrophysical Journal*, 640(2):L187–L190, Apr 2006. doi: 10.1086/503419.

[66] Christopher D. Matzner. Protostellar Outflow-driven Turbulence. *The Astrophysical Journal*, 659(2):1394–1403, Apr 2007. doi: 10.1086/512361.

[67] Fumitaka Nakamura and Zhi-Yun Li. Protostellar Turbulence Driven by Collimated Outflows. *The Astrophysical Journal*, 662(1):395–412, Jun 2007. doi: 10.1086/517515.

[68] S. S. R. Offner and J. Chaban. Impact of Protostellar Outflows on Turbulence and Star Formation Efficiency in Magnetized Dense Cores. *The Astrophysical Journal*, 847:104, October 2017. doi: 10.3847/1538-4357/aa8996.

[69] Adele L. Plunkett, Héctor G. Arce, Stuartt A. Corder, Diego Mardones, Anneila I. Sargent, and Scott L. Schnee. CARMA Observations of Protostellar Outflows in NGC 1333. *The Astrophysical Journal*, 774(1):22, Sep 2013. doi: 10.1088/0004-637X/774/1/22.

[70] Stella S. R. Offner and Yue Liu. Turbulent action at a distance due to stellar feedback in magnetized clouds. *Nature Astronomy*, 2:896–900, Sep 2018. doi: 10.1038/s41550-018-0566-1.

[71] Donald E. Osterbrock and Gary J. Ferland. *Astrophysics of gaseous nebulae and active galactic nuclei*. 2006.

[72] Bengt Strömgren. The Physical State of Interstellar Hydrogen. *The Astrophysical Journal*, 89:526, May 1939. doi: 10.1086/144074.

[73] Lyman Spitzer. *Physical processes in the interstellar medium*. 1978. doi: 10.1002/9783527617722.

[74] Mordecai-Mark Mac Low, Jayashree Toraskar, Jeffrey S. Oishi, and Tom Abel. Dynamical Expansion of H II Regions from Ultracompact to Compact Sizes in Turbulent, Self-gravitating Molecular Clouds. *The Astrophysical Journal*, 668 (2):980–992, Oct 2007. doi: 10.1086/521292.

[75] S. K. Walch, A. P. Whitworth, T. Bisbas, R. Wünsch, and D. Hubber. Dispersal of molecular clouds by ionizing radiation. *Monthly Notices of the Royal Astronomical Society*, 427(1):625–636, Nov 2012. doi: 10.1111/j.1365-2966.2012.21767.x.

[76] E. W. Pellegrini, J. A. Baldwin, and G. J. Ferland. Structure and Feedback in 30 Doradus. II. Structure and Chemical Abundances. *The Astrophysical Journal*, 738(1):34, Sep 2011. doi: 10.1088/0004-637X/738/1/34.

[77] Laura A. Lopez, Mark R. Krumholz, Alberto D. Bolatto, J. Xavier Prochaska, and Enrico Ramirez-Ruiz. What Drives the Expansion of Giant H II Regions?: A Study of Stellar Feedback in 30 Doradus. *The Astrophysical Journal*, 731(2):91, Apr 2011. doi: 10.1088/0004-637X/731/2/91.

[78] Laura A. Lopez, Mark R. Krumholz, Alberto D. Bolatto, J. Xavier Prochaska, Enrico Ramirez-Ruiz, and Daniel Castro. The Role of Stellar Feedback in the Dynamics of H II Regions. *The Astrophysical Journal*, 795(2):121, Nov 2014. doi: 10.1088/0004-637X/795/2/121.

[79] S. Walch, P. Girichidis, T. Naab, A. Gatto, S. C. O. Glover, R. Wünsch, R. S. Klessen, P. C. Clark, T. Peters, D. Derigs, and C. Baczynski. The SILCC (SImulating the LifeCycle of molecular Clouds) project - I. Chemical evolution of the supernova-driven ISM. *Monthly Notices of the Royal Astronomical Society*, 454:238–268, November 2015. doi: 10.1093/mnras/stv1975.

[80] M. Padovani, A. Marcowith, P. Hennebelle, and K. Ferrière. Protostars: Forges of cosmic rays? *Astronomy & Astrophysics*, 590:A8, May 2016. doi: 10.1051/0004-6361/201628221.

[81] Brandt A. L. Gaches and Stella S. R. Offner. Exploration of Cosmic-ray Acceleration in Protostellar Accretion Shocks and a Model for Ionization Rates in Embedded Protoclusters. *The Astrophysical Journal*, 861:87, Jul 2018. doi: 10.3847/1538-4357/aac94d.

[82] R. Schlickeiser, M. Caglar, and A. Lazarian. Cosmic Rays and MHD Turbulence Generation in Interstellar Giant Molecular Clouds. *The Astrophysical Journal*, 824(2):89, Jun 2016. doi: 10.3847/0004-637X/824/2/89.

[83] A. Dalgarno. Interstellar Chemistry Special Feature: The galactic cosmic ray ionization rate. *Proceedings of the National Academy of Science*, 103:12269–12273, August 2006. doi: 10.1073/pnas.0602117103.

[84] Rachael E. Ainsworth, Anna M. M. Scaife, Tom P. Ray, Andrew M. Taylor, David A. Green, and Jane V. Buckle. Tentative Evidence for Relativistic Electrons Generated by the Jet of the Young Sun-like Star DG Tau. *The Astrophysical Journal*, 792(1):L18, Sep 2014. doi: 10.1088/2041-8205/792/1/L18.

[85] Adriana Rodríguez-Kamenetzky, Carlos Carrasco-González, Anabella Araudo, Gustavo E. Romero, José M. Torrelles, Luis F. Rodríguez, Guillem Anglada, Josep Martí, Manel Perucho, and Carlos Valotto. The Highly Collimated Radio Jet of HH 80-81: Structure and Nonthermal Emission. *The Astrophysical Journal*, 851(1):16, Dec 2017. doi: 10.3847/1538-4357/aa9895.

[86] C. Ceccarelli, C. Dominik, A. López-Sepulcre, M. Kama, M. Padovani, E. Caux, and P. Caselli. Herschel Finds Evidence for Stellar Wind Particles in a Protostellar Envelope: Is This What Happened to the Young Sun? *The Astrophysical Journal Letters*, 790:L1, July 2014. doi: 10.1088/2041-8205/790/1/L1.

[87] L. Podio, B. Lefloch, C. Ceccarelli, C. Codella, and R. Bachiller. Molecular ions in the protostellar shock L1157-B1. *Astronomy & Astrophysics*, 565:A64, May 2014. doi: 10.1051/0004-6361/201322928.

[88] C. Favre, A. López-Sepulcre, C. Ceccarelli, C. Dominik, P. Caselli, E. Caux, A. Fuente, M. Kama, J. Le Bourlot, B. Lefloch, D. Lis, T. Montmerle, M. Padovani, and C. Vastel. The onset of energetic particle irradiation in Class 0 protostars. *Astronomy & Astrophysics*, 608:A82, December 2017. doi: 10.1051/0004-6361/201630177.

[89] C. Favre, C. Ceccarelli, A. López-Sepulcre, F. Fontani, R. Neri, S. Manigand, M. Kama, P. Caselli, A. Jaber Al-Edhari, C. Kahane, F. Alves, N. Balucani, E. Bianchi, E. Caux, C. Codella, F. Dulieu, J. E. Pineda, I. R. Sims, and P. Theulé. SOLIS IV. Hydrocarbons in the OMC-2 FIR4 Region, a Probe of Energetic Particle Irradiation of the Region. *The Astrophysical Journal*, 859: 136, June 2018. doi: 10.3847/1538-4357/aabfd4.

[90] Brandt A. L. Gaches, Stella S. R. Offner, Erik W. Rosolowsky, and Thomas G. Bisbas. Astrochemical Correlations in Molecular Clouds. *The Astrophysical Journal*, 799:235, Feb 2015. doi: 10.1088/0004-637X/799/2/235.

[91] S. C. O. Glover and M.-M. Mac Low. On the relationship between molecular hydrogen and carbon monoxide abundances in molecular clouds. *Monthly Notices of the Royal Astronomical Society*, 412:337–350, mar 2011. doi: 10.1111/j.1365-2966.2010.17907.x.

[92] R. Shetty, S. C. Glover, C. P. Dullemond, and R. S. Klessen. Modelling CO emission - I. CO as a column density tracer and the X factor in molecular clouds. *Monthly Notices of the Royal Astronomical Society*, 412:1686–1700, apr 2011. doi: 10.1111/j.1365-2966.2010.18005.x.

[93] A. Bacmann, B. Lefloch, C. Ceccarelli, A. Castets, J. Steinacker, and L. Loinard. The degree of CO depletion in pre-stellar cores. *Astronomy & Astrophysics*, 389: L6–L10, July 2002. doi: 10.1051/0004-6361:20020652.

[94] E. A. Bergin and M. Tafalla. Cold Dark Clouds: The Initial Conditions for Star Formation. *Annual Review of Astronomy and Astrophysics*, 45:339–396, September 2007. doi: 10.1146/annurev.astro.45.071206.100404.

[95] S. Hocuk, S. Cazaux, and M. Spaans. The impact of freeze-out on collapsing molecular clouds. *Monthly Notices of the Royal Astronomical Society*, 438:L56–L60, February 2014. doi: 10.1093/mnrasl/slt158.

[96] A. A. Goodman, J. A. Barranco, D. J. Wilner, and M. H. Heyer. Coherence in Dense Cores. II. The Transition to Coherence. *The Astrophysical Journal*, 504: 223–246, September 1998. doi: 10.1086/306045.

[97] A. J. Porras, S. R. Federman, D. E. Welty, and A. M. Ritchey. OH^+ in Diffuse Molecular Clouds. *The Astrophysical Journal Letters*, 781:L8, jan 2014. doi: 10.1088/2041-8205/781/1/L8.

[98] Jürgen Ott, Michael Burton, Paul Jones, and David S. Meier. Shock structure and shock heating in the Galactic central molecular zone. In L. O. Sjouwerman, C. C. Lang, and J. Ott, editors, *The Galactic Center: Feeding and Feedback in a Normal Galactic Nucleus*, volume 303 of *IAU Symposium*, pages 104–105, May 2014. doi: 10.1017/S1743921314000283.

[99] E. W. Rosolowsky, J. E. Pineda, J. B. Foster, M. A. Borkin, J. Kauffmann, P. Caselli, P. C. Myers, and A. A. Goodman. An Ammonia Spectral Atlas of Dense Cores in Perseus. *The Astrophysical Journal Supplement Series*, 175: 509–521, apr 2008. doi: 10.1086/524299.

[100] E. Rosolowsky, J. E. Pineda, and Y. Gao. Minimal HCN emission from molecular clouds in M33. *Monthly Notices of the Royal Astronomical Society*, 415: 1977–1984, aug 2011. doi: 10.1111/j.1365-2966.2011.18851.x.

[101] P. Sanhueza, J. M. Jackson, J. B. Foster, G. Garay, A. Silva, and S. C. Finn. Chemistry in Infrared Dark Cloud Clumps: A Molecular Line Survey at 3 mm. *The Astrophysical Journal*, 756:60, sep 2012. doi: 10.1088/0004-637X/756/1/60.

[102] Nanase Harada, Denise Riquelme, Serena Viti, Karl Menten, Miguel Requena-Torres, Rolf Güsten, and Stefan Hochgürtel. Molecules in the circumnuclear disk of the Galactic center. In L. O. Sjouwerman, C. C. Lang, and J. Ott, editors, *The Galactic Center: Feeding and Feedback in a Normal Galactic Nucleus*, volume 303 of *IAU Symposium*, pages 78–82, May 2014. doi: 10.1017/S1743921314000209.

[103] T. Vasyunina, A. I. Vasyunin, E. Herbst, H. Linz, M. Voronkov, T. Britton, I. Zinchenko, and F. Schuller. Organic Species in Infrared Dark Clouds. *The Astrophysical Journal*, 780:85, jan 2014. doi: 10.1088/0004-637X/780/1/85.

[104] M. Röllig, N. P. Abel, T. Bell, F. Bensch, J. Black, G. J. Ferland, B. Jonkheid, I. Kamp, M. J. Kaufman, J. Le Bourlot, F. Le Petit, R. Meijerink, O. Morata, V. Ossenkopf, E. Roueff, G. Shaw, M. Spaans, A. Sternberg, J. Stutzki, W.-F. Thi, E. F. van Dishoeck, P. A. M. van Hoof, S. Viti, and M. G. Wolfire. A photon dominated region code comparison study. *Astronomy & Astrophysics*, 467:187–206, may 2007. doi: 10.1051/0004-6361:20065918.

[105] S. Bruderer, A. O. Benz, S. D. Doty, E. F. van Dishoeck, and T. L. Bourke. Multidimensional Chemical Modeling of Young Stellar Objects. II. Irradiated Outflow Walls in a High-Mass Star-Forming Region. *The Astrophysical Journal*, 700:872–886, jul 2009. doi: 10.1088/0004-637X/700/1/872.

[106] P. Woitke, I. Kamp, and W.-F. Thi. Radiation thermo-chemical models of protoplanetary disks. I. Hydrostatic disk structure and inner rim. *Astronomy & Astrophysics*, 501:383–406, jul 2009. doi: 10.1051/0004-6361/200911821.

[107] M. Spaans and E. F. van Dishoeck. Physical models of photon-dominated regions: influence of clumpiness and geometry for S 140. *Astronomy & Astrophysics*, 323:953–962, July 1997.

[108] M. Cubick, J. Stutzki, V. Ossenkopf, C. Kramer, and M. Röllig. A clumpy-cloud photon-dominated regions model of the global far-infrared line emission of the Milky Way. *Astronomy & Astrophysics*, 488:623–634, sep 2008. doi: 10.1051/0004-6361:20079270.

[109] C. Kramer, M. Cubick, M. Röllig, K. Sun, Y. Yonekura, M. Aravena, F. Bensch, F. Bertoldi, L. Bronfman, M. Fujishita, Y. Fukui, U. U. Graf, M. Hitschfeld, N. Honingh, S. Ito, H. Jakob, K. Jacobs, U. Klein, B.-C. Koo, J. May, M. Miller, Y. Miyamoto, N. Mizuno, T. Onishi, Y.-S. Park, J. L. Pineda, D. Rabanus, H. Sasago, R. Schieder, R. Simon, J. Stutzki, N. Volgenau, and H. Yamamoto. Clumpy photon-dominated regions in Carina. I. [C I] and mid-J CO lines in two 4'x4' fields. *Astronomy & Astrophysics*, 477:547–555, January 2008. doi: 10.1051/0004-6361:20077815.

[110] P. P. Papadopoulos, W.-F. Thi, and S. Viti. CI lines as tracers of molecular gas, and their prospects at high redshifts. *Monthly Notices of the Royal Astronomical Society*, 351:147–160, June 2004. doi: 10.1111/j.1365-2966.2004.07762.x.

[111] Simon C. O. Glover, Paul C. Clark, Milica Micic, and Faviola Molina. Modelling [C I] emission from turbulent molecular clouds. *Monthly Notices of the Royal Astronomical Society*, 448:1607–1627, Apr 2015. doi: 10.1093/mnras/stu2699.

[112] S. S. R. Offner, T. G. Bisbas, T. A. Bell, and S. Viti. An alternative accurate tracer of molecular clouds: the 'X_{CI}-factor'. *Monthly Notices of the Royal Astronomical Society*, feb 2014. doi: 10.1093/mnrasl/slu013.

[113] M. G. Wolfire, D. Hollenbach, and C. F. McKee. The Dark Molecular Gas. *The Astrophysical Journal*, 716:1191–1207, jun 2010. doi: 10.1088/0004-637X/716/2/1191.

[114] J. K. Truelove, R. I. Klein, C. F. McKee, J. H. Holliman, II, L. H. Howell, J. A. Greenough, and D. T. Woods. Self-gravitational hydrodynamics with three-dimensional adaptive mesh refinement: Methodology and applications to molecular cloud collapse and fragmentation. *The Astrophysical Journal*, 495:821–852, March 1998. doi: 10.1086/305329.

[115] R. I. Klein. Star formation with 3-D adaptive mesh refinement: the collapse and fragmentation of molecular clouds. *Journal of Computational and Applied Mathematics*, 109:123–152, sep 1999.

[116] S. S. R. Offner, T. G. Bisbas, S. Viti, and T. A. Bell. Modeling the Atomic-to-molecular Transition and Chemical Distributions of Turbulent Star-forming Clouds. *The Astrophysical Journal*, 770:49, jun 2013. doi: 10.1088/0004-637X/770/1/49.

[117] J. K. Truelove, R. I. Klein, C. F. McKee, J. H. Holliman, II, L. H. Howell, and J. A. Greenough. The Jeans Condition: A New Constraint on Spatial Resolution in Simulations of Isothermal Self-gravitational Hydrodynamics. *The Astrophysical Journal Letters*, 489:L179+, nov 1997. doi: 10.1086/316779.

[118] M. R. Krumholz, C. F. McKee, and R. I. Klein. Embedding Lagrangian Sink Particles in Eulerian Grids. *The Astrophysical Journal*, 611:399–412, August 2004. doi: 10.1086/421935.

[119] B. T. Draine. Photoelectric heating of interstellar gas. *The Astrophysical Journal Supplement Series*, 36:595–619, apr 1978. doi: 10.1086/190513.

[120] K. M. Górski, E. Hivon, A. J. Banday, B. D. Wandelt, F. K. Hansen, M. Reinecke, and M. Bartelmann. HEALPix: A Framework for High-Resolution Discretization and Fast Analysis of Data Distributed on the Sphere. *The Astrophysical Journal*, 622:759–771, apr 2005. doi: 10.1086/427976.

[121] S. Cazaux and A. G. G. M. Tielens. Molecular Hydrogen Formation in the Interstellar Medium. *The Astrophysical Journal Letters*, 575:L29–L32, aug 2002. doi: 10.1086/342607.

[122] S. Cazaux and A. G. G. M. Tielens. H_2 Formation on Grain Surfaces. *The Astrophysical Journal*, 604:222–237, mar 2004. doi: 10.1086/381775.

[123] M. Asplund, N. Grevesse, A. J. Sauval, and P. Scott. The Chemical Composition of the Sun. *Annual Review of Astronomy and Astrophysics*, 47:481–522, September 2009. doi: 10.1146/annurev.astro.46.060407.145222.

[124] S. Viti, M. P. Collings, J. W. Dever, M. R. S. McCoustra, and D. A. Williams. Evaporation of ices near massive stars: models based on laboratory temperature programmed desorption data. *Monthly Notices of the Royal Astronomical Society*, 354:1141–1145, nov 2004. doi: 10.1111/j.1365-2966.2004.08273.x.

[125] E. Falgarone, T. G. Phillips, and J. C. Pearson. First Detection of $^{13}CH^+$ (J=1-0). *The Astrophysical Journal Letters*, 634:L149–L152, dec 2005. doi: 10.1086/499047.

[126] E. Falgarone, J. Pety, and P. Hily-Blant. Intermittency of interstellar turbulence: extreme velocity-shears and CO emission on milliparsec scale. *Astronomy & Astrophysics*, 507:355–368, nov 2009. doi: 10.1051/0004-6361/200810963.

[127] V. V. Guzmán, J. R. Goicoechea, J. Pety, P. Gratier, M. Gerin, E. Roueff, F. Le Petit, J. Le Bourlot, and A. Faure. The IRAM-30 m line survey of the Horsehead PDR. IV. Comparative chemistry of H_2CO and CH_3OH. *Astronomy & Astrophysics*, 560:A73, December 2013. doi: 10.1051/0004-6361/201322460.

[128] S. C. O. Glover and P. C. Clark. Approximations for modelling CO chemistry in giant molecular clouds: a comparison of approaches. *Monthly Notices of the Royal Astronomical Society*, 421:116–131, March 2012. doi: 10.1111/j.1365-2966.2011.20260.x.

[129] F. L. Schöier, F. F. S. van der Tak, E. F. van Dishoeck, and J. H. Black. An atomic and molecular database for analysis of submillimetre line observations. *Astronomy & Astrophysics*, 432:369–379, mar 2005. doi: 10.1051/0004-6361:20041729.

[130] E. W. Rosolowsky, A. A. Goodman, D. J. Wilner, and J. P. Williams. The Spectral Correlation Function: A New Tool for Analyzing Spectral Line Maps. *The Astrophysical Journal*, 524:887–894, oct 1999. doi: 10.1086/307863.

[131] P. Padoan, A. A. Goodman, and M. Juvela. The Spectral Correlation Function of Molecular Clouds: A Statistical Test for Theoretical Models. *The Astrophysical Journal*, 588:881–893, may 2003. doi: 10.1086/374240.

[132] M. Yeremi, M. Flynn, S. Offner, J. Loeppky, and E. Rosolowsky. Comparing Simulated Emission from Molecular Clouds Using Experimental Design. *The Astrophysical Journal*, 783:93, mar 2014. doi: 10.1088/0004-637X/783/2/93.

[133] R. B. Larson. Turbulence and star formation in molecular clouds. *Monthly Notices of the Royal Astronomical Society*, 194:809–826, March 1981.

[134] R. Plume, D. T. Jaffe, K. Tatematsu, N. J. Evans, II, and J. Keene. Large-Scale C I Emission from Molecular Clouds with Associated Ultraviolet Sources. *The Astrophysical Journal*, 512:768–783, February 1999. doi: 10.1086/306780.

[135] M. Ikeda, H. Maezawa, T. Ito, G. Saito, Y. Sekimoto, S. Yamamoto, K. Tatematsu, Y. Arikawa, Y. Aso, T. Noguchi, S.-C. Shi, K. Miyazawa, S. Saito, H. Ozeki, H. Fujiwara, M. Ohishi, and J. Inatani. Large-Scale Mapping Observations of the C I ($^3P_1$- $^3P_0$) and CO (J = 3-2) Lines toward the Orion A Molecular Cloud. *The Astrophysical Journal Letters*, 527:L59–L62, December 1999. doi: 10.1086/312395.

[136] M. Ikeda, T. Oka, K. Tatematsu, Y. Sekimoto, and S. Yamamoto. The Distribution of Atomic Carbon in the Orion Giant Molecular Cloud 1. *The Astrophysical Journal Supplement Series*, 139:467–485, April 2002. doi: 10.1086/338761.

[137] C. A. Kulesa, A. L. Hungerford, C. K. Walker, X. Zhang, and A. P. Lane. Large-Scale CO and [C I] Emission in the ρ Ophiuchi Molecular Cloud. *The Astrophysical Journal*, 625:194–209, May 2005. doi: 10.1086/426096.

[138] Y. Shimajiri, T. Sakai, T. Tsukagoshi, Y. Kitamura, M. Momose, M. Saito, T. Oshima, K. Kohno, and R. Kawabe. Extensive [C I] Mapping toward the Orion-A Giant Molecular Cloud. *The Astrophysical Journal Letters*, 774:L20, September 2013. doi: 10.1088/2041-8205/774/2/L20.

[139] Jan Forbrich, Karin Öberg, Charles J. Lada, Marco Lombardi, Alvaro Hacar, João Alves, and Jill M. Rathborne. Some like it cold: molecular emission and effective dust temperatures of dense cores in the Pipe Nebula. *Astronomy & Astrophysics*, 568:A27, Aug 2014. doi: 10.1051/0004-6361/201423913.

[140] W. D. Langer, T. Velusamy, J. L. Pineda, K. Willacy, and P. F. Goldsmith. A Herschel [C ii] Galactic plane survey. II. CO-dark H_2 in clouds. *Astronomy & Astrophysics*, 561:A122, January 2014. doi: 10.1051/0004-6361/201322406.

[141] Y. Aikawa, N. Ohashi, S.-i. Inutsuka, E. Herbst, and S. Takakuwa. Molecular Evolution in Collapsing Prestellar Cores. *The Astrophysical Journal*, 552:639–653, May 2001. doi: 10.1086/320551.

[142] E. A. Bergin, J. Alves, T. Huard, and C. J. Lada. N_2H^+ and $C^{18}O$ Depletion in a Cold Dark Cloud. *The Astrophysical Journal Letters*, 570:L101–L104, May 2002. doi: 10.1086/340950.

[143] S. D. Rodgers and S. B. Charnley. Interstellar diazenylium recombination and nitrogen isotopic fractionation. *Monthly Notices of the Royal Astronomical Society*, 352:600–604, August 2004. doi: 10.1111/j.1365-2966.2004.07953.x.

[144] M. Tafalla, P. C. Myers, P. Caselli, C. M. Walmsley, and C. Comito. Systematic Molecular Differentiation in Starless Cores. *The Astrophysical Journal*, 569: 815–835, April 2002. doi: 10.1086/339321.

[145] M. Tafalla, P. C. Myers, P. Caselli, and C. M. Walmsley. On the internal structure of starless cores. I. Physical conditions and the distribution of CO, CS, N_2H^+, and NH_3 in L1498 and L1517B. *Astronomy & Astrophysics*, 416: 191–212, March 2004. doi: 10.1051/0004-6361:20031704.

[146] B. T. Draine and E. E. Salpeter. On the physics of dust grains in hot gas. *The Astrophysical Journal*, 231:77–94, July 1979. doi: 10.1086/157165.

[147] D. C. Morton. Interstellar absorption lines in the spectrum of zeta Ophiuchi. *The Astrophysical Journal*, 197:85–115, April 1975. doi: 10.1086/153490.

[148] Brandt A. L. Gaches and Stella S. R. Offner. A Model for Protostellar Cluster Luminosities and the Impact on the CO-H_2 Conversion Factor. *The Astrophysical Journal*, 854:156, Feb 2018. doi: 10.3847/1538-4357/aaaae2.

[149] M. Heyer and T. M. Dame. Molecular Clouds in the Milky Way. *Annual Review of Astronomy and Astrophysics*, 53:583–629, August 2015. doi: 10.1146/annurev-astro-082214-122324.

[150] J. E. Pineda, P. Caselli, and A. A. Goodman. CO Isotopologues in the Perseus Molecular Cloud Complex: the X-factor and Regional Variations. *The Astrophysical Journal*, 679:481-496, May 2008. doi: 10.1086/586883.

[151] D. Narayanan, M. R. Krumholz, E. C. Ostriker, and L. Hernquist. A general model for the CO-H_2 conversion factor in galaxies with applications to the star formation law. *Monthly Notices of the Royal Astronomical Society*, 421:3127–3146, April 2012. doi: 10.1111/j.1365-2966.2012.20536.x.

[152] P. C. Clark and S. C. O. Glover. Does the CO-to-H_2 conversion factor depend on the star formation rate? *Monthly Notices of the Royal Astronomical Society*, 452:2057–2070, September 2015. doi: 10.1093/mnras/stv1369.

[153] C. d. P. Lagos, E. Bayet, C. M. Baugh, C. G. Lacey, T. A. Bell, N. Fanidakis, and J. E. Geach. Predictions for the CO emission of galaxies from a coupled simulation of galaxy formation and photon-dominated regions. *Monthly Notices of the Royal Astronomical Society*, 426:2142–2165, November 2012. doi: 10.1111/j.1365-2966.2012.21905.x.

[154] T. G. Bisbas, P. P. Papadopoulos, and S. Viti. Effective Destruction of CO by Cosmic Rays: Implications for Tracing H_2 Gas in the Universe. *The Astrophysical Journal*, 803:37, April 2015. doi: 10.1088/0004-637X/803/1/37.

[155] D. Narayanan and P. F. Hopkins. Why is the Milky Way X-factor constant? *Monthly Notices of the Royal Astronomical Society*, 433:1223–1229, August 2013. doi: 10.1093/mnras/stt784.

[156] D. Seifried and S. Walch. Modelling the chemistry of star forming filaments - I. H_2 and CO chemistry. *Monthly Notices of the Royal Astronomical Society*, March 2016. doi: 10.1093/mnrasl/slw035.

[157] C. Safranek-Shrader, M. R. Krumholz, C.-G. Kim, E. C. Ostriker, R. I. Klein, S. Li, C. F. McKee, and J. M. Stone. Chemistry and radiative shielding in star-forming galactic discs. *Monthly Notices of the Royal Astronomical Society*, 465:885–905, February 2017. doi: 10.1093/mnras/stw2647.

[158] M. R. Krumholz, R. I. Klein, and C. F. McKee. Radiation-hydrodynamic Simulations of the Formation of Orion-like Star Clusters. I. Implications for the Origin of the Initial Mass Function. *The Astrophysical Journal*, 740:74, October 2011. doi: 10.1088/0004-637X/740/2/74.

[159] M. R. Bate, T. S. Tricco, and D. J. Price. Collapse of a molecular cloud core to stellar densities: stellar-core and outflow formation in radiation magnetohydrodynamic simulations. *Monthly Notices of the Royal Astronomical Society*, 437:77–95, January 2014. doi: 10.1093/mnras/stt1865.

[160] P. P. Papadopoulos. A Cosmic-ray-dominated Interstellar Medium in Ultra Luminous Infrared Galaxies: New Initial Conditions for Star Formation. *The Astrophysical Journal*, 720:226–232, September 2010. doi: 10.1088/0004-637X/720/1/226.

[161] T. G. Bisbas, E. F. van Dishoeck, P. P. Papadopoulos, L. Szűcs, S. Bialy, and Z.-Y. Zhang. Cosmic-ray Induced Destruction of CO in Star-forming Galaxies. *The Astrophysical Journal*, 839:90, April 2017. doi: 10.3847/1538-4357/aa696d.

[162] C. F. McKee and S. S. R. Offner. The Protostellar Mass Function. *The Astrophysical Journal*, 716:167–180, June 2010. doi: 10.1088/0004-637X/716/1/167.

[163] F. H. Shu. Self-similar collapse of isothermal spheres and star formation. *The Astrophysical Journal*, 214:488–497, June 1977. doi: 10.1086/155274.

[164] C. F. McKee and J. C. Tan. The Formation of Massive Stars from Turbulent Cores. *The Astrophysical Journal*, 585:850–871, March 2003. doi: 10.1086/346149.

[165] C. A. Tout, O. R. Pols, P. P. Eggleton, and Z. Han. Zero-age main-seqence radii and luminosities as analytic functions of mass and metallicity. *Monthly Notices of the Royal Astronomical Society*, 281:257–262, July 1996. doi: 10.1093/mnras/281.1.257.

[166] S. S. R. Offner and H. G. Arce. Investigations of Protostellar Outflow Launching and Gas Entrainment: Hydrodynamic Simulations and Molecular Emission. *The Astrophysical Journal*, 784:61, March 2014. doi: 10.1088/0004-637X/784/1/61.

[167] K. R. Sembach, J. C. Howk, R. S. I. Ryans, and F. P. Keenan. Modeling the Warm Ionized Interstellar Medium and Its Impact on Elemental Abundance Studies. *The Astrophysical Journal*, 528:310–324, January 2000. doi: 10.1086/308173.

[168] H. J. Habing. The interstellar radiation density between 912 A and 2400 A. *Bull. Astron. Inst. Netherlands*, 19:421, January 1968.

[169] N. Indriolo, T. R. Geballe, T. Oka, and B. J. McCall. H^+_3 in Diffuse Interstellar Clouds: A Tracer for the Cosmic-Ray Ionization Rate. *The Astrophysical Journal*, 671:1736–1747, December 2007. doi: 10.1086/523036.

[170] N. Indriolo, D. A. Neufeld, M. Gerin, P. Schilke, A. O. Benz, B. Winkel, K. M. Menten, E. T. Chambers, J. H. Black, S. Bruderer, E. Falgarone, B. Godard, J. R. Goicoechea, H. Gupta, D. C. Lis, V. Ossenkopf, C. M. Persson, P. Sonnentrucker, F. F. S. van der Tak, E. F. van Dishoeck, M. G. Wolfire, and F. Wyrowski. Herschel Survey of Galactic OH^+, H_2O^+, and H_3O^+: Probing the Molecular Hydrogen Fraction and Cosmic-Ray Ionization Rate. *The Astrophysical Journal*, 800:40, February 2015. doi: 10.1088/0004-637X/800/1/40.

[171] M. Padovani, D. Galli, and A. E. Glassgold. Cosmic-ray ionization of molecular clouds. *Astronomy & Astrophysics*, 501:619–631, July 2009. doi: 10.1051/0004-6361/200911794.

[172] E. Kryukova, S. T. Megeath, J. L. Hora, R. A. Gutermuth, S. Bontemps, K. Kraemer, M. Hennemann, N. Schneider, H. A. Smith, and F. Motte. The Dependence of Protostellar Luminosity on Environment in the Cygnus-X Star-forming Complex. *Astronomical Journal*, 148:11, July 2014. doi: 10.1088/0004-6256/148/1/11.

[173] M. J. Maureira, H. G. Arce, S. S. R. Offner, M. M. Dunham, J. E. Pineda, M. Fernandez-Lopez, X. Chen, and D. Mardones. A turbulent origin for the complex envelope kinematics in the young low-mass core Per-Bolo 58. *ArXiv e-prints*, October 2017.

[174] M. L. Enoch, N. J. Evans, II, A. I. Sargent, J. Glenn, E. Rosolowsky, and P. Myers. The Mass Distribution and Lifetime of Prestellar Cores in Perseus, Serpens, and Ophiuchus. *The Astrophysical Journal*, 684:1240-1259, September 2008. doi: 10.1086/589963.

[175] F. Le Petit, M. Ruaud, E. Bron, B. Godard, E. Roueff, D. Languignon, and J. Le Bourlot. Physical conditions in the central molecular zone inferred by H_3^+. *Astronomy & Astrophysics*, 585:A105, January 2016. doi: 10.1051/0004-6361/201526658.

[176] J. Kamenetzky, N. Rangwala, and J. Glenn. Warm and cold molecular gas conditions modelled in 87 galaxies observed by the Herschel SPIRE Fourier transform spectrometer. *Monthly Notices of the Royal Astronomical Society*, 471:2917–2931, November 2017. doi: 10.1093/mnras/stx1595.

[177] E. Corbelli, J. Braine, R. Bandiera, N. Brouillet, F. Combes, C. Druard, P. Gratier, J. Mata, K. Schuster, M. Xilouris, and F. Palla. From molecules to young stellar clusters: the star formation cycle across the disk of M 33. *Astronomy & Astrophysics*, 601:A146, May 2017. doi: 10.1051/0004-6361/201630034.

[178] M. S. Yun, I. Aretxaga, M. A. Gurwell, D. H. Hughes, A. Montaña, G. Narayanan, D. Rosa-González, D. Sánchez-Argüelles, F. P. Schloerb, R. L. Snell, O. Vega, G. W. Wilson, M. Zeballos, M. Chavez, R. Cybulski, T. Díaz-Santos, V. De La Luz, N. Erickson, D. Ferrusca, H. B. Gim, M. H. Heyer, D. Iono, A. Pope, S. M. Rogstad, K. S. Scott, K. Souccar, E. Terlevich, R. Terlevich, D. Wilner, and J. A. Zavala. Early Science with the Large Millimeter Telescope: CO and [C II] Emission in the z = 4.3 AzTEC J095942.9+022938 (COSMOS AzTEC-1). *Monthly Notices of the Royal Astronomical Society*, 454: 3485–3499, December 2015. doi: 10.1093/mnras/stv1963.

[179] P. Madau and M. Dickinson. Cosmic Star-Formation History. *Annual Review of Astronomy and Astrophysics*, 52:415–486, August 2014. doi: 10.1146/annurev-astro-081811-125615.

[180] H. Chen, J. Braine, Y. Gao, J. Koda, and Q. Gu. Dense Gas in the Outer Spiral Arm of M51. *The Astrophysical Journal*, 836:101, February 2017. doi: 10.3847/1538-4357/836/1/101.

[181] Y. Gao, C. L. Carilli, P. M. Solomon, and P. A. Vanden Bout. HCN Observations of Dense Star-forming Gas in High-Redshift Galaxies. *The Astrophysical Journal Letters*, 660:L93–L96, May 2007. doi: 10.1086/518244.

[182] M. Lebrón, J. G. Mangum, R. Mauersberger, C. Henkel, A. B. Peck, K. M. Menten, A. Tarchi, and A. Weiß. Dense gas in nearby galaxies. XVII. The distribution of ammonia in NGC 253, Maffei 2, and IC 342. *Astronomy & Astrophysics*, 534:A56, October 2011. doi: 10.1051/0004-6361/201117533.

[183] P. Hofner, S. Kurtz, E. Churchwell, C. M. Walmsley, and R. Cesaroni. Massive Star Formation in the Hot, Dense Cloud Core of G9.62+0.19. *The Astrophysical Journal*, 460:359, March 1996. doi: 10.1086/176975.

[184] T. J. Sodroski, N. Odegard, E. Dwek, M. G. Hauser, B. A. Franz, I. Freedman, T. Kelsall, W. F. Wall, G. B. Berriman, S. F. Odenwald, C. Bennett, W. T. Reach, and J. L. Weiland. The Ratio of H 2 Column Density to 12CO Intensity in the Vicinity of the Galactic Center. *The Astrophysical Journal*, 452:262, October 1995. doi: 10.1086/176297.

[185] A. W. Strong, I. V. Moskalenko, O. Reimer, S. Digel, and R. Diehl. The distribution of cosmic-ray sources in the Galaxy, γ-rays and the gradient in the CO-to-H_2 relation. *Astronomy & Astrophysics*, 422:L47–L50, July 2004. doi: 10.1051/0004-6361:20040172.

[186] J. Roman-Duval, J. M. Jackson, M. Heyer, J. Rathborne, and R. Simon. Physical Properties and Galactic Distribution of Molecular Clouds Identified in the Galactic Ring Survey. *The Astrophysical Journal*, 723:492–507, November 2010. doi: 10.1088/0004-637X/723/1/492.

[187] K. M. Sandstrom, A. K. Leroy, F. Walter, A. D. Bolatto, K. V. Croxall, B. T. Draine, C. D. Wilson, M. Wolfire, D. Calzetti, R. C. Kennicutt, G. Aniano, J. Donovan Meyer, A. Usero, F. Bigiel, E. Brinks, W. J. G. de Blok, A. Crocker, D. Dale, C. W. Engelbracht, M. Galametz, B. Groves, L. K. Hunt, J. Koda, K. Kreckel, H. Linz, S. Meidt, E. Pellegrini, H.-W. Rix, H. Roussel, E. Schinnerer, A. Schruba, K.-F. Schuster, R. Skibba, T. van der Laan, P. Appleton, L. Armus, B. Brandl, K. Gordon, J. Hinz, O. Krause, E. Montiel, M. Sauvage, A. Schmiedeke, J. D. T. Smith, and L. Vigroux. The CO-to-H_2 Conversion Factor and Dust-to-gas Ratio on Kiloparsec Scales in Nearby Galaxies. *The Astrophysical Journal*, 777:5, November 2013. doi: 10.1088/0004-637X/777/1/5.

[188] T. Hosokawa, S. S. R. Offner, and M. R. Krumholz. On the Reliability of Stellar Ages and Age Spreads Inferred from Pre-main-sequence Evolutionary Models. *The Astrophysical Journal*, 738:140, September 2011. doi: 10.1088/0004-637X/738/2/140.

[189] F. H. Shu, J. Najita, E. C. Ostriker, and H. Shang. Magnetocentrifugally Driven Flows from Young Stars and Disks. V. Asymptotic Collimation into Jets. *The Astrophysical Journal Letters*, 455:L155, December 1995. doi: 10.1086/309838.

[190] N. Vaytet and T. Haugbolle. VizieR Online Data Catalog: A grid of 1D low-mass star formation models (Vaytet+, 2017). *VizieR Online Data Catalog*, 359, November 2016.

[191] M. Audard, P. Ábrahám, M. M. Dunham, J. D. Green, N. Grosso, K. Hamaguchi, J. H. Kastner, Á. Kóspál, G. Lodato, M. M. Romanova, S. L. Skinner, E. I. Vorobyov, and Z. Zhu. Episodic Accretion in Young Stars. *Protostars and Planets VI*, pages 387–410, 2014. doi: 10.2458/azu_uapress_9780816531240-ch017.

[192] W. J. Fischer, S. T. Megeath, E. Furlan, B. Ali, A. M. Stutz, J. J. Tobin, M. Osorio, T. Stanke, P. Manoj, C. A. Poteet, J. J. Booker, L. Hartmann, T. L. Wilson, P. C. Myers, and D. M. Watson. The Herschel Orion Protostar Survey: Luminosity and Envelope Evolution. *The Astrophysical Journal*, 840: 69, May 2017. doi: 10.3847/1538-4357/aa6d69.

[193] D. R. Soderblom, L. A. Hillenbrand, R. D. Jeffries, E. E. Mamajek, and T. Naylor. Ages of Young Stars. *Protostars and Planets VI*, pages 219–241, 2014. doi: 10.2458/azu_uapress_9780816531240-ch010.

[194] A. B. Fletcher and S. W. Stahler. The luminosity functions of embedded stellar clusters. 1: Method of solution and analytic results. *The Astrophysical Journal*, 435:313–328, November 1994. doi: 10.1086/174815.

[195] I. A. Grenier, J. H. Black, and A. W. Strong. The Nine Lives of Cosmic Rays in Galaxies. *Annual Review of Astronomy and Astrophysics*, 53:199–246, August 2015. doi: 10.1146/annurev-astro-082214-122457.

[196] W. D. Watson. Interstellar molecule reactions. *Reviews of Modern Physics*, 48: 513–552, October 1976. doi: 10.1103/RevModPhys.48.513.

[197] N. Indriolo, G. A. Blake, M. Goto, T. Usuda, T. Oka, T. R. Geballe, B. D. Fields, and B. J. McCall. Investigating the Cosmic-ray Ionization Rate Near the Supernova Remnant IC 443 through H^+_3 Observations. *The Astrophysical Journal*, 724:1357–1365, December 2010. doi: 10.1088/0004-637X/724/2/1357.

[198] E. Amato. The origin of galactic cosmic rays. *International Journal of Modern Physics D*, 23:1430013, May 2014. doi: 10.1142/S0218271814300134.

[199] M. Padovani, P. Hennebelle, A. Marcowith, and K. Ferrière. Cosmic-ray acceleration in young protostars. *Astronomy & Astrophysics*, 582:L13, October 2015. doi: 10.1051/0004-6361/201526874.

[200] M. Padovani, P. Hennebelle, and D. Galli. Cosmic-ray ionisation in collapsing clouds. *Astronomy & Astrophysics*, 560:A114, December 2013. doi: 10.1051/0004-6361/201322407.

[201] M. Padovani, D. Galli, P. Hennebelle, B. Commerçon, and M. Joos. The role of cosmic rays on magnetic field diffusion and the formation of protostellar discs. *Astronomy & Astrophysics*, 571:A33, November 2014. doi: 10.1051/0004-6361/201424035.

[202] L. I. Cleeves, F. C. Adams, and E. A. Bergin. Exclusion of Cosmic Rays in Protoplanetary Disks: Stellar and Magnetic Effects. *The Astrophysical Journal*, 772:5, July 2013. doi: 10.1088/0004-637X/772/1/5.

[203] M. Gounelle. The origin of short-lived radionuclides in the solar system. *New A Rev.*, 50:596–599, October 2006. doi: 10.1016/j.newar.2006.06.053.

[204] S. J. Desch, H. C. Connolly, Jr., and G. Srinivasan. An Interstellar Origin for the Beryllium 10 in Calcium-rich, Aluminum-rich Inclusions. *The Astrophysical Journal*, 602:528–542, February 2004. doi: 10.1086/380831.

[205] G. E. Bricker and M. W. Caffee. Solar Wind Implantation Model for ^{10}Be in Calcium-Aluminum Inclusions. *The Astrophysical Journal*, 725:443–449, December 2010. doi: 10.1088/0004-637X/725/1/443.

[206] M. Gounelle, M. Chaussidon, and C. Rollion-Bard. Variable and Extreme Irradiation Conditions in the Early Solar System Inferred from the Initial Abundance of ^{10}Be in Isheyevo CAIs. *The Astrophysical Journal Letters*, 763:L33, February 2013. doi: 10.1088/2041-8205/763/2/L33.

[207] C. Rab, M. Güdel, M. Padovani, I. Kamp, W.-F. Thi, P. Woitke, and G. Aresu. Stellar energetic particle ionization in protoplanetary disks around T Tauri stars. *Astronomy & Astrophysics*, 603:A96, July 2017. doi: 10.1051/0004-6361/201630241.

[208] D. Rodgers-Lee, A. M. Taylor, T. P. Ray, and T. P. Downes. The ionizing effect of low-energy cosmic rays from a class II object on its protoplanetary disc. *Monthly Notices of the Royal Astronomical Society*, 472:26–38, November 2017. doi: 10.1093/mnras/stx1889.

[209] L. Hartmann, G. Herczeg, and N. Calvet. Accretion onto Pre-Main-Sequence Stars. *Annual Review of Astronomy and Astrophysics*, 54:135–180, September 2016. doi: 10.1146/annurev-astro-081915-023347.

[210] T. Umebayashi and T. Nakano. Fluxes of Energetic Particles and the Ionization Rate in Very Dense Interstellar Clouds. *Publications of the Astronomical Society of Japan*, 33:617, 1981.

[211] L. Drury. On particle acceleration in supernova remnants. *Space Sci. Rev.*, 36: 57–60, September 1983. doi: 10.1007/BF00171901.

[212] A. V. Ivlev, M. Padovani, D. Galli, and P. Caselli. Interstellar Dust Charging in Dense Molecular Clouds: Cosmic Ray Effects. *The Astrophysical Journal*, 812:135, October 2015. doi: 10.1088/0004-637X/812/2/135.

[213] C. M. Johns-Krull. The Magnetic Fields of Classical T Tauri Stars. *The Astrophysical Journal*, 664:975–985, August 2007. doi: 10.1086/519017.

[214] J. Krause, G. Morlino, and S. Gabici. CRIME - cosmic ray interactions in molecular environments. In A. S. Borisov, V. G. Denisova, Z. M. Guseva, E. A. Kanevskaya, M. G. Kogan, A. E. Morozov, V. S. Puchkov, S. E. Pyatovsky, G. P. Shoziyoev, M. D. Smirnova, A. V. Vargasov, V. I. Galkin, S. I. Nazarov, and R. A. Mukhamedshin, editors, *34th International Cosmic Ray Conference (ICRC2015)*, volume 34 of *International Cosmic Ray Conference*, page 518, July 2015.

[215] N. J. Turner and J. F. Drake. Energetic Protons, Radionuclides, and Magnetic Activity in Protostellar Disks. *The Astrophysical Journal*, 703:2152–2159, October 2009. doi: 10.1088/0004-637X/703/2/2152.

[216] P. F. Goldsmith. Molecular Depletion and Thermal Balance in Dark Cloud Cores. *The Astrophysical Journal*, 557:736–746, August 2001. doi: 10.1086/322255.

[217] M. Padovani, A. V. Ivlev, D. Galli, and P. Caselli. Cosmic-ray ionisation in circumstellar discs. *ArXiv e-prints*, March 2018.

[218] M. N. Machida, S.-i. Inutsuka, and T. Matsumoto. Magnetic Fields and Rotations of Protostars. *The Astrophysical Journal*, 670:1198–1213, December 2007. doi: 10.1086/521779.

[219] R. M. Crutcher. Magnetic Fields in Molecular Clouds. *Annual Review of Astronomy and Astrophysics*, 50:29–63, September 2012. doi: 10.1146/annurev-astro-081811-125514.

[220] M. K. Kim, T. Hirota, M. Honma, H. Kobayashi, T. Bushimata, Y. K. Choi, H. Imai, K. Iwadate, T. Jike, S. Kameno, O. Kameya, R. Kamohara, Y. Kan-Ya, N. Kawaguchi, S. Kuji, T. Kurayama, S. Manabe, M. Matsui, N. Matsumoto, T. Miyaji, T. Nagayama, A. Nakagawa, C. S. Oh, T. Omodaka, T. Oyama, S. Sakai, T. Sasao, K. Sato, M. Sato, K. M. Shibata, Y. Tamura, and K. Yamashita. SiO Maser Observations toward Orion-KL with VERA. *Publications of the Astronomical Society of Japan*, 60:991–999, October 2008. doi: 10.1093/pasj/60.5.991.

[221] N. Crimier, C. Ceccarelli, B. Lefloch, and A. Faure. Physical structure and water line spectrum predictions of the intermediate mass protostar OMC2-FIR4. *Astronomy & Astrophysics*, 506:1229–1241, November 2009. doi: 10.1051/0004-6361/200911651.

[222] A. López-Sepulcre, V. Taquet, Á. Sánchez-Monge, C. Ceccarelli, C. Dominik, M. Kama, E. Caux, F. Fontani, A. Fuente, P. T. P. Ho, R. Neri, and Y. Shimajiri. High-angular resolution observations towards OMC-2 FIR 4: Dissecting an intermediate-mass protocluster. *Astronomy & Astrophysics*, 556:A62, August 2013. doi: 10.1051/0004-6361/201220905.

[223] E. Furlan, S. T. Megeath, M. Osorio, A. M. Stutz, W. J. Fischer, B. Ali, T. Stanke, P. Manoj, J. D. Adams, and J. J. Tobin. On the Nature of the Deeply Embedded Protostar OMC-2 FIR 4. *The Astrophysical Journal*, 786:26, May 2014. doi: 10.1088/0004-637X/786/1/26.

[224] F. Fontani, C. Ceccarelli, C. Favre, P. Caselli, R. Neri, I. R. Sims, C. Kahane, F. O. Alves, N. Balucani, E. Bianchi, E. Caux, A. Jaber Al-Edhari, A. Lopez-Sepulcre, J. E. Pineda, R. Bachiller, L. Bizzocchi, S. Bottinelli, A. Chacon-Tanarro, R. Choudhury, C. Codella, A. Coutens, F. Dulieu, S. Feng, A. Rimola, P. Hily-Blant, J. Holdship, I. Jimenez-Serra, J. Laas, B. Lefloch, Y. Oya, L. Podio, A. Pon, A. Punanova, D. Quenard, N. Sakai, S. Spezzano, V. Taquet, L. Testi, P. Theulé, P. Ugliengo, C. Vastel, A. I. Vasyunin, S. Viti, S. Yamamoto, and L. Wiesenfeld. Seeds of Life in Space (SOLIS). I. Carbon-chain growth in the Solar-type protocluster OMC2-FIR4. *Astronomy & Astrophysics*, 605:A57, September 2017. doi: 10.1051/0004-6361/201730527.

[225] L. I. Cleeves, E. A. Bergin, C. Qi, F. C. Adams, and K. I. Öberg. Constraining the X-Ray and Cosmic-Ray Ionization Chemistry of the TW Hya Protoplanetary Disk: Evidence for a Sub-interstellar Cosmic-Ray Rate. *The Astrophysical Journal*, 799:204, February 2015. doi: 10.1088/0004-637X/799/2/204.

[226] L. Ingleby, N. Calvet, G. Herczeg, A. Blaty, F. Walter, D. Ardila, R. Alexander, S. Edwards, C. Espaillat, S. G. Gregory, L. Hillenbrand, and A. Brown. Accretion Rates for T Tauri Stars Using Nearly Simultaneous Ultraviolet and Optical Spectra. *The Astrophysical Journal*, 767:112, April 2013. doi: 10.1088/0004-637X/767/2/112.

[227] E. G. Berezhko and D. C. Ellison. A Simple Model of Nonlinear Diffusive Shock Acceleration. *The Astrophysical Journal*, 526:385–399, November 1999. doi: 10.1086/307993.

[228] E. G. Berezhko. Maximum energy of cosmic rays accelerated by supernova shocks. *Astroparticle Physics*, 5:367–378, October 1996. doi: 10.1016/0927-6505(96)00037-0.

[229] A. E. Glassgold and W. D. Langer. Heating of Molecular-Hydrogen Clouds by Cosmic Rays and X-Rays. *The Astrophysical Journal*, 186:859–888, December 1973. doi: 10.1086/152552.

[230] M. E. Rudd, Y.-K. Kim, D. H. Madison, and J. W. Gallagher. Electron production in proton collisions: total cross sections. *Reviews of Modern Physics*, 57:965–994, October 1985. doi: 10.1103/RevModPhys.57.965.

[231] M. E. Rudd. Differential and total cross sections for ionization of helium and hydrogen by electrons. *Phys. Rev. A*, 44:1644–1652, August 1991. doi: 10.1103/PhysRevA.44.1644.

[232] Brandt A. L. Gaches, Stella S. R. Offner, and Thomas G. Bisbas. The Astrochemical Impact of Cosmic Rays in Protoclusters I: Molecular Cloud Chemistry. *arXiv e-prints*, art. arXiv:1905.02232, May 2019.

[233] Christopher F. McKee. Photoionization-regulated Star Formation and the Structure of Molecular Clouds. *The Astrophysical Journal*, 345:782, October 1989. doi: 10.1086/167950.

[234] A. W. Strong, I. V. Moskalenko, and V. S. Ptuskin. Cosmic-Ray Propagation and Interactions in the Galaxy. *Annual Review of Nuclear and Particle Science*, 57:285–327, November 2007. doi: 10.1146/annurev.nucl.57.090506.123011.

[235] P. Caselli, C. M. Walmsley, R. Terzieva, and Eric Herbst. The Ionization Fraction in Dense Cloud Cores. *The Astrophysical Journal*, 499:234–249, May 1998. doi: 10.1086/305624.

[236] David Hollenbach, M. J. Kaufman, D. Neufeld, M. Wolfire, and J. R. Goicoechea. The Chemistry of Interstellar OH^+, H_2O^+, and H_3O^+: Inferring the Cosmic-Ray Ionization Rates from Observations of Molecular Ions. *The Astrophysical Journal*, 754:105, Aug 2012. doi: 10.1088/0004-637X/754/2/105.

[237] S. R. Federman, J. M. C. Rawlings, S. D. Taylor, and D. A. Williams. Synthesis of interstellar CHˆ+ without OH. *Monthly Notices of the Royal Astronomical Society*, 279:L41–L46, April 1996. doi: 10.1093/mnras/279.3.L41.

[238] R. Visser, E. F. van Dishoeck, and J. H. Black. The photodissociation and chemistry of CO isotopologues: applications to interstellar clouds and circumstellar disks. *Astronomy & Astrophysics*, 503:323–343, August 2009. doi: 10.1051/0004-6361/200912129.

[239] T. G. Bisbas, A. Schruba, and E. F. van Dishoeck. Simulating the atomic and molecular content of molecular clouds using probability distributions of physical parameters. *Monthly Notices of the Royal Astronomical Society*, 485:3097–3111, May 2019. doi: 10.1093/mnras/stz405.

[240] Philipp Girichidis, Thorsten Naab, Stefanie Walch, Michał Hanasz, Mordecai-Mark Mac Low, Jeremiah P. Ostriker, Andrea Gatto, Thomas Peters, Richard Wünsch, Simon C. O. Glover, Ralf S. Klessen, Paul C. Clark, and Christian Baczynski. Launching Cosmic-Ray-driven Outflows from the Magnetized Interstellar Medium. *The Astrophysical Journal*, 816:L19, Jan 2016. doi: 10.3847/2041-8205/816/2/L19.

[241] R. Meijerink, M. Spaans, A. F. Loenen, and P. P. van der Werf. Star formation in extreme environments: the effects of cosmic rays and mechanical heating. *Astronomy & Astrophysics*, 525:A119, January 2011. doi: 10.1051/0004-6361/201015136.

[242] E. Bayet, D. A. Williams, T. W. Hartquist, and S. Viti. Chemistry in cosmic ray dominated regions. *Monthly Notices of the Royal Astronomical Society*, 414: 1583–1591, June 2011. doi: 10.1111/j.1365-2966.2011.18500.x.

[243] P. C. Clark, S. C. O. Glover, S. E. Ragan, R. Shetty, and R. S. Klessen. On the Temperature Structure of the Galactic Center Cloud G0.253+0.016. *The Astrophysical Journal Letters*, 768:L34, May 2013. doi: 10.1088/2041-8205/768/2/L34.

[244] A. W. Strong and I. V. Moskalenko. Models for galactic cosmic-ray propagation. *Advances in Space Research*, 27:717–726, 2001. doi: 10.1016/S0273-1177(01)00112-0.

[245] I. V. Moskalenko, A. W. Strong, and S. G. Mashnik. Propagation of Cosmic Rays: Nuclear Physics in Cosmic-Ray Studies. In R. C. Haight, M. B. Chadwick, T. Kawano, and P. Talou, editors, *International Conference on Nuclear Data for Science and Technology*, volume 769 of *American Institute of Physics Conference Series*, pages 1612–1617, May 2005. doi: 10.1063/1.1945315.

[246] Carmelo Evoli, Daniele Gaggero, Andrea Vittino, Giuseppe Di Bernardo, Mattia Di Mauro, Arianna Ligorini, Piero Ullio, and Dario Grasso. Cosmic-ray propagation with DRAGON2: I. numerical solver and astrophysical ingredients. *Journal of Cosmology and Astro-Particle Physics*, 2017:015, February 2017. doi: 10.1088/1475-7516/2017/02/015.

[247] L. I. Cleeves, E. A. Bergin, and F. C. Adams. Exclusion of Cosmic Rays in Protoplanetary Disks. II. Chemical Gradients and Observational Signatures. *The Astrophysical Journal*, 794:123, October 2014. doi: 10.1088/0004-637X/794/2/123.

[248] L. Oc. Drury. REVIEW ARTICLE: An introduction to the theory of diffusive shock acceleration of energetic particles in tenuous plasmas. *Reports on Progress in Physics*, 46:973–1027, August 1983. doi: 10.1088/0034-4885/46/8/002.

[249] John G. Kirk. Particle Acceleration (With 26 figures). In *Saas-Fee Advanced Course 24: Plasma Astrophysics*, page 225, January 1994.

[250] Don B. Melrose. Acceleration mechanisms. In Robert A. Meyers, editor, *Encyclopedia of Complexity and Systems Science*, pages 21–42. Springer, 2009. ISBN 978-0-387-75888-6. doi: 10.1007/978-0-387-30440-3_2. URL `https://doi.org/10.1007/978-0-387-30440-3_2`.

[251] Frank Bertoldi and Christopher F. McKee. Pressure-confined Clumps in Magnetized Molecular Clouds. *The Astrophysical Journal*, 395:140, August 1992. doi: 10.1086/171638.

[252] T. G. Bisbas, J. C. Tan, T. Csengeri, B. Wu, W. Lim, P. Caselli, R. Güsten, O. Ricken, and D. Riquelme. The inception of star cluster formation revealed by [C II] emission around an Infrared Dark Cloud. *Monthly Notices of the Royal Astronomical Society*, 478:L54–L59, July 2018. doi: 10.1093/mnrasl/sly039.

[253] I. V. Moskalenko and A. W. Strong. Production and Propagation of Cosmic-Ray Positrons and Electrons. *The Astrophysical Journal*, 493:694–707, January 1998. doi: 10.1086/305152.

[254] E. C. Stone, A. C. Cummings, F. B. McDonald, B. C. Heikkila, N. Lal, and W. R. Webber. Voyager 1 Observes Low-Energy Galactic Cosmic Rays in a Region Depleted of Heliospheric Ions. *Science*, 341:150–153, July 2013. doi: 10.1126/science.1236408.

[255] A. Dalgarno and G. W. Griffing. Energy per Ion Pair for Electron and Proton Beams in Atomic Hydrogen. *Proceedings of the Royal Society of London Series A*, 248:415–428, November 1958. doi: 10.1098/rspa.1958.0253.

[256] K. Takayanagi. Molecule Formation in Dense Interstellar Clouds. *Publications of the Astronomical Society of Japan*, 25:327, January 1973.

[257] N. Indriolo and B. J. McCall. Investigating the Cosmic-Ray Ionization Rate in the Galactic Diffuse Interstellar Medium through Observations of H^+_3. *The Astrophysical Journal*, 745:91, January 2012. doi: 10.1088/0004-637X/745/1/91.

[258] L. P. Theard and W. T. Huntress. Ion-molecule reactions and vibrational deactivation of $H_2{}^+$ ions in mixtures of hydrogen and helium. *JChPh*, 60:2840–2848, April 1974. doi: 10.1063/1.1681453.

[259] J. B. A. Mitchell. The dissociative recombination of molecular ions. *PhR*, 186: 215–248, 1990.

[260] Z. Karpas, V. Anicich, and W. T. Huntress. An ion cyclotron resonance study of reactions of ions with hydrogen atoms. *JChPh*, 70:2877–2881, March 1979. doi: 10.1063/1.437823.

[261] B. J. McCall, A. J. Huneycutt, R. J. Saykally, N. Djuric, G. H. Dunn, J. Semaniak, O. Novotny, A. Al-Khalili, A. Ehlerding, F. Hellberg, S. Kalhori, A. Neau, R. D. Thomas, A. Paal, F. Österdahl, and M. Larsson. Dissociative recombination of rotationally cold H^+_3. *Phys. Rev. A*, 70(5):052716, November 2004. doi: 10.1103/PhysRevA.70.052716.

[262] S. J. Klippenstein, Y. Georgievskii, and B. J. McCall. Temperature Dependence of Two Key Interstellar Reactions of H3+: O(3P) + H3+and CO + H3+. *Journal of Physical Chemistry A*, 114:278–290, January 2010. doi: 10.1021/jp908500h.

[263] J. K. Jørgensen. Imaging chemical differentiation around the low-mass protostar L483-mm. *Astronomy & Astrophysics*, 424:589–601, September 2004. doi: 10.1051/0004-6361:20040247.

[264] S. Storm, L. G. Mundy, K. I. Lee, M. Fernández-López, L. W. Looney, P. Teuben, H. G. Arce, E. W. Rosolowsky, A. M. Meisner, A. Isella, J. Kauffmann, Y. L. Shirley, W. Kwon, A. L. Plunkett, M. W. Pound, D. M. Segura-Cox, K. Tassis, J. J. Tobin, N. H. Volgenau, R. M. Crutcher, and L. Testi. CARMA Large Area Star Formation Survey: Dense Gas in the Young L1451 Region of Perseus. *The Astrophysical Journal*, 830:127, October 2016. doi: 10.3847/0004-637X/830/2/127.

[265] J. Pety, V. V. Guzmán, J. H. Orkisz, H. S. Liszt, M. Gerin, E. Bron, S. Bardeau, J. R. Goicoechea, P. Gratier, F. Le Petit, F. Levrier, K. I. Öberg, E. Roueff, and A. Sievers. The anatomy of the Orion B giant molecular cloud: A local template for studies of nearby galaxies. *Astronomy & Astrophysics*, 599:A98, January 2017. doi: 10.1051/0004-6361/201629862.

[266] M. W. Pound and F. Yusef-Zadeh. The CARMA 3 mm survey of the inner 0.7 deg x 0.4 deg of the Central Molecular Zone. *Monthly Notices of the Royal Astronomical Society*, 473:2899–2929, January 2018. doi: 10.1093/mnras/stx2490.

[267] Ewine F. van Dishoeck. Astrochemistry of dust, ice and gas: introduction and overview. *Faraday Discussions*, 168:9, Jan 2014. doi: 10.1039/C4FD00140K.

[268] Jes K. Jørgensen, Ruud Visser, Nami Sakai, Edwin A. Bergin, Christian Brinch, Daniel Harsono, Johan E. Lindberg, Ewine F. van Dishoeck, Satoshi Yamamoto, Suzanne E. Bisschop, and Magnus V. Persson. A Recent Accretion Burst in the Low-mass Protostar IRAS 15398-3359: ALMA Imaging of Its Related Chemistry. *The Astrophysical Journal*, 779:L22, Dec 2013. doi: 10.1088/2041-8205/779/2/L22.

[269] J. K. Jørgensen, R. Visser, J. P. Williams, and E. A. Bergin. Molecule sublimation as a tracer of protostellar accretion. Evidence for accretion bursts from high angular resolution $C^{18}O$ images. *Astronomy & Astrophysics*, 579:A23, Jul 2015. doi: 10.1051/0004-6361/201425317.

[270] C. de Boisanger, F. P. Helmich, and E. F. van Dishoeck. The ionization fraction in dense clouds. *Astronomy & Astrophysics*, 310:315–327, June 1996.

[271] F. F. S. van der Tak and E. F. van Dishoeck. Limits on the cosmic-ray ionization rate toward massive young stars. *Astronomy & Astrophysics*, 358:L79–L82, June 2000.

[272] D. A. Neufeld, J. R. Goicoechea, P. Sonnentrucker, J. H. Black, J. Pearson, S. Yu, T. G. Phillips, D. C. Lis, M. de Luca, E. Herbst, P. Rimmer, M. Gerin, T. A. Bell, F. Boulanger, J. Cernicharo, A. Coutens, E. Dartois, M. Kazmierczak, P. Encrenaz, E. Falgarone, T. R. Geballe, T. Giesen, B. Godard, P. F. Goldsmith, C. Gry, H. Gupta, P. Hennebelle, P. Hily-Blant, C. Joblin, R. Kołos, J. Krełowski, J. Martín-Pintado, K. M. Menten, R. Monje, B. Mookerjea, M. Perault, C. Persson, R. Plume, M. Salez, S. Schlemmer, M. Schmidt, J. Stutzki, D. Teyssier, C. Vastel, A. Cros, K. Klein, A. Lorenzani, S. Philipp, L. A. Samoska, R. Shipman, A. G. G. M. Tielens, R. Szczerba, and J. Zmuidzinas. Herschel/HIFI observations of interstellar OH^+ and H_2O^+ towards W49N: a probe of diffuse clouds with a small molecular fraction. *Astronomy & Astrophysics*, 521:L10, October 2010. doi: 10.1051/0004-6361/201015077.

[273] David A. Neufeld and Mark G. Wolfire. The Cosmic-Ray Ionization Rate in the Galactic Disk, as Determined from Observations of Molecular Ions. *The Astrophysical Journal*, 845:163, August 2017. doi: 10.3847/1538-4357/aa6d68.

[274] Tobias Albertsson, Jens Kauffmann, and Karl M. Menten. Atlas of Cosmic-Ray-induced Astrochemistry. *The Astrophysical Journal*, 868:40, November 2018. doi: 10.3847/1538-4357/aae775.

[275] Paul C. Clark, Simon C. O. Glover, Ralf S. Klessen, and Ian A. Bonnell. How long does it take to form a molecular cloud? *Monthly Notices of the Royal Astronomical Society*, 424:2599–2613, Aug 2012. doi: 10.1111/j.1365-2966.2012.21259.x.

[276] D. Seifried, S. Walch, P. Girichidis, T. Naab, R. Wünsch, R. S. Klessen, S. C. O. Glover, T. Peters, and P. Clark. SILCC-Zoom: the dynamic and chemical evolution of molecular clouds. *Monthly Notices of the Royal Astronomical Society*, 472:4797–4818, Dec 2017. doi: 10.1093/mnras/stx2343.

[277] P. B. Rimmer, E. Herbst, O. Morata, and E. Roueff. Observing a column-dependent ζ in dense interstellar sources: the case of the Horsehead nebula. *Astronomy & Astrophysics*, 537:A7, Jan 2012. doi: 10.1051/0004-6361/201117048.

[278] J. L. Pineda, W. D. Langer, T. Velusamy, and P. F. Goldsmith. A Herschel [C ii] Galactic plane survey. I. The global distribution of ISM gas components. *Astronomy & Astrophysics*, 554:A103, Jun 2013. doi: 10.1051/0004-6361/201321188.

[279] Paul C. Clark, Simon C. O. Glover, Sarah E. Ragan, and Ana Duarte-Cabral. Tracing the formation of molecular clouds via [C II], [C I] and CO emission. *Monthly Notices of the Royal Astronomical Society*, page 1076, Apr 2019. doi: 10.1093/mnras/stz1119.

[280] A. A. Goodman, P. J. Benson, G. A. Fuller, and P. C. Myers. Dense Cores in Dark Clouds. VIII. Velocity Gradients. *The Astrophysical Journal*, 406:528, Apr 1993. doi: 10.1086/172465.

[281] J. Jijina, P. C. Myers, and Fred C. Adams. Dense Cores Mapped in Ammonia: A Database. *The Astrophysical Journal Supplement Series*, 125:161–236, Nov 1999. doi: 10.1086/313268.

[282] M. Wienen, F. Wyrowski, F. Schuller, K. M. Menten, C. M. Walmsley, L. Bronfman, and F. Motte. Ammonia from cold high-mass clumps discovered in the inner Galactic disk by the ATLASGAL survey. *Astronomy & Astrophysics*, 544: A146, Aug 2012. doi: 10.1051/0004-6361/201118107.

[283] P. Caselli and C. Ceccarelli. Our astrochemical heritage. *A&A Rv*, 20:56, October 2012. doi: 10.1007/s00159-012-0056-x.

[284] E. Redaelli, F. O. Alves, P. Caselli, J. E. Pineda, R. K. Friesen, A. Chacón-Tanarro, C. D. Matzner, A. Ginsburg, E. Rosolowsky, J. Keown, S. S. R. Offner, J. Di Francesco, H. Kirk, P. C. Myers, A. Hacar, A. Cimatti, H. H. Chen, M. C. Chen, K. I. Lee, and Y. M. Seo. The Green Bank Ammonia Survey: Unveiling the Dynamics of the Barnard 59 Star-forming Clump. *The Astrophysical Journal*, 850:202, Dec 2017. doi: 10.3847/1538-4357/aa9703.

[285] S. J. Kenyon, L. W. Hartmann, K. M. Strom, and S. E. Strom. An IRAS survey of the Taurus-Auriga molecular cloud. *Astronomical Journal*, 99:869–887, March 1990. doi: 10.1086/115380.

[286] E. I. Vorobyov. Variable Accretion in the Embedded Phase of Star Formation. *The Astrophysical Journal*, 704:715–723, October 2009. doi: 10.1088/0004-637X/704/1/715.

[287] Karin I. Öberg. Photochemistry and astrochemistry: Photochemical pathways to interstellar complex organic molecules. *Chemical Reviews*, 116(17):9631–9663, 2016. doi: 10.1021/acs.chemrev.5b00694. URL `https://doi.org/10.1021/acs.chemrev.5b00694`. PMID: 27099922.

[288] Tatsuhiko I. Hasegawa and Eric Herbst. New gas-grain chemical models of quiscent dense interstellar clouds :the effects of H2 tunnelling reactions and cosmic ray induced desorption. *Monthly Notices of the Royal Astronomical Society*, 261:83–102, Mar 1993. doi: 10.1093/mnras/261.1.83.

[289] S. Frimann, J. K. Jørgensen, P. Padoan, and T. Haugbølle. Protostellar accretion traced with chemistry. Comparing synthetic $C^{18}O$ maps of embedded protostars to real observations. *Astronomy & Astrophysics*, 587:A60, Feb 2016. doi: 10.1051/0004-6361/201527622.

[290] Thomas J. Haworth, Simon C. O. Glover, Christine M. Koepferl, Thomas G. Bisbas, and James E. Dale. Synthetic observations of star formation and the interstellar medium. *New Astronomy Reviews*, 82:1–58, Aug 2018. doi: 10.1016/j.newar.2018.06.001.

[291] C. Baczynski, S. C. O. Glover, and R. S. Klessen. <monospace>Fervent</monospace>: chemistry-coupled, ionizing and non-ionizing radiative feedback in hydrodynamical simulations. *Monthly Notices of the Royal Astronomical Society*, 454:380–411, Nov 2015. doi: 10.1093/mnras/stv1906.

[292] R. Wünsch, S. Walch, F. Dinnbier, and A. Whitworth. Tree-based solvers for adaptive mesh refinement code FLASH - I: gravity and optical depths. *Monthly Notices of the Royal Astronomical Society*, 475:3393–3418, Apr 2018. doi: 10.1093/mnras/sty015.

[293] A. L. Rosen, M. R. Krumholz, J. S. Oishi, A. T. Lee, and R. I. Klein. Hybrid Adaptive Ray-Moment Method (HARM^2): A highly parallel method for radiation hydrodynamics on adaptive grids. *Journal of Computational Physics*, 330:924–942, Feb 2017. doi: 10.1016/j.jcp.2016.10.048.

[294] Dominik A. Riechers, Riccardo Pavesi, Chelsea E. Sharon, Jacqueline A. Hodge, Roberto Decarli, Fabian Walter, Christopher L. Carilli, Manuel Aravena, Elisabete da Cunha, Emanuele Daddi, Mark Dickinson, Ian Smail, Peter L. Capak, Rob J. Ivison, Mark Sargent, Nicholas Z. Scoville, and Jeff Wagg. COLDz: Shape of the CO Luminosity Function at High Redshift and the Cold Gas History of the Universe. *The Astrophysical Journal*, 872(1):7, Feb 2019. doi: 10.3847/1538-4357/aafc27.

[295] Simon C. O. Glover and Paul C. Clark. Is atomic carbon a good tracer of molecular gas in metal-poor galaxies? *Monthly Notices of the Royal Astronomical Society*, 456(4):3596–3609, Mar 2016. doi: 10.1093/mnras/stv2863.

[296] Q. Remy, I. A. Grenier, D. J. Marshall, and J. M. Casandjian. Cosmic rays, gas and dust in nearby anticentre clouds. I. CO-to-H_2 conversion factors and dust opacities. *Astronomy & Astrophysics*, 601:A78, May 2017. doi: 10.1051/0004-6361/201629632.

[297] Padelis P. Papadopoulos, Thomas G. Bisbas, and Zhi-Yu Zhang. New places and phases of CO-poor/C I-rich molecular gas in the Universe. *Monthly Notices of the Royal Astronomical Society*, 478(2):1716–1725, Aug 2018. doi: 10.1093/mnras/sty1077.

[298] M. Gong, E. C. Ostriker, and C.-G. Kim. The X $_{CO}$ Conversion Factor from Galactic Multiphase ISM Simulations. *The Astrophysical Journal*, 858:16, May 2018. doi: 10.3847/1538-4357/aab9af.

[299] N. Lo, M. R. Cunningham, P. A. Jones, L. Bronfman, P. C. Cortes, R. Simon, V. Lowe, L. Fissel, and G. Novak. Tracing H_2 Column Density with Atomic Carbon (C I) and CO Isotopologs. *The Astrophysical Journal*, 797(2):L17, Dec 2014. doi: 10.1088/2041-8205/797/2/L17.

[300] D. Downes and P. M. Solomon. Rotating Nuclear Rings and Extreme Starbursts in Ultraluminous Galaxies. *The Astrophysical Journal*, 507(2):615–654, Nov 1998. doi: 10.1086/306339.

[301] Padeli P. Papadopoulos and E. R. Seaquist. The State of the Molecular Gas in a Luminous Starburst/Seyfert 2 Galaxy: NGC 1068 Revisited. *The Astrophysical Journal*, 516(1):114–126, May 1999. doi: 10.1086/307090.

[302] Padelis P. Papadopoulos, Paul van der Werf, E. Xilouris, Kate G. Isaak, and Yu Gao. The Molecular Gas in Luminous Infrared Galaxies. II. Extreme Physical Conditions and Their Effects on the X_{co} Factor. *The Astrophysical Journal*, 751(1):10, May 2012. doi: 10.1088/0004-637X/751/1/10.

[303] Dragan Salak, Naomasa Nakai, and Shoko Kitamoto. CO (J = 3 - 2) observations of the starburst galaxy NGC 1808 with ASTE. *Publications of the Astronomical Society of Japan*, 66(5):96, Oct 2014. doi: 10.1093/pasj/psu074.

[304] R. Meijerink, M. Spaans, and F. P. Israel. Irradiated ISM: Discriminating between Cosmic Rays and X-Rays. *The Astrophysical Journal*, 650:L103–L106, Oct 2006. doi: 10.1086/508938.

[305] Ewine F. van Dishoeck and John H. Black. The Photodissociation and Chemistry of Interstellar CO. *The Astrophysical Journal*, 334:771, Nov 1988. doi: 10.1086/166877.

[306] B. T. Draine and Frank Bertoldi. Structure of Stationary Photodissociation Fronts. *The Astrophysical Journal*, 468:269, Sep 1996. doi: 10.1086/177689.

[307] Jeong-Eun Lee, Edwin A. Bergin, and II Evans, Neal J. Evolution of Chemistry and Molecular Line Profiles during Protostellar Collapse. *The Astrophysical Journal*, 617(1):360–383, Dec 2004. doi: 10.1086/425153.

[308] J. Stutzki, F. Bensch, A. Heithausen, V. Ossenkopf, and M. Zielinsky. On the fractal structure of molecular clouds. *Astronomy & Astrophysics*, 336:697–720, Aug 1998.

[309] S. C. O. Glover and M.-M. Mac Low. Simulating the Formation of Molecular Clouds. I. Slow Formation by Gravitational Collapse from Static Initial Conditions. *The Astrophysical Journal Supplement Series*, 169:239–268, April 2007. doi: 10.1086/512238.

[310] John H. Wise and Tom Abel. ENZO+MORAY: radiation hydrodynamics adaptive mesh refinement simulations with adaptive ray tracing. *Monthly Notices of the Royal Astronomical Society*, 414(4):3458–3491, Jul 2011. doi: 10.1111/j.1365-2966.2011.18646.x.

[311] T. J. Harries. Radiation-hydrodynamical simulations of massive star formation using Monte Carlo radiative transfer - I. Algorithms and numerical methods. *Monthly Notices of the Royal Astronomical Society*, 448:3156–3166, April 2015. doi: 10.1093/mnras/stv158.

[312] T. J. Harries, T. J. Haworth, D. Acreman, A. Ali, and T. Douglas. The TORUS radiation transfer code. *Astronomy and Computing*, 27:63, Apr 2019. doi: 10.1016/j.ascom.2019.03.002.

[313] P. S. Li, D. F. Martin, R. I. Klein, and C. F. McKee. A Stable, Accurate Methodology for High Mach Number, Strong Magnetic Field MHD Turbulence with Adaptive Mesh Refinement: Resolution and Refinement Studies. *The Astrophysical Journal*, 745:139, February 2012. doi: 10.1088/0004-637X/745/2/139.

[314] Christopher D. Matzner and Christopher F. McKee. Bipolar Molecular Outflows Driven by Hydromagnetic Protostellar Winds. *The Astrophysical Journal*, 526 (2):L109–L112, Dec 1999. doi: 10.1086/312376.

[315] Andrew J. Cunningham, Richard I. Klein, Mark R. Krumholz, and Christopher F. McKee. Radiation-hydrodynamic Simulations of Massive Star Formation with Protostellar Outflows. *The Astrophysical Journal*, 740(2):107, Oct 2011. doi: 10.1088/0004-637X/740/2/107.

[316] Anna T. P. Schauer, Bhaskar Agarwal, Simon C. O. Glover, Ralf S. Klessen, Muhammad A. Latif, Lluís Mas-Ribas, Claes-Erik Rydberg, Daniel J. Whalen, and Erik Zackrisson. Lyman-Werner escape fractions from the first galaxies. *Monthly Notices of the Royal Astronomical Society*, 467(2):2288–2300, May 2017. doi: 10.1093/mnras/stx264.

[317] Leisa K. Townsley, Patrick S. Broos, Gordon P. Garmire, Gemma E. Anderson, Eric D. Feigelson, Tim Naylor, and Matthew S. Povich. The Massive Star-forming Regions Omnibus X-ray Catalog, Second Installment. *The Astrophysical Journal Supplement Series*, 235(2):43, Apr 2018. doi: 10.3847/1538-4365/aaaf67.

[318] E. Winston, S. J. Wolk, R. Gutermuth, and T. L. Bourke. Chandra Detection of an Evolved Population of Young Stars in Serpens South. *Astronomical Journal*, 155(6):241, Jun 2018. doi: 10.3847/1538-3881/aabe82.

[319] S. P. Reynolds. Supernova remnants at high energy. *Annual Review of Astronomy and Astrophysics*, 46:89–126, Sep 2008. doi: 10.1146/annurev.astro.46.060407.145237.

[320] M. L. McCollough, R. K. Smith, and L. A. Valencic. Cygnus X-3's Little Friend. *The Astrophysical Journal*, 762(1):2, Jan 2013. doi: 10.1088/0004-637X/762/1/2.

[321] M. L. McCollough, L. Corrales, and M. M. Dunham. Cygnus X-3: Its Little Friend's Counterpart, the Distance to Cygnus X-3, and Outflows/Jets. *The Astrophysical Journal*, 830(2):L36, Oct 2016. doi: 10.3847/2041-8205/830/2/L36.